IPP-Report

Max-Planck-Institut für Plasmaphysik

Jurrian Boom

# Characterization of edge localized modes in tokamak plasmas

**IPP 10/47**
**Februar, 2013**

# Characterization of edge localized modes in tokamak plasmas

Jurrian Boom

# Characterization of edge localized modes in tokamak plasmas

PROEFSCHRIFT

ter verkrijging van de graad van doctor aan de
Technische Universiteit Eindhoven, op gezag van de
rector magnificus, prof.dr.ir. C.J. van Duijn, voor een
commissie aangewezen door het College voor
Promoties in het openbaar te verdedigen
op woensdag 7 november 2012 om 14.00 uur

door

Jurrian Esmond Boom
geboren te Eindhoven

Dit proefschrift is goedgekeurd door de promotor:

prof.dr. A.J.H. Donné

Copromotoren:
dr. P.C. de Vries
en
dr.ir. I.G.J. Classen

A catalogue record is available from the Eindhoven University of Technology Library

Boom, J.E.
Characterization of edge localized modes in tokamak plasmas /
by Jurrian Boom.- Eindhoven : Technische Universiteit Eindhoven, 2012.
Proefschrift.
ISBN : 978-90-386-3258-2
NUR : 926

Trefwoorden: plasmafysica / kernfusie / tokamaks / magnetohydrodynamica / plasma instabiliteit / plasmadiagnostiek
Subject headings: plasma physics / nuclear fusion / tokamaks / magnetohydrodynamics / plasma instability / plasma diagnostics

This work described in this thesis was performed as part of a research programme of the Foundation for Fundamental Research on Matter (FOM) with financial support from the Netherlands Organisation for Scientific Research (NWO), the Max-Planck-Institut für Plasmaphysik (IPP) and EURATOM. It was carried out at the Max-Planck-Institut für Plasmaphysik (IPP) in collaboration with FOM Institute DIFFER. The views and opinions expressed herein do not necessarily reflect those of the European Commission.

Cover design : Alan Boom / image of an ELM tree

*Aan Gundula en Casimir*

# Samenvatting

Aan het begin van de twintigste eeuw ontdekten wetenschappers het proces dat de zon doet branden: kernfusie. Ze realiseerden zich toen vrijwel direct dat het controleren van dit proces mogelijk ook een enorme bron van energie zou kunnen zijn op aarde. Om de fusie reactie (deuterium-tritium) tot stand te brengen, moeten de waterstof isotopen wederzijds binnen de reikwijdte van de aantrekkingskracht van de kernkracht komen. Hiervoor moet de omgeving een extreem hoge temperatuur hebben (meer dan 100 miljoen K), waardoor alle atomen volledig geioniseerd worden en een plasma vormen. Deze ionisatie van de deeltjes biedt de mogelijkheid om zo'n plasma magnetisch op te sluiten. Tot nu toe lukt dit het beste in een tokamak. Een tokamak is een torusvormige machine, waarin magnetische veldlijnen een helisch pad rond de torus volgen.

In een efficiënte fusie reactor moet het plasma niet alleen bij hoge temperatuur worden opgesloten maar ook bij hoge dichtheid. Bovendien moet de energie opsluitingstijd lang genoeg zijn om te voorkomen dat de opgewekte fusie energie al te snel wegvloeit. Wanneer zowel de temperatuur als de dichtheid toeneemt, stijgt de plasma druk. Boven een zekere drempelwaarde ondergaat het plasma een bifurcatie van een lage naar een hoge opsluitingstoestand: de zogenaamde H-mode. In de H-mode, echter, lijdt de opsluiting onder een instabiliteit die ELM genoemd wordt (in het Engels 'Edge Localized Mode'). Gedurende het cyclisch instorten van de plasmarand, worden door de ELM instabiliteit hete delen van het opgesloten plasma uitgeworpen. Voor grote tokamaks zoals ITER (die op dit moment gebouwd wordt om de haalbaarheid van kernfusie als energiebron aan te tonen) kunnen de uitgeworpen filamenten een niet te tolereren warmtebelasting vormen voor de componenten van de machine die naar het plasma toe gericht zijn.

ELMs zijn een complex fenomeen en het analyseren ervan heeft zich tegenwoordig ontwikkeld tot een belangrijke tak binnen het kernfusie onderzoek. Tot nu toe zijn verschillende typen ELMs geclassificeerd: naast het meest voorkomende, maar ook het meest agressieve regiem van type-I ELMs zijn er ook omstandigheden waaronder de impact van ELMs veel goedaardiger is (bijvoorbeeld in de regiems van kleine ELMs zoals type-II en/of -III). Om het gedrag van ELMs te kunnen voorspellen voor grotere tokamaks is het cruciaal om de fysica van ELMs te begrijpen en een consistent model te ontwikkelen voor de verliezen tijdens ELMs. Tegelijkertijd is er nog steeds intensief onderzoek gaande op het gebied van kleine ELMs, afwezigheid van ELMs en actieve controle van ELMs.

Het werk, beschreven in dit proefschrift, is uitgevoerd op ASDEX Upgrade (AUG), een tokamak die goed uitgerust is om een aantal van de hierboven genoemde onderwerpen te behandelen. Op AUG worden plasmas in de H-mode routinematig gemaakt en verschillende soorten van ELM-regiems verkregen. Het belangrijkste instrument gebruikt voor het onderzoek van ELMs is de Electron Cyclotron Emissie imaging (afbeeldings) diagnostiek (ECEI). Deze diagnostiek werd op AUG geïnstalleerd als onderdeel van dit project. ECEI is een diagnostiek die een 2D meting levert van de electronentemperatuur ($T_e$) met de hoge ruimtelijke en tijdsresolutie die nodig is om de dynamica van ELMs vast te leggen. De 2D eigenschap maakt het mogelijk om $T_e$ fluctuaties te volgen in de verticale richting, in de poloïdale doorsnede waar de metingen opgenomen worden. Met de ECEI diagnostiek kwam voor het eerst de mogelijkheid beschikbaar om de verscheidenheid van $T_e$ fluctuaties geassocieerd met verschillende ELM-typen te observeren. Het beschrijven van de karakteristieken en de dynamica van deze verschillende modes en hun rol in de ELM-cyclus vormt het belangrijkste deel van dit werk.

In de type-I ELM-cyclus zijn drie verschillende soorten $T_e$ fluctuaties geobserveerd. Ten eerste, in de laatste paar tientallen $\mu$s voor de ELM crash is een mode waargenomen die roteert in de richting van de electronen diamagnetische drift. Gedurende zijn korte levensduur is gezien dat het poloïdale modegetal toeneemt, tegelijk met een toename van de poloïdale snelheid. Dit wordt gevolgd door de eigenlijke ELM crash, d.w.z. het zeer snel afnemen van de temperatuur van de plasmarand. Gedurende deze fase, ten tweede, zijn meerdere filament-achtige structuren geobserveerd net buiten de rand van het opgesloten plasma. De meesten van deze filamenten roteren in dezelfde richting als de mode die gezien is vlak voor de crash, hoewel soms ook gezien is dat de eerste voorbijkomende filamenten in de tegenovergestelde richting roteren. Een derde vorm van $T_e$ fluctuatie die is gezien, is gerelateerd aan het verschil tussen lange en korte ELM periodes (ook wel ‘langzame’ en ‘snelle’ ELMs genoemd). Deze mode wordt eigenlijk alleen gevonden vóór een langzame ELM en vertoont een uitgesproken poloïdale asymmetrie van zijn amplitude: de amplitude van de $T_e$ fluctuatie heeft een minimum op het equatoriaalvlak en maxima daarboven en -beneden. Hoewel de aanwezigheid van deze mode niet de gehele duur bestrijkt van het verschil tussen de langzame ELM-cyclus vergeleken met de snelle, suggereert dit toch dat deze fluctuatie de plasmarand op een dusdanige manier reguleert dat een stabiele situatie een paar ms langer standhoudt tot de $T_e$ crash komt.

Het type-II ELM-regiem is een regiem van kleine ELMs dat een goede opsluiting combineert met lage energieverliezen. Het wordt bereikt door een sterk driehoekig gevormd plasma met hoge randdichtheid en wordt op AUG regelmatig verkregen. Metingen met ECEI hebben een breedbandige $T_e$ fluctuatie laten zien, karakteristiek voor type-II ELMs. Deze mode bevindt zich net aan de binnenkant van de top van de transportbarrière aan de rand en vlakt hier het $T_e$ profiel compleet af, tegelijkertijd blijft de gradient van de pedestal (d.w.z. de stap-vorm van het temperatuursprofiel) onveranderd. Bij middeling over langere tijd laat de 2D verdeling van de amplitude van deze fluctuatie ook een uitgesproken minimum zien rond het equatoriaalvlak. De observatie van een zweving met een lage zwevingsfrequentie suggereert dat de breedbandige eigenschap in feite veroorzaakt wordt door de coëxistentie van meerdere modes met licht verschillende modegetallen of frequenties.

Sinds de installatie van een set spoelen voor magnetische stoorvelden dicht bij het plasma (in de loop van dit project) is het mogelijk geworden op AUG om omstandigheden te bereiken waaronder de grote type-I ELMs onderdrukt zijn. Het precieze mechanisme dat deze onderdrukking veroorzaakt is nog niet volledig begrepen (in het bijzonder lijkt de rol van de drempelwaarde van de electronendichtheid aan de rand kritisch). Hoewel sommige van de eigenschappen van de kleine ELMs (die overblijven na het onderdrukken van de type-I ELMs) vergelijkbaar zijn met type-I en/of type-II ELMs, kunnen deze kleine ELMs duidelijk onderscheiden worden van beide typen. Vergeleken met type-I ELMs vertonen de kleine ELMs een tegengesteld verband met betrekking tot veranderingen van de dichtheid aan de rand: waar de type-I ELM frequentie afneemt met toenemende dichtheid neemt de frequentie van de kleine ELMs juist toe. Het grote verschil tussen deze kleine ELMs en de type-II ELMs is dat de laatste continue $T_e$ fluctuaties laten zien, terwijl de $T_e$ fluctuaties bij de kleine ELMs enkel voor een korte duur gezien worden. Het is bovendien ook niet eenvoudig om een direct verband te leggen tussen deze kleine ELMs en de type-III ELMs die gezien worden direct na de overgang naar de H-mode. Als het toch zou blijken, ondanks wat verschillen, dat de kleine ELMs het meest verwant zijn met de type-III ELMs, kan dit bijdragen aan een verklaring voor het feit dat in sommige gevallen de type-I ELMs al onderdrukt worden voordat de magnetische stoorvelden ingeschakeld zijn.

Hoewel de verschillende typen modes gemeten met ECEI in de diverse ELM-regiems eigenschappen vertonen waarmee ze duidelijk van elkaar zijn te onderscheiden, zijn er ook overeenkomsten die de verscheidene observaties met elkaar verbinden. Een vergelijkbare poloïdale asymmetrie wordt bijvoorbeeld gevonden in de amplitude van zowel de mode die alleen in de langzame type-I ELM-cyclus gezien is, als in de breedband $T_e$ flucuatie die de type-II ELM karakteriseert. Waar, bovendien, de ene mode de komst van de volgende $T_e$ crash lijkt te vertragen (in de type-I ELM-cyclus), lijkt de andere mode de volledige afwezigheid van $T_e$ crashes te veroorzaken (in het geval van type-II ELMs). Beide modes hebben ook vergelijkbaar hoge poloïdale modegetallen. Een andere overeenkomst die de verschillende ELM typen met elkaar verbindt wordt geobserveerd tijdens de overgang naar kleine ELMs. Bij zowel de overgang van type-I naar type-II als van type-I naar de kleine ELMs die overblijven als de type-I ELMs afgezwakt zijn bij het gebruik van magnetische stoorvelden, worden de ELMs van het vervangende type al gezien voordat het voorkomen van type-I ELMs gestopt is.

Tenslotte: alle geobserveerde modes (m.u.v. de filamenten) roteren in dezelfde richting, bevinden zich in de buurt van de top van de transportbarrière aan de rand, en bestaan uit (meerdere) coherente oscillaties in hetzelfde frequentiebereik met middelhoge tot hoge poloïdale modegetallen. Deze eigenschappen suggereren dat de geobserveerde modes inderdaad (peeling-) ballooning-modes zijn; het meest geaccepteerde theoretische model dat de lineaire aanzet tot de ELM crash beschrijft.

# Summary

In the early twentieth century, scientists found out what process keeps the Sun burning: nuclear fusion. At that time, they almost instantly realized that controlling this process could also be a huge potential energy source on Earth. In order to make the fusion reaction (deuterium-tritium) happen, the hydrogen isotopes must be within the mutual attraction range of their nuclear forces. This requires an environment of extremely high temperature (more than 100 million K), in which all atoms are fully ionized and form a plasma. The ionization of the particles offers an opportunity to magnetically confine such a plasma. To date, this is most successfully done with the tokamak concept. A tokamak is a device in the shape of a torus, where magnetic field lines follow helical paths around the torus.

In an efficient fusion reactor, the plasma must not only be contained at high temperature, but also at high density. Moreover, the energy confinement time should be sufficiently long to prevent the generated fusion energy from being released too fast. When temperature and density are increased, the plasma pressure rises. At a certain threshold, a bifurcation occurs that brings the plasma from a low- to a high-confinement state: the so-called H-mode. In the H-mode, however, the confinement suffers from an instability known as the edge localized mode (ELM). During a cyclic collapse of the plasma edge, the ELM instability ejects hot parts of the confined plasma. For large tokamaks such as ITER (which is currently being built to demonstrate the viability of nuclear fusion as an energy source) the ejected filaments could lead to intolerable power loads on the plasma facing components of the device.

ELMs are a complex phenomenon and their survey has developed into an important field of contemporary nuclear fusion research. Hitherto, various types of ELMs have been classified: apart from the most common, but also most violent, type-I ELM regime, there are also conditions under which the impact of ELMs is more benign (e.g. in the small ELM regimes of type-II and/or -III). In order to predict ELM behaviour in larger tokamaks, understanding ELM physics and developing a consistent model of ELM losses is crucial. Simultaneously, intensive research is still ongoing in the areas of small or no ELM regimes and active ELM control.

The work described in this thesis has been conducted at ASDEX Upgrade (AUG), a tokamak well suited to address several of the topics mentioned above. At AUG, plasmas in H-mode are routinely made and different kinds of ELM regimes can be obtained. The main tool used for the survey of ELMs is the Electron Cyclotron Emission imaging (ECEI) diagnostic, installed at AUG as a part of this project. ECEI is

a diagnostic that provides a 2D measurement of the electron temperature ($T_e$) at the high temporal and spatial resolution required for capturing ELM dynamics. The 2D capability allows following $T_e$ fluctuations in the vertical direction, in the poloidal cross section where the measurements are acquired. This was previously not possible with a standard 1D ECE system, which measures only radially along a single line of sight. For the first time, it became possible to observe a variety of $T_e$ fluctuations associated with different ELM types with the ECEI diagnostic. Describing the characteristics and dynamics of these various modes and their roles in the ELM cycle forms the major part of this work.

In the type-I ELM cycle, three distinct types of $T_e$ fluctuations have been observed. First, in the last few tens of $\mu$s before the ELM crash, a mode is observed that rotates in the electron diamagnetic drift direction. During its short life-time, the poloidal mode number has been seen to increase, simultaneously with an increase of the mode's poloidal velocity. This is followed by the actual ELM crash, i.e. where the temperature of the plasma edge rapidly decreases. During this crash phase, secondly, multiple filamentary structures are seen just outside the confined plasma. Most of these filaments rotate in the same direction as the mode observed just before the crash, although sometimes the first occurring filaments are seen to rotate in the opposite direction. A third kind of $T_e$ fluctuation that has been observed is associated with the difference between long and short ELM periods (also known as 'slow' and 'fast' ELMs). This mode is actually only found before slow ELMs and it displays a distinct poloidal asymmetry of its amplitude: the amplitude of the $T_e$ fluctuations has a minimum on the plasma mid-plane and maxima above and below. Although the presence of this mode does not cover the full delay of the slow ELM cycle compared to the fast one, it does suggest that this fluctuation regulates the plasma edge in such a way that a stable situation is prolonged a few ms longer until the $T_e$ crash comes.

The type-II ELM regime is a regime of small ELMs that combines both good confinement and small energy losses. It is obtained by triangular plasma shaping at high edge density and is regularly accessed at AUG. Measurements with ECEI revealed a broadband $T_e$ fluctuation, characteristic for type-II ELMs. This mode is situated just inside the top of the edge transport barrier and completely flattens the $T_e$ profile at this location, whilst leaving the pedestal gradient unaffected. After averaging over a longer time, the 2D distribution of this fluctuation's amplitude also shows a distinguished minimum around the mid-plane. The observation of a beat wave with a low beat frequency suggests that the broadband feature is actually caused by the coexistence of multiple modes with slightly different mode numbers or frequencies.

Since the installation of a set of magnetic perturbation coils close to the plasma (during the course of this project), it has become possible at AUG to achieve conditions under which the large type-I ELMs are mitigated. The exact mechanism that causes this mitigation is not fully understood yet (especially the role of the edge electron density threshold seems critical). Although some of the features of the small ELMs (remaining after mitigation of the type-I ELMs) are shared with type-I and/or type-II ELMs, these small ELMs are clearly distinguishable from either type. Compared to type-I ELMs, the small ELMs show opposite behaviour with respect to the variation of the edge density: while the type-I ELM frequency decreases with increasing density, the frequency of the small ELMs increases. The main difference between these small ELMs and the type-II ELMs is that the latter display continuous $T_e$ fluctuations, whereas the $T_e$ fluctuations during the small ELMs are only seen for very short times. It is furthermore not straightforward to directly relate these small ELMs to the type-III ELMs observed directly after the transition to H-mode. If, despite some differences, the small ELMs are nevertheless most closely related to type-III ELMs, this could help explain the fact that sometimes suppression of type-I ELMs already occurs before activation of the magnetic perturbation coils.

Although the different types of modes measured with ECEI in the various ELM regimes display features that clearly distinguish them from each other, there are also similarities that closely link the different observations together. For example, a comparable poloidal asymmetry is found in the amplitudes of both the mode that is only observed in the slow type-I ELM cycle and the broadband $T_e$ fluctuation that characterizes type-II ELMs. Moreover, whereas the one mode appears to delay the occurrence of the next $T_e$ crash (in the type-I cycle), the other mode seems to cause the complete absence of $T_e$ crashes (in the type-II case). Both modes also display equally high poloidal mode numbers. Another similarity that connects the different ELM types is observed during the transitions to small ELM regimes. In both the transition from type-I to type-II and the transition from type-I to the small ELMs that remain after the mitigation of type-I ELMs with magnetic perturbations, it is seen that the substituting type is already present before the type-I ELMs have stopped occurring.

Finally, all observed modes (the filaments excluded) rotate in the same direction, are located in the vicinity of the top of the edge transport barrier, and consist of (multiple) coherent oscillations in the same frequency range and with medium-high to high poloidal mode numbers. These properties suggest that the observed modes are in fact (peeling-) ballooning modes; the most widely accepted theoretical model that describes the linear onset to the ELM crash.

# Zusammenfassung

Anfang des zwanzigsten Jahrhunderts entdeckten Wissenschaftler den Prozess der die Sonne brennen lässt: die Kernfusion. Damals erkannten sie fast zur gleichen Zeit, dass sich durch die Kontrolle dieses Prozesses möglicherweise eine enorme Energiequelle auf der Erde auftun könnte. Um die Fusionsreaktion (Deuterium-Tritium) zu ermöglichen, müssen sich die Wasserstoffisotope innerhalb der Reichweite der Kernkraft befinden. Dies setzt einen Zustand mit extrem hohen Temperaturen (mehr als 100 Million K) voraus, bei der alle Atome vollständig ionisiert sind und ein Plasma bilden. Die Ionisation der Teilchen ermöglicht es, ein Plasma magnetisch einzuschließen. Derzeit wird dies am erfolgreichsten mithilfe des Tokamak Konzepts erreicht. Ein Tokamak ist ein torusförmiges Gerät in dem Magnetfeldlinien auf spiralförmigen Bahnen um den Torus verlaufen.

In einem effizienten Fusionsreaktor soll das Plasma nicht nur eine hohe Temperatur, sondern auch hohe Dichte aufweisen. Zusätzlich soll die Energieeinschlusszeit lang genug sein, um zu verhindern, dass das Plasma die erzeugte Fusionsenergie zu schnell verliert. Wenn sowohl die Temperatur als auch die Dichte erhöht werden, steigt der Plasmadruck an. Oberhalb eines bestimmten kritischen Wertes erfährt das Plasma dann eine Bifurkation von einem niedrigen zu einem hohen Einschlusszustand, der sogenannten H-Mode. In der H-Mode leidet jedoch der Einschluss unter einer Instabilität, die ELM genannt wird (engl.: 'Edge Localized Mode'). Während des zyklischen Zusammenbruchs des Plasmarandes werden aufgrund der ELM-Instabilität heiße Teile des eingeschlossenen Plasmas ausgestoßen. Für große Tokamaks wie ITER (ITER ist zur Zeit im Bau, um die Machbarkeit der Kernfusion als Energiequelle zu zeigen) könnten diese ausgestoßenen Filamente zu einer nicht tolerierbaren Wärmebelastung für die plasmazugewandten Komponenten führen.

ELMs sind ein komplexes Phänomen und ihre Analyse hat sich zu einem wichtigen Bereich der zeitgenössischen Kernfusionsforschung entwickelt. Bisher wurden verschiedene Typen von ELMs klassifiziert: zusätzlich zu dem am häufigsten vorkommenden, aber auch aggressivsten Regime des Typ-I ELMs gibt es auch Umstände, unter denen die Auswirkungen der ELMs gutartiger sind (z.B. in den Regime der kleinen ELMs wie Typ-II und/oder Typ-III). Um das Verhalten von ELMs für größere Tokamaks vorhersagen zu können, ist es notwendig die Physik der ELMs zu verstehen und ein konsistentes Modell für die Verluste während der ELMs zu entwickeln. Gleichzeitig wird noch in den Regime der kleinen ELMs, in den Regime ohne ELMs und im Bereich der aktiven Kontrolle der ELMs intensiv geforscht.

Diese Doktorarbeit wurde bei ASDEX Upgrade (AUG) durchgeführt. Das ist ein Tokamak der die idealen Voraussetzungen hat, um einige der oben genannten Themen zu behandeln. An AUG werden H-Mode Plasmen routinemäßig erzeugt und verschiedene Arten von ELM-Regime beobachtet. Das wichtigste Instrument, das für die Untersuchung der ELMs verwendet wird, ist die Elektron-Zyklotron Emission Imaging Diagnostik (ECEI). Diese Diagnostik wurde im Rahmen dieses Projektes an AUG installiert. ECEI ist eine Diagnostik die eine 2D-Messung der Elektronen-Temperatur ($T_e$) bei hoher zeitlicher und örtlicher Auflösung liefert die für die Erfassung der ELM-Dynamik erforderlich ist. Die 2D-Fähigkeit ermöglicht das Verfolgen der $T_e$-Fluktuationen in der vertikalen Richtung (in dem poloidalen Querschnitt der Messstelle). Dies war bisher mit einem Standard ECE-System, das nur radial entlang einer einzigen Sichtlinie misst (1D), nicht möglich. Mit der ECEI Diagnostik wurde es zum ersten Mal möglich, eine Vielzahl von $T_e$ Fluktuationen, die mit unterschiedlichen ELM-Typen verbunden sind, zu beobachten. Die Beschreibung der Eigenschaften und der Dynamik dieser verschiedenen Moden und ihre Rolle im ELM-Zyklus bildet den Hauptteil dieser Arbeit.

Bei der Beobachtung des Typ-I ELM-Zyklusses wurden drei verschiedene Arten von $T_e$-Fluktuationen erkannt. Erstens: in den letzten Zehntel $\mu$s vor dem ELM-Crash wird eine Mode beobachtet, die in der diamagnetischen Driftrichtung der Elektronen rotiert. Während der kurzen Lebensdauer dieser Mode wurde beobachtet, dass sich die poloidale Modenzahl erhöht und dass sich gleichzeitig auch die poloidale Geschwindigkeit der Mode erhöht. Darauf folgt der tatsächliche ELM-Crash, d.h.: eine sehr schnelle Abnahme der Temperatur am Plasmarand. Zweitens: während dieser Phase werden mehrere Filament-ähnliche Strukturen außerhalb des eingeschlossenen Plasmas beobachtet. Die meisten dieser Filamente rotieren in der gleichen Richtung wie die Mode, die unmittelbar vor dem Crash beobachtet wurde. Es kann jedoch vorkommen, dass die jeweils ersten Filamente in entgegengesetzter Richtung zu den folgenden rotieren. Drittens: es gibt eine $T_e$-Fluktuation die den Unterschied zwischen langen und kurzen ELM-Perioden darstellt (auch "langsame" und "schnelle" ELMs genannt). Diese Mode wird eigentlich nur bei langsamen ELMs gefunden und weist eine ausgeprägte poloidale Asymmetrie in ihrer Amplitude auf: die Amplitude der Fluktuation hat ein Minimum an der Äquatorialebene und sowohl oberhalb als auch unterhalb davon zwei Maxima. Obwohl das Vorhandensein von dieser Mode nicht den gesamten Zeitunterschied zwischen dem langsamen und dem schnellen ELM-Zyklus abdeckt, deutet dies darauf hin, dass diese Fluktuationen den Plasmarand stabilisieren und ihn wenige ms länger in einer stabilen Lage halten, bis der $T_e$-Crash kommt.

Das Regime der Typ-II ELMs ist ein Regime von kleinen ELMs, das einen guten Einschluss und einen kleinen Energieverlust aufweist. Es wird durch eine ausgeprägte trianguläre Plasmaform bei hohen Randdichten erreicht und regelmäßig an AUG beobachtet. Messungen mit ECEI zeigen eine breitbandige $T_e$-Fluktuation auf, die für Typ-II ELMs charakteristisch ist. Diese Mode ist an der Oberseite der Rand-Transport-Barriere lokalisiert und flacht das $T_e$-Profil an dieser Stelle stark ab. Gleichzeitig bleibt der Gradient des Pedestals (d.h. die Stufenform des Temperaturprofils) unverändert. Gemittelt über eine längere Zeit zeigt die 2D-Verteilung der Amplitude der $T_e$-Fluktuation auch ein ausgeprägtes Minimum um die Äquatorialebene. Die Beobachtung einer Schwebung mit einer niedrigen Schwebungsfrequenz deutet darauf hin, dass die Breitbandeigenschaft eigentlich durch die Koexistenz von mehreren Moden mit leicht unterschiedlichen Modenzahlen oder Frequenzen verursacht wird.

Seit der Installation von Spulen, die magnetische Störfelder im Plasma erzeugen können (im Lauf des Projektes), ist es unter gewissen Bedingungen möglich geworden, die großen Typ-I ELMs an AUG zu unterdrücken. Der genaue Mechanismus, der für diese Unterdrückung verantwortlich ist, ist noch nicht vollständig geklärt (insbesondere ein Schwellenwert in der Elektronendichte am Rand scheint kritisch zu sein). Obwohl einige der Eigenschaften der kleinen ELMs (die nach der Unterdrückung der Typ-I ELMs übrigbleiben) mit dem Typ-I und/oder Typ-II ELMs vergleichbar sind, kann man diese kleinen ELMs von beiden Typen eindeutig unterscheiden. Im Vergleich zu den Typ-I ELMs weisen die kleinen ELMs eine gegensätzliche Korrelation in Bezug auf Änderungen der Randdichte auf: wenn die Typ-I ELM-Frequenz mit zunehmender Dichte abnimmt, nimmt die Frequenz der kleinen ELMs zu. Der wesentliche Unterschied zwischen diesen kleinen ELMs und den Typ-II ELMs liegt darin, dass der letztere kontinuierliche $T_e$-Fluktuationen zeigt, während die $T_e$-Fluktuationen bei den kleinen ELMs immer nur für eine kurze Dauer beobachtet werden. Darüberhinaus ist es nicht einfach, einen direkten Zusammenhang zwischen den kleinen ELMs und den Typ-III ELMs (die unmittelbar nach dem Übergang in der H-Mode beobachtet werden) nachzuweisen. Wenn es sich herausstellen würde, dass die kleinen ELMs den Typ-III ELMs von der Art her dennoch am nächsten kommen (trotz einiger Unterschiede), könnte dies möglicherweise eine Erklärung dafür sein, dass die Unterdrückung von Typ-I ELMs manchmal bereits vor der Aktivierung der magnetischen Störung auftritt.

Obwohl die mit ECEI beobachteten $T_e$-Fluktuationen sich grundlegend unterscheiden, gibt es auch Ähnlichkeiten, die die verschiedenen Beobachtungen miteinander verbinden. In den Amplituden in dem langsamen Typ-I ELM-Zyklus, sowie auch in den breitbandigen $T_e$-Fluktuationen (die die Typ-II ELMs kennzeichnen), wurde zum Beispiel eine vergleichbare poloidale Asymmetrie gefunden. Außerdem wurde herausgefunden dass die eine Mode den ELM-Crash verzögert (im Typ-I Zyklus) und die andere ihn vollkommen unterdrückt (im Falle der Typ-II ELMs). Beide Moden zeigen auch gleich hohe poloidale Modenzahlen an. Eine weitere Ähnlichkeit, die die verschiedenen ELM-Typen verbindet, wird während der Übergänge zum kleinen ELM-Regime beobachtet. In beiden Übergängen, sowohl von Typ-I zu Typ-II ELMs als auch von Typ-I zu den kleinen ELMs, wird beobachtet dass der neue Typ bereits erscheint bevor das Auftreten der Typ-I ELMs aufgehört hat.

Zum Abschluss: alle beobachteten Moden (die Filamente ausgenommen) drehen in der gleichen Richtung und sind in der Nähe der Oberseite der Rand-Transport-Barriere lokalisiert. Des Weiteren bestehen sie aus (mehreren) kohärenten Schwingungen im selben Frequenzbereich und mit mittleren bis hohen poloidalen Modenzahlen. Diese Eigenschaften deuten darauf hin, dass die beobachteten Moden (Peeling-) Ballooning-Moden sind: dies ist das am meisten akzeptierte theoretische Modell, das den linearen Ansatz eines ELM-Crashes beschreibt.

# Contents

# Chapter 1

# Introduction

## 1.1. Energy gain from nuclear fusion

In March 1920, Francis William Aston conducted a systematic study to precisely measure the masses of a series of different atoms. Amongst many results (he was actually looking for isotopes of neon) his measurements showed "*in an unmistakable manner that the mass of He is less than twice that of $H_2$*" [Aston20]. The nucleus of hydrogen ($H_2$) is composed of two protons and that of helium (He) consists of two protons plus two neutrons. However, since the masses of protons and neutrons are nearly the same (i.e. < 0.2 % difference), this observation was indeed truly astonishing.

At that time, scientists had already been searching for ages for the mechanism that supplies the energy for the Sun to burn. The implications of Aston's measurements were immediately clear to the astrophysicist Arthur Eddington. Using Albert Einstein's famous relation between mass and energy, $E = mc^2$ [Einstein05], he estimated the amount of energy liberated when helium were made out of hydrogen and, in August of that same year, he concluded that "*If 5% of a star's mass consists initially of hydrogen atoms...we need look no further for the source of a star's energy*" [Eddington20]. Painting a remarkably profound vision in the same lecture, Eddington went on to state:

*"If, indeed, the sub-atomic energy in the stars is being freely used to maintain their great furnaces, it seems to bring a little nearer to fulfilment our dream of controlling this latent power for the well-being of the human race — or for its suicide."*

What Eddington called 'sub-atomic energy' results, in fact, from the nuclear force that binds protons and neutrons together. From Figure 1.1(a) it can be understood how energy can indeed be obtained from nuclear reactions: when the binding energy per nucleon ($E_b/A$) after a reaction is actually greater than before. The binding energy curve peaks in the region of the nickel-iron group (mass number $A \approx 60$) [Audi03], which means that either the splitting of heavier nuclei or the combining of lighter nuclei will result in nuclei which are more tightly bound, i.e. less mass per nucleon and consequently a release of energy. It can furthermore be seen from Figure 1.1(a) that helium has an exceptionally high binding energy per nucleon. The reason for this is that the nuclear force favours binding of pairs of protons or neutrons with opposite spin and in addition favours binding of pairs of pairs. With a pair of protons combined with a pair of neutrons, the latter is exactly the case here and this makes helium energetically very favourable as a fusion product.

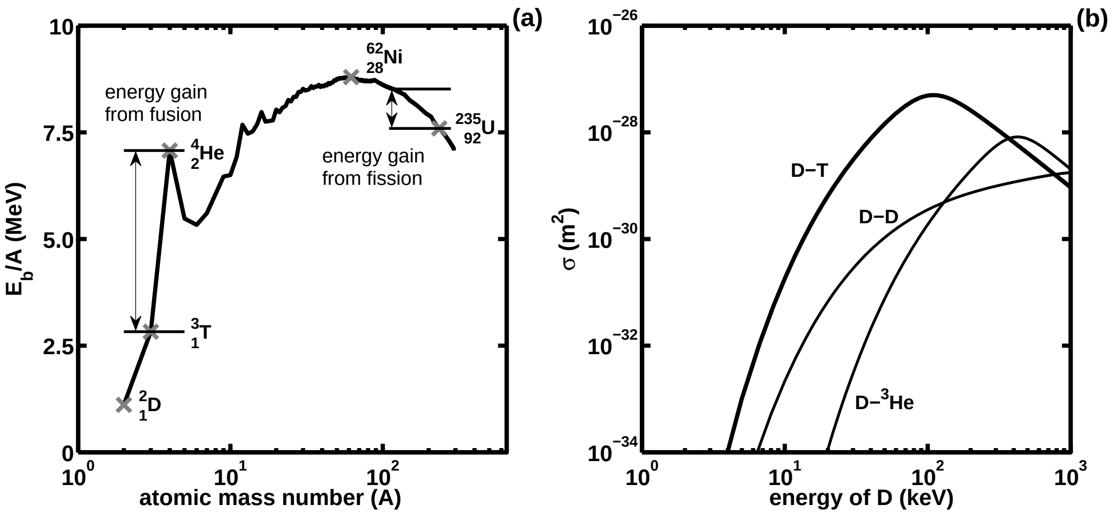


**Figure 1.1** *The curve shown in (a) displays the binding energy per nucleon ($E_b/A$) as a function of the mass number A which has its maximum in the nickel-iron region of A ≈ 60. Energy is released when either heavier nuclei are split or lighter nuclei are combined. From the reaction cross sections shown in (b), it can be seen that the highest cross section occurs for the D-T fusion reaction.*

As a consequence, most viable fusion reactions combine isotopes of hydrogen to form helium. There are several combinations thinkable of lighter isotopes that can fuse to make helium [Stott05]. However, as can be seen from Figure 1.1(b), the probability of a fusion reaction as measured by the reaction cross section $\sigma$ is highest for the reaction between the hydrogen isotopes of deuterium (D) and tritium (T) [Xing08]. Deuterium has an atomic mass number of two: it consists of one neutron plus one proton. For tritium, with two neutrons plus one proton, the mass number is three. At 17.6 MeV, this reaction also has a relatively large energy release compared to other possible reactions. Therefore, the foreseen candidate for energy production on Earth is the following nuclear reaction:

$$ {}^{2}_{1}\mathrm{D} + {}^{3}_{1}\mathrm{T} \rightarrow {}^{4}_{2}\mathrm{He}\ (3.5\ \mathrm{MeV}) + {}^{1}_{0}\mathrm{n}\ (14.1\ \mathrm{MeV}) \qquad (1.1)$$

From a straightforward calculation, it follows that the energy released from 1 kg of D-T fusion fuel is $3.4\times10^{14}$ J. As can already be estimated from Figure 1.1(a), the energy yield of a fission reaction is about a factor of four lower: the fission of 1 kg uranium releases $8.8\times10^{13}$ J. In contrast to these nuclear reactions, the energy release from chemical reactions results from the binding energy of the electrons to their atoms. For comparison, and in order to get an impression of the energy obtained from the burning of fossil fuels, 1 kgoe (kilogram of oil equivalent) is defined as $4.2\times10^{7}$ J. Of course, these levels of released energy are not directly available for usage and energy conversion losses must be taken into account for all three processes.

Currently, the world's total primary energy supply has reached a level of 12 Gtoe per year [IEA11] and its population has increased to seven billion people [UNFPA11]. On average, that gives an energy demand of $7\times10^{10}$ J per person per year. This, however, varies widely across the globe: in developed countries it is a factor three higher and in undeveloped countries a factor three lower. Furthermore, with population growth rates being positive (and highest in the undeveloped countries), the energy demand can be expected to increase considerably in the near future [Bartlett78]. Nevertheless, at today's levels, the energy released from 1 kg of fusion fuel would be enough to cover the yearly demand of thousands of people. For that reason, and as can easily be seen from the sheer differences in order of magnitude for the above estimated energy releases, it remains worthwhile chasing Eddington's dream of controlling nuclear fusion reactions.

## 1.2. Tokamak operation

In order for the fusion reaction (1.1) to happen, the hydrogen isotopes must be within the attraction range of the nuclear force, which acts at a typical distance of $2\times10^{-15}$ m. However, before the nuclei are able to come so close together, they must first overcome the electrical repulsion caused by the positive charges of their protons. The energy required for two protons to surmount this so-called Coulomb barrier is $E = 6\times10^{-14}$ J, which is the total initial kinetic energy for both fusion nuclei assuming a head-on collision.

It is only at extremely high temperatures that atoms can have this much energy. The average translational kinetic energy of a gas molecule at temperature $T$ is $3/2k_BT$ (where $k_B$ is Boltzmann's constant: $k_B = 1.38\times10^{-23}$ $JK^{-1}$). From this, it follows that the Coulomb barrier can be overcome at a temperature of $3\times10^9$ K. The energy required to overcome the repulsion is furthermore proportional to the total charge of the nuclei. Hydrogen isotopes, which have the smallest charge, therefore react at the lowest temperatures. This is also reflected in Figure 1.1(b), where the D-T reaction not only has the highest cross section but it occurs at the lowest energy as well. Fortunately, due to quantum-mechanical effects (tunnelling) and the fact that there is a significant fraction of particles in the Maxwellian tail of the velocity distribution, fusion reactions are already possible at lower temperatures than suggested above. The resulting temperature at which D-T fusion can be obtained at substantial rate is about 10 keV, which is approximately 120 million K (1 eV = $1.6\times10^{-19}$ J = 11604 K).

At these high temperatures, all atoms are fully ionised, which means that the electrons and ions are no longer bound to each other and form a plasma. In the Sun and the stars, it is the gravitational force that keeps the plasma particles together. On Earth, the separation in electrically charged particles provides another opportunity to confine the plasma. The motion of charged particles perpendicular to a magnetic field line is in fact limited by the Lorentz force on the one hand. Particle movement along the field lines, on the other hand, is almost unlimited. This calls for a confinement shape that allows closure of the magnetic field lines on themselves. In Figure 1.2, the main components are shown of a concept that is widely used for the magnetic confinement of fusion plasmas, the so-called tokamak [Wesson04]. This is an acronym of '**то**роидальная **ка**мера и **ма**гнитная **к**атушка', which reflects its Russian origin and means 'toroidal chamber with magnetic coils'.

As can be seen in Figure 1.2, toroidal magnetic field lines are produced by toroidal field coils placed all around the plasma. In case only a toroidal magnetic field existed, charge separation and plasma loss due to $\boldsymbol{E}\times\boldsymbol{B}$-, curvature $\boldsymbol{B}$-, and $\nabla\boldsymbol{B}$-drifts would occur. To prevent this, the magnetic field also needs a poloidal component which is obtained from an induced toroidal current in the plasma. This current can be achieved

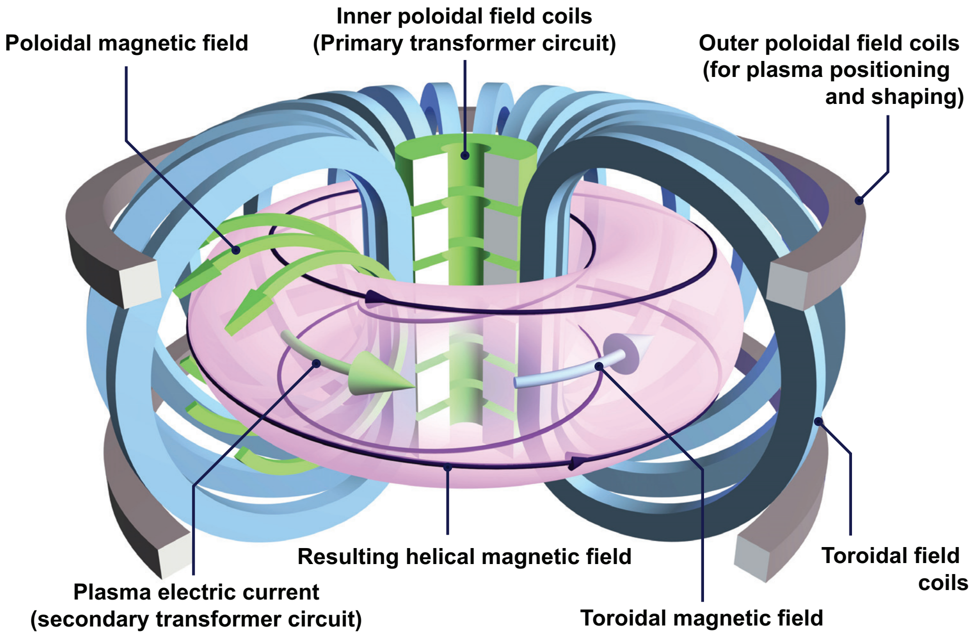


**Figure 1.2** *Basic components of a tokamak: the inner poloidal field coils induce a toroidal plasma current, and consequently a poloidal magnetic field. Combined with the toroidal field, this results in a helical magnetic field which confines the plasma. (Image courtesy of EFDA-JET)*

by using the plasma as the secondary circuit of a transformer, with the primary circuit being formed by the inner poloidal field coils. A current ramp in the primary coils induces a loop voltage inside the vessel and as a result, after plasma breakdown, a toroidal current flows in the plasma (which, beneficially, also contributes to heating the plasma via Ohmic dissipation).

The combination of toroidal and poloidal magnetic fields, as can then be seen in Figure 1.2 as well, results in helical field lines that confine the plasma. The combined helical field lines form nested surfaces of constant poloidal magnetic flux and pressure. Due to the fast equilibration of temperature fluctuations along field lines, these flux surfaces are also isothermal.

The outer poloidal field coils are furthermore necessary to keep the plasma in force equilibrium. Their vertical magnetic field induces a force that compensates the hoop force, which is the combined effect of plasma kinetic pressure and the $\boldsymbol{j}\times\boldsymbol{B}$-force trying to expand the plasma radially outwards. Additional poloidal field coils can be used to shape the plasma's elongation ($\kappa$) and triangularity ($\delta$), in this way enhancing the plasma performance.

## 1.3. H-mode and edge localized modes

Whereas a high plasma temperature is necessary to overcome the Coulomb barrier, it is not a sufficient condition for making the fusion reaction (1.1) work. A second requirement is that the D and T nuclei collide frequently enough; in other words, the particle number density $n$ has to be adequately high as well. As a third constraint, the plasma energy should be confined long enough to sustain the fusion reaction, i.e. it demands a minimum energy confinement time $\tau_E$. Consequently, in order to sustain an efficient fusion reaction these three requirements (on $T$, $n$, and $\tau_E$) must be met simultaneously [Lawson57]. If the process should even be self-sustaining (i.e. the energy of the produced helium is completely maintained in the plasma), the triple product of the above physical quantities must satisfy Lawson's criterion:

$$n T \tau_E > 5\times10^{21}\ m^{-3} keV s \ . \tag{1.2}$$

When both density and temperature are increased, the plasma pressure ($nk_BT$) rises. The ratio of plasma pressure to the magnetic pressure used to contain the plasma ($B^2/(2\mu_0)$) is called $\beta$. Ideally, $\beta$ should be only slightly lower than unity in order to maintain a stable plasma at minimum excess of magnetic force. Typical values of $\beta$, however, were less than 1 % for the first generation tokamaks. In an effort to increase plasma performance by increasing $\beta$, a new discovery was made in the ASDEX tokamak in 1982 [Wagner82]. It was found that by increasing the heating power above a certain threshold, the plasma undergoes a bifurcation to another state. The plasma confinement in this state is typically a factor two higher than in plasmas that are heated below the power threshold; hence the two states are named H-mode and L-mode.

The H-mode is characterized by steep density and temperature gradients at the plasma edge, as is schematically shown in Figure 1.3(a). While the confinement in L-mode is limited by turbulent transport across the magnetic flux surfaces, the steep gradients in H-mode indicate the presence of an edge transport barrier (ETB) that suppresses heat and/or particle transport and increases confinement [Connor00]. The plasma performance in the core could even be further improved when an internal transport barrier is created [Connor04].

Apart from these confinement improving mechanisms, several plasma instabilities that degrade the overall confinement exist as well. Common instabilities such as magnetic islands or sawteeth can occur in the core of both L- and H-mode plasmas. Additionally, in H-mode, the steep pressure gradient of the ETB can trigger instabilities known as edge localized modes (ELMs). These ELMs are repetitive events, which cause a partial collapse of the ETB as is shown in Figure 1.3(b). With each crash, large amounts of particles and energy are suddenly expelled from the confined plasma into the scrape-off layer (SOL). There, the bursts cause high transient heat loads onto the plasma facing components which could suffer severe damage. Despite this major issue, ELMs are not entirely unfavourable to the H-mode. The particle exhaust caused by them in fact helps prevent impurity accumulation in the plasma and therefore allows stationary operation whilst profiting from the steep edge gradients. Furthermore, ELM outbursts could also play a beneficial role in the removal of helium ash that is produced from the fusion reaction (1.1) in the core and would otherwise suffocate the plasma [Reiter90].

To modern-day tokamaks, ELMs do not constitute the serious concerns described above; the lifetime of plasma facing components is not yet unendurably affected by the transient power loads. At present, the construction of a new generation tokamak is being prepared [Ikeda10]. This next step device, ITER, will be much larger in size than existing tokamaks in order to demonstrate a positive energy balance for a fusion reactor. However, when the expelled energy of ELMs is extrapolated to such large a tokamak, it is anticipated that the transient heat loads could lead to an intolerable lifetime reduction of vital reactor components [Leonard99], [Federici03].

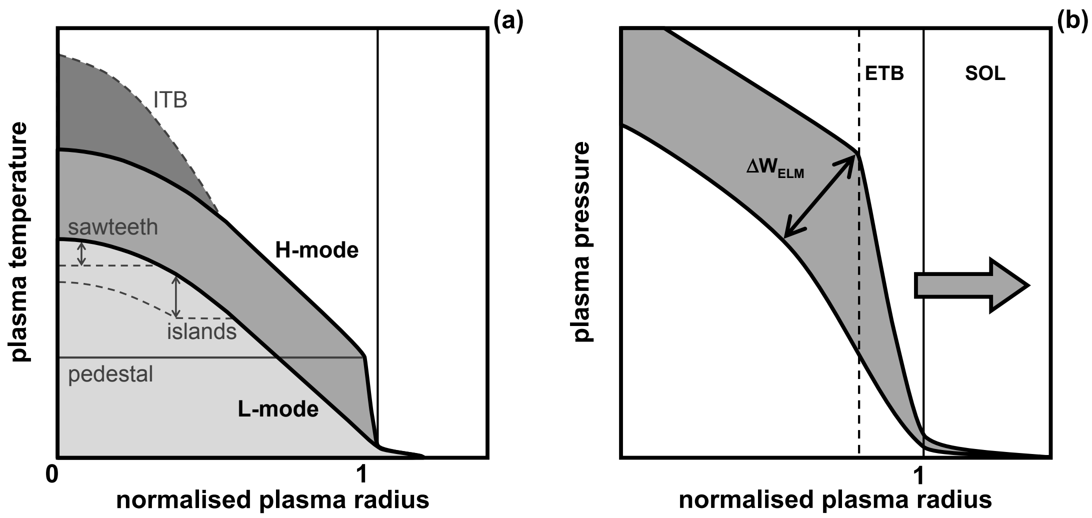


**Figure 1.3** *Schematic temperature profiles from plasma core to edge are shown in (a). The steep gradient at the plasma edge lifts the L-mode temperature profile onto the pedestal in H-mode. Instabilities such as magnetic islands or sawteeth are detrimental to the core temperature, whereas an internal transport barrier (ITB) could be beneficial (adapted from* [Parail02]*). In (b), the effect of an ELM crash is illustrated: as the pressure profile of the edge transport barrier (ETB) collapses repeatedly, particles and energy are expelled into the scrape-off layer (SOL).*

For its goal of a tenfold power multiplication, ITER relies on obtaining H-mode plasmas. This means that a compromise has to be found between the good energy-confinement provided by the ETB and, regarding ELMs, tolerable power loads and sufficient particle exhaust. For this purpose, several techniques are available to mitigate, or even completely suppress ELMs. It is e.g. empirically known that the ELM size, $\Delta W_{\mathrm{ELM}}$, is inversely proportional to the ELM frequency. So, by injecting small pellets of frozen fuel, ELMs can deliberately be triggered more often than their natural frequency which decreases their impact [Pacher11]. A second method to reduce the impact is to perturb the magnetic field at the plasma edge and make it an ergodic region. Consequently, the ELM-induced transient transport can be replaced with a more constant transport process, profiting at the same time from the benefits of the H-mode pedestal [Evans04], [Liang10], [Suttrop11a].

In brief, while the H-mode is necessary for future tokamaks to demonstrate the viability of nuclear fusion as a power source, the energy expelled by the ELMs that come with it could at the same time be damaging for first wall components. There are several techniques available to influence the effect of ELMs. The theory of ELMs, however, is not yet fully understood; though the so-called peeling-ballooning model is widely believed to explain some aspects in terms of a linear, ideal magnetohydrodynamic (MHD) instability [Wilson12]. The purpose of this thesis is to contribute to the experimental characterization of ELM dynamics in order to gain understanding of this phenomenon. With increased understanding, the effectiveness of mitigation techniques might be improved to further diminish the harmful effect of ELMs, or perhaps eliminate them altogether.

## 1.4. This thesis

ELMs are a complex phenomenon and their survey has developed into an important field of present nuclear fusion research. In order to predict ELM behaviour in larger tokamaks, understanding the underlying physics of ELM and developing a consistent model to predict (large) ELM losses is crucial. At the same time intensive research is ongoing in developing plasma scenarios with small or no ELM regimes, as well as with active ELM control.

The work described in this thesis has been conducted at ASDEX Upgrade, a tokamak well suited to address several of these topics. Here, H-mode plasmas are commonly achieved and apart from the (common) large type-I ELMs there are also scenarios at hand to achieve small ELM regimes (such as the type-II ELMs). Furthermore, since the installation of a set of magnetic perturbation coils, it is also possible to manipulate the magnetic field topology at the plasma edge and influence the behaviour of ELMs. The main diagnostic (installed and) used for this work, is ECE-imaging: it provides a 2D measurement of electron temperature fluctuations at high enough temporal resolution needed for capturing ELM dynamics. Whereas most diagnostics view radially along a single line of sight, ECE-imaging also allows following temperature fluctuations in the vertical direction.

In general, the focus of this work has been on the following research themes:

- determining the applicability of ECE-imaging as a suitable diagnostic for performing plasma edge temperature measurements in H-modes,
- characterizing the properties of various instabilities observed in different ELM regimes,
- resolving the influence of these instabilities on the edge pedestal and ELM cycle.

Before the experimental results are presented, a more refined description of the H-mode edge transport barrier and ELMs is given in Chapter 2. The ASDEX Upgrade tokamak, its (edge) diagnostics, and its plasma perturbation tools are subsequently described in Chapter 3. The details of the ECE-imaging diagnostic, which is primarily used for the work of this thesis, and the physical principles it is based on are separately given in Chapter 4.

In Chapter 5, where the first ECE-imaging measurements of type-I ELMs are shown, answers will be presented to the following, more specific questions:

· What determines the length of the ELM cycle?
· How does the ELM crash develop and is the ejection of filaments seen?
· Does the 2D feature of ECE-imaging allow for mode number determination?

The following research questions on the (small) type-II ELMs will be addressed in Chapter 6:

· Where exactly are the broadband fluctuations (common for type-II ELMs) located?
· How does the edge pedestal change over the type-I to type-II ELM transition?
· What causes the atypical amplitude distribution of the broadband MHD instability?

Prompted by some of the observations in both type-I and -II ELMy H-modes, possible influences of electron density fluctuations on the measurements of ECE-imaging are presented in Chapter 7. Here, the following questions will be answered:

· Can observed atypical temperature fluctuations be caused by edge density fluctuations close to the cut-off condition?
· How should a density perturbation be localized in order to bend an ECE-imaging line of sight?
· What do ECE-imaging temperature measurements reveal far from the cut-off condition?

As ASDEX Upgrade is equipped with a set of magnetic perturbation coils that can influence the ELM, the following questions will be addressed in Chapter 8:
· What characterizes the small ELMs observed during the mitigation of type-I ELMs (in comparison to observations of type-I and -II ELM regimes)?
· Is it the mitigation of type-I ELMs that allows for the emergence of small ELMs?
· To what extent are these small ELMs related to type-III ELMs?

Finally, a discussion of the results and an outlook towards future research topics is presented in Chapter 9.

## 1.5. List of publications

In this section, a list is given of publications and conference contributions acquired during the course of this Ph.D. Those related to the work of this thesis are marked with an asterisk.

**Journal publications**
***** J.E. Boom *et al.*
'Characterization of broadband MHD fluctuations during type-II edge localized modes as measured in 2D with ECE-imaging at ASDEX Upgrade',
*Nucl. Fusion* **52** 114004 (2012)

***** R.P. Wenninger, H. Zohm, J.E. Boom *et al.*
'Solitary magnetic perturbations at the ELM onset',
*Nucl. Fusion* **52** 114025 (2012)

***** J.E. Boom *et al.*
'2D ECE measurements of type-I edge localized modes at ASDEX Upgrade',
*Nucl. Fusion* **51** 103039 (2011)

***** E. Wolfrum, M. Bernert, J.E. Boom *et al.*
'Characterisation of edge profiles and fluctuations in discharges with type-II and nitrogen-mitigated edge localized modes in ASDEX Upgrade',
*Plasma Phys. Control. Fusion* **53** 085026 (2011)

***** B. Tobias, A.J.H. Donné, H.K. Park, J.E. Boom *et al.*
'Imaging Techniques for Microwave Diagnostics',
*Contrib. Plasma Phys.* **51** 111 (2011)

***** B. Tobias, N.C. Luhmann Jr., C.W. Domier, X. Kong, T. Liang, S. Che, R. Nazikian, L. Chen, G. Yun, W. Lee, H.K. Park, I.G.J. Classen, J.E. Boom *et al.*
'Recent progress on microwave imaging technology and new physics results',
*Plasma Fusion Res.* **6** 2106042 (2011)

* I.G.J. Classen, J.E. Boom *et al.*
'2D electron cyclotron emission imaging at ASDEX Upgrade',
*Rev. Sci. Instrum.* **81** 10D929 (2010)

* B. Tobias, C. W. Domier, T. Liang, X. Kong, L. Yu, G. S. Yun, H. K. Park, I. G. J. Classen, J.E. Boom *et al.*
'Commissioning of electron cyclotron emission imaging instrument on the DIII-D tokamak and first data',
*Rev. Sci. Instrum.* **81** 10D928 (2010)

* B. Tobias, X. Kong, T. Liang, A. Spear, C. W. Domier, N. C. Luhmann, Jr., I. G. J. Classen, J. E. Boom *et al.*
'Advancements in electron cyclotron emission imaging demonstrated by the TEXTOR ECEI diagnostic upgrade',
*Rev. Sci. Instrum.* **80** 093502 (2009)

I.G.J. Classen, Ph. Lauber, D. Curran, J.E. Boom, *et al.*
'Investigation of fast particle driven instabilities by 2D Electron Cyclotron Emission Imaging on ASDEX Upgrade and DIII-D',
*Plasma Phys. Control. Fusion* **53** 124018 (2011)

F. Sommer, S. Günter, A. Kallenbach, M. Maraschek, J. Boom *et al.*
'Characterization and interpretation of the Edge Snake in between type-I edge localized modes at ASDEX Upgrade',
*Plasma Phys. Control. Fusion* **53** 085012 (2011)

M.A. Van Zeeland, W.W. Heidbrink, R.K. Fischer, M. García Muñoz, G.J. Kramer, D.C. Pace, R.B. White, S. Aekaeslompolo, M.E. Austin, J.E. Boom *et al.*
'Measurements and modeling of Alfvén eigenmode induced fast ion transport and loss in DIII-D and ASDEX Upgrade',
*Phys. Plasmas* **18** 056114 (2011)

B.J. Tobias, R.L. Boivin, J.E. Boom *et al.*
'On the application of electron cyclotron emission imaging to the validation of theoretical models of magnetohydrodynamic activity',
*Phys. Plasmas* **18** 056107 (2011)

B.J. Tobias, C.W. Domier, N.C. Luhmann, Jr., J.E. Boom *et al.*
'Sawtooth Precursor Oscillations on DIII-D',
*IEEE Trans. Plasma Science* **39** 3022 (2011)

V. Igochine, J. Boom *et al.*
'Structure and dynamics of sawteeth crashes in ASDEX Upgrade',
*Phys. of Plasmas* **17** 122506 (2010)

G.W. Spakman, G.M.D. Hogeweij, R.J.E. Jaspers, F.C. Schüller, E. Westerhof, J.E. Boom *et al.*
'Heat pulse propagation studies around magnetic islands induced by the Dynamic Ergodic Divertor in TEXTOR',
*Nucl. Fusion* **48** 115005 (2008)

**Conference contributions**

G. Kocsis, L. Barrera, J.E. Boom, *et al.*
'Investigating pellet ablation dynamics at ASDEX Upgrade',
*39th EPS Conference on Plasma Physics, P-1.093 (Sweden, Stockholm, 2012)*

B.J. Tobias, M.E. Austin, J.E. Boom, *et al.*
'ECE-Imaging of the H-mode pedestal',
*39th EPS Conference on Plasma Physics, P-4.019 (Sweden, Stockholm, 2012)*

* J.E. Boom *et al*.
'Comparison of edge electron temperature fluctuations in different ELM regimes as observed by ECE-Imaging at ASDEX Upgrade'
*13th H-mode Workshop* (United Kingdom, Oxford, 2011)

* J.E. Boom *et al.*
'2D ECE-Imaging measurements of Type-II Edge Localized Modes (ELMs) at ASDEX Upgrade',
*38th EPS Conference on Plasma Physics*, P-1.123 (France, Strasbourg, 2011)

* M. Hölzl, W.-C. Müller, G. Huysmans, P. Merkel, S. Günter, C. Konz, R. Wenninger, J. Boom, *et al.*
'Reduced-MHD Simulations of Edge Localized Modes in ASDEX Upgrade',
*38th EPS Conference on Plasma Physics, P-2.078 (France, Strasbourg, 2011)*

* J.E. Boom *et al.*
'2D ECE-Imaging measurements of Edge Localised Modes (ELMs) at ASDEX Upgrade',
*37th EPS Conference on Plasma Physics*, P-2.119 (Ireland, Dublin, 2010)

* E. Wolfrum, A. Burckhart, J.E. Boom, *et al.*
'Edge profile and MHD characterization of the type-II ELMy regime in ASDEX Upgrade',
*37th EPS Conference on Plasma Physics, P-2.196 (Ireland, Dublin, 2010)*

* H.K. Park, N.C. Luhmann, Jr., A.J.H. Donné, B. Tobias, G.S. Yun, I. Classen, J.E. Boom, *et al.*
'2-D microwave imaging on TEXTOR, AUG, DIII-D, and KSTAR',
*37th EPS Conference on Plasma Physics, O-5.182 (Ireland, Dublin, 2010)*

I.G.J. Classen, J.E. Boom *et al.*
'ECE-Imaging measurements of the 2D mode structure of Reversed Shear Alfvén Eigenmodes at ASDEX Upgrade',
*37th EPS Conference on Plasma Physics, P-4.182 (Ireland, Dublin, 2010)*

# Chapter 2

# H-mode transport barrier and ELMs

In this chapter, in the first section, a further introduction is given on tokamaks and how the high confinement regime (H-mode) is achieved. In section 2.2, a description is given of the plasma edge instability that is most strongly associated with the H-mode, the so-called edge localized mode (ELM). In the third section, a short introduction is given on magnetohydrodynamics and, commencing from this, the leading theoretical candidates to describe the ELM.

## 2.1. H-modes in tokamaks

### *2.1.1. Plasma configuration*

A tokamak, as was already introduced in section 1.2, is a toroidal device with a strong toroidal magnetic field produced by coils placed around the torus. The poloidal magnetic field is generated by the plasma current flowing toroidally through the plasma. The plasma current itself is induced by using the plasma as the secondary circuit of a transformer (cf. Figure 1.2).

The combination of the poloidal magnetic field $B_\mathrm{p}$ and the toroidal magnetic field $B_\mathrm{t}$ results in helical magnetic field lines. The combined sets of helical field lines form an infinite number of nested surfaces of constant poloidal magnetic flux and pressure, the so-called (magnetic) flux surfaces. This is schematically shown in Figure 2.1(a). The helicity of the magnetic field lines on a flux surface is described by the factor $q$, which is given by

$$q = \frac{1}{2\pi} \oint \frac{1}{R} \frac{B_\mathrm{t}}{B_\mathrm{p}} \mathrm{d}s \ . \qquad (2.1)$$

Here, d$s$ is a line element in the poloidal plane, and the closed integral is carried out over one poloidal circuit around the flux surface (at radius $r$ cf. the coordinate system shown in Figure 2.1(a)). In other words, the helicity $q$ specifies the number of toroidal turns that is necessary for a field line to perform one poloidal turn. This means that for rational numbers of $q$, i.e. where $q$ equals the ratio of two integers $m/n$, the field lines close upon themselves after completing $m$ toroidal and $n$ poloidal turns. For irrational numbers of $q$, the field lines are not closed and cover the whole flux surface after an infinite number of toroidal turns. The rational flux surfaces are therefore more prone to plasma instabilities, since they consist of closed field lines which are much easier brought to resonate. In general, the $q$-profile typically ranges

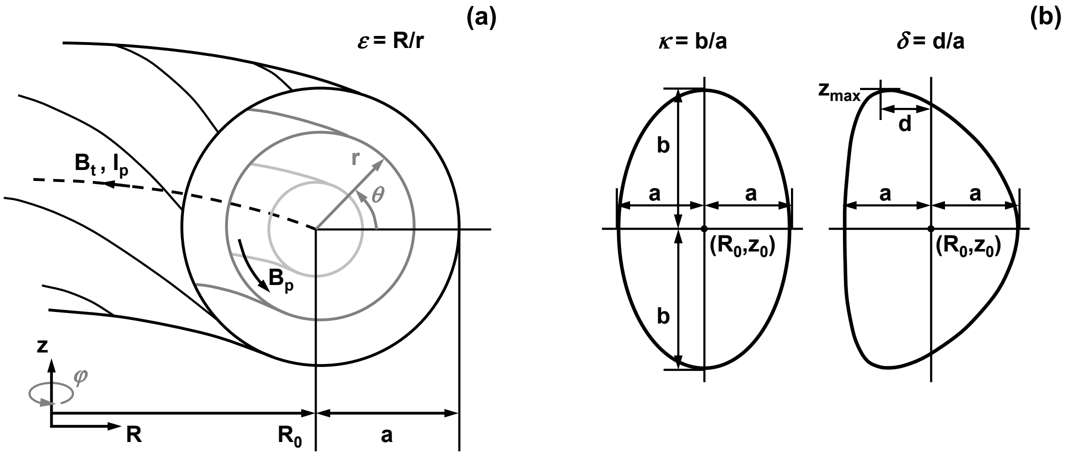


**Figure 2.1** *In (a), the coordinate system most commonly used for tokamaks is shown. Here, R is the distance from the centre of the torus (with $R_0$ the major radius of the tokamak) and r is the distance from magnetic axis (with a the overall minor radius of the tokamak). The aspect ratio $\varepsilon$ is defined as R/r. The angle $\varphi$ is used for the toroidal direction, and for the poloidal direction (e.g. of the poloidal magnetic field $B_p$ caused by the plasma current) the angle $\theta$. For non-circular plasma cross sections, the definitions of elongation $\kappa$ and triangularity $\delta$ are shown in (b).*

from near unity in the centre of the plasma to values of two to eight near the edge. The helicity $q$ is also known as the winding number or safety factor. The latter term refers to the fact that larger values of $q$ are associated with plasmas that have higher ratios of $B_\mathrm{t}$ to $I_\mathrm{p}$ (via $B_\mathrm{p}$) and therefore endure less risk of current-driven (kink) plasma instabilities. Directly related to $q(r)$ is the magnetic shear $s(r)$, which describes the variation of $q$ across the flux surfaces and is (again, for circular cross sections) defined as

$$s(r) = \frac{r}{q}\frac{\mathrm{d}q}{\mathrm{d}r} \; . \tag{2.2}$$

Another quantity often used for describing the stability of the plasma, is the efficiency with which the plasma pressure is confined by the magnetic field. As already stated in section 1.3, this is simply expressed by the ratio of the two:

$$\beta = \frac{\langle p \rangle_V}{B^2 / 2\mu_0} \; , \tag{2.3}$$

where $\langle p \rangle_V$ is the plasma pressure averaged over the total plasma volume $V$, $B$ is the total magnetic field (usually taken at the magnetic axis), and $\mu_0$ is the magnetic constant $4\pi \times 10^{-7}$ V s A$^{-1}$ m$^{-1}$. Closely related to $\beta$ is the poloidal beta, which expresses the plasma's level of dia- or paramagnetism and is defined as

$$\beta_\mathrm{p} = \frac{\langle p \rangle_S}{\langle B_\mathrm{p} \rangle_S^2 / 2\mu_0} \; . \tag{2.4}$$

Here, the pressure $p$ and the poloidal magnetic field $B_p$ are now averaged over the flux surface area $S$ at the plasma boundary.

As mentioned before, high values of the edge safety factor ($q_a$) provide more stable plasmas. Now, for large aspect ratio tokamaks with circular cross sections, Ampère's law (cf. equation (2.12)) can be written in the form

$$2\pi r B_p = \mu_0 I(r) \ . \tag{2.5}$$

So that it is easily found from combining equations (2.1) and (2.5) that $q$ at the plasma boundary is given by

$$q_a = \frac{2\pi a^2 B_t}{\mu_0 I_p R} \ . \tag{2.6}$$

Here, it can be seen that $q_a$ is proportional to $\pi a^2$, which is the flux surface area of the circular cross section covered by the closed integral of equation (2.1). For elongated cross sections, as e.g. shown in Figure 2.1(b), this area is given by $\kappa\pi a^2$, which means that the edge $q$-value of elongated plasmas is higher (by a factor $(1 + \kappa^2)/2$) than that resulting from equation (2.6) for a given $I_p$. Or, in other words, for a fixed $q$ at the edge, the plasma current can be much higher which is generally favourable for the energy confinement time $\tau_E$ (cf. equation (1.2)) [Goldston84]. By further optimizing the triangularity $\delta$ as well (see Figure 2.1(b)), and so obtaining more D-shaped plasmas, the plasma stability can even be further increased (see also paragraph 2.3.2, or [Reimerdes00], [Aiba07]).

### *2.1.2. Limiters and divertors*

A limiter, see Figure 2.2(a), is a solid surface that defines the edge of the plasma: the flux surface touching the limiter is the last closed flux surface (LCFS). Field lines outside the LCFS in the scrape-off layer (SOL) will inevitably end up on the limiter at some point. In tokamaks, limiters are used to protect the wall from the plasma in case of instabilities and to localize the plasma-surface interaction and particle recycling. However, a major disadvantage of using a limiter is that neutral impurity atoms, which are sputtered of its surface, directly penetrate into the confined plasma region.

Originally, as an alternative to limiters, the divertor configuration was designed with the aim of reducing the amount of impurities in the plasma. Consequently, this leads to a reduction of line radiation and therefore improvement of the energy confinement of the plasma. Simultaneously, however, divertor tokamaks also allow for more flexible plasma shaping and can easily be combined with D-shaped or elliptical cross sections. As just shown at the end of the previous paragraph, this contributes significantly to the improvement of the energy confinement time. In order to obtain a separation of open and closed flux surfaces such as shown in Figure 2.2(b), a magnetic null in the poloidal field is produced by toroidal conductors. In divertor configurations, the flux surface that separates the open from the closed surfaces is usually referred to as the separatrix, instead of the LCFS. The point, in poloidal cross section, of the magnetic null is called X-point. Note that the creation of an X-point also implies that the $q$-value at the separatrix approaches infinity as all field lines go around the torus horizontally. Configurations with one X-point are referred to as single null configurations. Usually

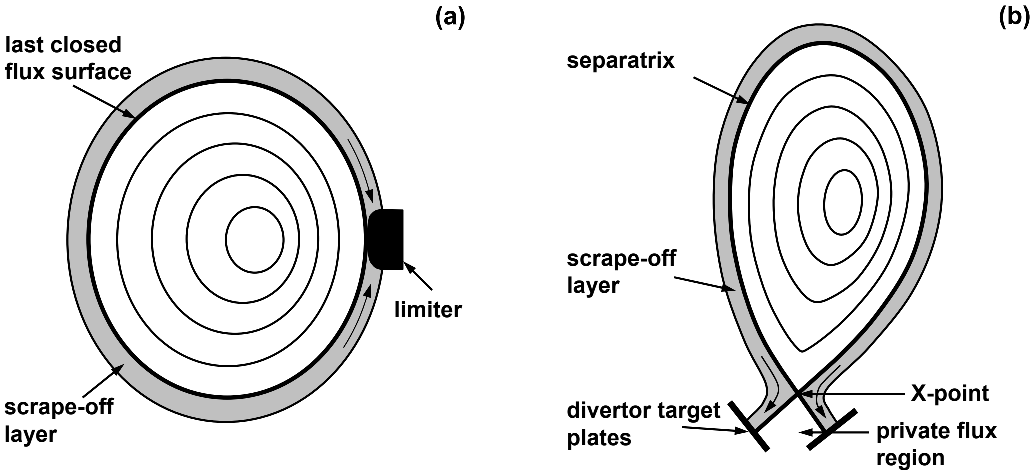


**Figure 2.2** *Comparison of plasma cross sections in two different confinement methods: in limiter configuration (a), the plasma comes into direct contact with a component of the vessel and the last closed flux surface (LCFS) is the flux surface touching the limiter. In divertor configuration (b), an X-point is formed by creating a null in the poloidal field which separates the closed flux surfaces from the scrape-off layer (SOL).*

the X-point is located at the bottom, since that is where divertors are more easily constructed, and the plasma is said to be in lower single null (LSN). However, by padding the ceiling with target plates, most tokamaks are also prepared for upper single null (USN) discharges. This also allows for so-called double null (DN) configurations, which have two X-points. The points where the separatrix hits the divertor target plates are referred to as the strike points. As each X-point creates two strike points, there is one strike point in the inner and one in the outer leg of the divertor. All particles in the SOL of a divertor configuration are conveyed to the target plates in the exhaust region, far away from the closed flux surfaces. As pressure is conserved along field lines in the SOL, the plasma hitting the target plates can have low temperature and high density. This way, tokamaks that employ a divertor configuration manage to achieve reduced impurity influx in the plasma, simultaneously with a reduction of target plate erosion and an increased pumping efficiency.

*2.1.3. Transport*

The quality of the plasma confinement in a tokamak is governed by the radial transport of energy (and particles) from the plasma centre to the edge. In the simplest approximation of a tokamak, i.e. a cylindrical plasma in a homogeneous magnetic field, the collisional transport of particles and energy is determined by a simple diffusion process [Wesson04]. This is known as the classical transport model, where the particle’s step length is given by the Larmor radius. Compared to experimental values of the confinement time, the classical predictions are several orders of magnitude too long.

In the so-called neoclassical model, the toroidal geometry of a tokamak is accounted for in the estimation of the collisional transport. Due to the spatial inhomogeneity of the magnetic field in a tokamak (which is inversely proportional to $R$ and hence varies over the poloidal cross section), there are certain particle drifts that inevitably occur. In particular, there are particles that become trapped in the lower magnetic field on the outside of the torus. These particles exhibit so-called banana orbits, which have a width much larger than the Larmor radius and therefore predict a greater diffusion. In the neoclassical model, several regimes of diffusivity exist. They are proportional to the frequency of the particle collisions, which is a quantity known as the collisionality $\nu^*$. (The collisionality mainly depends on the ratio of density over temperature squared; a commonly used expression for the electron collisionality $\nu^*_e$ is given by equation (6.1) in Chapter 6). However, even for the regime of highest collisionality (Pfirsch-Schlüter), the neoclassical prediction of the confinement time is still about two orders of magnitude longer than what is experimentally measured.

A second type of transport exists, which is fundamentally different from the collisional transport mechanism. This type is known as anomalous (Greek for 'law defying') or turbulent transport. Basically, plasma turbulence is the incoherent motion of the plasma, arising from small-scale fluctuations in quantities such as e.g. density, temperature, or the magnetic field strength. Gradients in these plasma parameters are known to be the driving forces of turbulence. It is generally agreed upon that the largest part of the radial transport is turbulence driven.

### *2.1.4. The H-mode*

As was already introduced in section 1.3, it was found that by increasing the heating power above a certain threshold, the plasma undergoes a transition to a state of much higher plasma confinement: the high confinement mode, or H-mode [Wagner82]. Due to their much better confinement properties, H-modes are primarily observed in (auxiliary heated) divertor tokamaks. It seems, furthermore, that one of the requirements for the plasma to stay in H-mode is that the temperature at the edge remains high. This is inherently prevented by flux surfaces touching limiters and therefore also favours divertor tokamaks [Stangeby90].

The transition of low confinement (L-) to H-mode occurs as a bifurcation and is seen as a sudden increase in particle and stored energy confinement. In Figure 2.3, a standard discharge in the ASDEX Upgrade tokamak is shown, with the L-H transition occurring just after $t = 1.40$ s. The larger stored energy in the H-mode is not just attributable to the increase in heating power, but also to a longer energy confinement time. The latter is defined as

$$\begin{aligned} \tau_E &= \frac{W}{P_{net}} \quad , \text{ with} \\ W &= \frac{3}{2}\int p \, \mathrm{d}V \ . \end{aligned} \tag{2.7}$$

Here, $W$ is the plasma stored energy, and $P_{net}$ the net input power that is delivered to the plasma.

In order to assess the quality of the confinement, a quantity called the $H_{98(y,2)}$-factor is commonly used, which is $\tau_E$ normalized to $\tau_{98(y,2)}$. Here, the latter is obtained from the regression analysis from a multi-machine scaling [ITER_PB99]. When the $H_{98(y,2)}$-factor is larger than unity, the plasma is considered to be in H-mode; as in Figure 2.3(d) from t = 1.45 s onwards. Below unity the confinement is poorer, which could be due to occurrences of instabilities or simply the plasma being in L-mode.

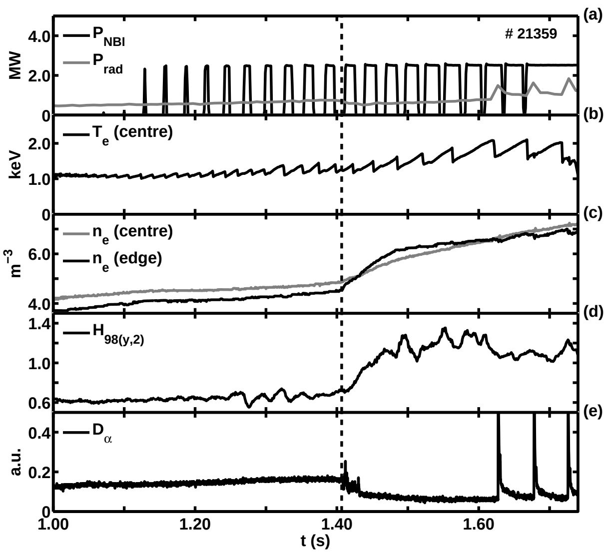


**Figure 2.3** *L-H transition in a standard H-mode (ASDEX Upgrade): in (a), it is shown how the input power ($P_{NBI}$) is slowly increased by increasing the duty cycle of the neutral beam. With increasing input power, the electron temperature $T_e$ (b) and density $n_e$ (c) increase as well, whereas the radiated power $P_{rad}$ stays constant. At the time of the L-H transition (just after t = 1.40 s, indicated by the vertical dashed line), the rate of increase in density suddenly becomes faster as does the rate of increase of the confinement factor $H_{98(y,2)}$ (d). The level of the $D_\alpha$-emission in the divertor abruptly falls, marking a decrease in recycling. This is followed, after a few ms, by $D_\alpha$ bursts originating from plasma particle losses, which indicate the occurrence of (type-I) ELMs.*

For a large part, the improved confinement of the H-mode comes from a small layer (typically a few cm wide) at the plasma edge: the edge transport barrier, or ETB. It is here that particle and energy transport is greatly reduced, which allows for large gradients to be built up. The differences between L- and H-mode can be seen in Figure 2.4. Here, the electron kinetic profiles (i.e. temperature, density and pressure) are shown, taken from before and after the L-H transition presented in Figure 2.3. Compared to L-mode, the electron temperature in H-mode is strongly increased at the plasma edge (Figure 2.4(a)). For the density, the core H-mode profile has nearly the same shape as in L-mode, starting however from a much higher value at the plasma edge (Figure 2.4(b)). The resulting pressure profile, as shown in Figure 2.4(c), therefore mainly follows the trend of the temperature.

The region of the ETB is also well known as the pedestal, which originates from the above described observation that the core profiles appear to be elevated on top of the ETB. This notion of so-called profile stiffness seems to allow for separate study of the plasma core and edge phenomena. In cases where the plasma stored energy or confinement times are studied, this notion is sometimes also referred to as the two-term model.

Due to its increased energy and particle confinement, the H-mode is indeed considered the most favourable regime for future fusion reactors. However, the exact physical mechanisms that determine the triggering of the L-H transition are still under debate at present, [Biglari90] vs. [Schmitz12], [Fundamenski12]. What is known is that the

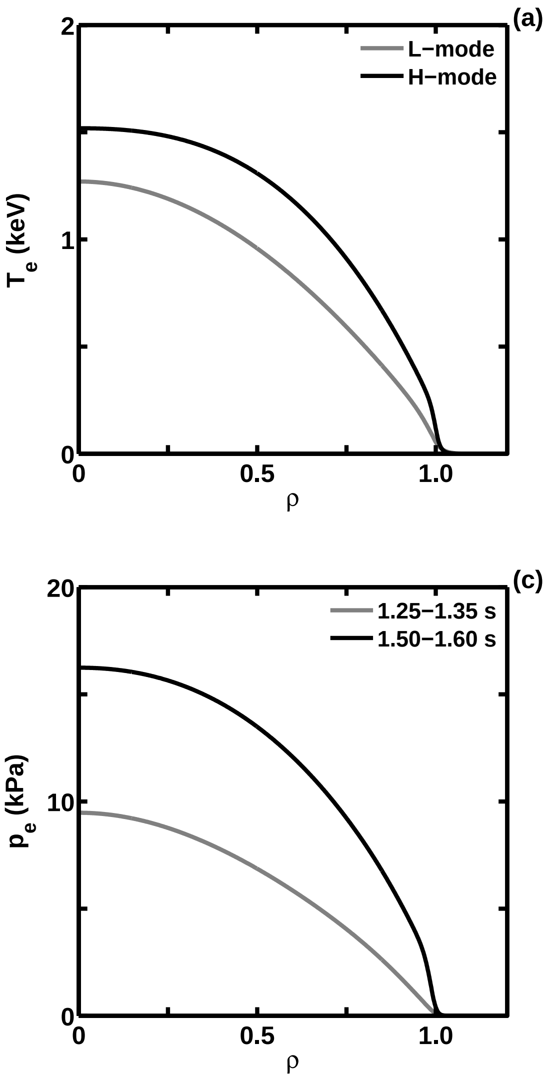


**Figure 2.4** *Differences in the radial kinetic profiles for L- and H-mode: from before and after the L-H transition shown in Figure 2.3, the electron temperature and density profiles and the resulting pressure profile are shown in (a)-(c). The profiles are shown as a function of normalized poloidal flux, where zero is at the magnetic axis and unity at the plasma edge (cf. equation (3.1)). The L-mode profile is averaged over the times between t = 1.25-1.35 s and the H-mode profile over those between t = 1.50-1.60 s.*

suppression of edge turbulence transport allows the large gradients to be sustained and form the pedestal. This is supported by observations of a strong reduction in H-mode of the radial correlation length of electron density fluctuations (which are associated with turbulent transport) [Schirmer05]. The observation (as shown in Figure 2.5) that the absolute value of the radial electric field in H-mode is increased by about one order of magnitude compared to L-mode is supportive of this idea.

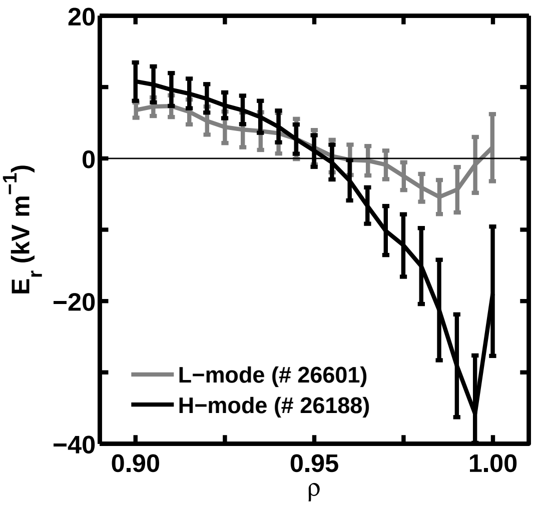


**Figure 2.5** *Radial electric field ($E_r$) edge profiles in L- and H-mode (as measured at ASDEX Upgrade [Viezzer12]). In both discharges the radial electric field displays a minimum below zero at the very edge. In the H-mode case, however, the absolute value of $E_r$ is about one order of magnitude larger than in the L-mode case.*

## 2.2. Edge localized modes

Shortly after the L-H transition, as could already be seen in Figure 2.3(e), the $D_\alpha$ light emission shows a sequence of bursts. This is a typical signature for the presence of the so-called edge localized mode (ELM). The ELM is a quasi-periodic relaxation of the ETB that expels energy and particles out of the confined plasma.

This is indeed what is concluded from the time trace shown in Figure 2.3(e), and in more detail in Figure 2.6(a). For the largest part, the emission of the $D_\alpha$ light, which is detected from the region of the divertor target plates, is caused by the interaction of electrons with neutral particles. This means that the sudden rise in emission results from electrons being ejected from the confined plasma region and travelling down into the divertor (along the open field lines in the SOL) where they interact with neutral particles. Of course ions are also ejected during the ELM but they move down on a longer timescale. They add as well to the number of neutral particles for the electrons to interact with, either by releasing more neutral particles from the target plates, or by becoming neutralized themselves. After a steep increase, the $D_\alpha$ light slowly decays as the amount of particles entering the divertor decreases following the ELM crash.

Apart from the $D_\alpha$ indicator, which is historically most often used, the cyclic ELM bursts are detected on many other diagnostics as well. The sudden particle influx in the divertor is e.g. also measured by divertor shunts (cf. paragraph 3.3.2) as shown in Figure 2.6(b). From the measurement of a magnetic pickup coil close to the plasma edge it can be seen that the magnetic equilibrium is disturbed at the time of the ELM event (Figure 2.6(c)). While there are sudden increases measured in the divertor region, at the edge of the confined plasma sudden decreases are simultaneously seen in e.g. soft X-ray radiation and electron temperature (cf. Figure 2.6(d) and (e)). From the latter two, it can also be seen that the ELM crash is of rather short duration (typically a few hundred $\mu$s or less) and that the recovery of the plasma takes much longer. These quasi-periodic particle and energy losses allow the discharge to become quasi-stationary.

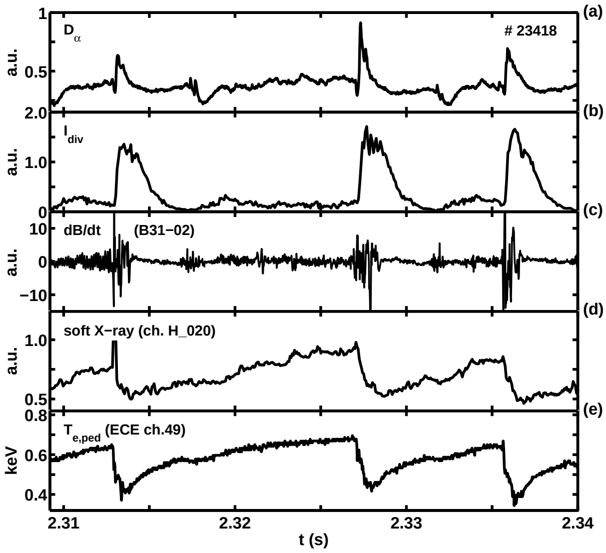


**Figure 2.6** *Signature time traces that demonstrate the presence of (type-I) ELMs: in (a) and (b), measurements from the divertor are shown, where both the $D_\alpha$ radiation and shunt currents illustrate the sudden influx of particles. The oscillation of the magnetic field, as measured by a magnetic pickup coil (c), simultaneously shows large fluctuations. Whereas sudden increases are measured in the divertor ((a) and (b)), the soft X-ray radiation and electron temperature at the edge of the confined plasma ((d) and (e)) show sudden decreases at the same time.*

The sudden expulsion of particles and energy from the confined plasma into the SOL, as described above, is caused by a partial breakdown of the edge pedestal (cf. Figure 1.3(b)). In a similar manner to Figure 2.4, this effect of the ELM on pedestal profiles is shown in Figure 2.7. Here, the collapse of the pedestal is shown as before and after ELM profiles of electron temperature, density and the resulting pressure. It can be seen that the outer 20 % of the plasma is affected by the crash, even though the ELM itself is known to be localized at the very edge.

Due to the ELM crash, the overall energy content of the plasma, $W$ cf. equation (2.7), decreases. The ELM energy loss $\Delta W_{\mathrm{ELM}}$, also known as the ELM size, is estimated as

$$\Delta W_{\mathrm{ELM}} = \frac{3}{2} \Delta p_{\mathrm{ped}} V \ , \qquad (2.8)$$

under the stiff-profile assumption that the core profiles are not affected. Here, $\Delta p_{\mathrm{ped}}$ is the loss of plasma pressure at the top of the pedestal (as can be seen in Figure 2.7(c)) and $V$ the total plasma volume. As the pedestal accounts for 30-50 % of the total plasma energy, the loss due to the ELM crash encompasses a considerable amount (5-10 %). Part of this energy will dissipate in the form of radiation in the SOL. The remaining energy will be deposited mainly on the divertor tiles. However, as is shown in Figure 2.8, particle ejection during an ELM also occurs in the form of so-called filaments. These are field-aligned structures that are observed to be accelerated radially far into the SOL and beyond, ending up on the plasma facing components.

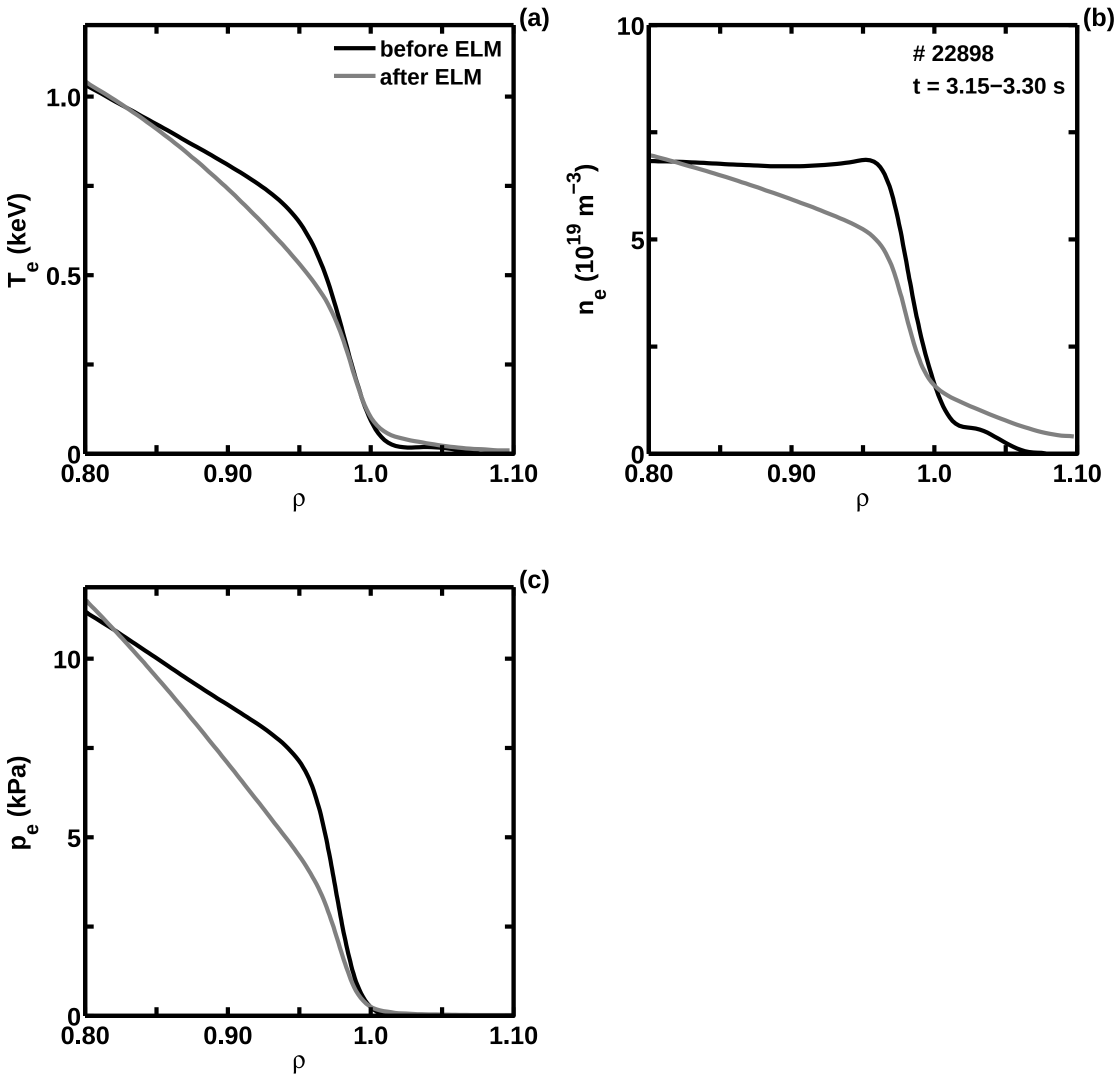


**Figure 2.7** *Differences in edge kinetic profiles between before and after type-I ELM phases (ASDEX Upgrade): in (a) and (b), the electron temperature and density profiles are shown. The resulting pressure profiles are shown in (c). Using an ELM synchronizing technique, these profiles have been obtained from a 150 ms phase in discharge # 22898 [Schneider12].*

Overall, the ELM losses lead to a decrease of the plasma's energy content and produce a transient heat load of considerable energy and short duration onto (a relatively small surface of) the plasma facing components. For present-day tokamaks, these heat loads are still tolerable and do not yet cause irreparable damages to the devices. However, extrapolations to larger tokamaks (such as ITER) predict that the expelled energy could e.g. lead to excessive erosion and an unacceptable lifetime reduction of the divertor target plates. On the other side, it should be kept in mind that ELMs are also beneficial for controlling the plasma density and impurity exhaust.

### *2.2.1. Classification of ELMs*

The description of the ELM, as given above, applies to the most commonly observed type of ELM: i.e. the so-called type-I. The whole range of different observations on plasma edge instabilities in H-mode is grouped in a standard classification scheme for ELMs according to their impact on the discharge [DIII-D Team91].

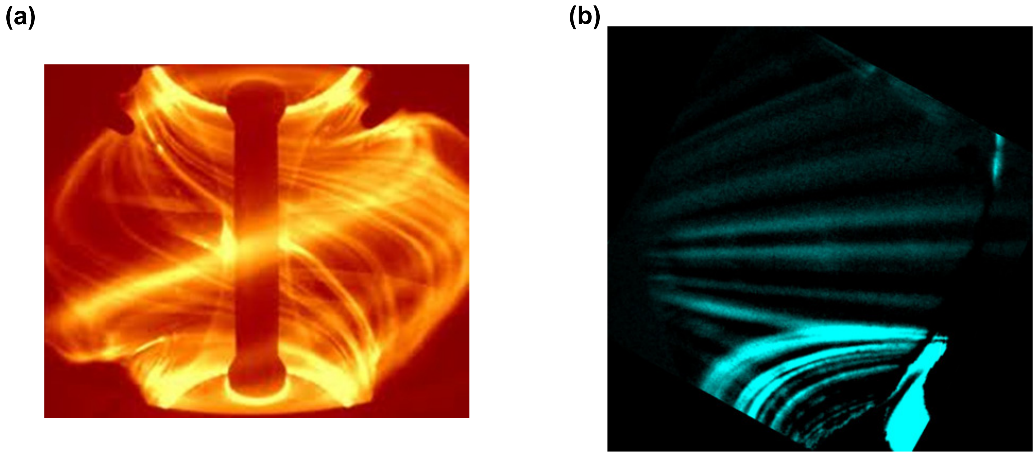


**Figure 2.8** *Image frames from high speed video cameras that show field aligned structures ejected out of the confined plasma far into the SOL at the MAST (a) and ASDEX Upgrade (b) tokamaks [Kirk12], [Kočan12]. These so-called filaments are observed to accelerate radially and decelerate toroidally.*

**Type-I and type-III ELMs**

If the $D_\alpha$ radiation shows large isolated bursts (cf. Figure 2.6(a)), the ELMs are of type-I and are called 'large' or sometimes 'giant'. If the bursts are smaller and more frequent, the ELMs are classified as type-III ELMs (sometimes also referred to as 'small' ELMs). Type-I and type-III ELMs are usually distinguished by their response to increased input power (cf. equation (2.7)). The ELM frequency (repetition rate) for type-I ELMs increases with increasing power, whereas it decreases for type-III ELMs.

Another way to distinguish these two types is to compare temperatures and densities at the pedestal top, as is shown in Figure 2.9. Here, it can be seen that the type-I ELM discharges are clustered around a hyperbola of constant, high pedestal pressure (which also suggests that this ELM instability is pressure driven). The type-III ELMs are seen to occur below a much lower pedestal pressure. They can be divided into two clusters: one at low $T_{e,ped}$ and high $n_{e,ped}$, the other at high $T_{e,ped}$ and low $n_{e,ped}$. The latter cluster is sometimes also referred to as type-IV ELMs. For the other type-III cluster, the low $T_{e,ped}$ indicates a high plasma resistivity. A more in-depth discussion of the possible driving mechanisms for the various ELM types follows in paragraph 2.3.2. From Figure 2.9, it can furthermore be seen that the pressures for which type-III ELMs occur are of the same magnitude as those observed around the L-H transition.

A final distinction between type-I and -III ELMs is their effect on the confinement quality of the discharge. For type-I ELMy H-modes, the overall plasma confinement is better in comparison to other ELM types. However, the ELM size of single type-I crashes is large and poses serious concerns for larger (future) tokamaks. The size of single type-III ELMs, on the other hand, is small and of no concern for tokamak operation. However, the overall plasma confinement during type-III ELMs is comparable to the level obtained in L-modes (most likely due to the low pressures) and is not foreseen for future generation tokamaks.

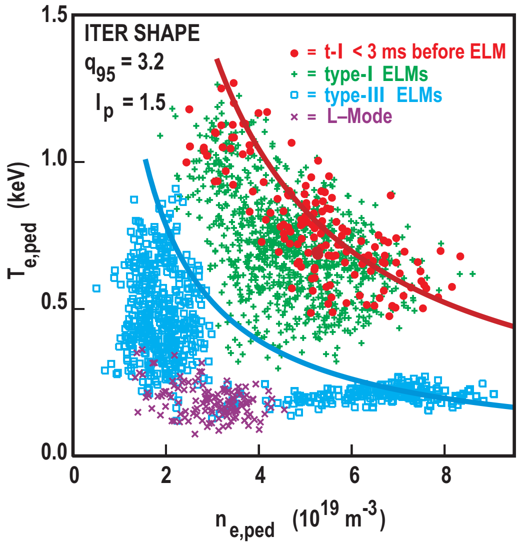


**Figure 2.9** *Operational diagram for different ELM types in the DIII-D tokamak [Osborne05]: it can be seen that the type-I ELMs cluster around the (upper) hyperbola of high constant pressure in the $n_{e,ped}$ - $T_{e,ped}$ space. This is the stability boundary for pressure driven ideal MHD ballooning modes (see section 2.3). The lower hyperbola of constant pressure shows the limit below which the type-III ELMs appear. Here, the ELMs from the cluster at lower density (on the right) are sometimes also referred to as type-IV ELMs.*

**Type-II ELMs**

It is possible, though, to obtain H-mode plasmas that combine both good confinement and tolerable ELM sizes. For the so-called type-II ELMs (also known as 'small' or 'grassy' ELMs), the magnitude of the bursts is lower and the frequency is higher than that of type-I ELMs, whereas at the same time the confinement stays almost as good.

However, type-II ELMs are observed only in strongly shaped plasmas, i.e. with high values for elongation $\kappa$ and triangulation $\delta$ (cf. Figure 2.1). Here, the latter was identified as having a more dominant influence. Further requirements for the plasma shape are that it should be in a close to double null configuration (as discussed in paragraph 2.1.2) and have a high $q$-value at the plasma edge. In addition, it was found that the edge collisionality should be sufficiently high, which is usually achieved by a high pedestal density. Although a simple criterion (such as the frequency dependence of type-I and -III ELMs) is lacking, the presence of type-II ELMs is often coinciding with broadband low frequency edge fluctuations.

## 2.3. Theory of ELMs

Due to the fast timescales at which the ELM develops and the presence of a magnetic perturbation (e.g. shown in Figure 2.6(c)), the ELM was identified as an ideal MHD instability soon after its discovery [Keilhacker84]. Therefore, a short introduction to the field of magnetohydrodynamics (MHD), based on [Freidberg87], is given in the first paragraph of this section. In the second paragraph, the peeling-ballooning model is described which is the leading theoretical candidate for explaining the type-I ELM. A short description of stability codes used for comparing theoretical predictions to experimental values is given in the last section.

*2.3.1. Magnetohydrodynamics*

In short, the ideal MHD model gives a single fluid description (i.e. combined ion and electron properties) of the long-wavelength, macroscopic plasma behaviour. The set of equations that describes MHD is a combination of two moments of the Boltzmann equation and Maxwell's equations of electromagnetism (in the low-frequency limit). These differential equations are solved simultaneously (analytically or numerically) in order to determine e.g. the force balance that holds a plasma in equilibrium, or the stability of a given plasma geometry against macroscopic disturbances.

**Ideal MHD**

The two moments from the Boltzmann equation, which are required for the derivation of the ideal MHD model, govern the time evolution of mass and momentum. The mass continuity balance is given by

$$\frac{\partial \rho}{\partial t} + \nabla \cdot \rho \boldsymbol{v} = 0 , \tag{2.9}$$

which implies that the total number of particles is conserved (i.e. processes such as ionization or charge exchange recombination are not accounted for). The momentum equation describes a fluid with three interacting forces. The magnetic force $\boldsymbol{J}\times\boldsymbol{B}$ has to balance the pressure gradient force $\nabla p$ and the inertial force $\rho\, \mathrm{d}\boldsymbol{v}/\mathrm{d}t$ :

$$\rho\left(\frac{\partial \boldsymbol{v}}{\partial t} + \boldsymbol{v}\cdot\nabla\boldsymbol{v}\right) = \boldsymbol{J}\times\boldsymbol{B} - \nabla p . \tag{2.10}$$

In ideal MHD, the electromagnetic behaviour is governed by the low-frequency Maxwell equations. Used here, are Faraday's law, which describes how a time varying magnetic field induces an electric field,

$$\nabla\times\boldsymbol{E} = -\frac{\partial \boldsymbol{B}}{\partial t} ; \tag{2.11}$$

Ampère’s circuital law, which relates magnetic fields to the electrical currents that produce them (this is the low-frequency part),

$$\nabla\times\boldsymbol{B} = \mu_0\boldsymbol{J} ; \tag{2.12}$$

and Gauss’s law for magnetism, which states that the magnetic field’s divergence equals zero:

$$\nabla\cdot\boldsymbol{B} = 0 . \tag{2.13}$$

The last MHD equation is Ohm’s law, which is the one that gives rise to the ideal part of the model. It implies that the electric field is zero in the reference frame moving with the plasma, which is to say that the plasma is a perfect conductor:

$$\boldsymbol{E} + \boldsymbol{v}\times\boldsymbol{B} = 0 . \tag{2.14}$$

In order to close the above set of equations, an equation of state has to be assumed. Under the assumptions that the plasma has a high collisionality (as introduced in the beginning of section 2.1), that its characteristic dimensions are much larger than the ion Larmor radius, and that its resistive diffusion is negligible (despite the high collisionality), the energy equation is given by

$$\frac{\mathrm{d}}{\mathrm{d}t}\left(\frac{p}{\rho^{\gamma}}\right) = 0 \ . \tag{2.15}$$

Here, $\gamma = 5/3$ is the ratio of specific heats for an adiabatic equation of state.

**Plasma stability and the energy principle**

As mentioned before, the above given self-consistent set of ideal MHD equations can be solved to determine the plasma equilibrium as a state where the sum of the forces acting on the plasma equals zero. If the plasma is disturbed from this state, the resulting perturbed forces can then either return the plasma to its original equilibrium (stability) or increase the initial disturbance and drive it further away from its equilibrium state (instability). In order to test for ideal MHD stability (in arbitrary three-dimensional geometry), the so-called energy principle is applied [Freidberg87]. This is a variational (minimizing) principle for the linearized equations of motion that exactly determines the stability boundaries for a given static equilibrium. It is based on the fact that energy is conserved in the ideal MHD model. In other words: when a plasma equilibrium with a total potential energy $W$ is considered, the energy principle calculates the effect of an arbitrary small displacement $\xi$. The system is stable if and only if $\delta W \geq 0$ for all allowable displacements. However, if $\delta W < 0$ for any displacement, the equilibrium is unstable. For an axisymmetric plasma, the potential energy of a linear perturbation around the equilibrium is given by

$$\begin{aligned} \delta W &= \delta W_{\mathrm{pl.}} + \delta W_{\mathrm{vac.}} \\ \delta W_{\mathrm{vac.}} &= \frac{1}{2}\int_{V_{\mathrm{vac.}}} \mathrm{d}\boldsymbol{r}\, \frac{|\boldsymbol{B}_1|^2}{\mu_0} \ , \end{aligned} \tag{2.16}$$

where $\delta W_{\mathrm{vac.}}$ describes the vacuum field line bending ($\boldsymbol{B}_1$ being the vacuum magnetic field), which is always stabilising. The plasma contribution $\delta W_{\mathrm{pl.}}$ is given by

$$\begin{aligned} \delta W_{\mathrm{pl.}} = \frac{1}{2}\int_{V_{\mathrm{pl.}}} \mathrm{d}\boldsymbol{r} \Bigg[ & \frac{|\boldsymbol{Q}_\perp|^2}{\mu_0} + \frac{B^2}{\mu_0}\left|\nabla\cdot\boldsymbol{\xi}_\perp + 2\boldsymbol{\xi}_\perp\cdot\boldsymbol{\kappa}\right|^2 + \gamma p\left|\nabla\cdot\boldsymbol{\xi}\right|^2 \\ & - 2(\boldsymbol{\xi}_\perp\cdot\nabla p)\left(\boldsymbol{\kappa}\cdot\boldsymbol{\xi}_\perp^*\right) - J_\parallel\left(\boldsymbol{\xi}_\perp^*\times\boldsymbol{b}\right)\cdot\boldsymbol{Q}_\perp \Bigg] \ . \end{aligned} \tag{2.17}$$

Here, $\xi$ is the arbitrary displacement of a plasma volume element (in parallel or perpendicular direction) and $J_\parallel$ the current density parallel to the magnetic field. Concerning the magnetic field: $\boldsymbol{Q}_\perp$ is the linear perturbation of the magnetic field, $\boldsymbol{b}$ the direction of the equilibrium magnetic field, and $\boldsymbol{\kappa}$ the curvature vector of the magnetic field.

The first three terms in equation (2.17) are positive definite and therefore stabilizing. Comparable to the vacuum contribution (cf. equation (2.16)), the first term describes the stabilizing contribution from field line bending. The second and third positive definite terms express the compression of magnetic field lines and the plasma compression, which are also stabilizing contributions. The last two terms in equation (2.17) are not (necessarily) positive and represent the driving forces of the ideal instabilities. The pressure gradient $\nabla p$ contribution is only destabilizing in plasma regions where the magnetic field line curvature is positive; i.e. on the LFS, where $\nabla p$ and $\kappa$ are in the same direction. The second destabilizing term describes the contribution of the current density parallel to the magnetic field ($J_{\|}$).

Due to the fact that field line bending has a stabilizing effect, instabilities preferably align with the equilibrium helical field lines. In the approach of a so-called straight tokamak, the equilibrium is symmetric in $\varphi$ and $\theta$ (cf. Figure 2.1(a)). This means that the displacement $\boldsymbol{\xi}$ can be Fourier decomposed as $\boldsymbol{\xi}(\boldsymbol{r}) = \xi(r)\, e^{i(m\theta - n\varphi)}$, with $m$ and $n$ the poloidal and toroidal mode numbers. This shows that an MHD instability with mode numbers $m$ and $n$ has a maximum amplitude on a flux surface with $q = m/n$ (as already mentioned in section 2.1). In the approach of a normal (toroidal) tokamak, the poloidal symmetry is lost, which means that the poloidal components of various modes can couple for a given toroidal mode number $n$ (so that $\boldsymbol{\xi}(\boldsymbol{r}) = e^{-in\varphi} \sum_m \xi(r)\, e^{im\theta}$).

*2.3.2. The peeling-ballooning model*

In the previous paragraph, it was shown from equation (2.17) that there are two possible sources of MHD instability: one proportional to the pressure gradient $\nabla p$ and the other to the (edge) current density $J_{\|}$. When the dominant destabilizing term is proportional to $\nabla p$, the instabilities are said to be pressure-driven. The pressure-driven instabilities are categorized as either interchange or ballooning modes. The term ballooning refers to the fact that, in three-dimensional geometry, the curvature of the magnetic field line often alternates between regions of favourable and unfavourable curvature. In tokamaks these regions are the HFS and LFS, respectively. This means that a perturbation becomes ballooning unstable when it varies along a field line in such a way that it is, on average, more concentrated in the unfavourable curvature region. Vice versa, this is also the reason for the improved stability associated with D-shaped plasmas (as mentioned in section 2.1), where a magnetic field line has a relatively large fraction of its trajectory located on the favourable curvature region on the HFS.

If the dominant destabilizing term for a certain instability is proportional to current density, the instability is called current-driven. Alternatively, these instabilities are also known as kink modes. As for the pressure-driven modes, there are two categories of kink modes as well. These are the internal and external kink modes, with the internal modes occurring in the confined plasma and the external modes at the edge surface.

Since their discovery, ELMs have been associated with both ballooning and kink modes (a historical overview is given in [Huysmans05]).

**Peeling modes**

On the one hand, ELMs have been thought of as a kink instability driven by the increased edge current density of the H-mode (due to higher edge temperatures compared to L-mode). In circular plasma approximation, it has been shown that low-$n$

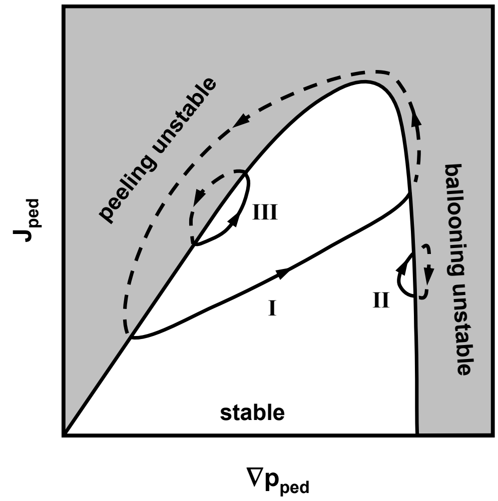


**Figure 2.10** *Based on ideal MHD instabilities, it is possible to imagine a variety of stable-unstable paths through the $J_{ped}$,$\nabla p_{ped}$ stability diagram. These simplified cycles can be related to the various ELM types that have been seen in experiments.*

kink modes are destabilized by the edge current density and stabilized by edge shear (with $n = 1$ being the most unstable external kink mode) [Manickam92]. Note that the shear decreases with increasing edge current (cf. equation (2.2)).

If the edge safety factor is just below a rational value, the so-called peeling mode becomes unstable [Laval74]. This is a specific type of kink mode, strongly localized and dominated by one single poloidal harmonic (as can be seen e.g. in Figure 2.12(b)). Furthermore, whereas the kink mode is directly associated with the derivative of $J_{||}$ (cf. equation (2.17)), the peeling mode is associated with the edge current density itself.

In addition to the increase of edge current density caused by the higher temperatures in H-mode, the bootstrap current was afterwards identified as the dominant source of current density at the edge [Strait93], [Ferron94]. The bootstrap current is driven by both the edge temperature and density gradients (but mainly by the latter), and strongly depends on the collisionality. Furthermore, it was found that not only has the increase in current density a destabilizing effect, but the pressure gradient has a stabilizing effect as well (through the equilibrium).

**Ballooning modes**

On the other hand, from experimental measurements of the pedestal pressure it was early on noted that the limit to $\nabla p$ seemed to agree with the ballooning stability limit for $n = \infty$ modes (which are the most unstable ballooning modes) [Gohil88]. However, after correctly accounting for the influence of the edge current density, it was then found that the $n = \infty$ ballooning stability limit actually disappears and it is speculated nowadays that the plasma is in the regime of so-called second stability [Huysmans95]. This regime is a somewhat surprising feature disclosed from analytical ideal MHD stability calculations for $n = \infty$ ballooning modes. In contrast to the first stability region, $n = \infty$ ballooning modes are unconditionally stable against $\nabla p$ in the second stable regime. From an experimental point of view, this second stability regime is indeed accessed by applying strong enough plasma shaping, high enough $\beta_p$, and a high enough $q$-value at the edge (which is the most accepted explanation [Huysmans09]).

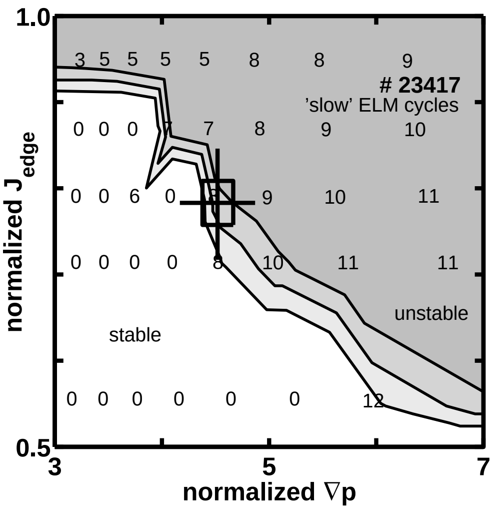


**Figure 2.11** *Stability diagram as obtained from MISHKA: for the various points in the normalized $J_{ped}$,$\nabla p_{ped}$ stability diagram it is shown whether the equilibrium is stable or unstable. In the latter case, the most unstable toroidal mode number n is also plotted. The big cross-hair on the stability border notes the actual point of the experimental equilibrium input.*

**Peeling-ballooning modes**

Finally, it is only by combining the stability of peeling modes, finite-*n* ballooning modes, and their interaction that a pressure limit is found for the ballooning modes (while simultaneously keeping the low-*n* kink modes stable). This is the so-called peeling-ballooning model [Hegna96], [Connor98a], [Wilson99], [Snyder02], [Snyder04]. It leads to a reduction of the stable region in the stability diagram such that both the edge current and the edge pressure gradient are destabilizing, as can be seen in Figure 2.10. The resulting (rather violent) instability represents the coupling between peeling modes and finite-*n* ballooning modes which is able to exploit the free energy in both the pressure and current density.

**ELM cycles**

Based on ideal MHD instabilities alone, it is possible to imagine a variety of ELM-cycles in the $J_{\mathrm{ped}}$,$\nabla p_{\mathrm{ped}}$ stability diagram which could correspond to different ELM types discussed in paragraph 2.2.1. As shown in Figure 2.10(b), three (simplified) cycles can be envisaged [Snyder02], [Wilson06].

The first cycle (I) sketches the usual scenario, where both pressure gradient and current density become high enough to violate both the ballooning and peeling mode stability criteria (peeling-ballooning mode). This occurs e.g. in a hot plasma where the pressure gradient rises to the ballooning boundary first, followed by a rise of the current density (assuming the current diffusion time is longer in hot plasmas) until the peeling stability limit is reached. The large crash event that then occurs could be associated with type-I ELMs. In low collisionality plasmas, with the pressure gradient at the ballooning boundary, the contribution from the bootstrap current actually suffices to drive the peeling mode unstable [Huysmans98].

The second cycle (II) in Figure 2.10(b) depicts the situation where the pressure gradient is high, but the current density is low, so that only the ballooning mode is triggered. This scenario is e.g. obtained when the edge density is high (causing high

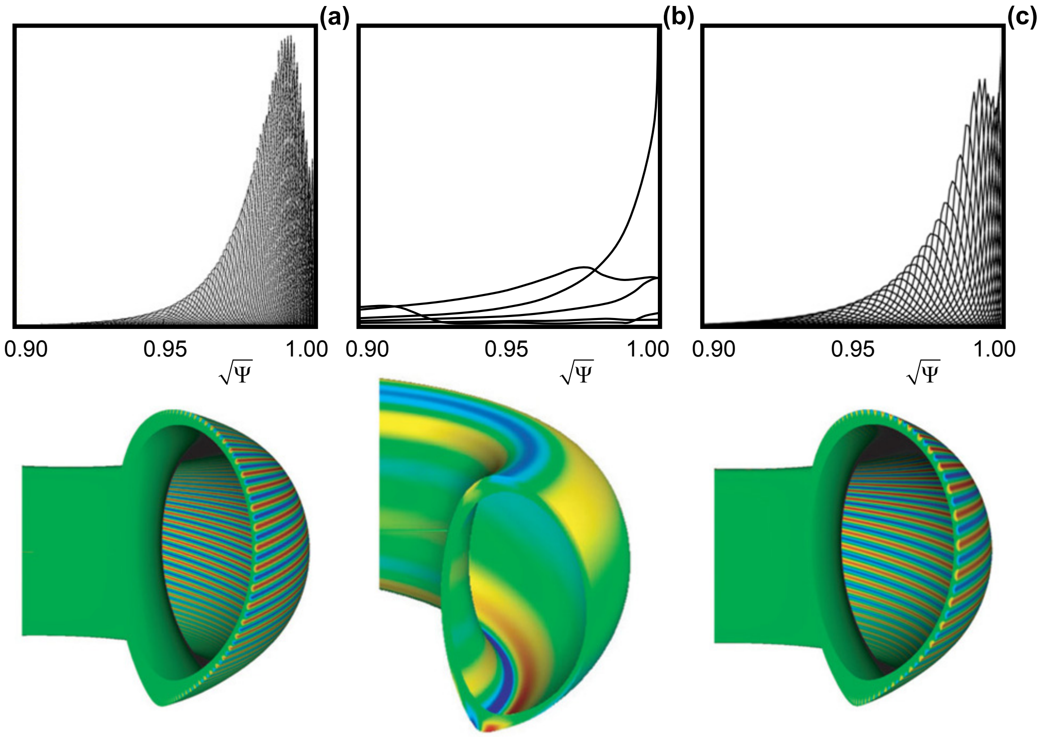


**Figure 2.12** *Typical radial mode structures as obtained from the global linear MHD stability code MISHKA [Huysmans05]: the top row shows the radial distribution of the mode amplitude for various poloidal modes. The bottom row shows the global structure of the most dominant n-number. In (a), the results for an $n = 32$ ballooning mode are shown, in (b) for an $n = 1$, $m = 5$ peeling mode, and in (c) for an $n = 20$ peeling-ballooning mode.*

collisionality) or the plasma shaping is strong (so that a larger bootstrap current is required for triggering the peeling mode). On the one hand, this instability could be just a soft limit to the pressure gradient (without ELMs), which would be self-stabilizing in the sense that increased edge transport will reduce the pressure gradient and stabilize the mode. On the other hand, it could also cause small ELMs, possibly of type-II.

The third cycle (III) visualizes the condition where the pressure gradient is low and the current density is high, which triggers the peeling mode. This situation could occur in cooler plasmas: if the current diffusion time is short enough, the peeling boundary could be crossed before the pressure gradient has reached the ballooning stability limit. Alternatively, a resistive ballooning mode (i.e. non-ideal MHD) could be at play, which is related to enhanced transport. This, in turn, could reduce the pressure gradient (due to decreased confinement in the pedestal region) and drive the peeling mode unstable. Due to the small radial extent of the peeling mode, the third cycle might be expected to give rise to small (type-III) ELMs.

### *2.3.3. Comparison of theory and experiment*

Using modern MHD stability codes, the stability of the edge pedestal in H-mode plasmas can be evaluated. As an example, the results of the global linear MHD stability code MISHKA are shown in Figure 2.11 and Figure 2.12. MISHKA is a stability code that finds the growth rate of a linear perturbation $\xi$ [Mikhailovskii97]. This is done for several pedestal profiles of $\nabla p$ and $J_{\|}$ around experimentally obtained values (while

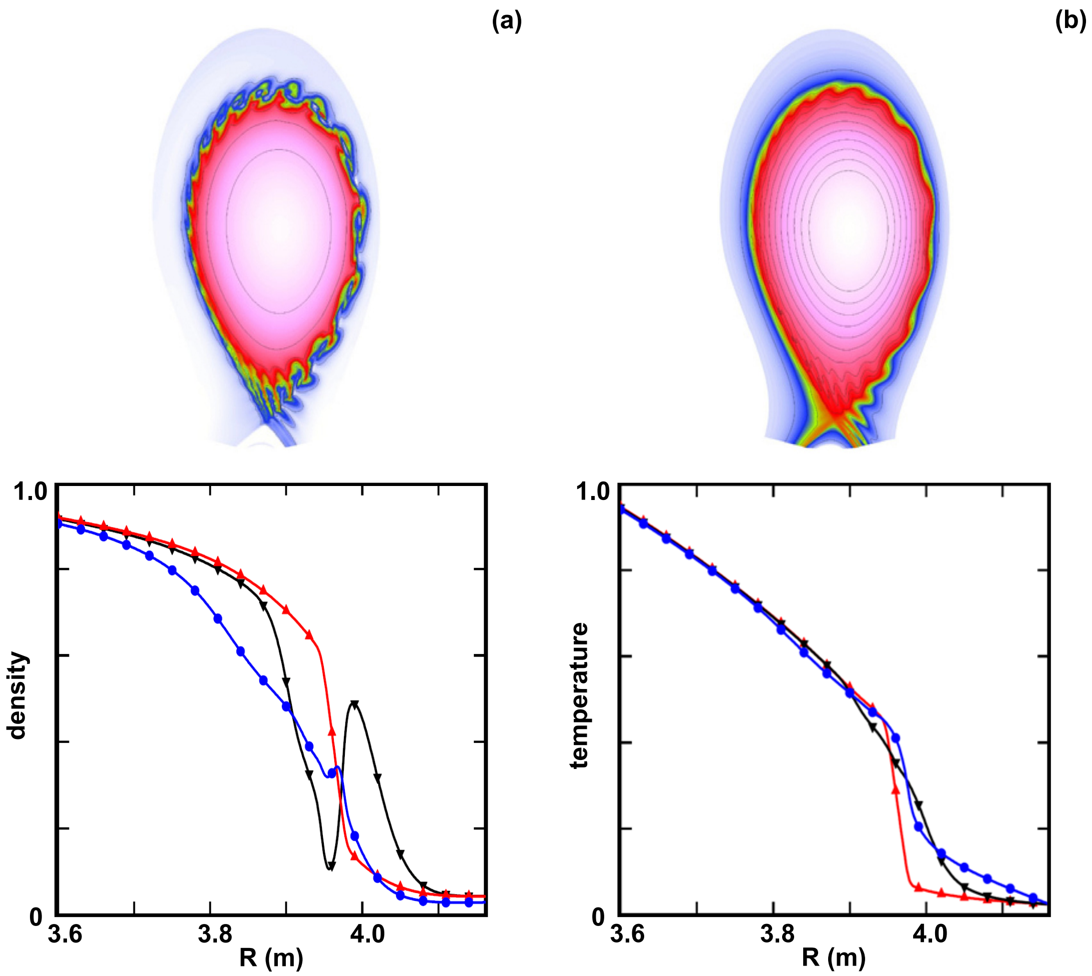


**Figure 2.13** *Example of JOREK's non-linear MHD simulations of the ELM dynamics [Huysmans09]: in (a) and (b), the density and temperature perturbations are shown respectively. The bottom row shows the radial profiles for three time points during the ELM: at the start (red), at the time of maximum perturbation (black), and at the end of the simulation (blue). The poloidal cross sections shown in the top row are taken at the time of maximum amplitude.*

keeping $\beta_p$ and $I_p$ constant) in order to construct a stability diagram such as shown in Figure 2.11. Under certain assumptions, like e.g. zero charge density and a small displacement current compared to the equilibrium current, a closed set of resistive MHD equations is obtained (which accounts for the effects of flow, viscosity, compressibility, and inertia). For each point in the stability diagram, solving this set of differential equations yields e.g. the growth rates for each toroidal and poloidal mode number $n$ and $m$, or the radial structures of the most unstable modes. As can be seen in Figure 2.11, the position of the experimental equilibrium is then found to be either stable or unstable and is plotted in the stability diagram together with the most unstable toroidal mode numbers (i.e. with the largest growth rates). In Figure 2.12, examples are shown of the radial distribution of the most unstable modes and the global structure of the most dominant $n$-number.

The linear (ideal) MHD peeling-ballooning model successfully describes the limits to the equilibrium pressure gradient and current density within error bars. Combined with its predictions for the radial and poloidal mode structure, these are quantities that can indeed be compared to experimental observations. However, linear models can only explain the onset of the ELM. As was shown in section 2.2, the ELM crash is an extremely fast event which displays explosive ejection of parts from the confined plasma (cf. Figure 2.8). For this kind of time development, non-linear models such as JOREK are needed [Huysmans09]. In general, non-linear models start off from an equilibrium unstable to medium-$n$ ballooning modes obtained from linear MHD and then numerically evaluate a complete set of MHD equations as a function of time (without linear assumptions). An example of the global mode structures, into which the temperature and density non-linearly develop, is given in Figure 2.13. One of the most important results from non-linear modelling is that ballooning modes are indeed seen to develop into filament-like structures expelling across the separatrix (similar to the measurements shown in Figure 2.8). Furthermore, a good agreement is found between the non-linear simulations and experimental observations of energy deposition patterns in the divertor.

# Chapter 3

# ASDEX Upgrade and its auxiliary systems

The ASDEX Upgrade (AUG) device is a tokamak with a divertor configuration, as is emphasized by its acronym: AxiSymmetric Divertor EXperiment. Although the 'Upgrade' part suggests otherwise, AUG is a completely new machine which shares no components with its predecessor (where, as mentioned in Chapter 1, the H-mode was discovered). As of 2007, it has developed into the first device with full tungsten coverage of all plasma facing components. In this way, AUG is able to operate under conditions comparable to the full tungsten wall which is foreseen for tokamak operation in the nuclear phase (i.e. DEMO). A second way in which AUG contributes to the design and physics base of future tokamaks is by its geometrical shape. Together with the JET tokamak, AUG forms a basis for extrapolations towards ITER since all three devices have similar shapes at absolute length scales of 1:2:4 (AUG:JET:ITER).

In this chapter, first a general description of AUG is given, followed by short explanation of the different heating methods used. An overview of the available diagnostics is given in the third section; with the exception of the ECE diagnostics, which will be separately described in Chapter 4. In the last section, a short explanation will be given on some of the plasma edge manipulation tools that are available at AUG.

## 3.1. The tokamak

With a major radius of $R_0 = 1.65$ m, and a minor (horizontal) radius of $a = 0.50$ m, AUG is a tokamak of medium size [Herrmann03], [Gruber09a]. As can be seen in Figure 3.1, AUG is geometrically scaled down by a factor four compared to ITER, and by a factor two compared to JET. The toroidal magnetic field $B_t$ is created by 16 D-shaped toroidal field coils [Streibl03]. In order to have a reactor relevant design, the poloidal magnetic field coils (which are required to form an elongated shape with an X-point) are placed outside the vacuum vessel and outside the toroidal field coils. The poloidal field system at AUG consists of three groups of coils [Pillsticker84]: five Ohmic heating (OH) coils provide a flux swing of the air-core OH transformer (9.5 Vs) to induce the toroidal plasma current $I_p$. The central OH coil is a solenoid with a height of 3 m, major and minor diameters of 1.02 m and 0.51 m, and 510 turns. The second group consists of eight vertical field coils to control the plasma equilibrium, i.e. plasma position, shape and divertor configuration. Finally, there is a group of six internal and external coils that is used to control the vertical stability of the elongated plasma. These are necessary since the passive stabilizing loop (PSL), which is located close to the plasma, only slows down the growth rate of the vertical plasma position instability but does not stabilize the whole system.

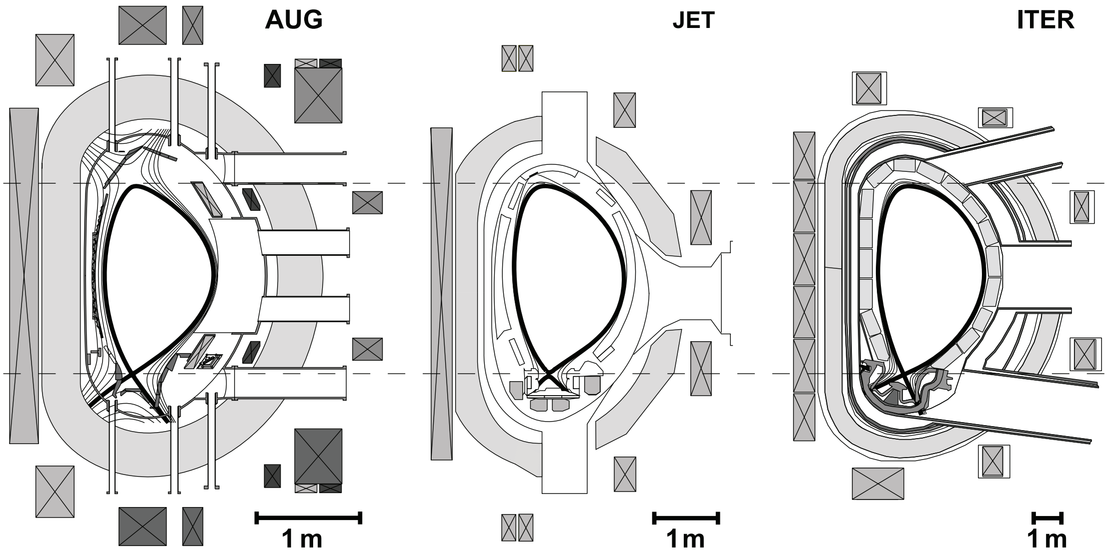


**Figure 3.1** *Poloidal cross sections of AUG, JET, and ITER showing geometrical similarity at different scale sizes.*

With these coils, a magnetic field of up to 3.1 T on the plasma axis can be reached and the highest achievable plasma current is 1.4 MA; the plasmas typically have $B_t = -2.5$ T and $I_p = 1.0$ MA though. The maximum pulse length of the plasmas is about 10 s. The main parameters of AUG are summarised in Table 3.1, combined with the values of JET (from [Wesson99]) and ITER (from [ProgIPB07]) for comparison.

**Table 3.1** *ASDEX Upgrade machine and typical plasma parameters*

| | AUG | JET | ITER | Units |
|---|---|---|---|---|
| major plasma radius ($R_0$) | 1.65 | 3.00 | 6.2 | m |
| minor horizontal radius | 0.50 | 0.96 | 2.00 | m |
| plasma volume | 14 | 80 | 830 | $m^3$ |
| maximal $\|B_t\|$ | 3.1 | 4.0 | 5.3 | T |
| maximal $\|I_p\|$ | 1.4 | 5.0 | 15 | MA |
| pulse length | ~ 10 | ~ 40 | > 400 | s |
| $P_\Omega$ | ~ 1 | < 1 | ~ 1 | MW |
| $P_{NBI}$ | 2 x 10 | 25 | 33-50 | MW |
| $P_{ICRH}$ | 8 | 9 | 20 | MW |
| $P_{ECRH}$ (upgrade in progress) | 2 (+ 4) | - | 20-40 | MW |
| $P_{LH}$ | - | 7 | 0-20 | MW |

## 3.2. Heating systems

Not only does AUG compare to ITER geometrically, its installed heating power also assures that the energy influx is of similar level. This quantity is usually expressed as the ratio of heating power and major radius [Lackner08]. As can be estimated from Table 3.1, the ratio $P/R$ is roughly 18 MW/m for AUG, whereas it is about 24 MW/m for ITER. This high $P/R$ ratio at AUG allows for a high flexibility in heat deposition, and in current drive and torque input as well. In Figure 3.2, an overview is shown of the different heating systems at AUG. The contribution of each system to the heating scheme is shortly explained in the paragraphs below.

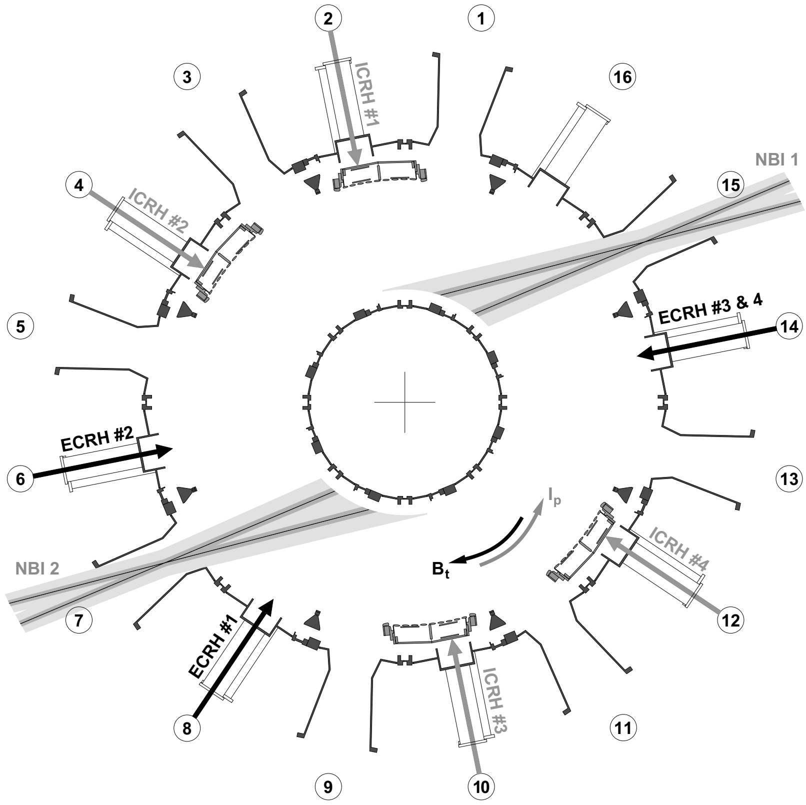


**Figure 3.2** *Top view of the AUG tokamak, showing the NBI and RF heating systems. For standard plasma operation, the directions of $I_p$ and $B_t$ are as indicated.*

*3.2.1. Ohmic heating*

As described in section 1.2, the current that confines the plasma is the result of a flux swing through the transformer. Due to the finite resistance of the plasma, this current also heats the plasma: this is Ohmic heating (for that reason primary coils are mostly referred to as OH-coils). The plasma's electrical resistance is approximately given by the so-called Spitzer conductivity, according to which the resistance decreases proportional to the electron temperature as $T_e^{-3/2}$. Ohmic heating is therefore less efficient at higher temperature and only works up to a certain maximum. Depending on the exact plasma scenario, Ohmic heating at AUG can be up to about 1MW.

*3.2.2. Neutral beam injection*

Neutral beam injection (NBI) is the major heating system at AUG: the 20 MW of power are delivered by two injectors with each four sources [Streibl03]. Neutral particles are used for this purpose, since they are not deflected by the magnetic field. They are produced by first ionising a gas (usually deuterium; but hydrogen could also be used). The ionised particles are then accelerated over an electrical grid and, after having gained energy, they are neutralised again for about 50 % in a gas target neutralizer. Before entering the plasma, the remaining ionised particles are deflected, so that a beam of highly energetic neutral particles remains. Once they have entered the plasma, the neutral particles will first be ionised by either electron impact ionisation ($D^0 + e^- \rightarrow D^+ + 2e^-$), ion impact ionisation ($D^0 + I^n \rightarrow D^+ + I^n + e^-$), or charge exchange ($D^0 + I^n \rightarrow D^+ + I^{n-1}$). Then they will gradually be thermalised: i.e. they will lose their high energy via Coulomb collisions with the bulk plasma until they are slowed down to thermal energies.

The full particle energy of NBI1 (Figure 3.2) is 60 keV, and for NBI2 it is 93 keV. This is the energy of the single D atoms. As there are also $D_2$ and $D_3$ molecules accelerated over the grid, there will be particles injected as well that have a half and a third of the full particle energy. Depending on this initial beam energy and on the energy of the plasma electrons and ions, the injected fast particles predominantly heat either the ions or the electrons and finally thermalise. As the injected particles not only transfer their energy but also their momentum, the NBI also provides a torque and therefore gives an angular momentum to the plasma. In standard operation, the main direction in which the beams inject is co-current (i.e. counter-clockwise); the magnetic field is pointed in the opposite direction. However, the different toroidal and poloidal angles at which the eight sources inject do allow for varying the power deposition profiles.

### *3.2.3. Radio frequency heating*

The two other heating systems at AUG are based on the principle of radio frequency (RF) heating: if the angular frequency of injected microwave radiation is equal to (one of the lower order harmonics of) the cyclotron frequency of a particle gyrating around magnetic field lines, then the electromagnetic (EM) wave will resonate with the gyrating particle and transmit its energy. Naturally, this heating method comes in two varieties: one for the electrons and one for the ions. Furthermore, since the gyro-frequency depends on the magnetic field strength, which varies over the plasma, RF heating allows for localised energy deposition.

For ion cyclotron resonance heating (ICRH), the AUG system consists of four generators with a frequency range of 30-120 MHz and an output power of 2 MW each [Bobkov10]. Via transmission lines and matching systems, the power from the generators is brought to the antennas in the vacuum vessel, which are shown in Figure 3.2. The antennas consist of two straps, each with opposite phasing of the strap currents. In standard configuration, two antennas operate simultaneously: antennas 1 and 2 form a pair, as do antennas 3 and 4. As mentioned before, absorption of the power occurs at the location where the frequency of the injected wave matches the local ion cyclotron frequency (or one of its higher harmonics). For the frequencies at which the plasma bulk ions resonate, coupling of the power to the plasma is not optimal. However, plasma heating can still be done by aiming at the resonance of a small concentration of resonating species amongst a majority of nonresonant ions. This so-called minority heating is the standard scenario at AUG, where the hydrogen minority is heated with a single pass absorption level above 90%.

The system for electron cyclotron resonance heating (ECRH) at AUG is made up of four gyrotrons, each of which can deliver 0.5 MW for two seconds [Leuterer09]. The microwaves are conveyed via waveguides to the vessel, where an adjustable mirror serves as beam launcher. The gyrotrons are operated at a frequency of 140 ± 0.5 GHz, which (for the standard AUG operation at $B_t = -2.5$ T) corresponds to the second harmonic of the electron cyclotron frequency in the plasma centre. Injection of the microwave in X-mode (i.e. with extraordinary polarization: $\boldsymbol{E}_{\text{wave}} \perp \boldsymbol{B}_t$) provides full absorption of the power, highly localised around the position of the resonance. After full installation in sector five (see, Figure 3.2), the newest addition to ECRH will be able to deliver 4 MW for the full duration of the discharge. It is a multi-frequency system designed to work at either 105 or 140 GHz, or as a step-tuneable gyrotron with the additional frequencies 117 and 127 Ghz [Wagner08]. Currently, ECRH 2 already routinely delivers 1-2 MW.

## 3.3. Diagnostics

Progress in the understanding of plasma performance often arises from the quantitative confrontation between theory and experiment [Hutchinson05]. This requires that theoretical models calculate in realistic configurations and circumstances. It also means that plasma properties should be measured as complete and accurate as possible. The latter is of course a key aspect for the actual operation of a tokamak device as well. However, a major challenge in plasma diagnosis originates from the fact that a plasma is fragile and has extremely high temperatures, which makes it very difficult to actively probe (deep into the core).

Important parameters necessary to obtain a good impression of the nature of a plasma discharge are the electron and ion temperatures ($T_e$, $T_i$) and densities ($n_e$, $n_i$, and the neutral density $n_0$), mean velocity ($V_i$) and electric current density ($j$), pressure ($p$), and electric and magnetic fields ($E$, $B$). Most of these physical quantities are constant on a flux surface, so that obtaining their radial profiles is sufficient. Deriving the gradients of such profiles is useful in transport analysis and for determining stability properties. However, for monitoring the development of plasma instabilities, it can also become important to have information available in more than the one radial dimension.

With approximately 70 diagnostics, AUG is well equipped and it is beyond the scope of this section to describe all of them [Herrmann03]. What follows here, is a short description of several basic techniques (and references to their implementation on AUG) that are used to obtain some of the important plasma parameters. In section 3.3.2, some of the plasma edge diagnostics at AUG are described in more detail. With the use of (pickup) coils, it is possible to determine the magnetic fields and derive the MHD equilibrium (paragraph 3.3.1). There are various types of (Langmuir) probes that are able to endure contact with the plasma (at the edge); from their measurements particle flows can be derived [Müller05]. Several diagnostics are depending on the effect of the plasma's refractive index $N$ on the transmission of EM-waves: e.g. the electron density can be determined from interferometry [Mlynek10], and using Doppler reflectometry it is possible to determine radial electric fields and electron density fluctuation characteristics [Conway07]. Observation of radiation emitted by free electrons can yield information on plasma properties such as the electron temperature (via cyclotron emission, see Chapter 4), the effective ion charge $Z_{eff}$ (via Bremsstrahlung, [Rathgeber10]), or perturbations of the flux surface geometry (via soft X-ray tomography, [Igochine10]). Spectroscopy of line radiation from atoms and ions that are not fully ionized can provide information about, for instance, the density and temperature of (impurity) ions and bulk plasma flow velocities (from passive CXRS, [Viezzer11]), or radiation losses (UV-bolometry, [Reiter09]). Measurements of the radiation scattered by plasma particles that are subjected to the injection of (nonperturbing) EM-waves yield detailed information on the distribution function of electrons (Thomson scattering, see paragraph 3.3.2) or ions (collective Thomson scattering, [Meo08]). Unlike charged ions, neutral atoms travel freely across the magnetic field; emitted neutral particles therefore provide information, such as the ion temperature [Verbeek86], from the plasma interior. From the atomic process related to the line radiation induced by injected neutral beams (paragraph 3.2.2), information about the plasma interior is obtained: ion temperatures, densities and rotation velocities are e.g. obtained from active CXRS [Viezzer12], and

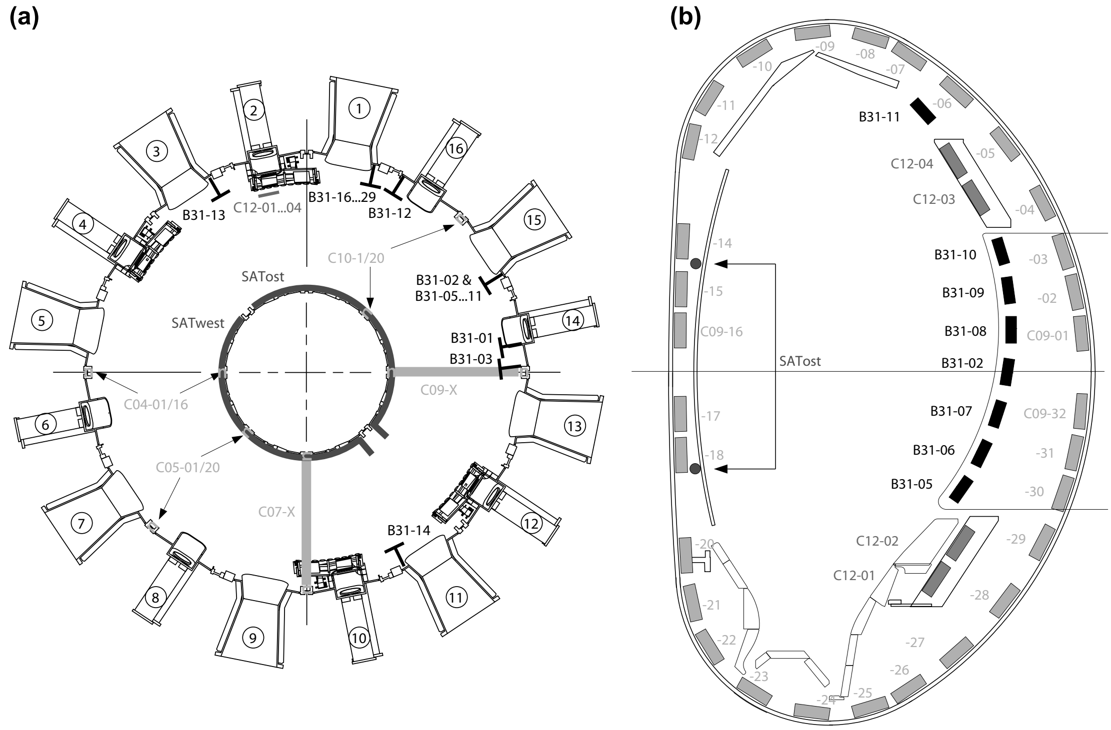


**Figure 3.3** *Overview of the toroidal (a) and poloidal (b) locations of the magnetic coils: the Mirnov coils (C07 and C09) and the four coils mounted on the PSL (C12) observe poloidal magnetic field fluctuation. The so-called ballooning coils (B31) and the two sets of saddle loops on the HFS (SATost and -west) measure radial magnetic field variations. The remaining rings of poloidal coils (C04, C05, and C10) are used for the measurement of the magnetic field itself; for all the C-coils (apart from C12), there are duplicate rings just outside the vacuum vessel.*

with a similar technique, information on the fast ion distribution function is also acquired [Geiger11]. Beam emission spectroscopy yields information about the electron density [Dux11], and polarimetric measurements of the motional Stark effect (MSE) provide the current density [Reich07] and radial electric field [Hobirk00]. A last category of plasma diagnostics is based on the measurement of nuclear reaction products or (injected) energetic ions: there are several detectors installed for detecting neutron- and $\gamma$-radiation and for fusion product measurements [Preis91], [Ullrich97], and there is a fast ion loss detector (see paragraph 3.3.2) that traces the origin of fast ions that have escaped the plasma.

In the paragraphs below, some of the diagnostics relevant for plasma edge analysis in general, or for this thesis in particular, are described in more detail. The main diagnostics used, ECE and ECE-imaging, are separately described in Chapter 4.

### *3.3.1. Magnetic pickup coils and equilibrium reconstruction*

There are over two hundred magnetic coils mounted inside the AUG vessel that measure magnetic fluctuations ($dB/dt$) [Gernhardt92]. The allocation of the coils is shown in the toroidal and poloidal cross sections of Figure 3.3.

The group of coils known as the Mirnov-diagnostic consists of two rings of 30 poloidal coils, plus six single coils at different toroidal locations. These are used for measuring fluctuations of the poloidal magnetic field (which is also done by the four coils mounted on the PSL). The so-called ballooning coils are used for measuring fluctuations in the radial magnetic field and they are distributed over two poloidal arrays plus six coils at different toroidal locations. From the two poloidal ballooning coil arrays, one is shown in Figure 3.3(b); the other, in sector one, is the high-resolution array which has twice as many coils (see e.g. Figure 6.2). Not shown in Figure 3.3 are the filament probe (which can be separately mounted on the mid-plane manipulator in sector eight on request) and the ballooning coils that have been installed on the HFS for the 2012 experimental campaign (one in sector fifteen and seven in sector four). Both the Mirnov-diagnostic and the ballooning coils measure at sampling rates of 2 MHz for the entire duration of the discharge.

Apart from the two rings of the Mirnov-diagnostic, there are three more rings of poloidal coils: one with 30 coils (C04) and the other two with 40 coils (C05 and C10), see Figure 3.3(a). With the use of integrators (with a decreased sampling rate of 250 kHz) the tangential magnetic field is determined from the coils of these three rings [Giannone09].

For the standard reconstruction of the MHD equilibrium, this tangential magnetic field is one of two required inputs; the other is the normal magnetic field, which is measured by several flux loops mounted in the vacuum vessel. The equilibrium provides a coordinate frame that allows transformation between machine and magnetic coordinates. At AUG, the equilibrium reconstruction is performed using the CLISTE code which solves the Grad-Shafranov equation [McCarthy99]. The standard equilibrium reconstruction can be further constrained by including extra measurements. When kinetic inputs are also provided (i.e. the combined $T_e$ and $n_e$ profiles that give the pressure) the current density profile can be determined [Dunne11]. The reconstruction can be improved with additional inputs, such as the pitch angle of the magnetic field (as determined from MSE) or the location of the strike points on the divertor (which narrow the location of the X-point).

Once resolved, the magnetic topology can be described in various coordinate systems. The most common coordinate systems are the geometrical system ($r$, $z$, $\varphi$), the toroidal system ($r$, $\theta$, $\varphi$), and the flux coordinate system ($\rho$, $\theta$, $\varphi$); here, $\theta$ and $\varphi$ are the poloidal and toroidal angles, and $r$ and $\rho$ are radial coordinates. In the toroidal system, $r$ is the (normalized) minor radius of the plasma. In the flux coordinate system, $\rho$ is the flux surface label expressed in terms of the normalized poloidal flux $\Psi$:

$$\rho = \sqrt{\frac{\Psi - \Psi_0}{\Psi_{sep} - \Psi_0}} \ . \tag{3.1}$$

Here, $\Psi_0$ and $\Psi_{sep}$ are the poloidal magnetic fluxes at the magnetic axis and the separatrix.

The nature of magnetic field line winding around the torus is such, that for equally sized steps $d\varphi$ in toroidal direction it is not generally so that equally sized steps $d\theta$ are made in poloidal direction. This effect becomes important when only a small portion of the geometrical poloidal angle is observed, especially on the LFS of non-circular plasmas (as can be seen in Figure 3.4(b)).

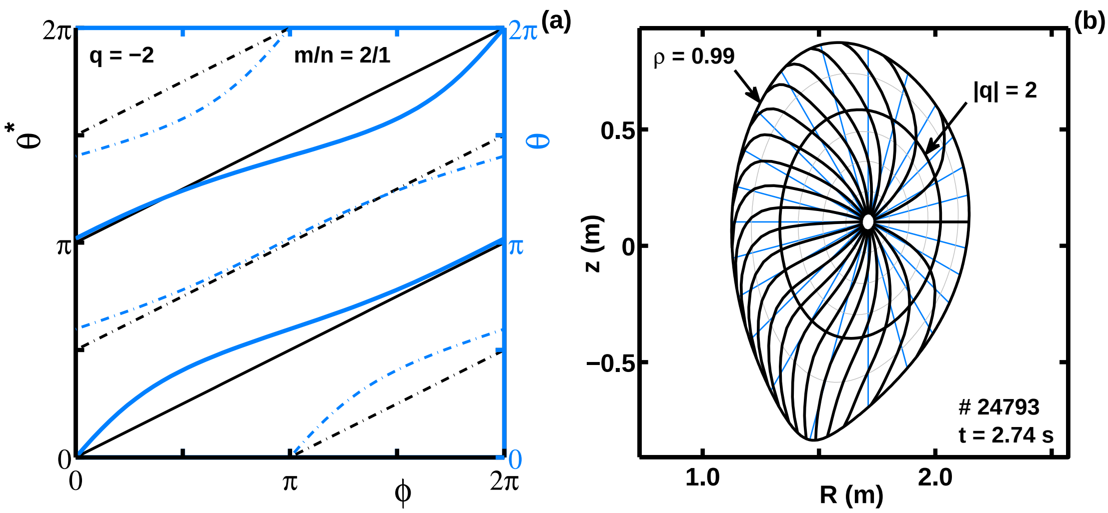


**Figure 3.4** *Geometrical and straight field line coordinate systems: in (a), the $q = -2$ flux surface is unfolded in two different ways. In geometrical coordinates ($\varphi$, $\theta$), it can be seen that the inclination of the magnetic field lines is strongest at the outer mid-plane ($0 < \theta < \pi/2$ and $3\pi/2 < \theta < 2\pi$). When this is corrected for, and the poloidal angle is expressed in terms of $\theta^*$, the magnetic field lines appear as straight lines on the unfolded flux surface. On the different flux surfaces shown in (b), the poloidal angles $d\theta^*$ have been calculated in steps of $d\theta = 2\pi/24$. In this representation, the geometrical angles $d\theta$ appear as straight lines. It can furthermore be seen that, for the outer flux surfaces, the divergence of the field lines in poloidal direction is largest on the outer mid-plane.*

In order to correct for this effect, the flux coordinate system ($\rho$, $\theta$, $\varphi$) is usally transformed into the straight field line coordinate system ($\rho$, $\theta^*$, $\varphi$) [Greene62], [D'haeseleer91], [Schittenhelm97]. In this coordinate system, as can be seen in Figure 3.4(a), the magnetic field lines appear straight on unfolded flux surfaces. The relation between the geometrical angle $\theta$ and the straight field line angle $\theta^*$, on a given flux surface, is given by

$$\theta^*(\theta) = \frac{2\pi \int_0^{\theta} \sqrt{g} R^{-2}\,\mathrm{d}\theta}{\int_0^{2\pi} \sqrt{g} R^{-2}\,\mathrm{d}\theta} . \tag{3.2}$$

In this expression, $\sqrt{g}$ is the Jacobian in cylinder coordinates, which is given by

$$\sqrt{g} = \left[\nabla\theta\cdot(\nabla\Psi\times\nabla\varphi)\right]^{-1} = r^2 R\left[(z-z_0)\frac{\partial\Psi}{\partial z}+(R-R_0)\frac{\partial\Psi}{\partial R}\right]^{-1} . \tag{3.3}$$

Using these equations, the straight field line angle $\mathrm{d}\theta^*$ can be calculated for an observed geometrical angle $\mathrm{d}\theta$ (which can then be linearly extrapolated to $2\pi$). This is for example done when deriving mode numbers of instabilities from measurements (see Chapter 5 and Chapter 6), or when calculating the effect of outside perturbations on flux surfaces (see Figure 3.6).

### *3.3.2. Edge diagnostics*

For determining high resolution electron density profiles at the plasma edge, one of the diagnostics employed at AUG is the lithium (Li) beam. It is an active diagnostic (meaning it provokes a local perturbation of the plasma) that injects high energy Li atoms (50 keV) into the plasma [Wolfrum93]. Together with the ECE diagnostics, the Li beam is installed in sector nine (cf. Figure 3.2). After excitation due to collisions, the atoms lose their excess energy under the emission of line radiation, the intensity of which is dependent on the electron density $n_e$. From above the Li beam, the $2p$-$2s$ line emission from impact excitation is observed using photomultiplier tubes at a temporal resolution of 20 kHz. For observations from below, a Li beam activated charge exchange (CX) spectroscopy system is installed, which has a time resolution of 250 Hz. The optics system is optimised for 35 channels to have a near tangential observation of the flux surfaces in the range of R = 2.05-2.15 m (at a height of z = 0.32-0.33 m). Each channel has an observation volume of about 5 mm in the radial direction and 12 mm along the flux surface. Apart from collisions, the Li beam is strongly attenuated by other plasma-beam interactions (e.g. ionization and scattering) that have to be accounted for using background subtraction techniques. This, however, requires the beam to be chopped which can be done at a 2 kHz frequency [Willensdorfer12]. The spatial resolution of the diagnostic allows for a good coverage of the steep edge density gradient. At the pedestal top (and for obtaining a complete density profile) the Li beam measurements are combined with those from the interferometer using a probabilistic (integrated) data analysis approach [Fischer08a].

A second active diagnostic at AUG, that not only measures $n_e$ but simultaneously the electron temperature $T_e$ as well, is Thomson scattering [Murmann92], [Kurzan11]. It relies on the process of scattering electromagnetic waves, in this case photons from a high energy laser, by free electrons in the plasma. The width of the measured scattering spectra is proportional to the square root of the electron temperature and the intensity is related to the electron density in the observed volume. The edge Thomson scattering system is equipped with six multi-pulse Nd:YAG lasers with a wavelength of 1065 nm (the core system has three lasers). One pulse, travelling vertically through the plasma, lasts 15 ns and has a pulse energy of about 1 J. With a lens just outside the vacuum vessel, the scattered light is focussed onto ten four-channel polychromators for the edge system (sixteen for the core system). Each detector measures scattered light from an observation volume with a vertical extent of 2.56 cm and a width of 0.5 mm (i.e. the FWHM of the Gaussian laser beam). The lasers have repetition rates of 20 Hz and each laser can be triggered independently. This means that, in standard operation, the Thomson scattering system operates at a 120 Hz time resolution. In profile mode, the lasers are fired in sequence with 100 $\mu$s intervals, making use of the fact that they are positioned 3 mm apart horizontally. This increases the radial resolution, albeit at the expense of the temporal resolution. For optimal coverage of the edge transport barrier, plasma shape and position have to be matched to the fixed radial position of the edge Thomson scattering lasers at R = 2.15-2.16 m. Alternatively, a short outward shift of the plasma is sometimes used.

Apart from diagnostics for the electrons, AUG is also equipped with several spectrometers for charge exchange recombination spectroscopy (CXRS). This technique is based on line emission by excited ions and provides a local measurement of temperature, velocity and density of the monitored impurity ions. Due to the high temperatures in the plasma core, all (light to medium weight) impurity ions are fully

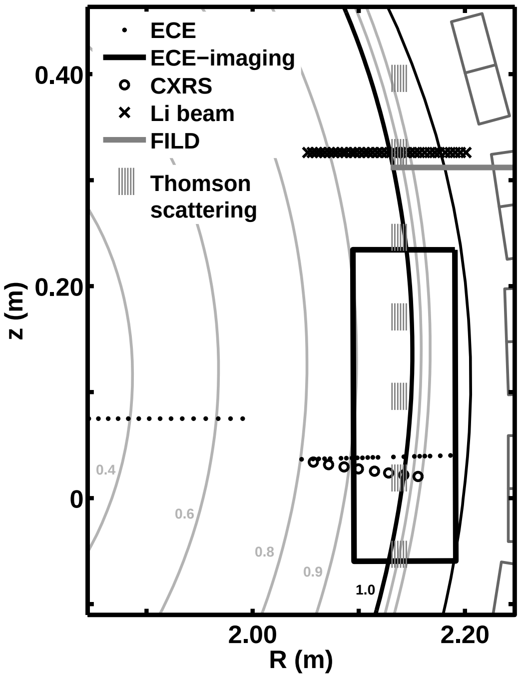


**Figure 3.5** *Overview of the location, in a poloidal cross section, of some edge diagnostics at AUG. The electron temperature diagnostics ECE and ECE-imaging are described in Chapter 4, the others here in section 3.3.2.*

stripped from their electrons. In order for these ions to send out line emission, they have to capture an electron in an excited state. This electron can be received in a charge exchange reaction from neutral particles e.g. injected by the NBI. The excited ion will loose its energy and cascade down to the ground state by emitting light at several (visible) wavelengths. The width of the Doppler broadened line is proportional to the temperature of the ions, the Doppler shift is related to the velocity of the ions (along the line of sight), and ion density can be derived from the intensity of the measured spectra. Using the ion velocity in the radial force balance equation, the radial electric field can be calculated, as was e.g. shown in Figure 2.5. There, the edge poloidal CXRS system has been used. This system observes beam three of NBI 1 (sector fifteen, cf. Figure 3.2) from the top. It is typically set up such that it has eight lines of sight, which are radially 1.25 cm apart at the intersection with the beam and have spot sizes of 5 mm. The shortest achievable exposure time of the poloidal edge CXRS system is 1.9 ms, which is (just) fast enough to resolve individual ELM cycles or to allow ELM synchronized analysis. Usually, however, the time resolution is set to 2.2 ms in order to match with the toroidal edge CXRS system. This system observes the same beam, but now horizontally from the side, and has the intersections of its eight lines of sight in nearly the same radial range as the poloidal edge system. With spot sizes of 3 mm and 1.00 cm between the lines of sight, the radial resolution of the toroidal edge CXRS system is a little better than that of the poloidal system. Its shortest exposure time, as just mentioned, is 2.2 ms [Viezzer12].

The fast ion loss detector (FILD) at AUG [García Muñoz09] is a scintillator-based detector similar in concept to $\alpha$-particle detectors which are commonly used on tokamaks. Ions that have escaped from the plasma can enter a scintillator chamber (collimated by the detector head aperture) and their impact on the scintillator plate generates a light pattern. This light pattern is then imaged on both a CCD camera and an array of photomultiplier tubes. The CCD camera provides a high energy-pitch angle resolution of the fast-ion loss pattern, albeit at a sampling rate of only 12 kHz. The array of photomultiplier tubes, on the other hand, measures at an overall bandwidth of 1 MHz. This high sampling rate allows for the identification of fast-ion losses, e.g. induced by MHD fluctuations, through the use of spectrograms.

Although not a direct measurement of a property of the confined plasma, the measurement of the thermocurrents in the divertor makes a useful diagnostic for ELM analysis. At AUG, this current ($I_{div}$) is measured as the sum of the currents through four shunts connected to the outer divertor tiles at a single toroidal location in sector fourteen (but different poloidal locations in the SOL). During the ELM, the (absolute value of the) current displays a strong rise. This is most likely due to a combination of the effects of sudden particle ejection from the confined plasma, of a reaction to the loss of bootstrap current, and of a change in the position of the magnetic axis. As $I_{div}$ is acquired with a temporal resolution of 100 kHz, this allows for providing time markers such as the onset time, duration, and ELM frequency.

## 3.4. ELM mitigation techniques

The aim of the AUG programme is to contribute to ITER's design and physics basis. Therefore, the tokamak is equipped with several tools to improve plasma performance and mitigate the damaging effect of ELM energy losses. Such tools are e.g.: magnetic perturbations, the injection of cryogenic pellets, impurity seeding, vertical kicks, and the application of small ELM (see also Chapter 6) or stationary ELM-free regimes. In the first paragraph below, the in-vessel saddle coils are described that have been used for the experiments from Chapter 7. For the sake of completeness, the second available tool is shortly presented in the second paragraph.

### *3.4.1. Magnetic perturbations*

As has been observed on other tokamaks, the presence of non-axisymmetric error fields can decrease the ELM size [Hender92], [Evans04]. One explanation is that the suppression is caused by ergodisation of the magnetic field in the ETB region. This could lead to increased radial heat transport and a reduction of the pressure gradient to values below the stability limits at the ELM onset. However, this interpretation is still under debate [Burrell05]. Therefore, to enhance the understanding of the physical principles, in-vessel saddle coils that can create such non-axisymmetric error fields have also been installed at AUG [Suttrop09].

The system consists of two sets of eight coils placed inside the vacuum vessel close to the plasma on the LFS, as can be seen in Figure 3.6(a). For the 2011 experimental campaign, four upper and four lower coils have been put in first; the remaining two sets of four coils were installed for the 2012 campaign.

The power supply for the coils allows for DC operation, but the coils are prepared for AC operation up to $f_{max} = 500$ Hz. With a single power supply unit, the coils can be operated in series and produce an error field with toroidal mode numbers $n = 1$, 2, or 4. When each coil is individually powered, a more flexible configuration can be obtained. In the $n = 2$ case (i.e. for the 2011 configuration), coils that are located toroidally next to one another carry currents with opposite polarity. Furthermore, the coils in the $B_u$ and $B_l$ rings can also have a 180° phase shift with respect to each other, which gives a

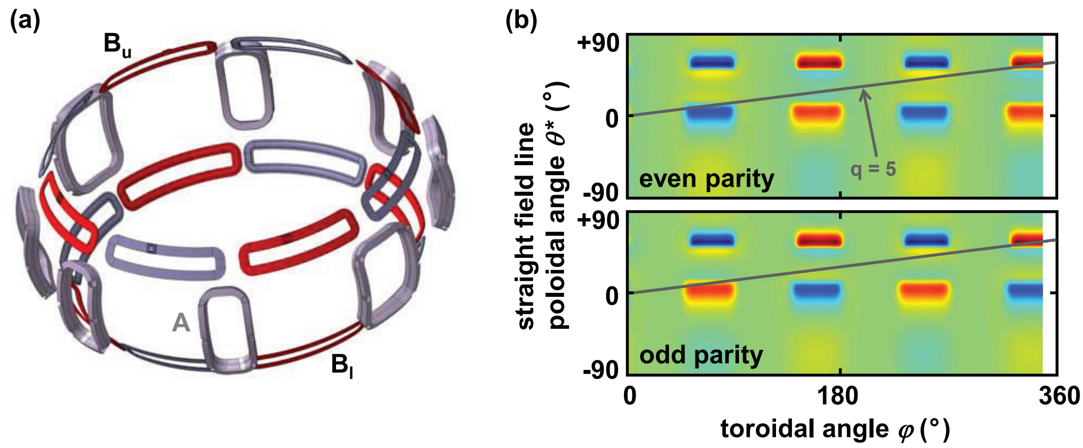


**Figure 3.6** *In (a), the full set of magnetic perturbation coils ($B_u$ and $B_l$) installed at AUG is shown. The red coils were installed first; the other B-coils followed one experimental campaign later. The normal perturbation field of the individual coils, as perceived by a field line on the $q = 5$ surface, is shown in (b) for even and odd parity.*

total of two different parity configurations. The difference between even and odd parity is shown in Figure 3.6(b), where it is shown how a field line on the $q = 5$ surface experiences the different perturbations of the individual coils. A positive coil current corresponds to a perturbation field that is directed radially outwards.

For a typical AUG H-mode discharge, assuming a monotonous $q$-profile, it is possible to calculate $m$, $n$ mode spectra of the normal vacuum field produced by the coils; this is the 2D Fourier transform of the perturbation amplitude as e.g. shown in Figure 3.6(b). From such spectra, which are symmetric around $m = 0$, resonances in the plasma are found for $n < 0$ and $|q| > 1$ ($n > 0$ represents the case of opposite helicity). Resonances occur when field lines, in the straight field line angle coordinate system, perceive the same sign of the perturbation. In other words, the resonant components of the applied perturbation field are those for which the $q$-value of the flux surface is equal to the $m/n$-value of the field's Fourier components. In the example of Figure 3.6(b), the odd parity configuration is therefore also referred to as 'resonant'. Due to the small magnetic shear at the outboard mid-plane, the resonant condition is valid for a wide range of flux surfaces.

### *3.4.2. Pellet injection*

A second technique that has been successfully applied for the improvement of plasma performance with respect to ELMs, is the injection of small deuterium pellets from the HFS [Lang12]. With this technique, the pellets are used to trigger the event of an ELM: by increasing the frequency of the injected pellets, the ELM frequency increases and, simultaneously, the energy expelled with each ELM decreases [Szepesi09].

As can be seen in Figure 3.7, the pellet injection system is based on the combination of a centrifuge accelerator and a looping transfer system. In the centrifuge, the pellets are accelerated and ejected away from the tokamak. In a roughly elliptical track, they are subsequently guided back and injected. The elliptical track consists of three parts: first, the scattered pellets are collected in a funnel. Then, a guiding tube (with a time of flight measurement at the end) transfers the pellets to the HFS of the torus. A third segment connects to the guiding tube and delivers the pellets to the plasma at an

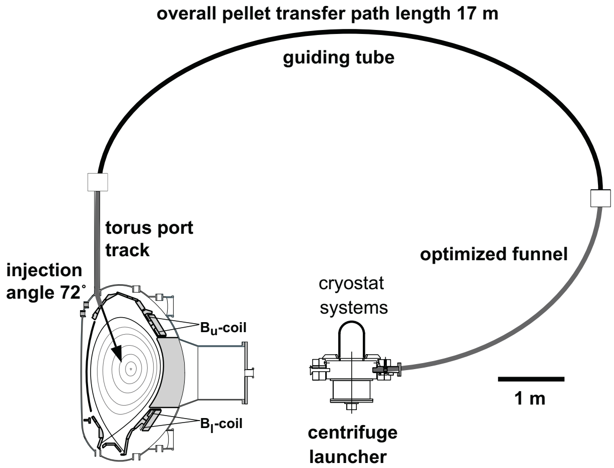


**Figure 3.7** *Overview of the HFS pellet launching system at AUG: the pellets are accelerated in the centrifuge and ejected away from the tokamak. Via an optimized funnel and a guiding tube, they are transported to the HFS of the torus where they are injected in the plasma.*

injection angle of 72°. Along the guiding section, friction between the pellets and the track surface is greatly reduced due to the Leidenfrost effect.

The injection system can deliver pellets with a nominal particle content of about $3 \times 10^{20}$ D, in a velocity range of 240-560 m s$^{-1}$, and with repetition rates of up to 47 Hz. In order to prevent pellet destruction, both speed and size are fixed within a given pellet train launched into the plasma. The repetition rate, however, can be changed to a fixed fraction of the centrifuge revolution frequency. The pellet observation system includes two ultra-fast CMOS cameras (with 1 megapixel images recorded at several hundred frames s$^{-1}$) that are capable of individual pellet tracking.

# Chapter 4

# ECE and ECE-imaging

In this chapter, the ECE-imaging diagnostic and its implementation on AUG are described. First, in section 4.1, a general introduction is given to the physical principles of electron cyclotron emission (ECE) measurements. Then, the ECE-imaging diagnostic is outlined in detail in the second section. In the last section of this chapter, the difficulties of interpreting ECE measurements at the plasma edge are described.

## 4.1. ECE radiometry

Coinciding with the era where tokamaks began to reach fusion relevant temperatures (i.e. in the keV range, cf. Figure 1.1(b)), the possibilities of ECE measurements in a spatially varying magnetic field were pointed out [Engelmann73], [Costley09]. From these measurements, information can in fact be obtained on the spatial profiles of the electron temperature (often with high temporal resolution) and derivatives of these profiles such as e.g. the location, type and size of MHD modes, information on the presence of suprathermal populations, or the amplitude and location of broadband temperature fluctuations. The basic principles of ECE as a measurement of the $T_e$ profiles are explained in this section.

### *4.1.1. Physical principles*

It is the combination of two principles that makes the measurement of ECE available as a diagnostic for electron temperature profiles. The first is that electrons gyrate around magnetic field lines, emitting and absorbing electromagnetic radiation at the ($n^{\mathrm{th}}$ harmonic of) the electron cyclotron frequency $\omega_{ce}$ [Bornatici83]:

$$\omega_{ce} = \frac{eB(R)}{m_e} \; . \tag{4.1}$$

Here, $B(R)$ is the magnetic field, which is primarily in toroidal direction in tokamaks and depends inversely on the major radius $R$: $B(R) = B_0R_0/R$ (with $B_0$ and $R_0$ the magnetic field and major radius at the centre of the tokamak). Furthermore, $e$ and $m_e$ are the electron charge and rest mass. The frequency $f_{ce}$ in Hz is easily calculated using $f_{ce} = \omega_{ce}/2\pi$. For the $2^{\mathrm{nd}}$ harmonic, used in most magnetic confinement devices, this yields frequencies in the order of 100-200 GHz and wavelengths of 1.5-3 mm.

The second principle is that, in the ideal case of the plasma emitting as a black body, the intensity of the emitted electromagnetic radiation can be related to its temperature.

In the Rayleigh-Jeans approximation, i.e. at low frequency where $\hbar\omega \ll T_e$, the intensity of the emission is given by Planck's radiation formula (with $T_e$ in J):

$$I_{BB}(\omega) = \frac{\omega^2 T_e}{8\pi^3 c^2} \ . \tag{4.2}$$

As a result, combining the effects described by equations (4.1) and (4.2), measurement of the radiation emission at a certain frequency directly yields a temperature measurement at the resonant position belonging to that frequency. Finally, electron temperature profiles are obtained when this method is expanded to the simultaneous intensity measurements at various frequencies.

In general, however, the absorption and emission processes are not as discrete as suggested by equation (4.1). The emission line is widened by Doppler and relativistic broadening, as will be described in more detail in paragraph 4.3.1. Furthermore, absorption and emissivity are low in optically thin plasmas, in which case the simple approximation of equation (4.2) no longer holds and the measured intensity becomes dependent on the plasma density as well. This plays an important role at the plasma edge, and its effect on the interpretation of ECE measurements in that region will be discussed in detail in section 4.3.

*4.1.2. Wave propagation*

For ECE radiation to be measured at all, the waves have to be able to propagate from the emitting location in the plasma to the detectors outside of it. Wave propagation can basically be described using Maxwell's equations along with taking the plasma response into account [Bornatici82], [Bornatici83]. In the 'cold plasma' approximation, where the electron velocity (on average) is assumed to be much smaller than $c$, wave propagation is described by the so-called Appleton-Hartree dispersion relation. This is expressed in terms of the refractive index $N = kc/\omega$, which depends on the angle $\theta$ between the direction of the wave propagation and the magnetic field:

$$\begin{aligned} N^2 &= 1 - \left(\frac{\omega_p}{\omega}\right)^2 \frac{2\left(\omega^2 - \omega_p^2\right)}{2\left(\omega^2 - \omega_p^2\right) - \omega\left(\sin^2\theta \mp \rho\right)} \ ; \\ \rho^2 &\equiv \sin^4\theta + 4\left(\frac{\omega^2 - \omega_p^2}{\omega\omega_{ce}}\right)^2 \cos^2\theta \ . \end{aligned} \tag{4.3}$$

Here, $\omega_p$ is the plasma frequency, which is a natural oscillation originating from spatial displacements of electrons and ions with respect to each other, and it is given by

$$\omega_p = \sqrt{\frac{n_e e^2}{\varepsilon_0 m_e}} \ . \tag{4.4}$$

Wave propagation is evaluated by reviewing the cut-offs ($N \to 0$) and resonances ($N \to \infty$) of waves. At a cut-off surface, radiation is reflected and no propagation is possible at frequencies below the cut-off frequency. At a resonance surface, radiation is either absorbed or converted to a non-propagating electrostatic oscillation. The $\mp$ sign

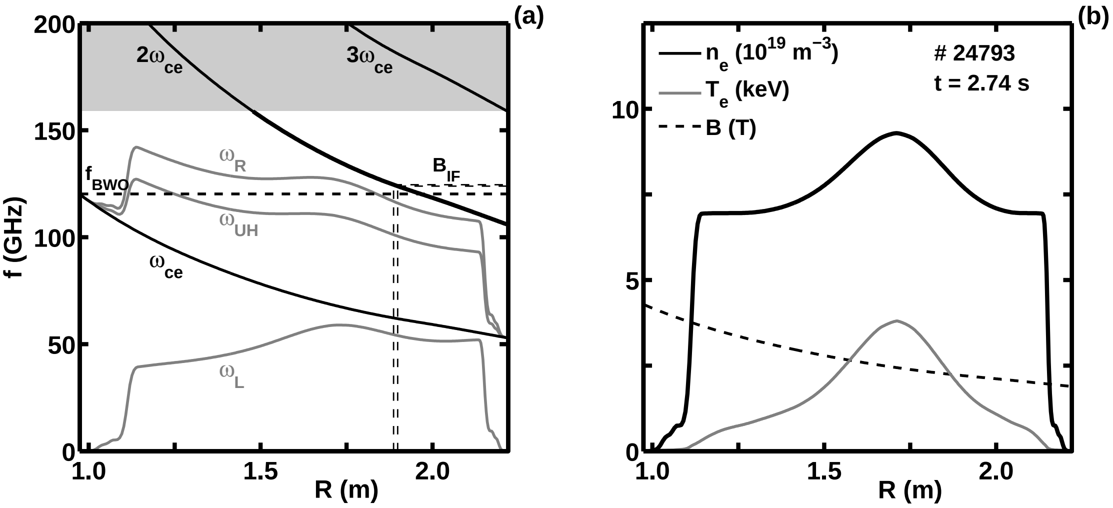


**Figure 4.1** *Overview (a) of the first, second and third harmonic of the electron cyclotron frequency for typical AUG discharge parameters (b). The left- and right-hand cut-offs are also shown, as well as the upper hybrid resonance. At high frequencies (shaded area), harmonic overlap of the third harmonic prevents observation of the second harmonic radiation. One of the LO frequencies used by the ECE-imaging system is also shown (with $f_{BWO}$ = 120 GHz). Here, it is indicated how radiation from an intermediate frequency band ($B_{IF}$) around this LO frequency originates from a small area in the plasma around R = 1.89 m. The $T_e$ profile shown in (b) is obtained as a fit to the ECE measurements shown in Figure 4.4(b).*

in equation (4.3) denotes the two different modes of wave propagation. The minus sign belongs to O-mode waves (i.e. ordinary mode), where the electric field component of the EM-wave oscillates parallel to the magnetic field $B$ and is therefore insensitive to its magnitude. Under perpendicular observation, the observation angle $\theta = \pi/2$ and consequently equation (4.3) reduces to $N^2 = 1 - (\omega_p/\omega)^2$ for O-mode radiation. This shows that the only cut-off frequency for O-mode radiation is the plasma frequency $\omega_p$. The positive sign in equation (4.3) represents X-mode waves (i.e. extraordinary mode), where the oscillations are perpendicular to the magnetic field. This time, for X-mode radiation under perpendicular observation ($\theta = \pi/2$), which is the angle most commonly used, the expression for equation (4.3) reduces to:

$$\left(N_\perp^X\right)^2 = 1 - \left(\frac{\omega_p}{\omega}\right)^2 \frac{\omega^2 - \omega_p^2}{\omega^2 - \omega_{ce}^2 - \omega_p^2} \ . \tag{4.5}$$

Evaluating equation (4.5) for cut-offs and resonances gives cut-offs at

$$\omega_{R,L} = \sqrt{\omega_p^2 + \frac{\omega_{ce}^2}{4}} \pm \frac{\omega_{ce}}{2} \ . \tag{4.6}$$

Here, $\omega_R$ is the cut-off frequency for the branch with the right-hand rotation of the wave's E-vector (plus sign), and $\omega_L$ is that for the left-hand branch (minus sign). Furthermore, a resonance appears at the upper hybrid frequency $\omega_{UH} = \sqrt{\omega_{ce}^2 + \omega_p^2}$. From this, it follows that X-mode radiation propagates perpendicular to the magnetic

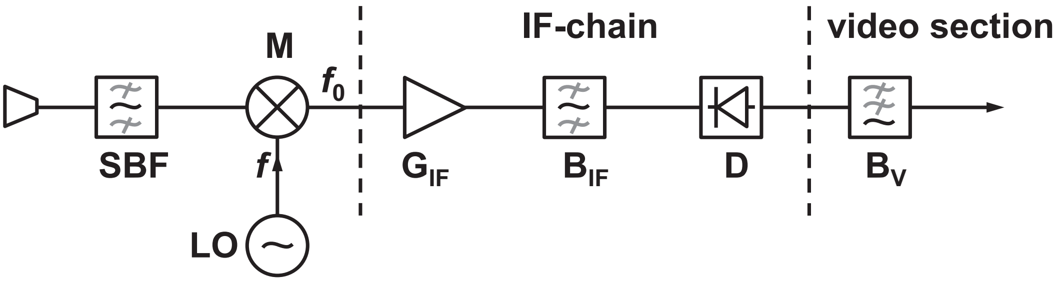


**Figure 4.2** *Block diagram showing the basic scheme of a heterodyne total power receiver: before being mixed (M) with the LO input, one sideband (above or below f) of the RF signal is filtered out by the SBF. In the IF chain, the signal with $f_0$ is then amplified ($G_{IF}$) and band-filtered with $B_{IF}$ before being detected (D) and low-pass filtered with $B_v$ (in the video section).*

field for frequencies above $\omega_L$ and $\omega_R$, but not in the range between $\omega_R$ and $\omega_{UH}$ and below $\omega_L$. Finally, wave propagation is not straight forward (literally) for refractive indices between $0 < N < 1$ when the plasma acts as a negative lens bending the lines of sight. This can occur for $\omega > \omega_p$ in O-mode, and for $\omega > \omega_R$ (in X-mode).

In order to make sure that only a certain type of polarization is measured, O- or X-mode, a selection has to be made at the antennas. This is done by either placing a polarizing grid in front of them (as is e.g. done for the 1D ECE, see paragraph 4.1.4) or by the orientation of the antennas themselves (as for ECE-imaging, cf. section 4.2). When using ECE systems to observe X-mode from the LFS, it should be comprehended there is no possibility at high frequencies to select and measure either the 2$^{nd}$ or the 3$^{rd}$ harmonic. So, in practice at AUG, measurements at radii smaller than R ≈ 1.50 m are not possible due to this harmonic overlap (i.e. the shaded area in Figure 4.1). Of course, by using HFS measurements this restriction on the 2$^{nd}$ harmonic can be overcome.

### *4.1.3. Basic heterodyne detection*

For a typical AUG discharge, as presented in Figure 4.1(a), ECE radiation of the second harmonic X-mode is emitted in the 100-160 GHz range. Signal processing at such high frequencies is not optimal, so the signal has to be converted to lower frequencies before it can be further amplified, filtered, and detected. Such a down-conversion can be done using a heterodyne technique. The basic electronic components required for this are shown in Figure 4.2.

In a heterodyne receiver, the input radio frequency (RF) signal is mixed with the coherent frequency of a local oscillator (LO) producing a beat wave at intermediate frequency (IF). For a given LO frequency $f$, there are always two input frequencies ($f_+$, and $f_-$) for which the difference to $f$ is equal to the IF $f_0$. Due to the varying magnetic field in a tokamak, $f_+$ and $f_-$ will originate from different radial positions in the plasma (as can be deduced from Figure 4.1). To make sure that the measured radiation comes from one position only, a sideband filter (SBF) is used to make the mixer sensitive to one of the two sidebands. The mixing process (M) itself is linear, which means that the output IF power is proportional to that of the input RF, and is phase-preserving as well. The resulting IF, with frequency $f_0$, is then amplified ($G_{IF}$) such that the whole dynamic range of the detector is used. Next, the bandwidth to which the detector (D) is sensitive

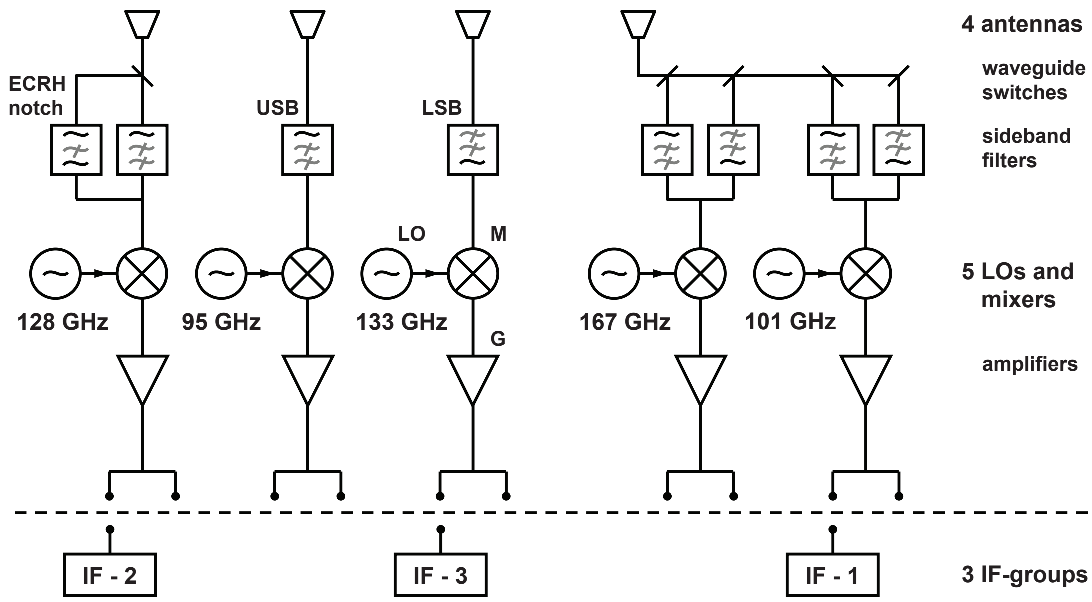


**Figure 4.3** *Schematic overview of the ECE diagnostic at AUG: the radiation is measured by four antennas. These antennas are connected to five receiver units: each consisting of one or two sideband filters, a local oscillator (LO), mixer (M), and amplifier (G). There are three IF-groups available, which can be arbitrarily connected to the receiver units.*

is defined by the IF bandwidth filter ($B_{IF}$). Finally, in the video section, the time-resolution of the diagnostic is determined by the video bandwidth ($B_v$). Here, the fluctuations with higher frequencies are averaged out so that the signal is matched to the sampling frequency of the data acquisition system (the averaging also reduces the noise level).

*4.1.4. Set-up of ECE at AUG*

With the basic (fixed LO frequency) heterodyne receiver described by Figure 4.2 it is only possible to measure radiation coming from one position in the plasma. At the beginning of this section 4.1 it was however stated that the measurement of ECE is to be employed in order to obtain information on the $T_e$ profile. The most common solution in that case is to use multiple IF-chains, which can be made by installing a power-splitter or multiplexer after the amplifier $G_{IF}$.

The employed ECE system at AUG is a multi-channel super-heterodyne radiometer, built according to the (single-sideband receiver) approach described in [Hartfuss97]. The specific instrument measures second harmonic X-mode radiation along a horizontal line of sight near the mid-plane [Salmon94], [Suttrop97]. Using three lenses and a polarizing grid (to select the requested polarization mode), radiation from a spot size of 5-7 cm in the plasma is quasi-optically focussed onto four waveguide antennas (see e.g. Figure 4.6). The radiometer is made up of five independent receiver units, each of which is connected to an antenna through a waveguide system of retractable mitre bends, as can be seen in Figure 4.3. Each receiver unit consists of a local oscillator, a down-convertor (mixer), and a low noise amplifier for the broadband intermediate frequency (IF) signal. The five available LO frequencies are $f_{LO}$ = 95, 101, 128, 133, and 167 GHz (the 101 and 167 GHz receivers share the same antenna). These are chosen such that measurement of ECE is possible in the range of

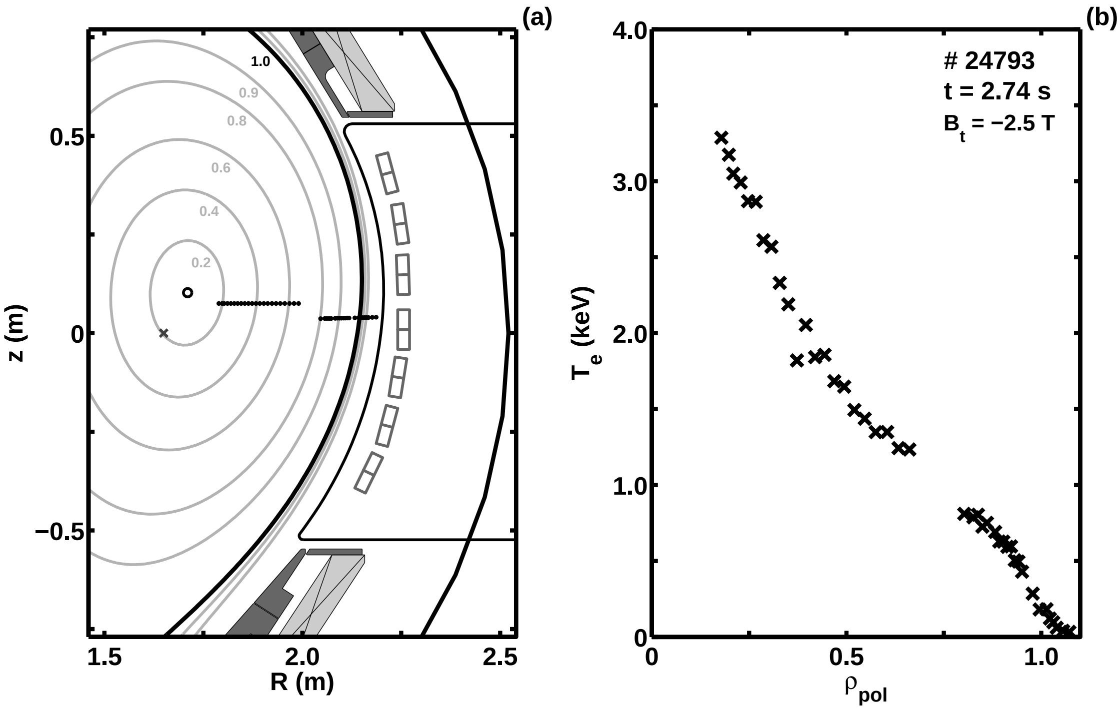


**Figure 4.4** *In the poloidal cross section (a), the positions where the different ECE channels measure are indicated by the dots near the mid-plane. The resulting $T_e$ profile is shown as a function of the normalized minor radius $\rho_{pol}$ in (b).*

89 to 187 GHz, which allows coverage of the plasma minor radius (as can be seen in Figure 4.4) at magnetic fields varying from 1.6 to 3.4 T.

There are three IF-groups available for handling the down-converted signals, which can be connected in arbitrary order to the receiver units. In each group, the IF signals are first broadband amplified and split into several chains with narrow-band channels at different central frequencies in the 2-18 GHz range. In one group (IF-1) there are 36 channels available with bandwidths of 300 MHz. This is well matched to the relativistically and Doppler-broadened ECE linewidth at 1 keV, and corresponds to a spatial resolution of 6-10 mm in the plasma. The other two groups have twelve channels each with 600 MHz bandwidths (i.e. a resolution of 12-20 mm), providing a combined total of 60 channels. By connecting two IF-groups to one receiver, the radial resolution can be increased. Finally, in each chain, the IF signals are detected by unbiased Schottky diodes, where the output voltage of each diode is proportional to the microwave power in the frequency bandwidth of the corresponding channel. This video signal is then pre-amplified at a bandwidth of 2.5 MHz before being passed to the data acquisition system. Since the sampling rate of that (CAMAC) system is 31.25 kHz, the ECE signals have accordingly been limited using an anti-aliasing Bessel filter (sixth order) with a cut-off frequency of 15 kHz. Given that the video preamplifiers have a much higher bandwidth, the ECE radiometer is currently being upgraded to routinely run at a data acquisition sampling rate of 2 MHz [Hicks10].

One more noteworthy feature of the heterodyne radiometer is that the temperature measurements are absolutely calibrated. This is done by measuring the black-body radiation of laboratory hot and cold sources (at temperatures of 773 and 77 K). These are placed outside the AUG vacuum vessel but with a beam path identical to that of

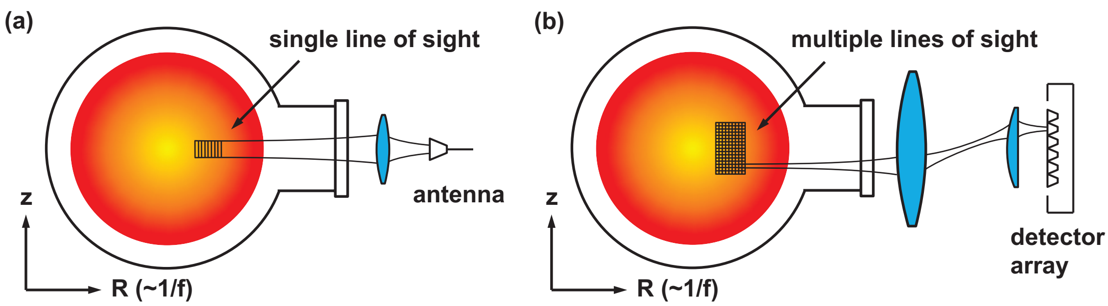


**Figure 4.5** *A conventional 1D ECE system (a) employs one antenna with which the temperature profile is measured along a single line of sight. For an ECEI diagnostic (b), the single antenna is replaced by a vertically aligned detector array. With an optical system, multiple horizontal lines of sight in the poloidal cross section of the plasma are imaged onto this array. By treating each detector as a conventional radiometer (a), a 2D image of the temperature distribution can be obtained.*

plasma measurements from inside the tokamak. The absolute calibration uncertainties obtained for all channels (connected to the receiver units in all possible combinations), are about 7 % of the measured intensities, which is mainly due to uncertainties in the transmission of the window and lens systems. This temperature calibration is performed two to three times per experimental campaign and therefore allows e.g. the ECE-imaging diagnostic to reliably cross-calibrate its measurements against the radiometer (see paragraph 4.2.3).

## 4.2. ECE-imaging

Commonly a single antenna at the low-field side, as just described in paragraphs 4.1.3 and 4.1.4, is used to detect the wideband ECE radiation which is then split into several small bands. Since these measurements are in fact along a single line of sight, as can be seen in Figure 4.5(a), systems that follow such designs are principally one dimensional (1D).

With an ECE-imaging diagnostic (ECEI), local $T_e$ measurements can be obtained in 2D [Cima97], [Deng99] and [Park04]. This 2D aspect is achieved by quasi-optically projecting the ECE radiation from a number of lines of sight onto a detector array of as much antennas. Each line of sight corresponds to a different vertical position, see Figure 4.5(b). By subsequently treating each detector as a conventional heterodyne radiometer, a 2D area in the poloidal plane can be imaged. The differences between a conventional (1D) ECE system and ECEI are schematically shown in Figure 4.5.

The ECEI system installed at AUG is the follow-up version of the system previously used at TEXTOR [Classen07]. At AUG, ECEI is located in sector nine (see Figure 3.2) in front of a 36 cm diameter quartz vacuum window [Classen10], [Tobias09]. With an optical system, sixteen horizontal lines of sight are projected onto a detector array. The radiation detected by each antenna in the array is subsequently split into eight small frequency bands. The optical system is also designed to be compatible with the ECE set-up described in paragraph 4.1.4, which shares the same window. This way, the full 1D temperature profile and a 2D area (covered in detail by 128 channels) are measured simultaneously in the same poloidal cross section of the plasma. The joint

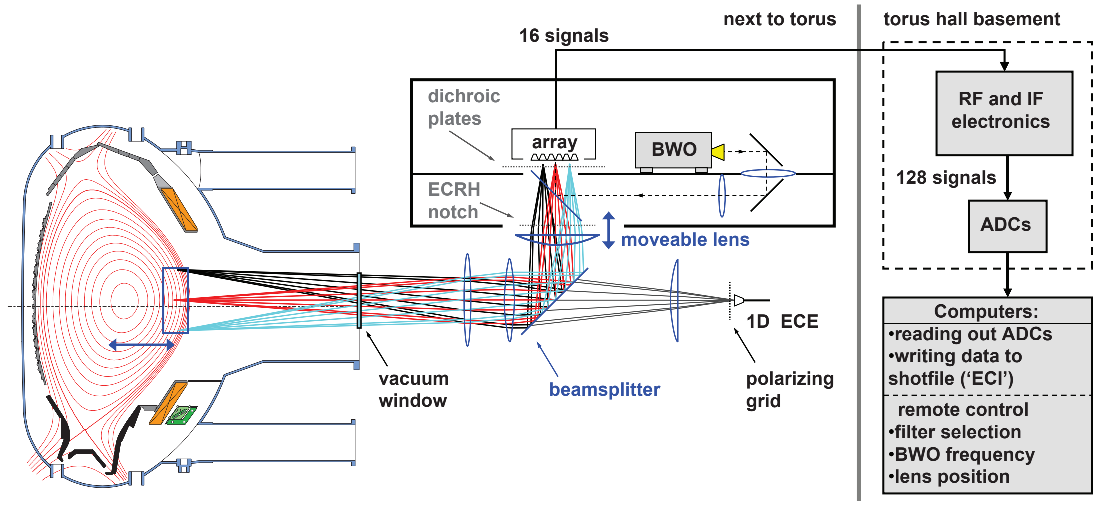


**Figure 4.6** *Overview of the optics and signal handling system of ECEI. The two lenses next to the vacuum window are on the same optical axis for both ECEI and the 1D system. With a beam splitter, the optical path of ECEI is reflected upwards to the detector array. A moveable lens is used to shift the focal plane in the plasma. Via a second beam splitter, radiation at a fixed BWO-frequency is mixed with the plasma radiation (first down-conversion). The dichroic plates are high pass filters used for sideband rejection. The signals from the sixteen antennas in the detector array are then down-converted a second time using eight LOs in the IF electronics. The position of the moveable lens, the selection of the dichroic plates, and the frequency setting of the BWO are all remotely controlled.*

measurement also facilitates a straightforward cross-calibration of ECEI against the absolutely calibrated ECE system. In Figure 4.6, an overview of the ECEI diagnostic is illustrated, showing how it is combined with the 1D system as well.

### *4.2.1. Optical system*

The full optical system of ECEI consists of two branches: in the first branch, the object plane at the antenna array is projected onto the focal plane in the plasma with the front side optics. In the second branch, a beam from the backward wave oscillator (BWO) is imaged onto the array with the LO side optics. The tuneable BWO radiation serves as a LO frequency that is mixed with the plasma radiation (cf. Figure 4.2) and thus realizes a first down-conversion step.

The front side optical system utilizes three lenses made of high density polyethylene. As can be seen in Figure 4.6, the two lenses closest to the vacuum window are shared such that the optical axis is the same for both ECEI and 1D ECE. Next, a beam splitter is used to reflect the optical path of ECEI upwards towards the detector array. The beam splitter is a thin dielectric foil with approximately 50 % reflection (and also transmission) over the whole used frequency range. The third lens of the front side optics is a moveable lens with which the position of the focal plane can be shifted to match the location of the measurement (as determined by the LO frequency of the BWO). The confocal length at this location is larger than the radial coverage of the eight channels, so all channels are in focus. In the detector array, sixteen dual dipole antennas are employed with a staggered pattern of sixteen miniature elliptical substrate lenses in front of them, which provides Gaussian beam waists of approximately 7 mm.

The optical system is designed to make optimal use of the window aperture, which is the limiting factor for the resolution in vertical direction. This is done by assuring that the Fourier plane (where all sixteen beam paths exactly overlap) is close to the position of the aperture. The smallest Gaussian beam waist ($1/e^2$) achievable is then calculated from $w_0 = 2d\lambda/\pi D$. Here, $\lambda$ is the wavelength at the location of the beam waist. With the distance from the window to the focal plane $d = 1.80$ m (close to the plasma centre), and the aperture size $D = 0.36$ m, it follows that the vertical spot size is about 15 mm. The Rayleigh length of 0.20 m assures that all eight channels are in focus.

In the second optical branch, microwave radiation from a backward wave oscillator (BWO) is imaged onto the detector array as well for the first down-conversion. The projection is done using two lenses (and two mirrors) that create an elongated Gaussian beam which covers the area of the detector array. With a second beam splitter, the BWO radiation is then merged with the first optical branch. The BWO produces 50 mW radiation at a tuneable frequency in the 90-140 GHz range (with a frequency stability of 0.02 %). In order to shield the device from stray magnetic fields, it is enclosed in an iron casing. The sideband rejection that comes before the first down-conversion (as described in 4.1.3) is done using a dichroic plate placed in the combined beam paths of the two optical systems (see Figure 4.6). Such a plate acts as a high-pass filter, allowing only the upper sideband and the BWO frequency to pass and mix onto the antenna. There are five plates available with cut-off frequencies of 99.1, 105.0, 111.7, 115.6, and 120.2 GHz, which also means that only five BWO frequencies (matched to these plates) can be used.

An additional filter included in the ECEI optical system is the ECRH notch filter, which enables measurement during ECRH operation. It consists of three quasi-optical notch filters that have a combined rejection of 60 dB at 140 GHz and so protect the antenna array against stray ECRH power. For the other ECRH frequencies, e.g. at 105 GHz, such notch filters are not available. However, it is of course possible to use one of the dichroic plates (with a cut-off above the applied ECRH frequency) instead. In dubious cases, the antenna array can always be shielded by placing a shutter in front.

In order to facilitate the operation of the diagnostic and prevent unnecessary access to the torus hall in between discharges, ECEI has been designed to be fully remote controlled. The position of the focussing lens and the selection of the dichroic plate (from a slide with five filters and a shutter) are both controlled by a stepper motor. The frequency and power settings of the BWO are computer controlled. Finally, the whole system can also be turned on or off remotely.

### *4.2.2. Down-conversion and detection*

Different from the 1D ECE system, which uses one down-conversion according to the basic heterodyne principle (see paragraphs 4.1.3 and 4.1.4), the ECEI signals are down-converted twice. The double down-conversion is schematically shown in Figure 4.7(a). As described above, the first down-conversion is the mixing of plasma radiation with the BWO frequency at the antenna array. With the dichroic plates acting as high-pass filters, this is a single (upper) sideband downconversion. The sixteen down-converted signals are subsequently passed on via microwave cables to as much electronic modules (in the basement of the torus hall, see Figure 4.6).

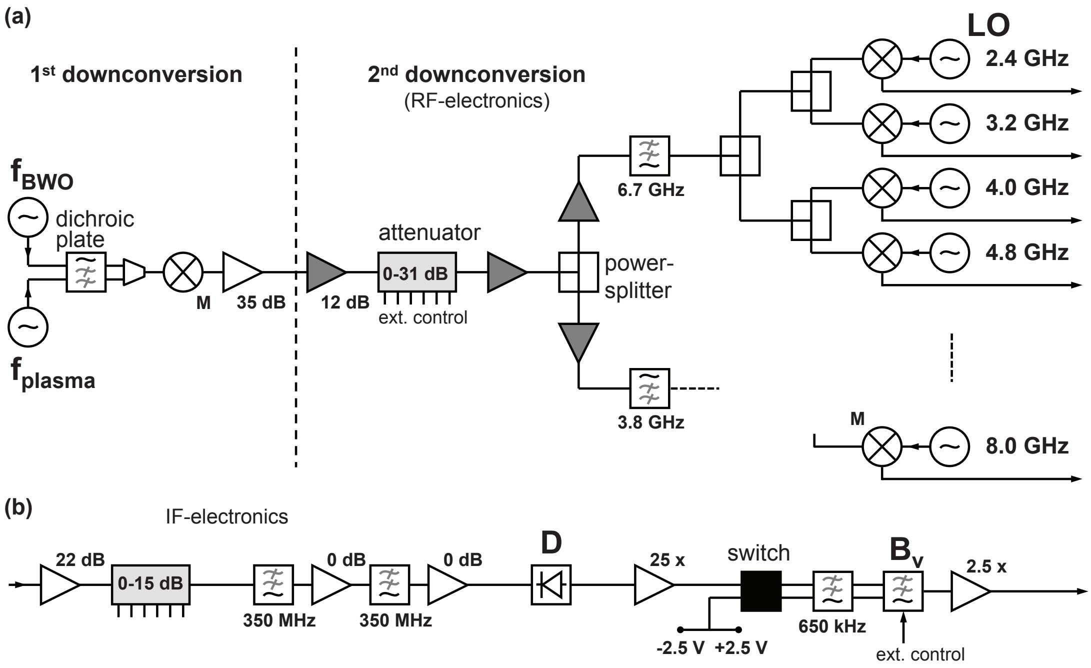


**Figure 4.7** *Block diagrams of the RF- and IF-electronics of ECEI. In (a), the double down-conversion is shown schematically: the radiation from the plasma is first mixed with the BWO-frequency. On the RF-board, this signal is then split into eight channels, each of which is down-converted a second time using LOs in the 2.4-8.0 GHz range. On the IF-board, each of the eight down-converted signals is subsequently amplified, low-pass filtered, detected (D), and then video amplified and low-pass filtered ($B_v$) according to the scheme shown in (b). The video bandwidth $B_v$ is set externally to 12.5, 25, 50, 100, 200, or 400 kHz; typically, this is half the sampling frequency.*

Each module consists of two printed circuit boards that are enclosed in a shielded box; these are the so-called RF- and IF-boards. The second down-conversion takes place on the RF-board, according to the scheme shown in Figure 4.7(a). With a five-bit digital attenuator, the pre-amplified signal level from each antenna is first adjusted, if necessary, to account for large variations in plasma temperature or receiver sensitivity (which applies equally to all eight channels per module). Then, the signal is split into eight portions and each signal is mixed with a (voltage controlled) local oscillator at a frequencies of $f_{LO} = 2.4\text{-}8.0$ GHz (with increments of 800 MHz). This time, the heterodyne mixing is a double sideband down-conversion that collects power on both sides of the LO frequency.

Via an internal connection, the output signals of the RF-board output are passed on to the IF-board in the same module. This consists of eight circuits that rectify the signals from the RF board to form eight video signals whose amplitudes are proportional to the ECE signal level strength. In each circuit, as can be seen in Figure 4.7(b), the signals are first amplified (they can then be attenuated independently for individual channels to adjust for fixed cable losses or variations in the frequency-gain response). Subsequently, they are bandpass filtered between 5-350 MHz. Due to the double sideband down-conversion around $f_{LO}$, this bandpass filtering translates to an effective bandwidth $B_{IF}$ of 700 MHz. After detection (D), the signals are video-amplified and low-pass video filtered ($B_v$) at a bandwidth that is typically half the sampling frequency. The video filter is controlled by a tenth-order switched capacitor filter with selectable cut-off frequencies of 12.5, 25, 50, 100, 200, or 400 kHz. Finally, each signal is recorded by twelve bit digitizers, capable of storing two million samples per channel at a maximum sampling rate of $2\times10^6$ samples $s^{-1}$.

*4.2.3. Signal-to-noise and cross-calibration*

The ECE radiation emitted from the plasma in thermal equilibrium is made up of many incoherent waves. The beating of these waves causes fluctuations of the signal level detected by the radiometer, which is known as wave noise or, more commonly, thermal noise [Cima97]. It is an intrinsic property of ECE radiation and is dominant over other noise sources such as IF amplifier noise or Johnson noise in the mixer, which are generally negligible [Blaney75]. The relative noise level caused by these inherent intensity fluctuations is determined by the ratio of the video bandwidth $B_v$ and the IF bandwidth $B_{IF}$ [Hartfuss97]:

$$\frac{\Delta T_{e,rms}}{T_e} = \sqrt{\frac{2B_v}{B_{IF}}} \ . \tag{4.7}$$

As described in the previous paragraph, the radial resolution is in first approximation determined by $B_{IF}$ and the time resolution follows from the setting of $B_v$. Equation (4.7) shows that there is an inverse relation between the spatiotemporal resolution and the relative noise level: the noise level increases, both when $B_{IF}$ is decreased (for better radial resolution) or when $B_v$ is increased (for better time resolution). The $B_v$ setting, used for all ECEI measurements described in this thesis, is $B_v$ 100 kHz. As described in the previous paragraph, the IF bandwidth of ECEI is $B_{IF}$ = 700 MHz; so, the relative noise level predicted by equation (4.7) is 1.7 %.

Even though the ECEI system is not absolutely calibrated, it is still possible to obtain absolute values for $T_e$. This is done by cross-calibrating (in $\rho$-space) against the 1D-ECE diagnostic which shares the same viewing window. As mentioned before in paragraph 4.1.4, this system is absolutely calibrated with an error margin of 7%.

When ECEI is set up to measure at the edge (as for most measurements in this thesis), some of the channels have their resonances located outside the separatrix. For those channels it is difficult to perform a direct cross-calibration against the 1D-ECE. In these cases, a slightly different method has been used. For discharges with ECEI in 'edge' setting (i.e. $f_{BWO}$ = 105 GHz) but with a magnetic field lower than the standard −2.5 T, all channels have their resonances well inside the separatrix. Averaged over a number of such discharges, calibration factors for all eight channels per LOS are determined and weighted with respect to each other. Now, when measuring at the plasma edge, only those channels located inside the separatrix are cross-calibrated on the $T_e$ profile whilst the others follow from the previously obtained weighted calibration factors.

## 4.3. Radial resolution at the plasma edge

As was already indicated in Figure 4.1(a), radiation detected in a certain bandwidth $B_{IF}$ originates from a small radial range in the plasma. A first order approximation of the radial resolution of any heterodyne ECE radiometer is therefore given by

$$\Delta f_{B_{\mathrm{IF}}} = n\frac{e\,B_0R_0}{m_\mathrm{e}}\left(\frac{1}{R+\Delta R} - \frac{1}{R}\right)\frac{1}{2\pi} \approx -n\frac{e\,B_0R_0\,\Delta R}{m_\mathrm{e}R^2}\frac{1}{2\pi} \ . \tag{4.8}$$

Evaluation of equation (4.8) results in a radial resolution of about 12 mm for ECEI, which has IF bandwidths of $\Delta\omega$ = 700 MHz for all channels (see paragraph 4.2.2).

*4.3.1. Emission profile broadening*

Contrary to what is suggested by equation (4.1), the emission and absorption of electrons gyrating around their field lines is not discrete. Due to relativistic and Doppler broadening, gyrating electrons emit and absorb radiation at a frequency more accurately described by [Bornatici83]

$$\begin{aligned} \omega &= \frac{n\,\omega_{\mathrm{ce}}}{\gamma} + k_{\|}v_{\|} \ ; \\ \gamma &= \frac{1}{\sqrt{1-\left(v_{\perp}/c\right)^2-\left(v_{\|}/c\right)^2}} \ . \end{aligned} \tag{4.9}$$

Here, $v$ is the electron's velocity (with components perpendicular and parallel to the magnetic field line), $\gamma$ is the relativistic factor, and $k_{\|}$ the parallel wave vector. These are the main two broadening mechanisms that cause the emission (and absorption) to appear as lines of finite width, which can be expressed as functions of $\omega$ at fixed $R$ or vice versa. There are additional broadening mechanisms such as natural broadening (due to the energy loss by the electron as it radiates) or collision broadening, but these effects are usually negligible for cyclotron radiation [Bekefi66].

In Figure 4.8(a), the shapes of the emission lines for both Doppler and relativistic broadening are shown. Here (following [Hutchinson05]), the distribution of the emissivity $j$ within each emission line is expressed as a shape function $\varphi(f-f_{\mathrm{res}})$ with

$$\begin{aligned} j_{\mathrm{res}}(f) &= j_{\mathrm{res}}\ \varphi(f-f_{\mathrm{res}}) \ , \\ \int\varphi(f)\,\mathrm{d}f &= 1 \ . \end{aligned} \tag{4.10}$$

The line shape of the emission profile caused by relativistic broadening only (for perpendicular propagation of a weakly relativistic Maxwellian distribution) is given by

$$\begin{aligned} \varphi_{\mathrm{rel}}(f) = {} & \frac{f}{2\sqrt{\pi}f_{\mathrm{res}}^2}\left(4\frac{c^2}{v_{\mathrm{th}}^2}\right)^{n+3/2}\frac{n!}{(2n+1)!}\left(1-\frac{f^2}{f_{\mathrm{res}}^2}\right)^{n+1/2} \\ & \times\ \exp\left[-\frac{c^2}{v_{\mathrm{th}}^2}\left(1-\frac{f^2}{f_{\mathrm{res}}^2}\right)\right] \ . \end{aligned} \tag{4.11}$$

Here, the thermal velocity $v_{\mathrm{th}}$ is defined as

$$v_{\mathrm{th}} = \sqrt{\frac{2T_\mathrm{e}}{m_\mathrm{e}}} \qquad \left(T_\mathrm{e}\text{ in J}\right) \ . \tag{4.12}$$

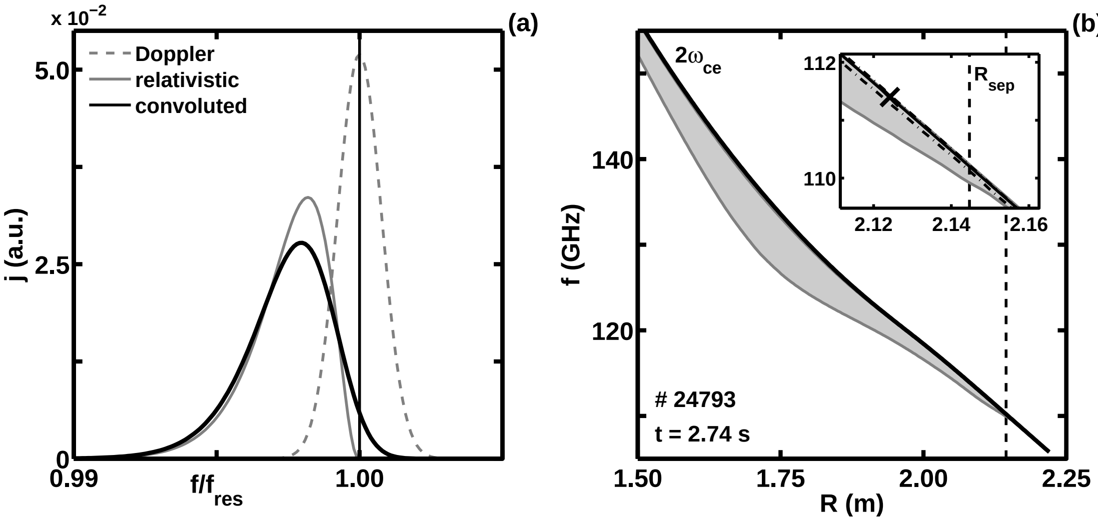


**Figure 4.8** *In (a), the line shapes for Doppler- and relativistic broadening are shown, as well as the shape of the emission profile that results from the convolution of the two. All three shapes are represented such that the areas under their curves equal unity (cf. (4.10)). The broadening effect on the 2nd harmonic cyclotron frequency (see Figure 4.1(a)) is depicted in (b). Here, the width ($1/e^2$) of the convoluted broadening profile is shown. For the profiles of (a), a resonance frequency of 111.4 GHz has been chosen, which corresponds to one of the frequencies of ECEI in 'edge' setting (i.e. with $f_{BWO}$ = 105 GHz). The spotsize is estimated to be $w_0$ = 18 mm. In the inset in (b), the measurement location for $f_{res}$ is indicated. At this location, $T_e$ is 370 eV (from Figure 4.1(b)). The part of the radiation that actually reaches the observer is also indicated (dash-dotted lines, see Figure 4.10 as well).*

Due to the relativistic mass increase, the shape of the emission line is asymmetric and completely shifted downward in frequency, as can be seen in Figure 4.8(a). In case of relativistic broadening only, as described by equation (4.11), the width of the emission profile is approximately equal to [Bornatici83]

$$\Delta f_{\mathrm{rel}} \approx f_{\mathrm{res}} \left( \frac{v_{\mathrm{th}}}{c} \right)^2 . \tag{4.13}$$

Doppler broadening is caused by the motion of the gyrating electrons along the magnetic field lines. So, generally, this plays an important role when the angle $\theta$ between the direction of the wave propagation and the magnetic field has a component in the parallel direction. Under perpendicular observation, however, Doppler broadening is also observed: due to the broadening of rays from the antennas, radiometers are in fact sensitive to a small fraction of the parallel radiation. Doppler broadening can therefore be regarded, alternatively, as the natural line width for ECE radiation caused by the finite time of flight of the electrons through the observation volume. When only Doppler broadening would be dominant, an expression for the line shape of the emission profile under perpendicular observation is given by

$$\varphi_{\mathrm{D}}(f-f_{\mathrm{res}}) \sim \exp\left[-\frac{\left(f-f_{\mathrm{res}}\right)^2}{2\left(\frac{1}{4\pi}\Delta k_{z\,1/2}\, v_{\mathrm{th}}\right)^2}\right] ;$$
$$\Delta k_{z\,1/2} = \sqrt{\ln(2)}\,\frac{2}{w_0} . \tag{4.14}$$

Here, $\Delta k_{z1/2}$ is the FWHM of the $k$-spectrum of the electric field of the Gaussian antenna beam at the beam waist $w_0$ [Sattler93] (which is a measure for the sensitivity of the antenna to the parallel direction of the magnetic field). In the optical design described in paragraph 4.2.1, $w_0$ is calculated to be 15 mm for ECEI channels. Really, due to an imperfect alignment during the acquirement of the measurements described in this thesis, $w_0$ is estimated to be close to 18 mm. From equation (4.14) it can be seen that the Doppler broadened emission profile is symmetric around $f_{\mathrm{res}}$. In that case, the width of the broadened emission profile is given by [Sattler93], [Watts04]

$$\Delta f_{\mathrm{D}} = \frac{\sqrt{2}\ln(2)}{\pi w_0} v_{\mathrm{th}} . \tag{4.15}$$

In reality, both broadening mechanisms occur simultaneously and, due to the high spatial resolution of ECEI, Doppler broadening is of the same order of magnitude as relativistic broadening and can therefore not be neglected. Consequently, the total radiation broadening follows from the convolution of the two line shapes (from equations (4.11) and (4.14)). In Figure 4.8(b), the $1/e^2$-width of the convoluted emission profile is shown for the observable range of the 2[nd] harmonic cyclotron frequency (cf. Figure 4.1(a)). The line shapes of Figure 4.8(a) are determined for the resonance frequency $f_{\mathrm{res}}$ = 111.4 GHz. This is one of the frequencies of ECEI in ‘edge’ setting, i.e. using $f_{\mathrm{BWO}}$ = 105 GHz. The measurement location of this $f_{\mathrm{res}}$ is indicated in the inset in Figure 4.8(b). For calculation of the line shapes, $T_{\mathrm{e}}$ is taken to be 370 eV (from Figure 4.1(b)). The FWHM of the convoluted radiation broadening, for this ECEI edge channel, is about 367 MHz or 6.3 mm.

### *4.3.2. Optical thickness and radial resolution*

The width of the total broadened emission profile, described above, is not what finally determines the radial resolution. In fact, the radiation emitted furthest away from the observer is reabsorbed for a large part before it arrives at the observer. Accounting for both emission and absorption along the line of sight of observation, the radiation transport of a single ray is described by the following differential equation [Bekefi66]:

$$\frac{\mathrm{d}}{\mathrm{d}s}\left[\frac{I(\omega)}{N^2}\right] = \frac{1}{N^2}\left[-\alpha(\omega)I(\omega) + j(\omega)\right] . \tag{4.16}$$

Here, $\alpha(\omega)$ is the absorption coefficient and $s$ the coordinate along the ray’s trajectory through the plasma. In thermal equilibrium the ECE intensity $I(\omega)$ is equal to $I_{\mathrm{BB}}(\omega)$, which is given in equation (4.2). When this assumption is applied to equation (4.16), it follows that absorption and emission are directly related to the black body intensity, which is known as Kirchhoff’s law:

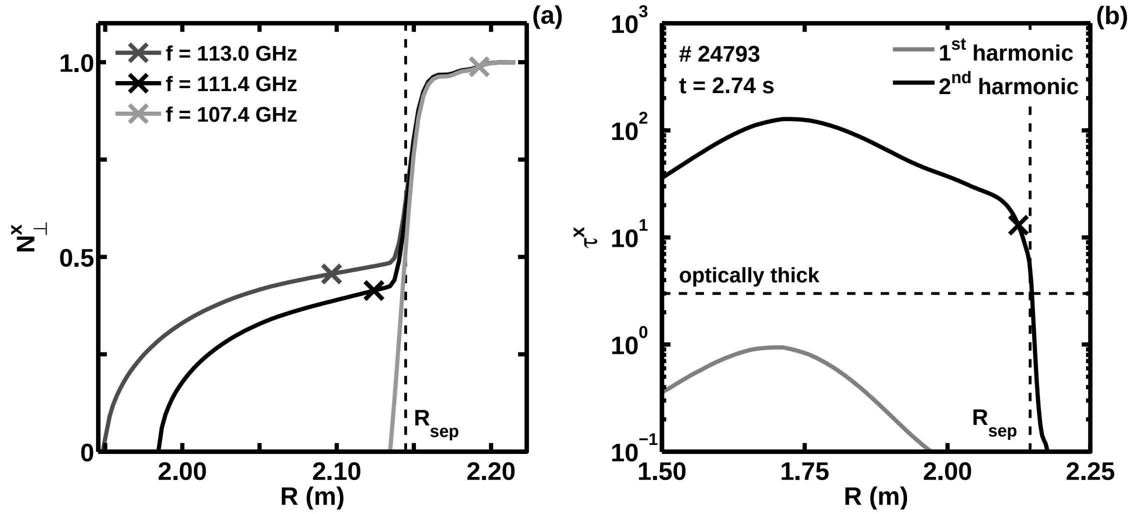


**Figure 4.9** *The refractive index that a single ray experiences is shown in (a), for which equation (4.5) has been used. This is done for three frequencies of ECEI in 'edge' setting (i.e. with $f_{BWO}$ = 105 GHz) and the location of the resonance is indicated on each curve. In (b), the optical thickness for the first and second harmonic X-mode is shown, according to the expressions of equations (4.19) and (4.20). At the location of the resonance frequency 111.4 GHz, used before in Figure 4.8, the optical thickness of the second harmonic X-mode has a value of $\tau_2^X$ = 13.*

$$\frac{j(\omega)}{\alpha(\omega)} = I_{\mathrm{BB}}(\omega) \ . \tag{4.17}$$

From equation (4.17) it can directly be seen that both emission $j(\omega)$ and absorption $\alpha(\omega)$ have the same shape, as is e.g. shown in Figure 4.8(a).

The total absorbed radiation, integrated along the ray's trajectory $s$, is expressed in terms of a parameter called the optical thickness:

$$\tau(\omega) \equiv \int_s \alpha(\omega)\mathrm{d}s \ . \tag{4.18}$$

High optical thickness, i.e. $\tau >> 1$, means that the plasma is fully absorbing and that the intensity of the emission is indeed equal to $I_{\mathrm{BB}}(\omega)$. For low optical thickness, the absorption of radiation by the plasma is reduced by a factor $e^{-\tau}$ and the emission is reduced by a factor $1-e^{-\tau}$.

For perpendicular observation ($\theta = \pi/2$), and under the assumption of a homogeneous plasma with certain $T_e$ and $n_e$, the local values of $\tau_1^X$ and $\tau_n^X$ ($n \geq 2$) are approximated by [Bornatici82]

$$\tau_1^X = \frac{5\pi}{4\sqrt{2}}\left(\frac{v_{\mathrm{th}}}{c}\right)^4\left(\frac{\omega_{\mathrm{ce}}}{\omega_{\mathrm{p}}}\right)^2\frac{\omega_{\mathrm{ce}}R}{c} \tag{4.19}$$

and

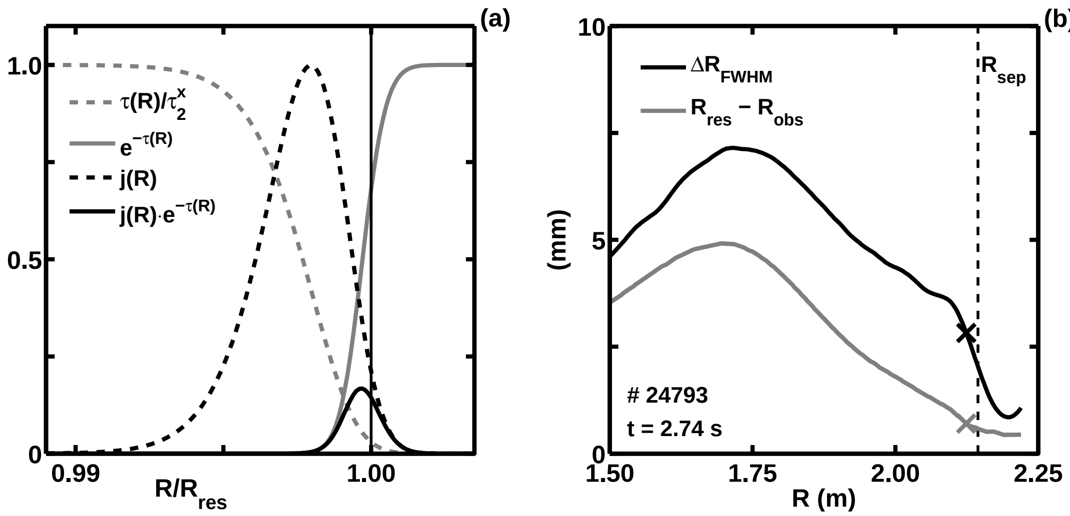


**Figure 4.10** *In (a), it is shown what part of the emission profile j(R) is observed; for j(R), the convoluted profile from Figure 4.8(a) has been used, this time normalized to its maximum. Due to the reabsorption (by a factor* $1-e^{-\tau(R)}$*) of the radiation emitted furthest away from the observer, only the radiation emitted from* $j(R)\cdot e^{-\tau(R)}$ *is finally seen. The width (FWHM) of this so-called 'last layer' and its shift relative to the cold resonance are shown in (b). Here, the location of the cold resonance for 111.4 GHz, used for (a), is indicated once more. As can be seen in (b), the FWHM of the observed emission is about 2.8 mm for a wide radial range; for the same range, the outward shift of the resonance is less then 1 mm.*

$$\tau^X_{n\,(n\geq 2)} = \frac{\pi\, n^{2(n-1)}}{2^{2n-1}(n-1)!}\left(\frac{v_{\mathrm{th}}}{c}\right)^{2(n-1)}\left(\frac{\omega_{\mathrm{p}}}{\omega_{\mathrm{ce}}}\right)^2\left(N_\perp^X\right)^{2n-3} \times\left(1+\frac{\left(\omega_{\mathrm{p}}/\omega_{\mathrm{ce}}\right)^2}{n\left(n^2-1-\left(\omega_{\mathrm{p}}/\omega_{\mathrm{ce}}\right)^2\right)}\right)^2\frac{\omega_{\mathrm{ce}}R}{c}\ . \tag{4.20}$$

As mentioned before, the emission and absorption lines are of finite width, and their shapes can be expressed as functions of $\omega$ at fixed $R$ or vice versa. In order to determine what part of the broadened emission profile actually reaches the observer, it is more practical to express $\tau(\omega)$ in terms of $R$. This means that equation (4.18) becomes

$$\tau(R) = \int_{R_{\mathrm{obs}}}^{R}\alpha(R)\mathrm{d}s\ , \tag{4.21}$$

where the integration along the ray's trajectory is from the location of the observer to emitting layer at position $R$. Since $\alpha(R)$ is related to $j(R)$ via Kirchhoff's law, equation (4.17), a normalized form of the convoluted emission shape can be used to determine $\tau(R)$ using equation (4.21). The shape of the broadened emission profile that is finally seen, is now given by $j(R)\cdot e^{-\tau(R)}$. The reconstruction of this so-called 'last layer' is shown in Figure 4.10(a), where the broadened emission profile of Figure 4.8(a) has been used. In Figure 4.10(b), the width (FWHM) and radial shift of the last layer are also shown.

The assumption of a homogeneous plasma, used in the derivation of equation (4.20), is of course a simplification of the real case. For a more accurate calculation of the optical thickness, the integration of equation (4.18) along the ray's trajectory should actually be performed using an expression for the absorption as described in [Bornatici82]. It turns out, however, that the expression of equation (4.20) can well be used as an underestimate of the optical thickness. Finally, it should be noted that for optical thickness values larger than about six, the possible influence of density fluctuations on the temperature measurement has completely vanished [Classen07].

# Chapter 5*

# 2D ECE measurements of type-I edge localized modes at ASDEX Upgrade

J.E. Boom[1], I.G.J. Classen[1], P.C. de Vries[1], T. Eich[2], E. Wolfrum[2], W. Suttrop[2], R.P. Wenninger[3], A.J.H. Donné[1,4], B.J. Tobias[5], C.W. Domier[6], N.C. Luhmann Jr[6], H.K. Park[7] and the ASDEX Upgrade Team

[1] FOM Institute for Plasma Physics Rijnhuizen, 3430 BE Nieuwegein, The Netherlands
[2] Max-Planck-Institut für Plasmaphysik, 85748 Garching bei München, Germany
[3] Universitätssternwarte, Ludwig-Maximilians-Universität, 81679 München, Germany
[4] Faculteit Technische Natuurkunde, Technische Universiteit Eindhoven, 5600 MB Eindhoven, The Netherlands
[5] Princeton Plasma Physics Laboratory, Princeton, NJ 08540, USA
[6] Department of Electrical and Computure Engineering, University of California at Davis, Davis, CA 95616, USA
[7] POSTECH, Pohang, Gyeongbuk, 790-784, Korea

**Abstract**
The installation of a 2D electron cyclotron emission imaging (ECEI) diagnostic on ASDEX Upgrade has provided a new means to observe the nature of edge localized modes (ELMs). For a series of ELMs in a typical type-I ELMy H-mode (with $q_{95} = 4.7$), the 2D dynamics have been characterized. Firstly, a clear distinction between so-called ‘fast’ and ‘slow’ ELMs was found to be the occurrence of an off-mid-plane fluctuation in case of the latter. This mode has its amplitude strongest off-mid-plane and its poloidal and toroidal mode numbers are $m \sim 110$ and $n \sim 30$. Secondly, prior to the onset of the ELM’s temperature collapse, a mode is observed that covers the whole ECEI-observation window. Here, the estimated poloidal and toroidal mode numbers are $m \sim 75$ and $n \sim 20$. These have been seen to increase towards the ELM crash, simultaneously with a velocity increase of the mode (in poloidal direction). Finally, filaments have been identified during the temperature collapse phase and their motion could be followed in the vertical direction. In contrast to both the off-mid-plane fluctuation and the ELM-onset mode, which only have been seen rotating in the electron diamagnetic drift direction, the first few filaments have sometimes been observed to move in the opposite direction as well.

* The work presented in this chapter is published in this form in *Nuclear Fusion* under the title ‘2D ECE measurements of type-I edge localized modes at ASDEX Upgrade’.
Boom J.E. et al. 2011 *Nucl. Fusion* **51** 103039

## 5.1. Introduction

The most successful scenario for fusion reactors, as currently foreseen, is tokamak operation in high confinement mode (H-mode) [Wagner82]. However, due to the steep pressure gradients at the plasma edge, in combination with high current densities, this regime is destabilized by the occurrence of instabilities known as edge localized modes (ELMs) [Zohm96], [Suttrop00]. In case of the most commonly observed ELMs, so-called type-I, the heat load of particles expelled during these periodic relaxations of the edge transport barrier (ETB) could prove difficult to handle in future fusion devices such as ITER [Loarte07]. For the development of ELM-control tools (e.g. [Suttrop07]) and for the extrapolation of models towards ITER, it is therefore crucial to understand the dynamics of the ELM cycle and its underlying physics.

In general, the type-I ELM cycle can be divided into three main phases [Maggi10], [Oyama04]: the first phase, at the ELM onset, is understood to be governed by the magnetohydrodynamic (MHD) stability limits within the peeling-ballooning model. This model describes, for type-I ELMs, that an increasing edge pressure gradient is limited by the onset of ballooning modes. When the edge current density continues to increase, due to the rise in bootstrap and Ohmic currents, the plasma can be driven across the peeling stability boundary as well. This results in a loss of edge confinement and causes the edge pressure gradient to drop, which then further destabilizes the peeling mode [Snyder02], [Connor98b]. Testing of the peeling-ballooning model can be done using numerical simulations, such as [Huysmans07], for the prediction of stability limits and growth rates of the modes. These can then be compared with precursor modes that are seen just before the ELM collapse, e.g. at ASDEX Upgrade (AUG) [Bolzonella04] and also on other tokamaks [Terry07], [Oyama11]. The second phase in the ELM cycle is non-linear of nature. It is characterized by the collapse of the temperature and density profiles at the edge, and the occurrence of helical, field-aligned structures on the low-field side (LFS). These so-called filaments are subsequently ejected from the edge and start to move into the scrape-off layer. This has been observed at spherical tokamaks [Kirk04], [Maingi05], as well as at conventional tokamaks such as AUG [Koch07], [Eich03], [Eich05], [Neuhauser08] or others [Oyama04], [Terry07], [Jakubowski09]. Non-linear MHD simulations are focused on modelling the development from the peeling-ballooning modes into filaments, and, e.g., their interactions with the plasma flows [Pamela10]. When the second phase has ended, usually after a few ms, the ETB starts to build up again completing the ELM cycle. Characterization of typical type-I ELM cycles at AUG has revealed that so-called ‘fast’ ELMs get triggered immediately after recovery of the ETB, whereas for ‘slow’ ELMs there is an extended phase where the ETB remains in its final shape before the crash occurs [Burckhart10]. However, the mechanism that triggers the onset of the next ELM is still unknown.

The installation of an electron cyclotron emission imaging diagnostic (ECEI) on AUG provides a new means to observe the 2D nature of ELM dynamics on a fast timescale, and can contribute to a better understanding in all phases of the ELM cycle. In this work, observations of the onset and development of type-I ELMs with this 2D diagnostic will be presented for the first time. First, the setup of the ECEI-system and the treatment of ECE measurements at the plasma edge will be described in section 5.2. After that, in section 5.3, the ECEI observations will be presented from a series of ELM crashes during a steady-state phase in a type-I ELMy H-mode on AUG. Here, the

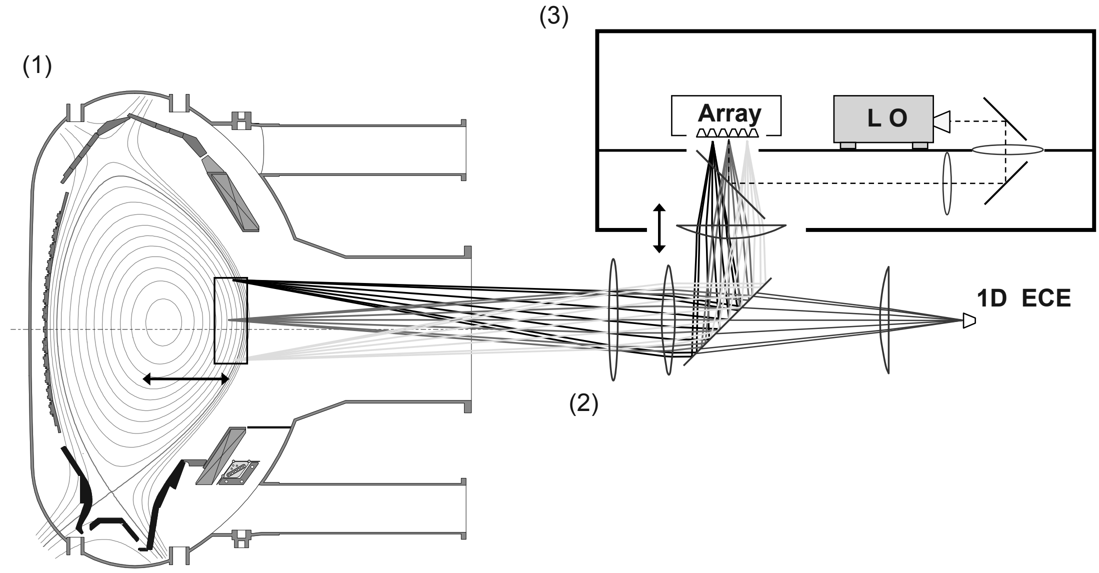


**Figure 5.1** *Schematic view of the ECEI diagnostic at AUG: a cross section of the tokamak with a standard magnetic flux surface configuration is depicted in (1). The optics of ECEI (2) consist, amongst others, of a beam splitter that separates the lines of sight of ECEI and the 1D-ECE system, and a moveable lens which can be used to shift the position of the focal plane in the plasma. In (3), plasma radiation is measured by the array of 16 detectors, after being down-converted by mixing with waves from a local oscillator (LO) that are coupled in through a second beam splitter.*

focus will be on the first and second phase of the ELM cycle, describing the details of the crash onset and the second, non-linear decay phase. A discussion on the observations and a conclusion is given in section 5.4.

## 5.2. ECE-imaging at ASDEX Upgrade

In this section, a short explanation is given on the ECEI diagnostic and on its optical arrangement for measurements at the plasma edge. In the second paragraph, it is explained how the system is cross-calibrated in order to obtain electron temperature measurements. The influence of decreasing optical thickness at the edge is discussed in the last paragraph.

*5.2.1. Description of the diagnostic and experimental setup*

The ECEI diagnostic, as it is installed at AUG consists of an array of 16 detectors, each of which acts as a standard (1D) ECE radiometer [Classen10], [Tobias09], [Park04]. That is, every detector measures the intensity of the emitted electron cyclotron radiation from different vertical positions, here in second harmonic X-mode (100-140 GHz). Provided the plasma is optically thick, the measured power is proportional to the intensity emitted by a black body at temperature $T_e$. The quasi-optical setup allows for the 16 lines of sight to be focused at the LFS edge with a waist of 1.5 cm at the focal plane (i.e. a FWHM of 1.75 cm). The radial coverage is determined by 8 local oscillator frequencies per line of sight, each frequency band corresponds to about 1.6 cm in the plasma. Hence, this matrix of 16×8 channels covers an observation area of about 40×13 cm$^2$ with spot sizes of 1.5×1.6 cm$^2$.

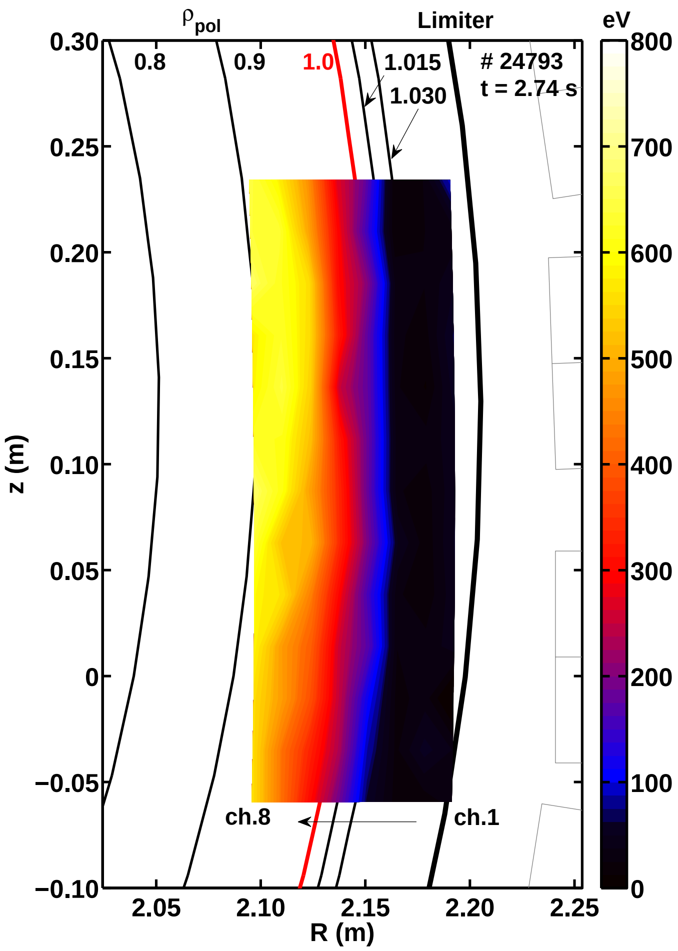


**Figure 5.2** *ECEI-observation window for measurements at the LFS: the $T_e$ profile shown is obtained using the cross-calibration method described in paragraph 5.2.2. It is measured during the quiet phase in between two ELMs (discharge # 24793 at 2.74 s). Also shown are flux surfaces at various $\rho_{pol}$, as follows from the CLISTE equilibrium reconstruction calculated at the time point nearest to the measurement. Here, the separatrix is labelled as 1.0; at the pedestal top, $\rho_{pol}$ = 0.94, $T_e$ = 600 eV. As indicated at the bottom, the eight channels are labelled outwards to inwards (the lines of sight are counted from top to bottom). It can also be seen that the mid-plane lies at about z = 0.10 m.*

With the system set up to measure at the LFS edge, Figure 5.1 and Figure 5.2 show this area in a poloidal cross section of AUG together with the 1D-ECE system, which shares the same observation window. The sampling rate of ECEI is typically set to 200 kHz; the whole length of the discharge is covered at this rate.

### *5.2.2. Cross-calibration method*

ECEI is not independently calibrated but cross-calibrated against the 1D-ECE diagnostic, which shares the same viewing window and is absolutely calibrated using the standard hot-cold method. When the ECEI system is set up to measure at the edge, as shown in Figure 5.2, some of the outer channels may have their ECE resonances at radii where the plasma temperatures are very low (<100 eV), usually around the foot of the temperature pedestal. In these cases, ECEI is cross-calibrated in (other) shots with lower magnetic fields, where all channels observe regions of high temperature at high optical thickness.

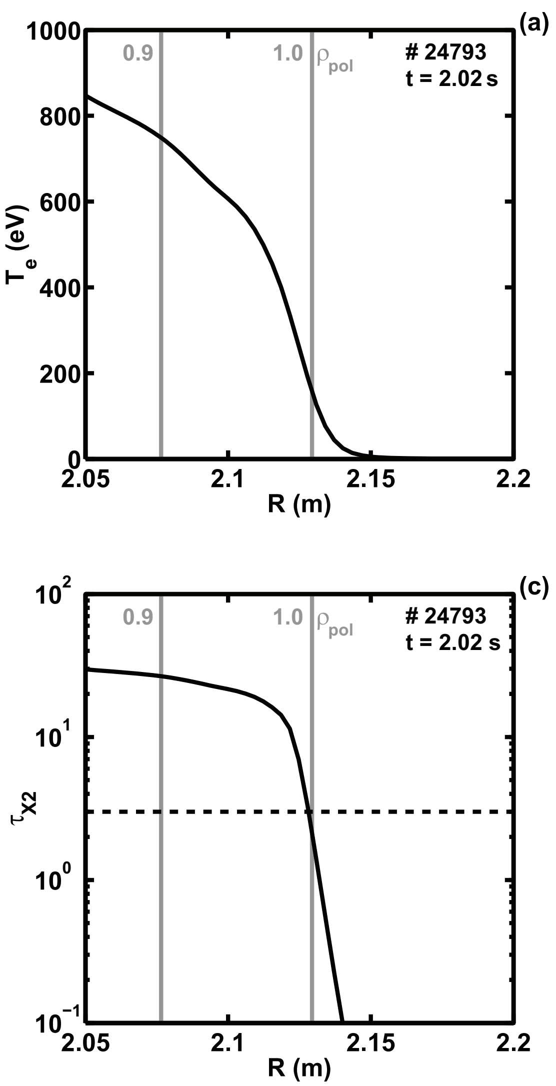


**Figure 5.3** *Using IDA for the combined measurements of the lithium beam, DCN interferometer, and ECE, $T_e$ and $n_e$ profiles are obtained for the quiet phase prior to an ELM (discharge # 24793 at 2.02 s), as shown in (a) and (b). Based on these profiles, the optical thickness $\tau$ of the second harmonic X-mode is calculated, as is shown in (c). From this zero-dimensional approximation, it can already be seen that the plasma is indeed optically thick, $\tau_{X2} > 3$, inside the separatrix ($\rho_{pol} = 1.0$).*

### *5.2.3. Optical thickness at the plasma edge*

In order to interpret the intensity of ECE radiation measurements in terms of local $T_e$, and also to ensure that the radial resolution is not broadened too much, the optical thickness $\tau$ of the plasma should be sufficiently high (i.e. $\tau > 3$). Based on the $T_e$ and $n_e$ profiles shown in Figure 5.3(a) and (b), the optical thickness of the second harmonic X-mode, $\tau_{X2}$, is calculated as shown in Figure 5.3(c) [Bornatici82]. Integrated data analysis (IDA) has been used here to get the kinetic profiles both inside and outside the separatrix; where IDA combines measurements from the lithium beam and the laser interferometer for $n_e$, and ECE for $T_e$ [Fischer08b]. The separatrix is defined where the normalized minor radius $\rho_{pol}$, given by the square root of the normalized poloidal flux, is equal to unity.

This calculation of $\tau_{X2}$ shown in Figure 5.3(c) is a zerodimensional approximation assuming a homogeneous plasma, with the given $T_e$ and $n_e$, for each radial point. The results strongly suggest that the plasma is indeed optically thick, i.e. $\tau_{X2} > 3$, inside the separatrix and that radiation transport calculations are not needed to obtain a local $T_e$ measurement. When $\tau_{X2} < 3$, the optical depth is marginal and measurements of $T_e$ could also be influenced by $n_e$. In this case, the measurements are referred to as $T_{rad}$, instead of $T_e$.

## 5.3. Characterization of the 2D electron temperature behaviour during the ELM cycle

This section describes the ECEI observations of the 2D $T_e$ dynamics for a series of 58 ELM crashes in one AUG discharge. The type-I ELMy H-mode, during which the measurements were taken, is introduced in the first paragraph. An overview of all the phases that are typically observed with ECEI during the ELM cycle is presented in paragraph 5.3.2. More detailed descriptions of the three main phases identified are given in the following three paragraphs.

### *5.3.1. Discharge description*

With the ECEI observational area positioned at the LFS plasma edge, as shown in Figure 5.2, the 2D $T_e$ evolution of the ELM cycle can be observed in detail. For this purpose, a typical type-I ELMy H-mode AUG discharge was used (# 24793), which has a phase of about 0.8 s where the main plasma parameters were kept constant. The discharge had a plasma current of $I_p = 1.0$ MA, a magnetic field of $B_t = -2.5$ T, and an edge safety factor of $q_{95} = 4.7$. The edge $T_e$ and $T_i$ were 500 and 700 eV, both measured at $R = 2.10$ m. The core line-integrated electron density was $n_e = 8\times10^{19}$ m$^{-2}$ and the line-integrated edge density (up to $\rho_{pol}$ 0.8) was $6\times10^{19}$ m$^{-2}$. The plasma was heated by 7MW from neutral beam injection (NBI), and 750 kW from electron cyclotron resonance heating (ECRH). An overview of the time-traces of this discharge is given in Figure 5.4, where also the analysed time window (t = 2.0-2.8 s) is indicated. Over the second half of this time window, from 2.4 to 2.8 s, the plasma is slightly shifted outwards by 1 cm, Figure 5.4(f), but the plasma edge remains well covered by the ECEI-observation window. The degradation in energy confinement from 3.12 s onwards, Figure 5.4(g), is caused by the occurrence of a large core magnetic island. The analysed time window is chosen such that any influence of this event on the observations at the edge is prevented.

The time-trace of the thermo-current in the outer divertor, i.e. when the heat pulse due to the ELM reaches the divertor, is used as an indicator for occurrences of ELMs as shown in Figure 5.5. The start time of an ELM crash is defined as the first time a predefined offset value in the thermo-current is transcended, and from this the ELM frequency is determined. As can be seen from Figure 5.5, the majority of the crashes come with a frequency (i.e. reciprocal time) of 67 ± 6 Hz but about 25% come with a frequency of more than 80 Hz. The two different cycles are known as so-called ‘slow’ and ‘fast’ ELMs [Burckhart10]. As will be discussed in detail in paragraphs 5.3.2 and 5.3.3, a specific off-mid-plane temperature fluctuation has been observed with ECEI that occurs for all (but one) of the ‘slow’ ELMs, which was not the case for any of the ‘fast’ ELMs.

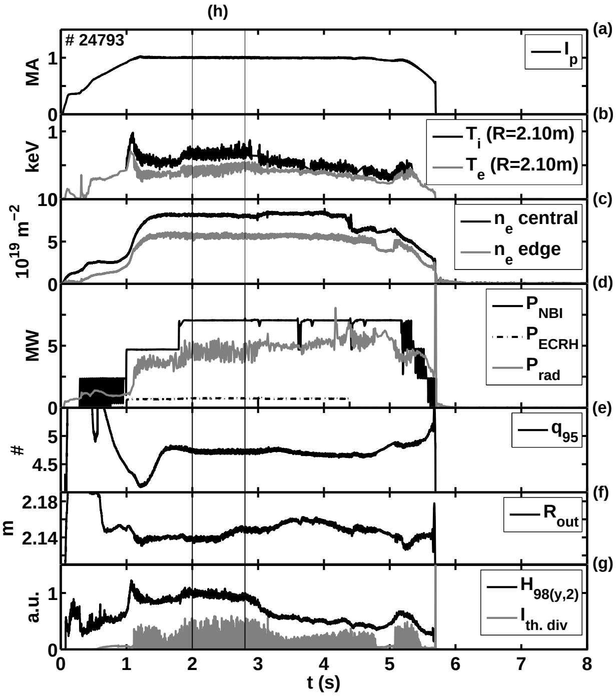


**Figure 5.4** *Overview of AUG discharge # 24793: (a) plasma current, (b) ion and electron temperatures near the edge (at major radius R = 2.10 m), (c) line-averaged electron density and density at the edge, (d) input powers of NBI and ECRH, and radiated power, (e) safety factor at the edge, (f ) position of the outer major radius of the confined plasma, (g) ratio of the thermal energy confinement time to the ITER 98(y,2) H-mode scaling value and the thermo-current in the outer divertor, (h) indication of the steady-state time window (t = 2.0-2.8 s) in which the ELMs are analysed.*

### *5.3.2. Overview of the ELM cycle*

In order to quickly obtain an impression of the spatiotemporal behaviour of phenomena that occur during an ELM cycle, the measurements from ECEI have first been averaged radially. This is done by dividing the area that is covered by the ECEI-observation window into two regions, and taking the radial average $\langle T_e \rangle_R$ of the inner four and outer four channels. Of course, the radial resolution is lost by taking this average. On the other hand, the features of interest mostly occur either inside the separatrix (inner four channels, R = 2.09-2.13 m) and prior to the crash, or outside (outer four channels, R = 2.15-2.19 m) and during the crash. This method, therefore, does provide a simultaneous impression of the largest deviations from $\langle T_e \rangle$ as a function of the vertical, or poloidal, direction and time.

Using the two sets of radially averaged temperatures, all ELMs in the t = 2.0-2.8 s time-slice of the discharge shown in Figure 5.4 have been analysed. From this, the following short description of a typical ‘slow’ ELM cycle is obtained. An example of such an ELM is shown in Figure 5.6, where features moving poloidally can clearly be seen as moving upwards in the graphs (Figure 5.6(c) and (d)). From these graphs, the velocity with which these features move can be determined from the slope. The different phases that have been identified are indicated by the numbers in brackets on top of Figure 5.6.

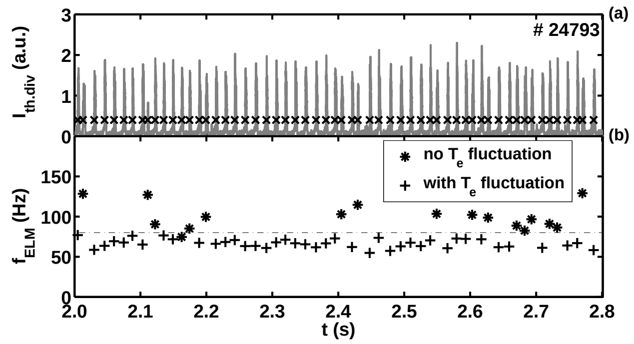


**Figure 5.5** *In (a), the time-trace of the thermo-current in the outer divertor is shown for the steady-state phase of AUG discharge # 24793 (2.0-2.8 s). The ELM frequency, as determined when the thermo-currents peak above a preset level, is shown in (b). It can be seen here that the ELMs come with two distinct frequencies: for all ELMs below 80 Hz ('slow' ELMs), with one exception, an off-mid-plane temperature fluctuation is observed, whereas this was not the case for any of the ELMs faster than 80 Hz ('fast' ELMs).*

For all observed 'slow' ELMs, the first sign of an upcoming crash is found as a temperature fluctuation which appears about 1.7 ms before the final crash (phase (1), Figure 5.6(b) and (c)), and which occurs markedly strongest off-mid-plane. Before the final ELM crash happens, a more quiescent phase sets in: during this phase the regular off-mid-plane oscillations have disappeared, but more often than not irregular temperature perturbations can be seen. It is this off-mid-plane fluctuation, and the following quiescent phase, that have not been observed for any of the 'fast' ELMs. The next phase (phase (2), Figure 5.6(b) and (c)) of the ELM cycle is the phase which leads up to the crash itself. A mode is observed over the whole height of the ECEI window, usually rotating faster than the earlier off-mid-plane fluctuation. This phase usually lasts just 100 $\mu$s and the end of this mode is defined here as the start ($t = t_0$) of each ELM crash, which occurs before the $t_{ELM}$ indicated by the thermo-currents (Figure 5.6(a)). Directly following the second mode the actual crash starts (phase (3)). It starts off with ECEI signals which behave chaotically and are difficult to interpret, followed by a phase that shows features passing by on the outer channels of the ECEI-observation window, here identified as filaments. Simultaneously, the temperature also collapses on the inner channels, Figure 5.6(b) and (d). After no more filaments occur on the outer channels, $T_e$ has reached its minimum on the inner channels and the ETB starts to build up again, completing the ELM cycle (phase (4)). In the next three paragraphs, the characteristics of the phases 1-3 described above will be discussed in more detail.

### *5.3.3. Off-mid-plane fluctuations and quiescent phase*

As just described in paragraph 5.3.2, a distinct off-mid-plane fluctuation and quiescent phase were found to precede the crash for almost all 'slow' ELMs.

This $T_e$ fluctuation is always seen to appear first and strongest above the mid-plane (on average 1.7 ms before the final crash), but if the phase lasts long enough it can be seen below the mid-plane as well (for 17 % of the 'slow' ELMs). An example of this is shown in Figure 5.7. Notably its amplitude has disappeared around the mid-plane. The duration of this phase is 0.15-1.70 ms and the movement of the off-mid-plane fluctuations is always directed upwards in the ECEI frame, i.e. in the electron

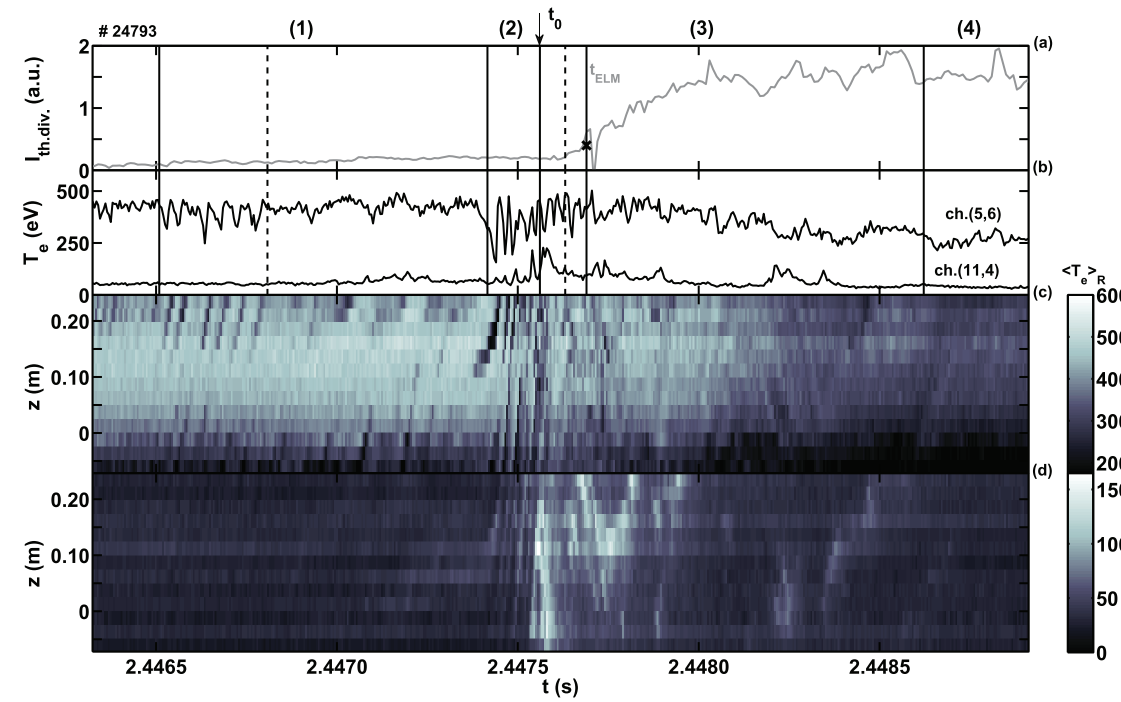


**Figure 5.6** *Overview of a typical ELM cycle: in (a) the divertor thermo-current signal is shown, from which the time $t_{ELM}$ is generally used as an indicator for the start of the ELM. Two $T_e$ time-traces of different ECEI channels are shown in (b): ch.(5,6) measures at R = 2.12 m, z = +0.16 m, above the mid-plane and just inside the separatrix at the top of the pedestal. The measurement location of ch.(11,4) is R = 2.15 m, z = −0.01 m, i.e. below the mid-plane and just outside the separatrix. The $<T_e>_R$ measurements are shown in (c) and (d); in (c) the $<T_e>_R$ of the inner four channels is shown, and in (d) that of the outer four. From (c) and (d), the different phases of the ELM cycle are identified: (1) indicates the phase where the off-mid-plane fluctuation is observed. During phase (2), a mode is seen that leads up to the ELM crash at $t_0$. The ELM crash phase (3), during which $T_e$ collapses, consists of a 'chaotic' stage at the beginning, followed by a series of filaments. In order to reveal the dynamics of these earlier stages, the largest part of the recovery phase (4) is omitted in this figure.*

diamagnetic drift direction, with velocities of 2-4 km $s^{-1}$. The fluctuation, with frequencies in the range of 20-50 kHz, manifests itself as a series of temperature dips and returns to the previous values, rather than as an oscillation around the previous temperature. This can be seen from the time-traces in Figure 5.7(a). The temperature dips can be as large as 60% of the pre-oscillation value and are even seen to reach values below those observed at the end of the following ELM crash.

The radial extension or position of this mode activity is not easily determined from the ECEI measurement and it is most likely to extend radially inwards with respect to the observation area. Therefore, as a first estimate, the poloidal mode number $m$ is estimated assuming that the mode is located on the $q = 4$ surface. From the off-mid-plane fluctuation shown in Figure 5.7(b), it is estimated that 3 periods fit into the ECEI-observation window, which has a height of 0.29 m. Next, the straight field line approximation has to be taken into account, which corrects for the fact that the derivative of the poloidal angle $\theta$ does not in general have the same direction as the

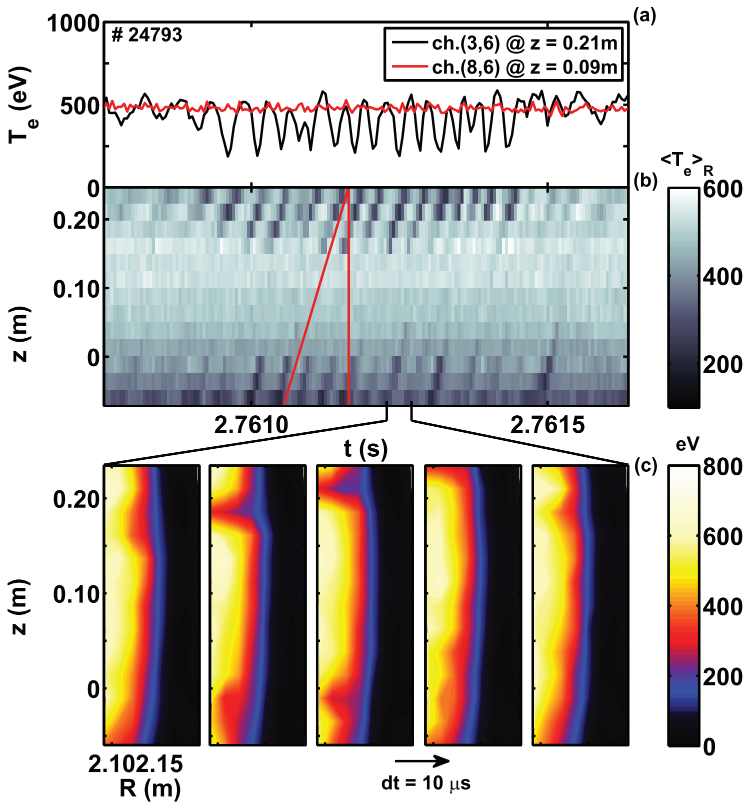


**Figure 5.7** *Example of an off-mid-plane fluctuation before an ELM crash: in (a), the time-traces of two ECEI channels are shown, where both channels measure inside the separatrix at the same major radius (R = 2.12 m). No $T_e$ fluctuations are observed just below the mid-plane, where ch.(8,6) measures. Whereas ch.(3,6), measuring about 10 cm above the mid-plane, clearly shows the off-mid-plane fluctuation appearing and disappearing again. Shown in (b) are the $<T_e>_R$ measurements of the inner four channels; comparable to Figure 5.6(c) but only showing the time window of an off-mid-plane oscillation. In this case, it can be seen that this fluctuation appears both above and below the mid-plane. As is deduced from the two straight lines, 3 periods fit into the ECEI-observation window. The five panels in (c) show the 2D $T_e$ (eV) evolution of this fluctuation.*

derivative of the poloidal magnetic field [Schittenhelm97]. This holds especially for the non-circular cross section of a flux surface in X-point configuration, which is the case here, and this method provides a poloidal angle $\theta^*$ which can be linearly extrapolated. As is determined from the straight field line angle calculation of $\theta^*$ shown in Figure 5.8, the ratio $d\theta/d\theta^*$ is about 3.65. From this, the poloidal mode number $m$ is estimated to be 112 ± 12 and, accordingly, the toroidal mode number $n = 28 \pm 7$. Here, the error margins originate from assuming the location of the mode to be on the neighbouring $q = 7/2$ and 9/2 flux surfaces.

As the off-mid-plane oscillations decrease in amplitude again, the plasma enters a quiescent phase (for 0.65 ms on average) where temperatures hover around the same levels as before. In many of the analysed cases, however, the quiescent phase is disturbed by irregular occurrences of single temperature dips, sometimes reminiscent to those seen during the off-mid-plane fluctuations.

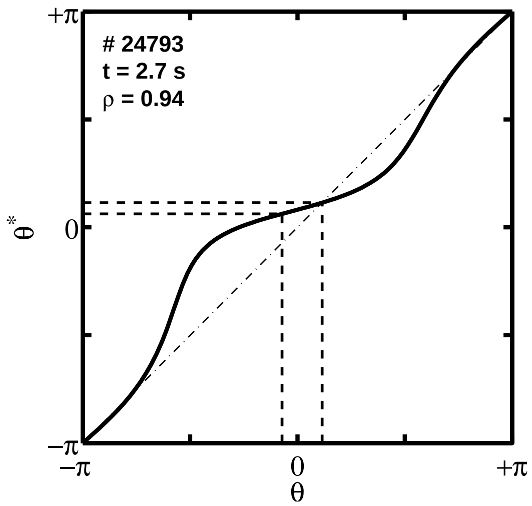


**Figure 5.8** *Relation of the straight field line angle $\theta^*$ to the poloidal angle $\theta$: based on the CLISTE equilibrium reconstruction that is nearest in time to the shown measurements, the relation of $\theta$ and $\theta^*$ is determined for the normalized radius $\rho_{pol}$ = 0.94 (where the centre of the mode is estimated to be, and the q = 4 surface is located). The ratio of $d\theta/d\theta^*$ is 3.65, as is deduced from the dashed lines.*

*5.3.4. Mode structure at the ELM onset*

As is indicated in Figure 5.6, the quiescent phase is followed by a phase of clear deformation of the temperature profile inside the separatrix. It is only at the end of this phase that the temperature finally starts to decrease. Here, this end is defined as the start time of the ELM crash. Due to the fact that the ECEI-observation window is located at the outer midplane, this moment occurs even before the thermo-currents in the divertor start to rise: on average 160 $\mu$s for ‘slow’ ELMs and 210 $\mu$s for ‘fast’ ELMs. For most ‘slow’ ELMs the observed deformation shows a coherent poloidal mode structure which lasts on average 80 $\mu$s. For the ‘fast’ ELMs, their occurrence lasts only 30 $\mu$s on average. A typical example of such a mode is shown in Figure 5.9. However, since different variations of the evolution of this mode have been observed, a short discussion of the variations is given at the end of this paragraph.

Similar to the previously discussed off-mid-plane fluctuation, the direction of this mode’s rotation is always upwards in the ECEI frame, i.e. in the electron diamagnetic drift direction. For the typical case shown in Figure 5.9, the observed mode has a poloidal wavelength of about 15 cm and a radial displacement of almost 3 cm.

Based on the 2D $T_e$ measurement in Figure 5.9(b) and the CLISTE equilibrium reconstruction that is nearest in time, the poloidal mode number $m$ can be calculated. Using the straight field line approximation (as described in paragraph 5.3.3 and cf. Figure 5.8), the poloidal mode number $m$ is estimated to be 74 ± 9 and, accordingly, the toroidal mode number $n$ = 18 ± 4. Again, the error margins originate from assuming the location of the mode to be on the neighbouring $q$ = 7/2 and 9/2 flux surfaces.

In 50% of the observed ‘slow’ ELM crashes, including the one shown in Figure 5.9, the mode is seen to increase in velocity towards the end of its life time. These modes start with a velocity of 4-5 km s$^{-1}$, which is similar to that of the preceding off-mid-plane

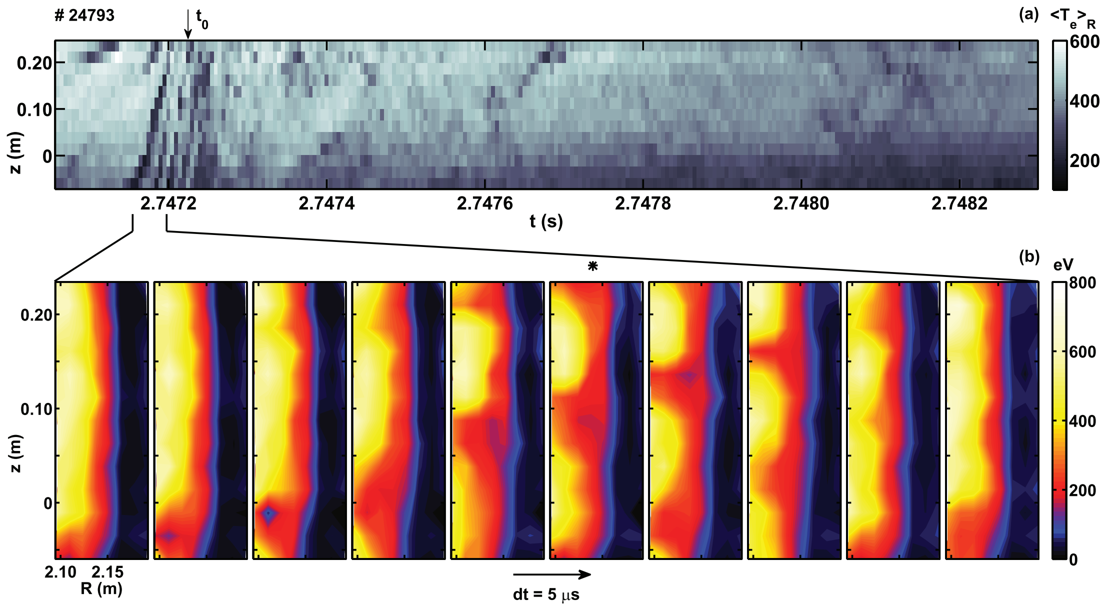


**Figure 5.9** *Mode development at the ELM onset: in (a), similar to figure 6(c), the $<T_e>_R$ of the inner four channels is shown as a function of the vertical position and time. Here, it can be seen that the mode occurs about 75 μs before the ELM crash at $t_0$.The $<T_{rad}>_R$ for the same time window, but then of the outer four channels, is shown in Figure 5.10. The ten panels in (b) are the consecutive frames (with dt = 5 μs) that show the 2D $T_e$ (eV) evolution of the mode. The frame in (b) indicated with * is used for the estimate of the mode numbers.*

fluctuation, and then increase to at least 7-9 km s$^{-1}$. Notably, from Figure 5.9(b), it is also seen that the mode number clearly increases in time; increasing as much as 50% in 10 $\mu$s towards the crash.

The description of the ELM-onset mode as given above applies to the majority of ELM crashes. However, some variations have been observed as well. From all analysed 'slow' ELMs (41), six crashes show different dynamics: three 'slow' ELMs have shown a quiescent phase after a mode that looked similar to the ELM-onset mode described above. In three other cases a mode was not even seen at all. Considering the 'fast' ELMs (17 in total), seven cases were found that showed different dynamics: a similar quiescent phase, occurring after an ELM-onset-like mode, was observed five times, and twice there was no mode at all.

### *5.3.5. ELM crash and filaments*

After the occurrence of the mode described in paragraph 5.3.4, the ELM crash phase starts: a chaotic phase comes first, where the coherent mode structures can no longer be identified (although sometimes remnants of the ELM-onset mode can be seen) and the temperatures of the inner ECEI channels eventually begin to collapse. This is followed by a phase where structures of increased temperature, so-called filaments, occur on the outer channels. It is only after the last filament has occurred, on average 1.6 ms after the ELM crash has started, that the temperatures in the inner channels stop decreasing and the recovery phase starts.

For 'slow' ELMs, the chaotic phase lasts on average 150 $\mu$s, and for 'fast' ELMs this is a bit shorter with 95 $\mu$s. The end of the chaotic phase is almost always marked by the

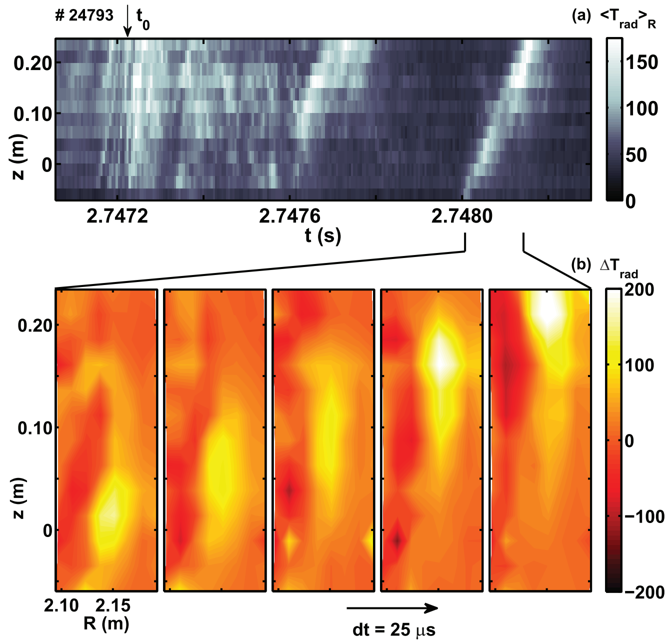


**Figure 5.10** *Example of a filament: in (a), similar to Figure 5.6(d), the $<T_{rad}>_R$ of the outer four channels is shown as a function of z and time; this is, in fact, for the same time window a shown in Figure 5.9. Here, it can be seen that at t = 2.7480 s a filament starts to move from bottom to top. In (b), five panels show the 2D measurements of this filament as it passes through the ECEI-observation window; here, in order to enhance the structure, $\Delta T_{rad} = T_{rad} - T_{rad,avg}$ is shown where $T_{rad,avg}$ is determined after the filament has passed.*

absence of any activity in the whole ECEI-observation window, or sometimes by the clear occurrence of the first filament.

For the ELMs analysed here, all structures appearing after the chaotic phase have been identified as filaments when an increased $<T_{\mathrm{rad}}>_{\mathrm{R}}$ (as described in paragraph 5.2.3) could be followed for a longer period of time and/or over multiple channels in the vertical direction. For both 'slow' and 'fast' ELMs, seven filaments on average could be identified after each ELM crash; with minimum and maximum numbers of 2 and 13. The first filament is usually seen within the first 200 $\mu$s after the end of the chaotic phase; depending on the number of filaments, the last filament can occur up to 2 ms after the first. The number of filaments that can be seen depends on the length of the temperature crash phase.

The measurements in Figure 5.10 show an example of a filament; in this case one that travels through the whole of the ECEI-observation window during the course of its lifetime. These measurements are taken following the exact same ELM-onset mode that was described in the previous paragraph and they show the filament as a poloidally localized structure of increased local temperature around the very edge. The filament has a height of 7 cm and rotates in the upward direction with a velocity of about 2 km s$^{-1}$. In order to enhance this structure, since it lies in the steep gradient region, $T_{\mathrm{rad}} - T_{\mathrm{rad,avg}}$ is shown in Figure 5.10(b) rather than the absolute (radiation) temperature $T_{\mathrm{rad}}$. Here, $T_{\mathrm{rad,avg}}$ is the average radiation temperature taken at the end of the crash. Assuming locally increased electron densities [Kurzan07] inside a filament, the optical thickness inside the structure could (marginally) be above unity [Classen10]. Hence, although these measurements are obtained from regions just at and outside the separatrix, the radiation temperatures (with maxima up to 200 eV) are still assumed to be strongly correlated with the electron temperature.

Usually the filaments move in upward direction with a typical speed of a few km $s^{-1}$. However, in 20 ELM crash phases (15 'slow' and 5 'fast' ones), filaments have been observed to move in the opposite direction of the preceding ELM-onset mode. In all these cases, it is observed that this downward movement only concerns the first filament, or first few, that occur after the 'chaotic' phase.

## 5.4. Discussion and conclusion

As has been shown, the 2D aspect of ECEI (and its fast measurement) has revealed several features of ELM dynamics that were previously inaccessible to ECE measurements. Firstly, it has been seen that a difference between 'slow' and 'fast' ELMs at AUG is the occurrence of a temperature fluctuation which has its amplitude strongest off mid-plane and is followed by the quiescent phase. Its poloidal and toroidal mode numbers are $m = 112 \pm 12$ and $n = 28 \pm 7$. Secondly, at the onset of the ELM crash, and a few tens of $\mu$s before the ELM crash is observed by the thermo-currents in the divertor, a mode is observed covering the entire ECEI-observation window. The estimated mode numbers are $m = 74 \pm 9$ and $n = 18 \pm 4$, which, most remarkably, are seen to increase towards the crash. Simultaneously, the velocity (in the poloidal direction) of the mode increases. Finally, during the temperature collapse phase, ELM filaments have been identified in the outer half of the ECEI-observation window and their motion can be followed in the vertical direction. In contrast to both the off-mid-plane fluctuation and the ELM-onset mode, which only have been seen rotating in the electron diamagnetic drift direction, sometimes the first few filaments have been observed to move in the opposite direction as well. Observations like these clearly show the benefit of the 2D ECEI diagnostic, since such features could not independently have been derived from 1D measurements.

With respect to the classification of the observed phases, it has to be stressed here that this is based on the analysis of a single, albeit typical, AUG type-I ELMy H-mode discharge with a $q_{95}$ of 4.7. In order to characterize the whole series of ELMs, the dimensionality of the ECEI measurements ($T_e$ as a function of $R$, $z$, and time) has been brought down by applying radial averaging over two halves of the observation window. The application of this averaging method, which enhances the radially coherent features, might also have suppressed incoherent features that could still be relevant. With regard to the off-mid-plane fluctuation, which has been found here to be a distinguishing factor between 'slow' and 'fast' ELM cycles, the following has to be taken into account. It was shown in [Burckhart10] that for 'slow' ELMs all edge profiles reached their final shape up to 7ms before the final crash. But since the observed off-mid-plane fluctuation occurs only in the last 2 ms, it cannot be the sole cause of the delay; also in the discharge analysed here, the difference between 'slow' and 'fast' ELMs was on average 5 ms. However, the presence of this fluctuation does suggest that it regulates the plasma edge condition in such a way that a stable situation is prolonged at least a little longer until the ELM crash finally comes.

Due to the quiescent phase that often occurs in between the off-mid-plane temperature oscillation and the onset mode, seen just prior to the start of the temperature crash, it is not clear whether or not this off-mid-plane fluctuation develops into the ELM-onset mode, or if the two are separate phenomena. The mode numbers that have been estimated are, however, of the same order of magnitude, with those for the off-midplane oscillation being slightly higher. With respect to the fast changes in mode number and velocity that have been observed for the ELM-onset mode, the ECEI measurements alone cannot reveal to what extent these effects are related to the slowing down (and stopping) of the edge plasma rotation [Pütterich09].

The duration of the temperature collapse phase differs for each ELM crash. Interestingly, the occurrence of filaments is only seen during this temperature collapse phase. With some of the first filaments seen moving in downward direction, it is uncertain to what extent their motion is related to the previously observed ELM-onset mode or whether it could be determined by the plasma flows in the scrape-off layer.

Compared with other observations, e.g. [Bolzonella04], [Terry07], [Maingi05], it is notable that the toroidal mode number $n$ of the off-mid-plane fluctuation presented here is much higher. However, these mode numbers have mostly been determined from a precursor that usually grows in amplitude in the last ~100 $\mu$s and is seen in the Mirnov coils. This is obviously not the case here, since the off-mid-plane fluctuation does not develop into the actual crash. It is noted, though, that the $n$ number of the presented ELM-onset mode is already lower than that of the off-mid-plane fluctuation. On the other hand, the existence of a high frequency (300-500 kHz) precursor oscillation, which is often observed in the magnetics, is possibly connected to high $n$ ballooning modes. It is also seen that these high frequency precursors drop in frequency during the final growth phase. Although most of the observed precursors are seen mainly in the magnetics, there are also examples that show the existence of a low frequency precursor that is not seen on the magnetics but only in the density [Oyama04].

Further study will be required to put these new observations in a broader perspective as well as in the context of the general ELM cycle as described in the introduction. In order to find the origin of the off-mid-plane fluctuation, a comparison will be made to the $T_e$ oscillations observed in type-II ELMs, which show similar behaviour [Wolfrum11]. Combining the ECEI measurements of filaments during the temperature collapse phase with measurements from (visual light) cameras, Langmuir probes and, e.g., the fast-ion-loss detector should resolve the different directions of motion observed. By slightly changing the magnetic field, or changing the settings of the diagnostic, the ECEI field of view will be shifted so the radial depth of the modes can be determined. It will also be investigated whether the observed phenomena occur in a similar way under other plasma conditions, e.g. different $q_{95}$ or edge collisionality. Finally, a direct comparison of the ECEI measurements of the mode observed at the ELM onset and the non-linear modelling of JOREK [Huysmans07], [Pamela10], [Huysmans09] might also reveal whether or not this could indeed be the ELM trigger.

## Acknowledgement

This work, supported by the European Communities under the Contract of Association between EURATOM-FOM, was carried out within the framework of the European Fusion Program, with financial support from NWO, FOM and EURATOM. The views and opinions expressed herein do not necessarily reflect those of the European Commission.

# Chapter 6*

# Broadband MHD fluctuations during type-II edge localized modes

J.E. Boom[1], E. Wolfrum[2], I.G.J. Classen[1], P.C. de Vries[1], M. Maraschek[2], W. Suttrop[2], C.P. Pérez von Thun[2], A.J.H. Donné[1,3], B.J. Tobias[4], C.W. Domier[5], N.C. Luhmann Jr[5], H.K. Park[6] and the ASDEX Upgrade Team

[1] FOM Institute DIFFER - Dutch Institute for Fundamental Energy Research, Association EURATOM-FOM, 3430 BE Nieuwegein, The Netherlands
[2] Max-Planck-Institut für Plasmaphysik, 85748 Garching bei München, Germany
[3] Faculteit Technische Natuurkunde, Technische Universiteit Eindhoven, 5600 MB Eindhoven, The Netherlands
[4] Princeton Plasma Physics Laboratory, Princeton, NJ 08540, USA
[5] Department of Electrical and Computure Engineering, University of California at Davis, Davis, CA 95616, USA
[6] POSTECH, Pohang, Gyeongbuk, 790-784, Korea

**Abstract**
The characterization of a broadband fluctuation that is typical for the type-II ELM regime at ASDEX Upgrade has been improved by using the 2D capabilities of ECE-Imaging. During the transition from the type-I to type-II ELMy phase, it has been found that electron temperature fluctuations form a broadband peak in the 19-65 kHz range. In the type-II phase, this broadband fluctuation reaches a maximum relative amplitude of almost 20 % just inside the top of the pedestal. Simultaneously, the electron temperature profile is completely flattened at this location. The 2D distribution of the amplitude of this broadband fluctuation is such that, when averaged over time, a minimum occurs around the mid-plane. From the measurements of the nearby magnetic pickup coils, a similar broadband fluctuation seems visible in the same frequency range. However, this is peaked at a slightly lower frequency and does not show a similar minimum. From the analysis of the fluctuations on small timescales, the poloidal and toroidal mode numbers are estimated to be $m \sim 100$ and $n \sim 21$. Furthermore, activity reminiscent of beat waves has been observed, which might partially account for the fluctuation's broadband nature and the seeming velocity variation of single fluctuation passages. Overall, similarities between the characteristics of this broadband fluctuation and various precursors to type-I ELMs suggest that this fluctuation can play an important role in regulating the ELM cycle.

* The work presented in this chapter is published in this form in Nuclear Fusion under the title 'Characterization of broadband MHD fluctuations during type-II edge localized modes as measured in 2D with ECE-imaging at ASDEX Upgrade'.
Boom J.E. et al. 2012 *Nucl. Fusion* **52** 114004

## 6.1. Introduction

In the high confinement mode (H-mode), tokamak operation is usually afflicted by edge localized modes (ELMs) which are triggered by the associated steep pressure gradient at the edge transport barrier (ETB). These modes expel plasma particles and energy into the scrape-off layer, giving rise to high power loads on the divertor target plates and possibly intolerable erosion of first wall materials (in case of steady state reactor operation). As a beneficial side effect, though, ELMs will also help control the plasma density and impurity accumulation. Apart from the most common type-I ELM regime, which exhibits the aforementioned large peak heat loads, ELM regimes with significantly lower energy losses per ELM event have also been observed; e.g. the Enhanced $D_\alpha$ mode seen at Alcator C-Mod [Snipes98], [Hutchinson99] or the type-V ELMs at NSTX [Sontag11].

The type-II ELM regime [DIII-D Team91] is one of the small ELM regimes that combines both good confinement and small energy losses. It was first observed on the DIII-D tokamak [Ozeki90], but has also been identified on JT-60U [Kamada00], [Kojima09] (where they are called 'grassy' ELMs), and on ASDEX Upgrade (AUG) [Stober01], [Saarelma03] and JET [Saibene02], [Lönnroth04], [Saibene05], [Nunes07]. The identification of the type-II regime is delicate due to the lack of a simple criterion (e.g. for the relation between ELM frequency and power, which defines the difference between type-I and -III ELMs). Generally, though, it can be said that the large type-I ELM bursts are replaced by smaller, more irregular oscillations (typically well above 100 Hz). Furthermore, type-II ELMs are usually obtained in plasmas which shapes have been highly tuned. In addition, this regime seems to be characterized by the presence of distinguishing broadband fluctuations near the plasma edge, as described by [Perez04], [VonThun08], and most recently by [Wolfrum11].

As well as possibly being an interesting operational scenario for future fusion reactors, understanding the physics that governs the dynamics of these type-II ELMs could also increase the understanding of pedestal stability for type-I ELMs. Furthermore, this might contribute to the extrapolation of ELM and pedestal models towards ITER or even to the development of ELM control tools.

The exact nature of pedestal stability in the type-II ELM regime is still unknown; it is e.g. not clear whether type-II ELMs are bursting or continuous (see [Stober01], [Stober05]). It has been proposed, though, that high frequency, low amplitude ELMs appear when the stability lies in between the first and second stable ballooning regimes [Ozeki90]. Due to diagnostic limitations, however, it is generally not straightforward to deduce stability conditions accurately from actual experiments. It has also been suggested that the edge gradients could be controlled by enhanced transport due to broadband magneto-hydrodynamic (MHD) fluctuations in the low frequency range [Perez04], [Smeulders99], which have also been observed in the density [Saibene02].

In this paper, the properties of these broadband MHD modes and the related temperature fluctuations are inspected in more detail. The availability of a (new) diagnostic that observes more than just alongside a radial direction allows for a closer look into the spatial extension of these characteristic fluctuations. Here, the focus is on describing the regulating role of this fluctuation on the pedestal during the type-II phase, as well as the transition from the type-I to type-II phase.

The outline of the paper is as follows: first, in section 6.2, the operational requirements for obtaining type-II ELMs in AUG will be described, combined with a short description of the main diagnostics used for the analysis. In section 6.3, a detailed description of the MHD activity will be shown, along with a comparison between the observations of the different diagnostics. A summary and conclusion of this analysis are given in the last section.

## 6.2. Type-II ELM experiments at AUG

The requirements for obtaining type-II ELMs at AUG are already well-known, see e.g. [Stober01], [VonThun08], [Wolfrum11] and references therein. In short, the type-II ELMs regime is reached using highly shaped plasmas in near double null (DN) configuration, with high triangularity $\delta$, high elongation $\kappa$, and high $q_{95}$. In order to reach the required high collisionality regime, the plasma density should also be sufficiently high. For an actual discharge, this means that the plasma is first shaped in lower single null (LSN) after which the input power is increased and the plasma enters the common type-I ELMy H-mode regime. Once that is achieved, the position of the magnetic axis is shifted upwards until the distance at the mid-plane between the inner and outer separatrix is reduced to a minimum and a configuration close to DN is reached. Under these circumstances, the large type-I ELMs disappear and when the reduction in confinement is simultaneously kept small compared to the type-I phase, the plasma has reached a state where type-II ELMs occur.

An overview of one of the discharges where type-II ELMs were created for this work is shown in Figure 6.1. In this case, the discharge (#26459) had a plasma current of $I_p = 0.8$ MA and a magnetic field of $B_t = -2.5$ T. As can be seen in Figure 6.1(a), the plasma is predominantly heated by neutral beam injection (NBI) with an input power of up to 7.5 MW, and type-I ELMs already occurring for an input power of 5 MW. A small amount of 900 kW of electron cyclotron resonance heating is additionally applied in the plasma core in order to prevent impurity accumulation. After the completion of a radial shift from 2.0-2.4 s, the upward shift of the magnetic axis $z_{mag}$ starts at 2.6 s and the near DN configuration is reached at 3.7 s (Figure 6.1(b)). As can be seen in the same graph, the mid-plane distance between the primary and secondary separatrix, $\Delta R_{sep}$, is reduced to 8 mm. By then, the plasma has reached its final shape close to DN, with an upper and lower triangularity of $\delta_{R,up} = 0.46$, $\delta_{R,low} = 0.33$, and an elongation of $\kappa = 1.66$. As is shown in Figure 6.1(c), the edge safety factor $q_{95}$ has reached a value of 5.4 here, which is slightly different from the $q_{95}$ in the lower single null configuration due to the changes in triangularity and elongation. The reduction in the power loads on the divertor can be seen in Figure 6.1(d), decreasing from a level up to 12 MW m$^{-2}$ during the type-I ELM phase to about 2 MW m$^{-2}$ in the near DN shape. In the same graph, it can be seen that the spikes in the divertor thermo-currents decrease accordingly (a more detailed description of the $I_{div}$ time-trace during the transition is shown in Figure 6.3(a)). Simultaneously, as indicated by the $H_{98(y,2)}$-factor in Figure 6.1(e), the reduction in confinement is only about 10 % and the $H_{98(y,2)}$-factor stays above unity. Altogether, the type-II ELMs occur from 3.7-4.5 s for discharge #26459 (indicated between the dashed vertical lines in Figure 6.1). The moment the strong gas fuelling of $8.3\times10^{21}$ D s$^{-1}$ is ramped down (Figure 6.1(f)), the type-I ELMs return again with decreasing density.

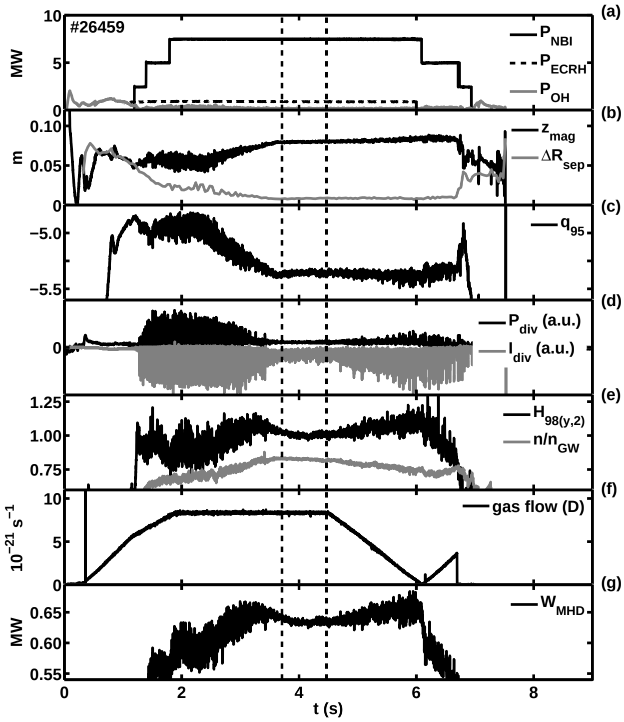


**Figure 6.1** *Overview of AUG discharge #26459: (a) the input powers of NBI, ECRH and the Ohmic input, (b) position of the magnetic axis $z_{mag}$ and the distance between the two separatrices $\Delta R_{sep}$ as a measure for closeness to DN, (c) the edge safety factor $q_{95}$, (d) power density $P_{div}$ and thermo-current $I_{div}$ in the divertor (e) the factor $H_{98(y,2)}$ and the ratio of the density over the Greenwald density $n/n_{GW}$, (f) fuelling rate for deuterium, (g) confined energy $W_{MHD}$. The time interval from 3.7-4.5 s (indicated by the vertical dashed lines) is where the type-II ELMs occur.*

Following [Oyama06], the collisionality $\nu^*_e$ at the plasma edge can be calculated using

$$\nu_e^* = 6.921\times10^{-18}\,\frac{R q_{95} Z_{eff} n_e \ln\Lambda_e}{\varepsilon^{3/2} T_e^2}\ . \tag{6.1}$$

Here, $R$ is the major radius of the magnetic axis (in m), $\varepsilon$ the inverse aspect ratio, $q_{95}$ the edge safety factor (cf. Figure 6.1(c)), and $Z_{\rm eff}$ the effective ion charge (estimated here to be 2). The electron temperature $T_{\rm e}$ (eV) and density $n_{\rm e}$ (m$^{-3}$) are determined at the top of the pedestal and, using these values, the Coulomb logarithm $\ln\Lambda_{\rm e}$ is defined as $\ln\Lambda_{\rm e} = 31.3 - \ln((n_{\rm e})^{1/2} / T_{\rm e})$. For the two different phases, the following values have been taken from Figure 6.4(a) and (c): in the type-I phase, $T_{\rm e,ped} = 515$ eV and $n_{\rm e,ped} = 6.2\times10^{19}$ m$^{-3}$, and in the type-II phase $T_{\rm e,ped} = 410$ eV and $n_{\rm e,ped} = 6.7\times10^{19}$ m$^{-3}$. From this, it follows that $\nu^*_{\rm e}$ has a value of 2.7 in the type-I ELM phase (at 2.0 s), and the collisionality has increased to 4.8 in the type-II ELM phase (at 4.1 s). The latter value is indeed above the collisionality threshold proposed in [Wolfrum11].

The main diagnostic that has been used for the analysis of type-II ELMs in this work is ECE-imaging (ECEI) [Park04], [Tobias09], [Classen10]. The ECEI system at AUG consists of an array of 16 detectors, each of which serves as a standard ECE radiometer. The measured power is proportional to the intensity emitted by a black

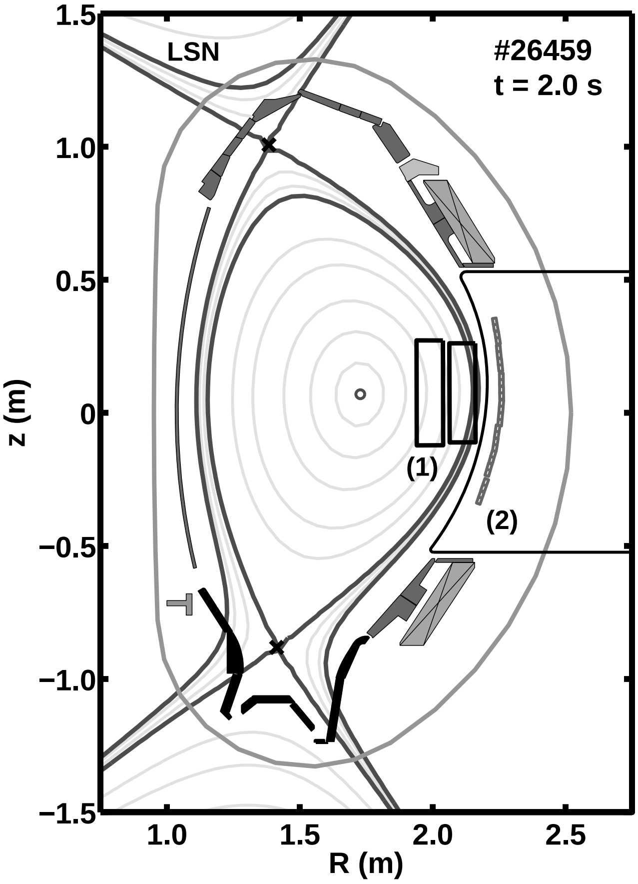


**Figure 6.2** *Overview of the two positions of ECEI measurements (1): for discharge #26459, the viewing window was set at the very edge (right box) and the setting one step inwards (left box) was used in discharge #26466. Furthermore, the location of the high resolution 'ballooning' pickup coils (2) is indicated. Toroidally, these pickup coils are positioned at $\phi = 275°$, whereas ECEI is located at $\phi = 191°$. The shown equilibrium is from early on in discharge #26459, where the plasma is still in lower single null (LSN) configuration. For comparison, the near DN equilibrium (where the type-II ELMs are analysed) is shown in Figure 6.5(b).*

body at temperature $T_e$, under the assumption that the plasma is optically thick. The quasi-optical setup allows for the 16 lines of sight (LOS) to be focussed at the low-field-side (LFS) edge with a waist of 1.5 cm at the focal plane. In the radial direction 8 local oscillator frequencies per line-of-sight determine the coverage; with each frequency band corresponding to about 1.6 cm in the plasma. Therefore, at the LFS, the total area covered is about 40×13 cm$^2$ (with spot sizes of 1.5×1.6 cm$^2$), as can be seen in Figure 6.2. The sampling rate of ECEI is set to 200 kHz, covering the entire duration of the discharge at this rate.

Pickup coils have been used for the measurement of magnetic fluctuations; in this case, from the so-called high resolution 'ballooning' coil array which is located close to the plasma on the LFS (as can be seen in Figure 6.2). These coils measure the perturbations of the radial magnetic field $B_r$ at different poloidal positions with a constant sampling rate of 2 MHz. A detailed overview of all magnetic pickup coils available at AUG is found in the appendix of [VonThun08].

## 6.3. 2D observation of broadband mode activity

### *6.3.1. Transition to type-II ELMs*

For the analysed discharge #26459 (introduced in Figure 6.1), the transition from the type-I to type-II ELMy phase is shown in more detail in Figure 6.3. As can be seen in Figure 6.3(a), the spiky signature on the divertor thermo-currents due to the type-I ELMs decreases, indicating a reduction of the power loads. With the magnetic axis moving upwards, the type-I ELM frequency slowly increases from 50 to 150 Hz and from 3.7 s onwards the type-I ELMs have completely disappeared (Figure 6.3(b)). In Figure 6.3(c) a spectrogram of one of the ECEI channels is shown from which the differences between the type-I and type-II phases can be seen. In the type-II phase (from $t_7$ onwards), a broadband temperature fluctuation can be seen that is characteristic for type-II ELMs and is constantly present during this phase. During the type-I phase (until $t_2$), $T_e$ fluctuations with similar characteristics can sometimes be observed between two crashes but only very shortly (a few hundred μs). At the transition to the type-II phase the frequency spectrum changes, as can be seen from Figure 6.3(c) and (e). Starting from the pure type-I phase, time windows $t_1$-$t_2$, the amplitude in the lowest frequency range (5-20 kHz) starts to increase. Next, with increasing ELM frequency, the amplitude in higher frequency ranges starts to increase as well ($t_3$-$t_5$). Finally, the transition to the pure type-II regime occurs in two ways as can be seen from the spectra over $t_6$ and $t_7$. On the one hand, the amplitude decreases in the low frequency range, i.e. below 30 kHz (indicated by the dash-dotted line in Figure 6.3(e)). On the other hand, the broadband fluctuation becomes peaked in the 19-65 kHz range, with a maximum at 42 kHz. The above described frequency behaviour during the transition can also be seen from Figure 6.3(d), where the development of the energy content is shown as a function of time. Here, the energy content is determined as the power spectral density integrated over either the 5-19 or the 19-65 kHz frequency range and divided by the length of the frequency range.

### *6.3.2. Amplitude distribution of the broadband mode*

In Figure 6.3(c)-(e), the development of the broadband mode characteristic for the type-II ELM phase has been shown using just one of the ECEI channels. When all 128 ECEI channels are considered, a normalized flux surface ($\rho_{pol}$) range of 0.82-1.05 is covered. This allows for following the increase of the broadband amplitude as a function of $\rho_{pol}$ across the transition to the type-II phase. In order to do so, frequency spectra similar to Figure 6.3(e) were made for all ECEI channels. They were averaged over $\Delta t = 100$ ms, and slid through the type-I to type-II transition in steps of 50 ms. From each obtained spectrum, the amplitude of the broadband mode has been calculated by integrating over the 19-65 kHz range. Dividing this by the local average $T_e$, and subsequently interpolating that on the 2D equilibrium, a flux surface averaged relative temperature perturbation $<A>_\rho$ (%) has been determined.

In Figure 6.4(b), the obtained profiles of the mode's amplitude are shown for the type-I and type-II phases, and for two intermediate time points (t = 3.3 s and t = 3.5 s). From this it can be seen that, during the type-I ELMy phase, the $<A>_\rho$ is about 5 % at the very edge ($\rho_{pol} > 0.95$) and that it is even less more inward. In the type-II phase, the amplitude of the $T_e$ fluctuation has increased to a peak value of almost 20 % at $\rho_{pol} = 0.94$, which is just inwards of the top of the pedestal. Simultaneously, with increasing fluctuation amplitude, it can be seen in Figure 6.4(a) that the $T_e$ profile

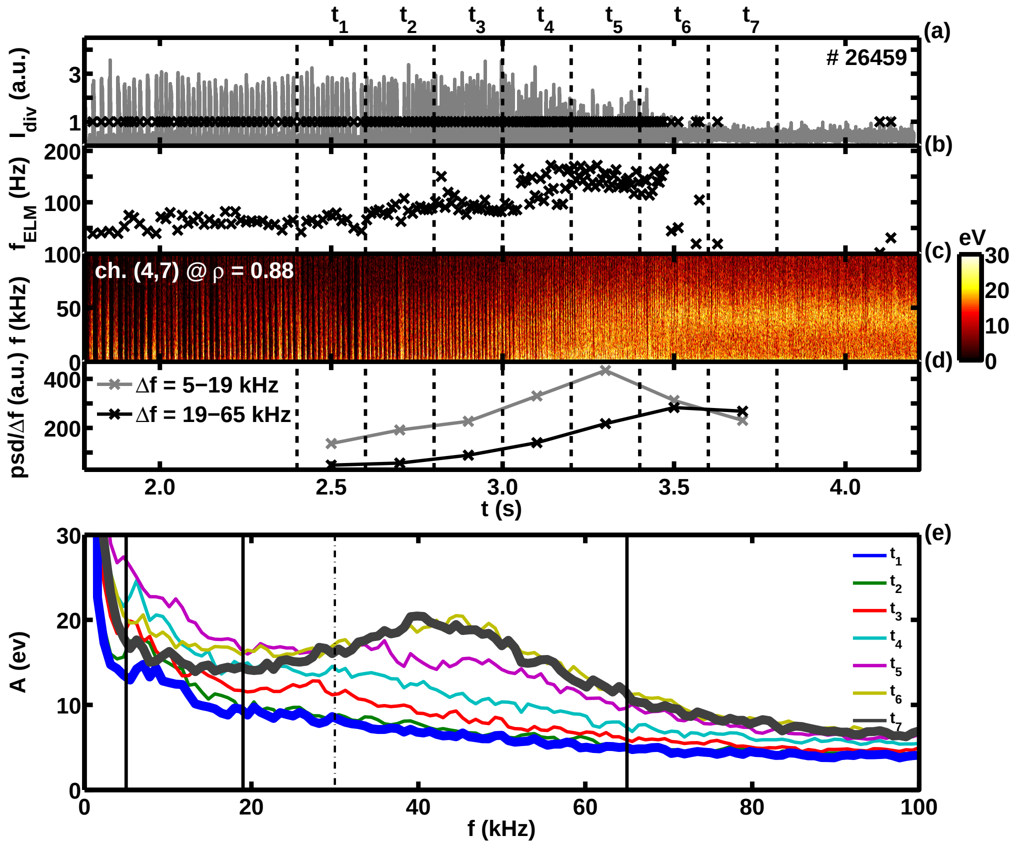


**Figure 6.3** *Transition from type-I to type-II phase: in (a), the time trace of the thermo-current in the outer divertor is shown once more (cf. Figure 6.1(d)), here zoomed in on the transition phase. From this time trace, the ELM frequency is determined as reciprocal time and shown in (b). In (c), a spectrogram is shown of one of the ECEI channels. From this spectrogram, the spectral amplitudes averaged over the indicated time windows $t_1$-$t_7$ are shown in (e). In the type-II phase, the broadband fluctuation becomes peaked between 19-65 kHz, with a maximum at 42 kHz. This can also be seen from (d), where the energy content (psd/Δf), integrated over the 5-19 kHz and 19-65 kHz frequency ranges, is shown for the $t_1$-$t_7$ time windows.*

becomes flattened just inside the top of the pedestal. The $T_e$ gradient of the pedestal, however, remains unaffected.

Exploiting the full 2D capabilities of the ECEI diagnostic, the amplitude distribution of the broadband fluctuation can also be visualized in the poloidal cross section. Two consecutive discharges, with the ECEI viewing window set to neighbouring positions (cf. Figure 6.2), allowed for a large 2D view of this distribution. The first discharge, #26459, has already been described in detail in section 6.2. The second one (#26466) was almost identical; however the near DN phase where the type-II ELMs appeared was not completely free of type-I ELMs. Therefore, in order to make a comparison between the two discharges, a time window of 22 ms (t = 4.0775-4.0995 s) was selected where no type-I ELMs were present in the second discharge, as shown in Figure 6.5(a). From spectra averaged over this whole time window, the broadband fluctuation's amplitude is integrated over the 19-65 kHz range, again for each of the 128 channels. In Figure 6.5(b) the obtained amplitude is shown relative to the local

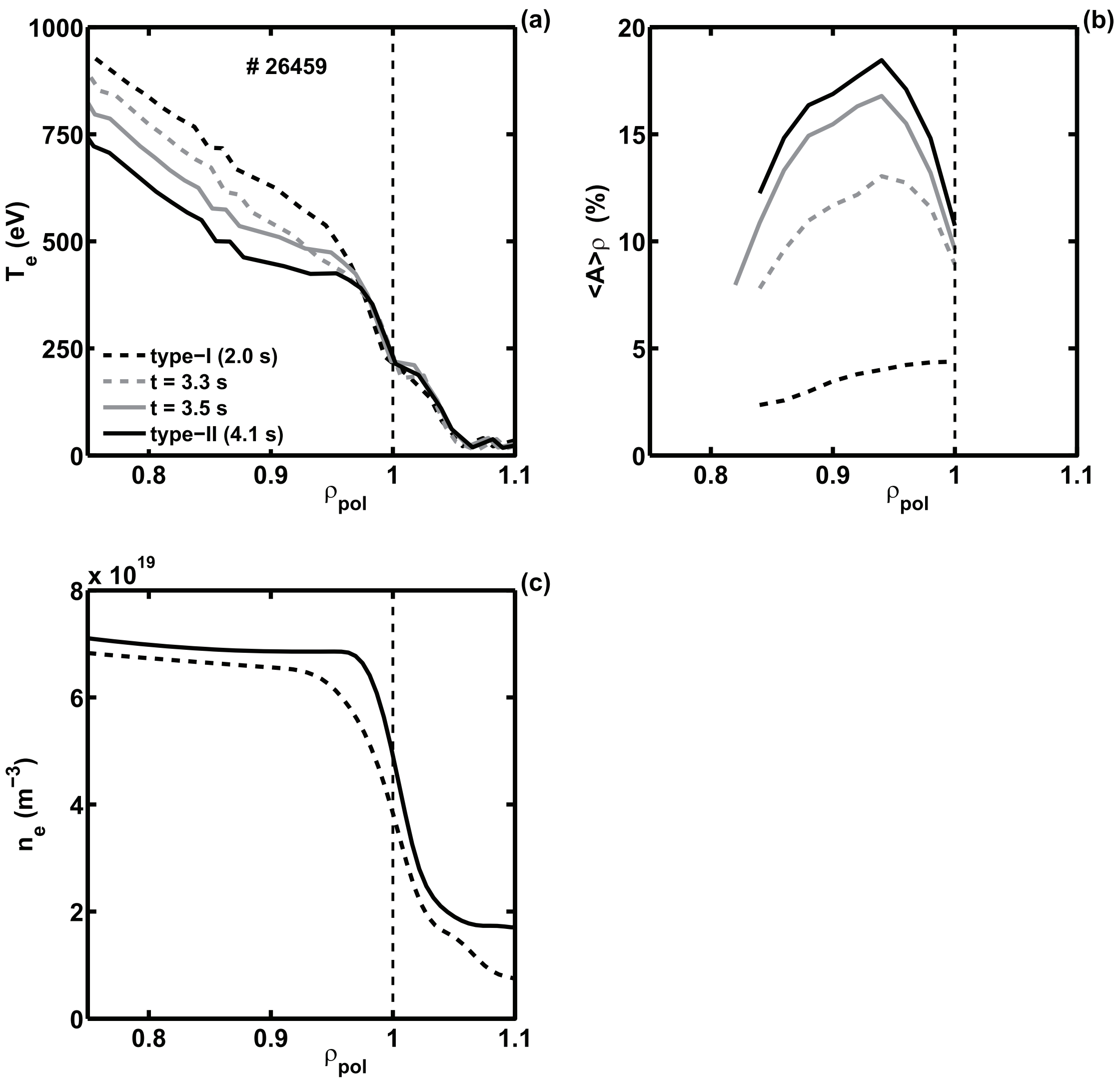


**Figure 6.4** *Influence of the broadband fluctuation on temperature profiles: (a) development of the $T_e$ flattening just inwards from the top of the pedestal. In (b) it is shown that the amplitude of the broadband fluctuation in the 19-65 kHz range, averaged over the flux surfaces covered by ECEI, increases over the transition to the type-II phase. In (c) the density profiles in the type-I and type-II phase are shown. For the calculation of $\nu^*_e$, described in section 6.2, the following values have taken from (a) and (c): $T_{e,ped} = 515$ eV and $n_{e,ped} = 6.2\times10^{19}$ $m^{-3}$ in the type-I phase, and $T_{e,ped} = 410$ eV and $n_{e,ped} = 6.7\times10^{19}$ $m^{-3}$ in the type-II phase.*

average temperature over the time window. Here, this normalisation was preferred over showing the 2D distribution of the displacement (i.e. the amplitude divided by the local $T_e$ gradient). The latter would namely give a biased picture due to the three different gradient regimes that are covered.

From Figure 6.5(b), it can be seen that the time-averaged relative amplitude distribution is such that there is a minimum around the mid-plane, i.e. between $z = 0$ cm and $z = 10$ cm. Note that the magnetic axis is located at $z = 8$ cm, determined from the equilibrium reconstruction. As was already shown in Figure 6.4(b), the fluctuation is localised near the top of the pedestal, but from this 2D distribution it

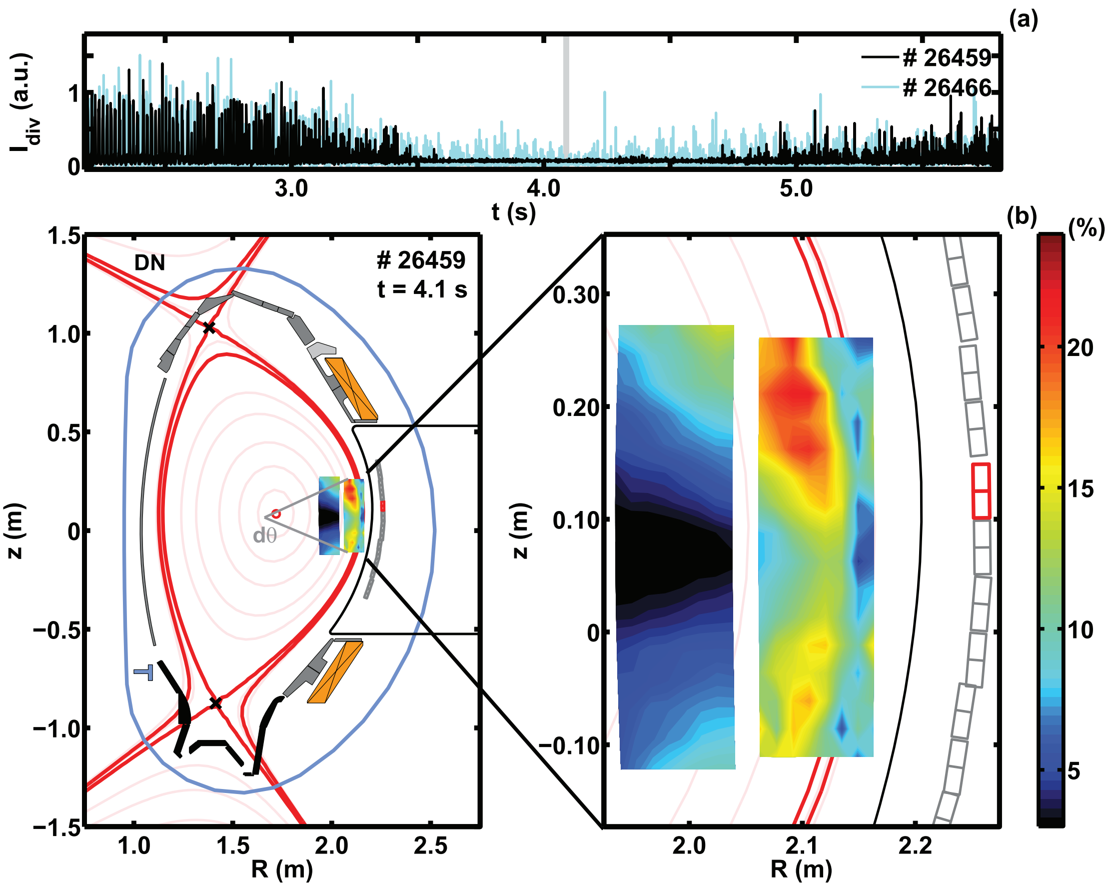


**Figure 6.5** *In (a), time traces are shown of the thermo-currents (inner divertor) for the two discharges used. Here, it can be seen that the large spikes due to the type-I ELMs do not completely disappear in discharge #26466. The time window of 22 ms, used for (b), is also indicated. In (b), the distribution of the relative amplitude of the broadband fluctuation is shown. On the left, an overview is shown of the whole cross section of AUG, the location of the two ECEI measurements, and the angle $d\theta$ used in the calculation of the mode number in paragraph 6.3.3. The zoom on the right shows the spatial distribution of the fluctuation's amplitude in more detail. The pickup coil used for the spectra shown in Figure 6.6(a) is indicated amidst the coils of the array.*

becomes clear that the off-mid-plane nature extends considerably deeper into the plasma.

In order to see if the broadband fluctuation also manifests itself as a magnetic fluctuation, the spectra from the nearby array of high resolution $B_r$ pickup coils (cf. Figure 6.2) have been analysed for comparison. In Figure 6.6(a), two spectra are shown which are taken from the pickup coil indicated on the right of Figure 6.5(b). For one spectrum, an average was taken over the time window $t_7$ (in the fully developed type-II phase) in order to compare to the results from Figure 6.3(e). From this spectrum, it can be seen that the pickup coils do seem to measure a broadband fluctuation within the 19-65 kHz range. However, compared to Figure 6.3(e), the broadband fluctuation measured by the pickup coils is peaked at a much lower frequency of 30 kHz (vs. 42 kHz for the ECEI measurement). For the other spectrum shown in Figure 6.6(a), the average was taken over the same time window of 22 ms that was used for obtaining

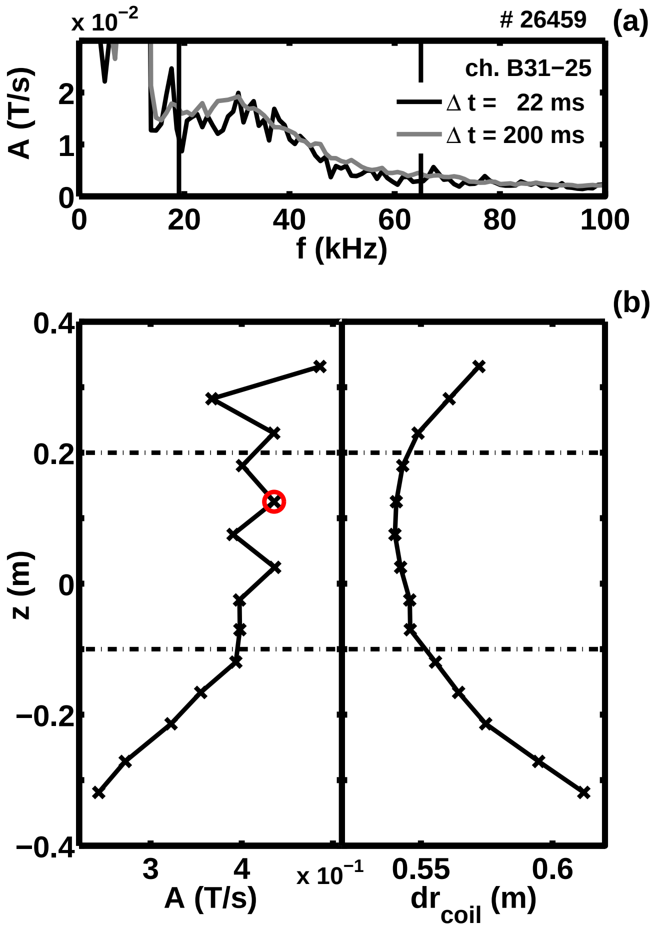


**Figure 6.6** *The frequency spectrum of one of the high resolution 'ballooning' coils is shown in (a); for the spectrum labelled $\Delta t = 22$ ms, the same time window was used as was done for Figure 6.5(b). Likewise, for the spectrum labelled $\Delta t = 200$ ms the time window $t_7$ (cf. Figure 6.3) was used. In (b) the amplitude of the broadband peak in the 22 ms time window is shown (left) as a function of the vertical position of each coil; the coil used for the spectra shown in (a) is indicated by the circle. For each coil, the distance to the magnetic axis is shown in the panel on the right.*

the 2D distribution shown in Figure 6.5(b). As was done for the ECEI channels, the amplitude of the broadband fluctuation was derived by integrating the spectra over 19-65 kHz for each of the coils in the array.

The poloidal distribution of this amplitude is shown as a function of the vertical position of the coils in the left panel of Figure 6.6(b). In the right panel, it is shown that all the pickup coils between $z = -10$ cm and $z = 20$ cm have approximately the same distance from the magnetic axis. From the ECEI measurements, the amplitude minimum around the midplane was found to be almost a factor of two smaller than the maximum above the mid-plane. The amplitude distribution obtained from the magnetic pickup coils shows a variation of 10 % between $-10$ cm $< z < +20$ cm, but does not show a minimum similar to ECEI within this range.

*6.3.3. Characteristics of the propagation of $T_e$ fluctuations*

Instead of considering frequency spectra which are time averaged over many milliseconds, the fast sampling rate of ECEI also allows studying the mode on much smaller timescales. The poloidal propagation of the $T_e$ fluctuations moving through the ECEI observation window is shown in Figure 6.7. In Figure 6.7(a) and (c), the temperature $\langle T_e \rangle_R$, averaged over all 8 radial channels, is shown as a function of vertical position. This way, the propagation of the mode can be followed in the poloidal direction, i.e. from bottom to top. In Figure 6.7(b) and (d), the $\langle T_e \rangle_R$ signals are normalised and shown for all LOSs placed underneath each other. These plots allow following the amplitude dynamics of the mode poloidally over several milliseconds.

The propagation of single $T_e$ fluctuations is best seen in Figure 6.7(a): here, they can be followed as they move from bottom to top, i.e. in the electron diamagnetic drift direction. From the indicative (orange) lines around $t = 4.1093$ s in Figure 6.7(a), the velocity of a single $T_e$ peak is determined to be about 5 km s$^{-1}$. The reciprocal time interval between single passes of $T_e$ dips and peaks falls within the 19-65 kHz range. It is, however, not very regular which reflects the broadband distribution shown in Figure 6.3(e).

Combining this observation of single fluctuation passes with their location, as described in paragraph 6.3.2, it is possible to make an estimate of the poloidal mode number $m$ in a similar way as was shown in [Boom11]. For such an estimate, it is assumed that the fluctuation continues to exist on the high field side, and that this is taken into account correctly by applying a straight field line angle correction. The calculation of the straight field line angle for the equilibrium and observation angle $\mathrm{d}\theta$ (shown in the left graph of Figure 6.5(b)) yields a ratio $\mathrm{d}\theta/\mathrm{d}\theta^*$ of approximately 3.69 for the flux surface at $\rho_{\mathrm{pol}} = 0.94$, which is where the fluctuation appears strongest (cf. Figure 6.4(b)). It is estimated from Figure 6.7(a) that 3-4 modes fit in the observation window of ECEI, and as a result the poloidal mode number $m$ is calculated to be $m = 100 \pm 20$. The rational $q$ flux surface nearest to $\rho_{\mathrm{pol}} = 0.94$ is 19/4, so that the toroidal mode number is estimated to be $n = 21 \pm 5$. Here, the error margins also include the assumption that the fluctuation could be located on a neighbouring rational flux surface.

When zooming out to the timescale of several milliseconds (Figure 6.7(c) and (d)), it becomes more difficult to follow individual $T_e$ fluctuations (Figure 6.7(c)). However, from the perspective of the fluctuation's amplitude dynamics (Figure 6.7(d)) it can be seen that there are subsequent periods of high and low amplitude on this larger timescale. This is most noticeably seen as the alternating darker and lighter areas in the time window between $t = 4.106$ s and 4.110 s (indicated by the red lines).

This is reminiscent of a beat wave resulting from the interference of two or more waves with marginally different frequencies. This would explain the periods of high fluctuation amplitude as phases where the two waves constructively interfere. When the two waves interfere destructively, that would result in periods of low amplitude. If that were the case here, and using the indicative (red) lines in Figure 6.7(d), the difference between the two frequencies would be about 1.4 kHz, i.e. the beat wave's frequency. This is not resolvable from spectra such as shown in Figure 6.3(e). At 0.5 km s$^{-1}$, the velocity with which this overall fluctuation passes by in front of ECEI is a factor of 10 slower than a single $T_e$ peak as shown in Figure 6.7(a) and (b). A single fluctuation will therefore pass through phases of maximum and minimum amplitude when moving from bottom to top through the ECEI observation window.

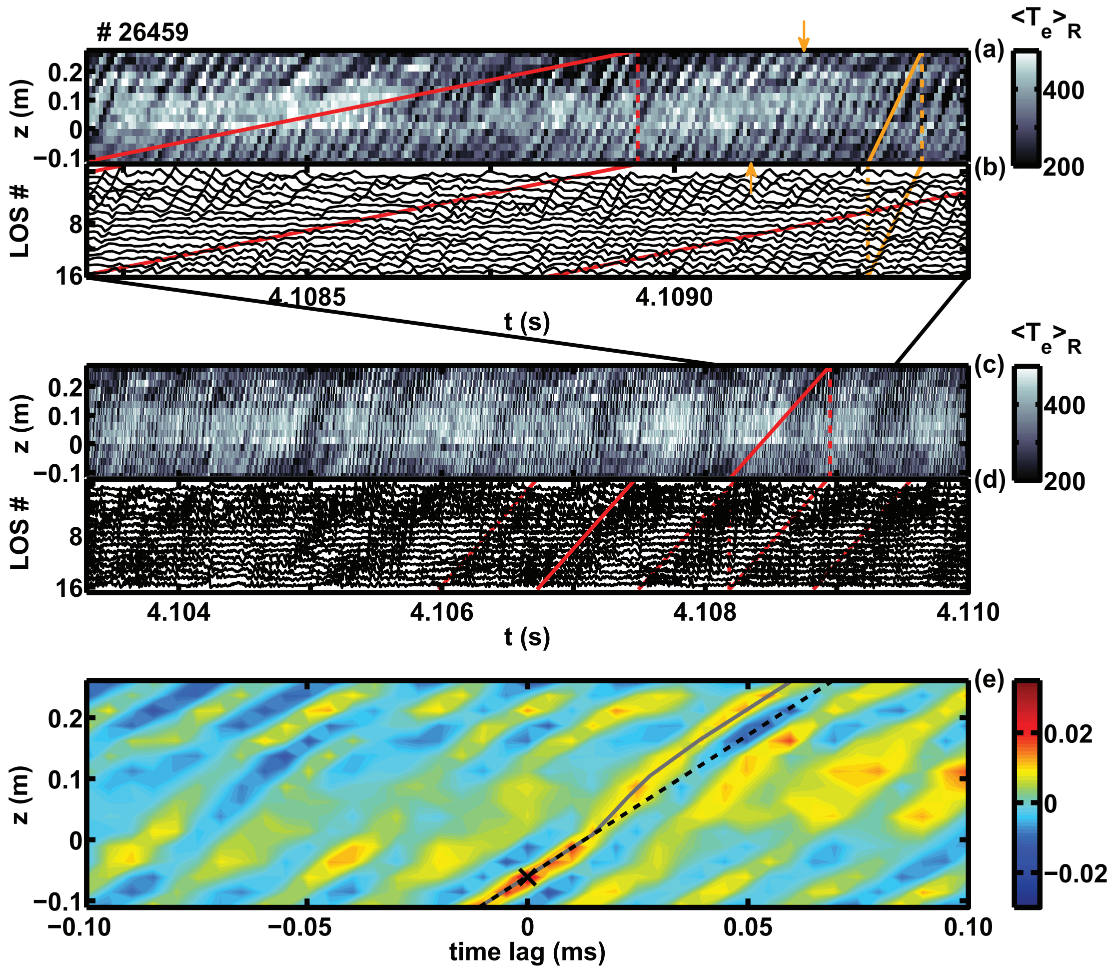


**Figure 6.7** *Propagation of $T_e$ fluctuations through the ECEI observation window during the type-II phase in #26459: in (a) and (c), the mean $T_e$ (averaged over the 8 radial channels per LOS) is shown as a function of time and vertical position. This allows following the propagation of the fluctuations in poloidal direction, i.e. from bottom to top. In (b) and (d), the $<T_e>_R$ is normalised and shown for all LOSs put underneath each other: this way, the amplitude dynamics of the fluctuations can be followed poloidally over several milliseconds. The propagation of single $T_e$ fluctuations is best seen in (a), as indicated by the orange lines on the right. Alternating periods of high and low amplitude (dark and light areas), reminiscent of a beat wave, are indicated by the red lines in (d). The velocity of the fluctuation passing by from bottom to top does not always appear constant, which gives an s-shaped curve as can e.g. be seen between the two arrows in (a). In (e), a contour plot is shown of the cross-correlation functions between a reference channel (at the height of X) and the other channels at different vertical positions. Here, the apparent varying velocity of the fluctuation is indicated by the s-shaped (grey) line.*

A further observation that can be made from fluctuation analysis on the small timescales is that the velocity of the fluctuation passing through the ECEI observation window does not always appear to be constant. The variation of the velocity follows an s-shaped curve: lower velocities at the top and/or bottom and higher over the mid-plane. This can be seen in Figure 6.7(a) between the two arrows. It is, however, most noticeably seen in Figure 6.7(e) where a contour plot is shown of the correlation functions of a reference ECEI channel with the other channels at different vertical positions. For this, the normalized signals from Figure 6.7(b) between $t = 4.1090$-$4.1095$ s have been used. The used reference channel is located at $z = -0.05$ m. In this contour plot, the apparent s-shaped variation of the fluctuation's velocity is indicated by the grey line. As stated before, the appearance of the broadband fluctuation is rather irregular when surveyed on the millisecond timescale. However, it seems that the s-shaped passage of single fluctuations is restricted to those phases where the apparent beat wave is destructively interfering on the midplane. If that were indeed the case, the s-shape could be explained for by a 180° phase jump over the region of the destructive interference. A single $T_e$ peak coming from below would then continue at a constant velocity as a valley after the phase jump (as suggested by the dashed line in Figure 6.7(e)).

## 6.4. Summary and conclusion

In this work, the properties of a broadband MHD fluctuation, typical for the type-II ELM regime, have been characterized using the full capabilities of the 2D ECEI diagnostic. Over the transition from the type-I to type-II ELM phase it is already seen that the amplitude of $T_e$ fluctuations forms a broadband peak in the frequency spectrum of one of the 128 ECEI channels. At the beginning of the transition, there is an increase in $T_e$ fluctuation amplitude over the whole observable frequency range. After that, when the type-II ELM regime is reached, the amplitude at low frequencies decreases again and a broadband peak of $T_e$ fluctuations in the 19-65 kHz range is formed.

It has been found that the relative amplitude of the fluctuation reaches a peak value of almost 20 % just inwards of the top of the $T_e$ pedestal in the type-II ELM regime. Simultaneously, the temperature profile flattens in this region. This indicates that the occurrence of the broadband fluctuation has a regulating function, affecting the top of the pedestal. Furthermore, the absence of type-I ELMs might suggest that the stability criteria for that type are particularly sensitive to this area of the ETB; the pedestal gradient was in fact found to be unaffected.

The 2D distribution of the fluctuation's amplitude confirms previous observations that, when averaged over a longer time window, a distinguished minimum occurs around the mid-plane. As is shown by the measurements in this paper, this division continues radially inwards. The nearby magnetic pickup coils also seem to measure a broadband fluctuation during the same time window, albeit with a maximum at lower frequency. However, an amplitude minimum was not found when applying the same analysis to these measurements. The differences between the spectra of ECEI and those of the pickup coils remain an open issue. The characteristic off-mid-plane distribution of the fluctuation's $T_e$ amplitude in the type-II phase is similar to what has been found before in pure type-I ELMy H-modes [Boom11]. There, a mode with high toroidal $n$ number and similar off-mid-plane characteristics was found to play a regulating role in the type-I ELM cycle: whenever this mode was present, it delayed the occurrence of the upcoming ELM crash for so-called 'slow' ELMs [Burckhart10].

Looking into the fluctuation on timescales where single $T_e$ dips and peaks can be followed passing through the ECEI observation window, it was found that the fluctuations rotate in the electron diamagnetic drift direction with a velocity of 5 km s$^{-1}$. From these observations, it is also possible to estimate the poloidal mode number, which yields a value of $m = 100 \pm 20$. From this, it follows that the toroidal mode number $n$ is $n = 21 \pm 5$. This high toroidal mode number suggests that the appearance of the broadband $T_e$ fluctuation is related to ballooning activity, which is indeed expected for type-II ELM plasma conditions [Saarelma09].

A novel point brought forward from the ECEI measurements, is the observation of an apparent beat wave with a low beat frequency. This beat wave might play a role in causing the observed amplitude minimum around the mid-plane. However, it cannot be the sole explanation since the beat wave passes multiple times during the longer time window from which the minimum in the 2D distribution of the fluctuation's amplitude became evident. On the other hand, beat waves could be an explanation for the s-shaped curve that is seemingly observed when single $T_e$ fluctuations pass by during a phase of destructive interference around the mid-plane. Observations of beat waves have been found before, e.g. as a precursor to type-I ELM crashes [Terry07].

One of the main requirements for obtaining type-II ELMs in AUG is high plasma edge collisionality, which is a regime that will not be easily achieved in ITER. However, the similarities between the broadband fluctuations described in this work and various precursors to type-I ELMs seen elsewhere are striking. This shows that studying type-II ELMs can indeed contribute to the general understanding of type-I ELM dynamics, particularly regarding the controlling role of instabilities just inwards of the pedestal top.

## Acknowledgement

This work, supported by the European Communities under the Contract of Association between EURATOM-FOM, was carried out within the framework of the European Fusion Program, with financial support from NWO, FOM and EURATOM. The views and opinions expressed herein do not necessarily reflect those of the European Commission.

# Chapter 7

# Influence of electron density fluctuations at the plasma edge

In this chapter, the effect of electron density fluctuations on ECEI measurements at the plasma edge is described. First, it is illustrated how density fluctuations at the pedestal top could affect ECEI measurements and how this could be a possible explanation for the observed off-mid-plane temperature fluctuations (described in Chapter 5 and Chapter 6). With the use of a ray tracing code on a 2D grid, the influence of various modelled density perturbations is determined for different ECEI channels.

## 7.1. Introduction

Because of the fast transport along magnetic field lines, it is generally the case that temperature and density are constant quantities on a flux surface. Therefore, from geometrical symmetry considerations, the mid-plane should not play a special role for any (poloidally) rotating fluctuation. However, temperature fluctuations have been observed in ECEI measurements of both type-I and type-II ELMs that are characterized by the fact that they are most strongly seen above and below the mid-plane. In case of the type-I ELM observations, the off-mid-plane fluctuation (as described in section 5.3.3) was found to be a distinguishing factor between the so-called ‘slow’ and ‘fast’ ELM cycles. For the broadband temperature fluctuation that characterises type-II ELMs, small amplitudes on the mid-plane (compared to large amplitudes above and below) were also found after time-averaging, see section 6.3.2.

In this chapter, the hypothesis is explored that the observed $T_e$ fluctuations are in fact caused by electron density fluctuations. Since the dominant component of the magnetic field is inversely proportional to the major radius, the position of the cold resonance basically is a vertical line at a given radius $R$ when observed in a poloidal cross section (as can e.g. be seen in Figure 7.2(a)). With regard to wave propagation, it was already mentioned in section 4.1.2, that a plasma refractive index $N$ between zero and unity causes bending of the wave’s propagation direction. Furthermore, from equations (4.4) and (4.5) it follows that the refractive index is inversely dependent on the electron density $n_e$. As can be seen in Figure 7.1(a), the cold resonance of the 2$^{nd}$ harmonic X mode comes close to the right-hand cut-off (equation (4.6)) near the plasma edge. Here, the equilibrium and profiles of the type-I ELMy H-mode described in Chapter 5 have been used; as also shown in Figure 7.1(b). Being so close to the cut-off condition, this means that a small increase in the electron density could cause a relatively large decrease in $N$, and hence a deflection of the beam from the ECEI antennas.

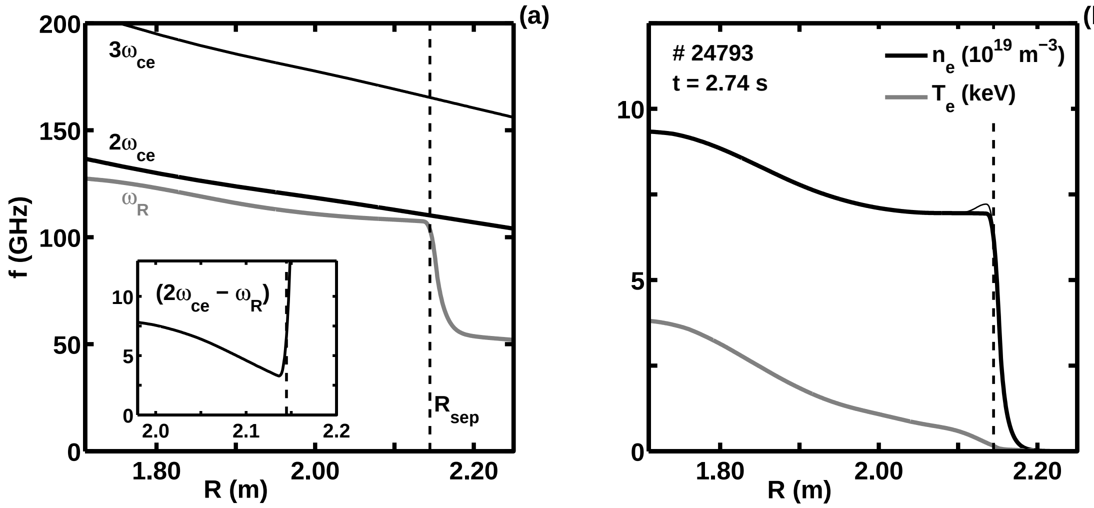


**Figure 7.1** *In (a), it is shown that the frequency of the 2nd harmonic cyclotron frequency comes closest to that of the right-hand cut-off at the pedestal top. The density profile, which strongly determines the shape of the cut-off, is shown in (b) with an* $n_{e,ped}$ *of* $6.95\times10^{19}$ $m^{-3}$. *As a first approach, a small density blob (here, 4 % of the local density) is modelled at the top of the pedestal for the ray tracing calculations described in section 7.3.*

The propagation of waves towards the ECEI antennas is here inversely treated as if they were a beam of EM waves injected from the antennas.

The electron temperature profile along the vertical line of the cold resonance has steep gradients above and below the mid-plane (as can e.g. be seen in Figure 7.3(b)). For the ECEI antennas, deflection of the beam could therefore result in the measurement originating from a different vertical position along the cold resonance chord. Since the plasma acts as a negative lens for $0 < N < 1$, the beams are deflected outwards. This means that the combined effect is twofold: first, the beams entering the plasma at the height of the mid-plane experience the smallest deflection (since they come in at a near perpendicular angle). Second, even if these central beams get deflected, the effect is small due to the shallow $T_e$ gradient along the resonance chord at this height. The opposite is the case for the upper and lower ECEI antennas: not only is the outward deflection largest for those beams, the steep $T_e$ gradient along the resonance could in addition cause the measured temperature to be considerably lower compared to that measured at the mid-plane.

## 7.2. Ray tracing on a 2D grid

In order to test the effect that density changes have on the beams of ECEI antennas, a ray tracing code has been adopted that works on a $(R, z)$-grid [Conway12]. This 2D ray tracing code first takes $B(R, z)$, $n_e(R, z)$, and $f_{ray}$ as input parameters and calculates the refractive index $N(R, z)$ using equations (4.1), (4.4), and (4.5). Next, as a starting point for the 2D code, a point is chosen on the $(R, z)$-grid that coincides with the principal ray calculated by the vacuum ray tracing code. The latter is normally used to determine the vertical position of the ECEI channels. Then, in an iterative loop, $\nabla N$ is calculated around each point which, combined with Snell's law, determines the direction of the new step. With decreasing $N$, the step size is accordingly adjusted so as to accurately approach the cut-off layer (where $N$ goes to zero).

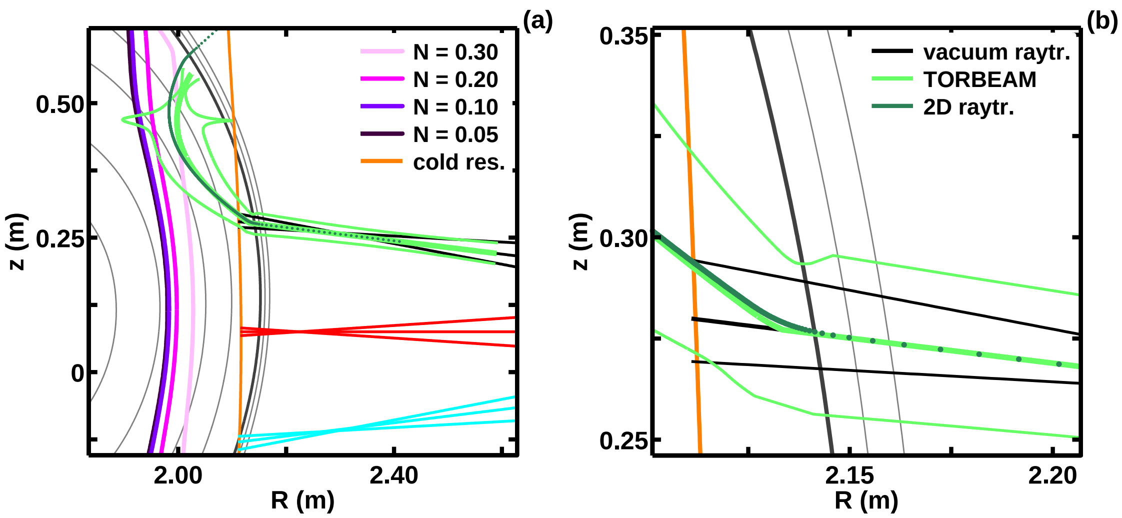


**Figure 7.2** *Different ray tracing methods for determining the vertical position of ECEI channels: in (a), the results of a ray tracing approach in vacuum is shown for the top, middle and bottom channel (black, red, and cyan). Here, for comparison, the results from TORBEAM and the 2D ray tracing code are overlaid for the top channel. In (b) it can be seen in closer detail that both TORBEAM and the 2D ray tracing code show an upward deflection of the upper ECEI beam, compared to the vacuum ray tracing code. This deflection results from the steep density gradient at the edge. The small difference between TORBEAM and the 2D code originates from the fact that TORBEAM takes too large a step across this steep gradient region.*

The main benefit of the 2D ray tracing code is that it can handle local density variations in ($R$, $z$) and therefore, indirectly, also deviations from smooth equilibrium shapes of flux-surfaces. For benchmarking, the 2D ray tracing code is compared to TORBEAM in the case without local density variations. TORBEAM calculates the propagation and absorption of a Gaussian wave beam in the GHz frequency range. It is a well-established code that is typically used to determine the deposition location of ECRH beams for arbitrary launching conditions on analytically or experimentally prescribed magnetic equilibria [Poli01]. However, TORBEAM takes only $n_e(\rho)$ as input (and calculates on smooth equilibrium flux surfaces) so it is not suited to investigate the influence of local $n_e$ perturbations.

In Figure 7.2(a), the results of the vacuum ray tracing approach are shown for top, middle and bottom ECEI channels. Here, $f_{ray} = 111.4$ GHz has been chosen, which is one of the frequencies of ECEI in 'edge' setting; the properties of which have been described in detail in section 4.3. For the top principal vacuum ray in Figure 7.2(a), the results from TORBEAM and the 2D ray tracing code are overlaid for comparison. Note that the results from TORBEAM indeed show the large Rayleigh length of the ECEI beams which assures that all eight channels are in focus (as mentioned in paragraph 4.2.1). In the detailed zoom of Figure 7.2(b), it can be seen that both TORBEAM and the 2D ray tracing code show the same upward deflection of the upper ECEI beam, compared to the vacuum ray tracing code. This deflection results from the steep density gradient at the edge. The small difference between the beam path of TORBEAM and that of the 2D code originates from the fact that TORBEAM takes too large a step across this steep gradient region. Apart from that, both codes reproduce the same result, and the 2D code can therefore confidently be used to address the problem of local $n_e$ perturbations.

## 7.3. Effects of density perturbations

### *7.3.1. Influence of a local density blob*

For a first approach, in order to investigate its influence on the ECEI rays, a local density blob has been modelled on top of the edge density pedestal (as already shown in Figure 7.1(b)).

The effect such a perturbation would have on the upper ray of ECEI is shown in Figure 7.3. Here, a density blob with a Gaussian FWHM of 3 cm is modelled at (R, z) = (2.12, 0.28) m. Its height is chosen as a percentage of the edge density pedestal top (which, at $\rho = 0.97$, has a value of $n_{e,ped} = 6.95\times10^{19}$ m$^{-3}$). In Figure 7.3(a), it is shown that the upper rays get more and more deflected upwards with increasing height of the density blob. For a local density increase of more than 6 %, a cut-off situation is encountered, where the beams do no longer reach the position of the cold resonance. For the used beam frequency, $f = 111.4$ GHz, the vertical temperature profile along the cold resonance chord is shown in Figure 7.3(b). Here, it can be seen that the intersection of the deflected beam with the resonance occurs for lower temperatures as the beam gets deflected more upwards with increasing density. In Figure 7.3(c), the relative temperature drop is shown as a function of the modelled density increase (compared to the temperature that would be measured in case the beam would have travelled straight through).

These first results show that large $T_e$ drops, such as e.g. observed in the off-mid-plane mode (Figure 5.7), could indeed be caused by a local density increase. However, it should also be noted that this occurs only in the small window of 99-100 % of the cut-off density (i.e. in a range of 5-6 % density increase as shown in Figure 7.3(c)): for larger local $n_e$ increases, the beam would get in cut-off directly on the density blob (i.e. reflected back along the incoming path). For a density increase smaller than 3 %, the maximum $T_e$ drop caused by beam deflection would be smaller than 10 %.

As a next step, a similar density blob as described above is rotated poloidally along its flux surface. This time, the deflection for both upper and central rays is also calculated for higher frequencies $f_{ray}$ in order to explore how far this effect extends further inwards. For this purpose, a local density increase of 5.80 % of $n_{e,ped}$ is chosen since that causes a large deflection. In Figure 7.4(a), the intersections of the upper and central ray of ECEI with the temperature profiles along the vertical resonance chords are shown for ECEI frequencies in the 111.4-119.7 GHz range. For all frequencies in this range, it can be seen here that the temperature variation, caused by the deflection, is indeed much larger for the upper channels than for the central channels. In Figure 7.4(b), the relative amplitude of this variation is shown as a function of major radius ($R$). As can be seen here, the $T_e$ variation that would be observed on central ECEI channels stays below 3 % at all radii. However, the temperature variation for the upper channels reaches values above 20 % at the plasma edge, but this then rapidly decreases to about 5 % for the inner upper channels.

In Chapter 6, it was shown that the amplitude distribution of the broadband mode observed during type-II ELMs extends further inwards. This is the reason that the

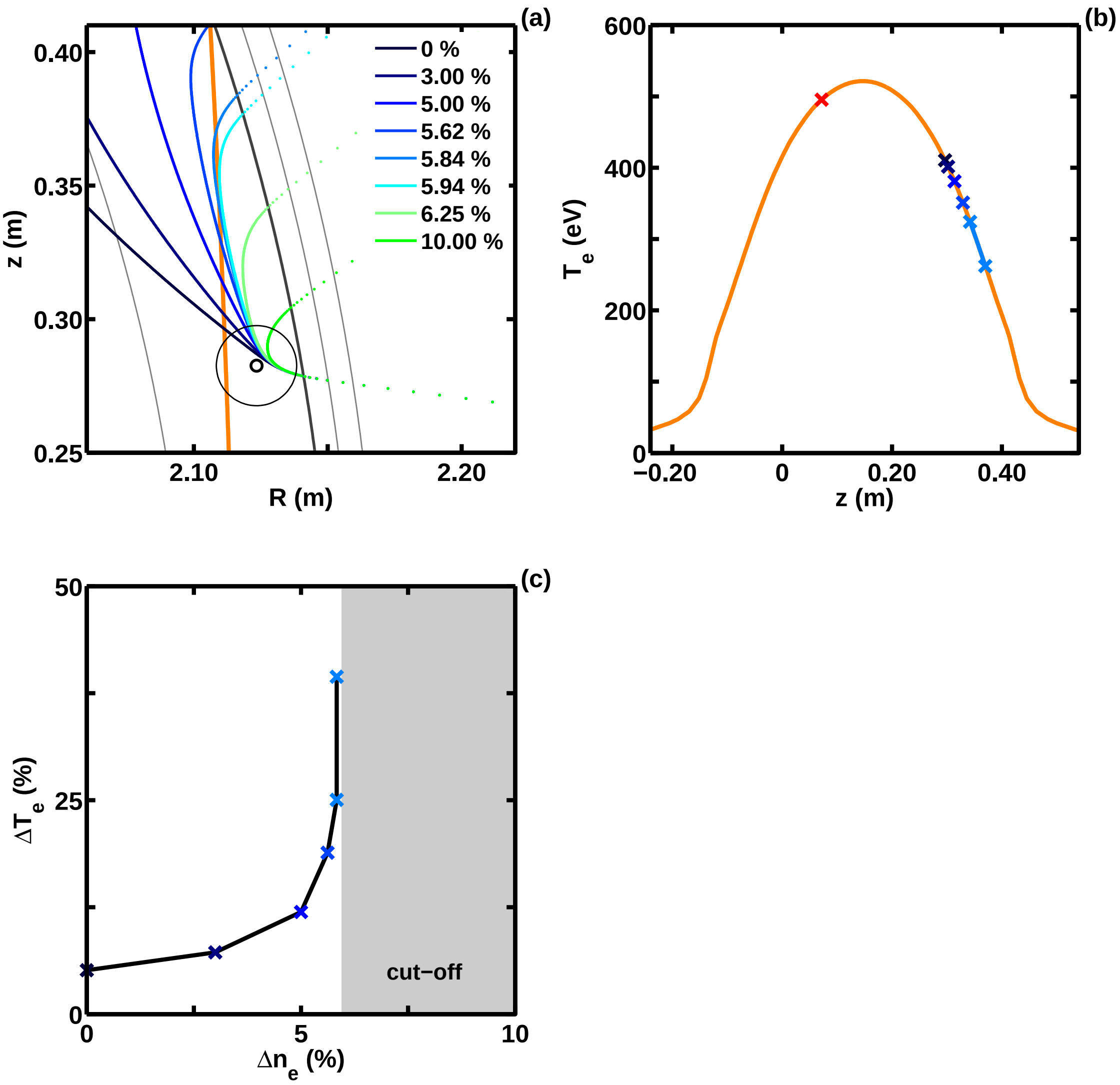


**Figure 7.3** *Beam deflection on a modelled local blob of increased density: in (a), various beam traces are shown for different heights of a blob at (R, z) = (2.12, 0.28) m. Here, its height is determined as a percentage of the density at the pedestal top, which is $6.95\times10^{19}$ $m^{-3}$ at $\rho = 0.97$. The vertical temperature profile along the cold resonance chord is shown in (b). Here, the intersections of the various deflected beams are indicated; note that the deflected beam does not reach a resonance for density blobs with a height above 5.94%. For comparison, the intersection from the centre LOS is indicated by the red cross. In (c), it is shown that large $T_e$ drops are only observed if the density blob has an intensity of 5-6 %. For $\Delta n_e = 0$ %, the $\Delta T_e$ of 5 % results from the difference with the vacuum ray which intersects in a straight path with the resonance chord (see Figure 7.2(b)).*

results obtained there are included in Figure 7.4(b) for comparison. Note that with a pedestal top density of $n_{e,\mathrm{ped}} = 6.85\times10^{19}$ $\mathrm{m}^{-3}$ (as determined from IDA), the type-II profile is comparable to the profile used in the ray tracing (cf. Figure 7.1). As can be seen, the measured $T_e$ variations show amplitudes in the same ballpark as those that would have been caused by the modelled density perturbation. However, there are two major differences: first, the $T_e$ variation measured by the central LOS increases from below 5 % to above 12 % towards the edge, which is not the case for the $T_e$ variation caused by the density blob. Secondly, for the upper channels, both the measured $T_e$

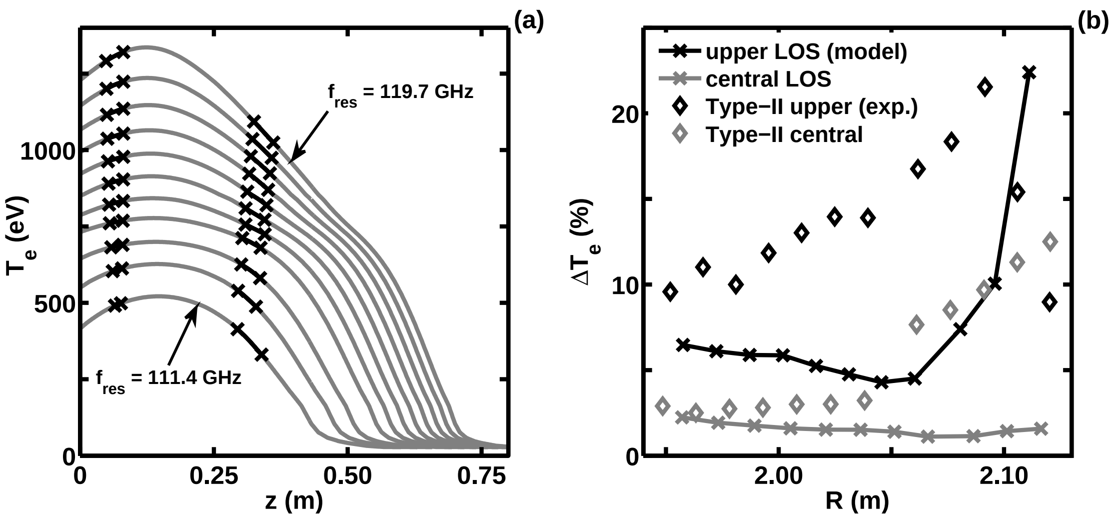


**Figure 7.4** *Beam deflection caused by a modelled rotating density blob at the plasma edge: in (a), the intersections of the upper and central rays of ECEI with the cold resonance chord are shown for different $f_{ray}$ frequencies. The resulting temperature variations are plotted as a function of radius in (b). Here, the amplitude of $T_e$ fluctuations measured during type-II ELMs is shown for comparison.*

fluctuation and that due to the passing density perturbation peak at a level of about 23 % at the edge. However, the amplitude decrease towards the plasma centre is much steeper for the modelled case of the passing density blob then for the measurement of the broadband mode. In the latter case, a minimum $T_e$ fluctuation of 5 % is reached already at 2.05 m which then even increases again towards the centre due to the increased $T_e$ gradient along the profile (as can also be seen in Figure 7.4(a)). The amplitude of $T_e$ fluctuations measured in the type-II ELM broadband mode falls off almost linearly and reaches values below 10 % at radii below about 1.95 m.

From Figure 7.4(b) it can be concluded that the effect of a local density blob at the edge does not extend considerably further inwards. This means that small passing edge density blobs cannot explain for the fact that broadband type-II $T_e$ fluctuations display an off-mid-plane distribution that also extends deeper into the plasma.

### *7.3.2. Rotating flux surface deformations*

Although local density blobs have been observed in AUG experiments, they were almost always located in the steep gradient region, or even outside the separatrix [Kurzan07]. Due to the fast equilibration on closed flux surfaces, local density blobs are actually not to be expected deeper inside the plasma. Therefore, as a second approach, the effect of a deformation of the outer flux surfaces on the rays of ECEI is investigated. For this purpose, a simple flux surface deformation is constructed in the style of a ballooning mode. This is done by adding a deviation $u$ to the minor radius $r$ of each angle $0 < \theta < 2\pi$ of a flux surface contour in the poloidal plane:

$$\begin{pmatrix} R \\ z \end{pmatrix} = \begin{pmatrix} R_{ax} \\ z_{ax} \end{pmatrix} + r(1+u)\cdot\begin{pmatrix} \cos(\theta) \\ \sin(\theta) \end{pmatrix} . \quad (7.1)$$

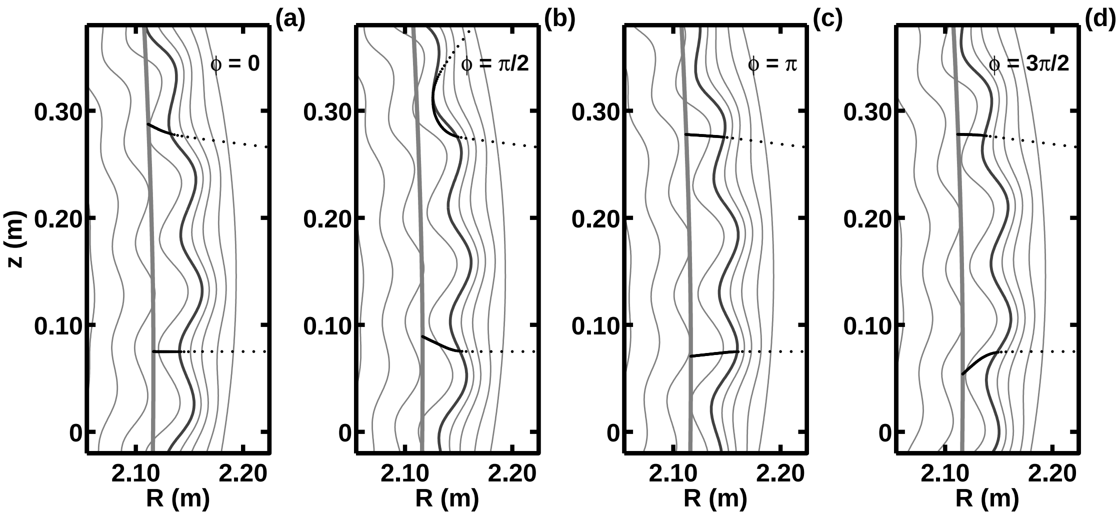


**Figure 7.5** *Beam tracing results for upper and central ECEI rays (of $f_{ray}$ = 111.4 GHz) in case of a ballooning-like flux surface perturbation at the edge. From (a) to (d), the phase $\varphi$ (equation (7.2)) has been varied. For these calculations, the unperturbed $n_e$ profile shown in Figure 7.1 has been used, but with an overall decrease of 15 % so as to have a $n_{e,ped}$ of $6.0\times10^{19}$ $m^{-3}$. The latter is necessary to prevent the central beam from not reaching the cold resonance.*

Here, $(R, z)_{ax}$ are the coordinates of the magnetic axis and $\theta$ is the poloidal angle, which is defined to be equal to zero at the outer mid-plane. The deviation $u$ is defined as:

$$u = A(a,\theta)\cdot\sin\left(m\theta^{*}-\varphi\right) \; ;$$
$$A(a,\theta) = a(\rho)\left[e^{-\frac{\theta^2}{2c^2}} + e^{-\frac{(\theta-2\pi)^2}{2c^2}}\right]. \tag{7.2}$$

In equation (7.2), $m$ is the poloidal mode number which is taken to be 110 (as derived for the off-mid-plane mode described in Chapter 5), $\theta^*$ is the straight field line angle belonging to each poloidal angle $\theta$ (cf. Figure 5.8), and $\varphi$ is an offset for the perturbation's phase at the mid-plane. In order to obtain the ballooning character for the perturbation (i.e. largest amplitude on the LFS mid-plane), the amplitude $A(a, \theta)$ of $u$ is constructed with $a(\rho)$, which determines the displacement at the mid-plane, and two exponentials that create a Gaussian envelope over $u$. Here, $a(\rho)$ is chosen such that the displacement is 1.5 cm for the flux surface at $\rho = 0.97$ (as before in paragraph 7.3.1) and falls off linearly to zero at $\rho = 0.85$ and 1.05. Finally, the constant $c$ in the exponentials is chosen such that the FWHM of the Gaussian envelope is equal to $2\pi/3$.

For the case of a rotating flux surface perturbation as described above, the results from the 2D beam tracing are shown in Figure 7.5. From Figure 7.5(a) to (d), the offset angle $\varphi$ (equation (7.2)) is varied and the intersection with the cold resonance of $f_{ray}$ = 111.4 GHz has been calculated for both upper and central ECEI rays. For these calculations, the unperturbed experimental $n_e$ profile shown in Figure 7.1 has been used. However, in order to prevent the central beam from reaching cut-off conditions

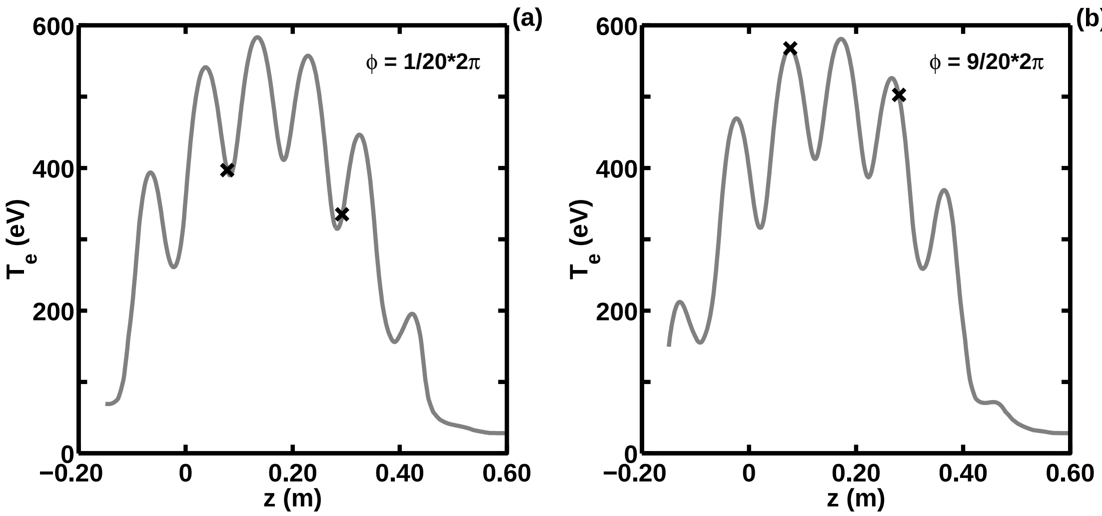


**Figure 7.6** *Temperature profiles along the vertical resonance chord in case of a rotating flux surface perturbation: in (a) and (b) the intersection of both the upper (around z = 0.30 m) and central (around z = 0.10 m) ECEI beam with the 111.4 GHz resonance chord are shown for two different phases $\varphi$. Due to the variation of the temperature profile along the resonance, $T_e$ variations of more than ±20 % compared to the unperturbed profile could be detected for both the upper and central rays.*

(which was not observed in the measurements of Chapter 5) it was necessary to lower this profile by 15 % overall to have an $n_{e,ped}$ of $6.0\times10^{19}$ m$^{-3}$.

In case of the rotating perturbed flux surfaces, the bending of the ECEI rays is not only caused by the fact that the local density now varies with the offset angle $\varphi$. The angle of the beam's deflection is also dependent on the angle between the local $\nabla N$ and the incoming beam, which varies with $\varphi$ as well. As a result of this, not only the upper ECEI ray, but also the beam on the mid-plane is deflected both up- and downwards as can be seen in Figure 7.5(b) and (d). In Figure 7.5(b) it can in addition be seen that the deflection of the upper beam, due to this combined effect, is so strong that the resonance chord is not reached at all. Furthermore, due to the flux surface deformation, the temperature profile along the vertical resonance chord no longer has a parabolic shape. As can be seen in Figure 7.6, $T_e$ variations of more than ±20 % compared to the unperturbed profile (shown in Figure 7.3(b)) could be possible for both the upper and central rays.

### *7.3.3. Observations at lower pedestal density*

In paragraph 7.3.1, it was shown that a local density blob near the plasma edge could indeed bend the rays of ECEI in such a way that the off-mid-plane channels would be affected the strongest. As was shown there, the main cause for the effect would be the closeness of the pedestal top density to the ECE cut-off condition. At the same time, this means that the effect should not play a role for cases where the pedestal top density is much lower.

For obtaining type-I ELMs in a discharge, the input power $P_{NBI}$ has to be high. Simultaneously, this means that the temperature in the divertor will be high, which requires active cooling measures. There are two approaches for keeping the divertor temperature low: first, increasing the radiation in front of the divertor by increasing the

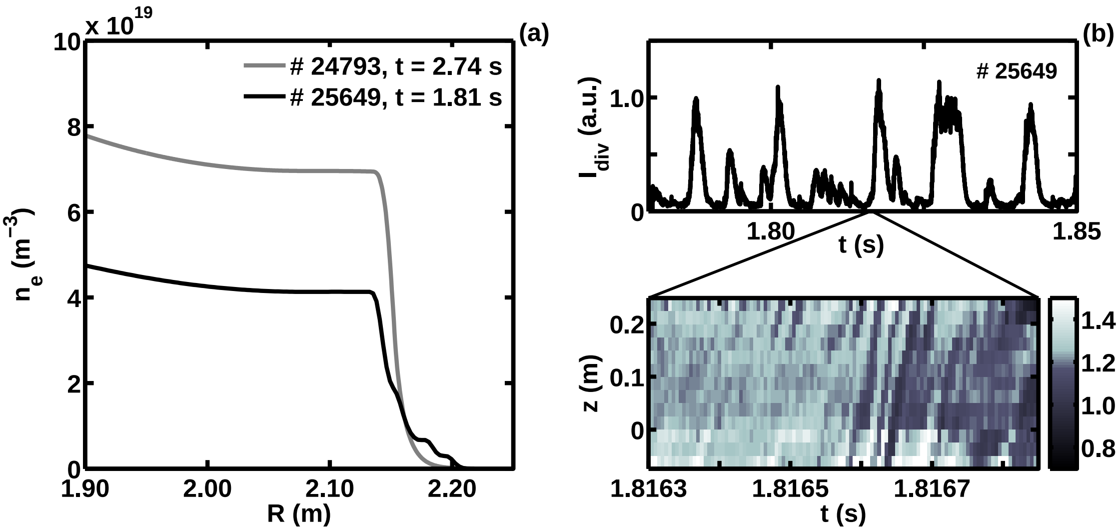


**Figure 7.7** *ECEI measurements in case of lower pedestal top density: in (a), the density profile of discharge # 25649 is shown in comparison with the density profile used for the modelling of paragraph 7.3.1 (cf. Figure 7.1). Both density profiles have been obtained using the IDA method, which gives a pedestal top density of $n_{e,ped} = 4.13\times10^{19}$ m$^{-3}$ for discharge # 25649. A time trace of the divertor thermo-current is shown in (b) as an indicator for the occurrence of type-I ELM crashes. In the lower panel of (b), an overview of the ECEI measurement of the crash around t = 1.81 s is shown in a similar way as in Chapter 5 and Chapter 6. As can be clearly seen here around t = 1.8165 s, the upper four LOSs show $T_e$ drops that are not seen in the central or lower LOSs. These temperature drops occur before the ELM onset fluctuations between t = 1.8166-1.8167 s and therefore seem of identical nature as the off-mid-plane mode observed for type-I ELMs (cf. Figure 5.6).*

fuelling (D). A second technique that is often applied is so-called nitrogen ($N_2$) seeding, which has been found to cool the divertor (also by increased radiation) and at the same time increase the ELM frequency [Gruber09b]. Usually, a mixed scheme is applied since the impurity content of the plasma increases when too much $N_2$ is used, which is prevented by including D in the fuelling mix. However, either approach leads to high pedestal top density values. This makes it difficult to find a discharge that has considerably lower $n_{\mathrm{e,ped}}$ but for the rest similar discharge parameters $I_{\mathrm{p}}$, $B_{\mathrm{t}}$, $P_{\mathrm{NBI}}$, $f_{\mathrm{ELM}}$, etc. to the discharge described in Chapter 5 in order to have comparable ELM cycles. A quantitative relation between gas puffing rates (and plasma shape and wall material) and the height of the edge density pedestal is not easily given [Kallenbach02]. However, as follows from a regression analysis of many discharges, the height of the pedestal density is in rough estimate determined by $I_{\mathrm{p}}$ and $B_{\mathrm{t}}$ [Schneider12]:

$$n_{\mathrm{e,ped}} \sim I_{\mathrm{p}}^{0.8\pm0.1} B_{\mathrm{t}}^{0.5\pm0.2} \quad . \tag{7.3}$$

Keeping $B_{\mathrm{t}}$ constant (at −2.5 T), because that too determines the cut-off value, this means that comparable discharges with lower pedestal densities are found at lower plasma current. In Figure 7.7(a), the density profile of such a discharge is shown. As can be seen there, for discharge # 25649 the pedestal top density had a value of $n_{\mathrm{e,ped}} = 4.13\times10^{19}$ m$^{-3}$ at a plasma current of $I_{\mathrm{p}} = 0.6$ MA. For comparison, the density profile from discharge # 24793 at $I_{\mathrm{p}} = 1.0$ MA is shown once more. Furthermore, it should be noted that the input power was $P_{NBI}$ = 5 MW in # 25649, which is lower than the 7 MW used in # 24793. However, this was still enough to bring the discharge in type-I ELMy H-mode regime. This can be seen in the upper panel of Figure 7.7(b), where the thermo-current in the outer divertor is shown as an indicator for the occurrence of ELMs. With a delay of more than 16 ms after the previous ELM, i.e. an ELM frequency of 61 Hz, the crash that occurs around $t$ = 1.81 s can be considered ‘slow’ in the terminology introduced in paragraph 5.3.1.

In the lower panel of Figure 7.7(b), an overview is given of the ECEI measurement of this crash. Here, in a similar way as used in Chapter 5 and Chapter 6, a radial average of the $T_e$ perturbation in the outer channels (covering a range of $\rho$ = 0.95-1.01) is shown for all vertical channels. Clearly seen in the time window of $t$ = 1.8166-1.8167 s is the ELM onset mode, which has $T_e$ perturbations covering the whole ECEI frame and which is rotating in the upward direction as described in paragraph 5.3.4. Most noticeable, however, are the $T_e$ drops that are seen to appear at $t$ = 1.8165 s in the upper four channels. Their occurrence before the ELM onset mode, the fact that they seem to disappear again, and their absence on the central (and lower) ECEI channels are in strong agreement with the phenomenology of the off-mid-plane fluctuation observed in type-I ELMy H-modes (as e.g. shown in Figure 5.6 and Figure 5.7).

## 7.4. Summary and conclusion

At the beginning of this chapter, the suggestion has been introduced that the off-mid-plane $T_e$ fluctuations (as observed in the type-I and -II ELMy H-modes described in Chapter 5 and Chapter 6) could in fact be caused by electron density fluctuations. Since the density at the top of the edge pedestal has a value that is already close to the right-hand cut-off, a small density increase could cause a large decrease of the refractive index, which would result in a large deflection of the ECEI lines of sight. For the off-mid-plane channels, this mechanism would affect in two ways: first, the outward deflection for those lines of sight would be largest and, in addition, the steep $T_e$ gradient along the resonance could cause the measured temperatures to be considerably lower compared to what is measured at the mid-plane.

In order to test this mechanism, a 2D ray tracing code has been applied that inversely treats the propagation of waves towards the ECEI antennas as if they were a beam of EM waves injected from the antennas. Starting from a point on the principal ray outside the plasma (where $N \sim 1$), $\nabla N$ is calculated around each point so that after applying Snell’s law the propagation direction is known. For a case of unperturbed plasma conditions, TORBEAM and the 2D code were compared from which it was concluded that the latter can be used with confidence for testing the influence of local $n_e$ perturbations.

Using the 2D code, it is first shown that a local density blob on top of the edge pedestal, and in the ray of an upper ECEI channel, can indeed cause the beam to be deflected. However, deflections that cause electron temperature drops of the magnitudes observed in type-I and -II ELMy H-modes (i.e. $T_e$ drops of more than 20 %) are only observed in a small range of local density increase. For the used density profile (taken from the experiment), it was found that the maximum deflection occurred in the small window of 99-100 % of the cut-off density (i.e. for increases of 5-6% of the pedestal top density): larger increases would logically result in direct cut-off on the modelled $n_e$ blobs, and increases below 3% would not cause large enough beam deflections. Density fluctuations of 3-5 % are, however, not unrealistic and could e.g. be observed by the lithium beam diagnostic which is even located in the same sector as ECEI (see paragraph 3.3.2).

As a next step, a modelled density blob is rotated poloidally along its flux surface, passing both a central and an upper ECEI beam. Here, the same experimental density profile has been used in combination with a local $n_e$ blob of a height that does cause a large deflection. For all ECEI frequencies in the 111.4-119.7 GHz range, it has been shown that the $T_e$ variation, caused by the deflection, is indeed much larger for the upper than for the central channels. However, when examining how far deeper in the plasma the beam deviation affects the $T_e$ variation, it was found that the effect due the passing density blob decreases much faster than e.g. observed during the broadband $T_e$ fluctuation of type-II ELMs.

For the last application of the 2D ray tracing code, a poloidally rotating flux surface deformation in the style of a ballooning mode was constructed. Here, it was found that not only the upper ECEI ray, but now also the beam on the mid-plane is deflected both up- and downwards due to varying angle between the local $\nabla N$ and the incoming beam. Furthermore, due to the flux surface deformation, the temperature profile along the vertical resonance chord no longer has a parabolic shape. This means that the deflection of beams on the mid-plane also results in $T_e$ variations in the order of 20 %.

Finally, an example has been shown of ECEI measurements of type-I ELMs in a discharge comparable to the one presented in Chapter 5, but at a 40 % lower edge pedestal density. In this discharge, in the period leading up to a ‘slow’ ELM crash, a $T_e$ fluctuation has been measured that has features similar to the off-mid-plane mode described in Chapter 5.

The overall conclusion, to the hypothesis that the observed $T_e$ fluctuations are in fact caused by density fluctuations, is that $n_e$ fluctuations alone can not be the sole explanation. Although the modelling of density blobs at the pedestal top supports the proposed mechanism for the off-mid-plane $T_e$ fluctuation in a small $n_e$ perturbation range, the effect is not visible as deep into the plasma as e.g. the type-II broadband fluctuations. When modelling edge density perturbation in the shape of a ballooning mode, as an alternative to local $n_e$ blobs in the plasma, it was found that $T_e$ fluctuations would also appear on the mid-plane which is in contradiction to the measurement. Here, it was however necessary to assume a density profile with a much lower pedestal top value in order to avoid direct cut-off of the central ECEI beam. This makes it somewhat more difficult to put the modelling results in perspective to the measurements.

Finally, it is important to note that off-mid-plane fluctuations have been found in ECEI measurements, even in discharges where the edge pedestal density is far from the cut-off condition.

# Chapter 8

# Mitigation of type-I ELMs with the use of magnetic perturbations

In this chapter, the observations of ECE-imaging are described for conditions in which mitigation of type-I ELMs occurs with the use of magnetic perturbations. In the first section, an introduction is given on the application of magnetic perturbations and it is also described how type-I ELM mitigation is achieved in an AUG discharge. In the phase of mitigated type-I ELMs, small ELMs remain; a characterization of them is given in the second section. Analysing the ELM frequencies of both the type-I and small ELMs over the transition to this phase, the hypothesis is tested that the activation of the perturbation coils acts in such a way that it suppresses type-I ELMs and so makes room for small ELMs. Finally, for comparison, an overview is presented of the type-III ELMs observed just after the L-H transition.

## 8.1. Introduction

To avoid intolerable erosion of divertor target plates while simultaneously taking advantage of the benefits from H-mode operation, it is necessary for future tokamaks to mitigate or even completely suppress (large) ELMs. On several tokamaks, it has been demonstrated that the application of non-axisymmetric perturbations of the magnetic field has various effects on the plasma. Early on, an influence of resonant magnetic perturbations (MPs) on magnetic islands has e.g. been found in COMPASS-D [Hender92]. Later, mitigating effects on ELMs have been found in other tokamaks. In JET, for example, external coils normally used for error field correction have been used instead for applying $n = 1$ or $n = 2$ perturbation fields, which resulted in a reduction of ELM losses [Liang10]. In DIII-D, a tokamak of comparable size to AUG, complete ELM suppression at low edge collisionality has been achieved using resonant perturbations [Evans04]. At high collisionality, and with non-resonant MPs, ELM mitigation could be shown as well [Evans05].

In order to contribute to the diversity of the experimental results and to enhance the understanding of the physical principles that underly ELM suppression, AUG has recently been equipped with a set of in-vessel saddle coils (as described in paragraph 3.4.1.) [Suttrop09]. With the first set of installed coils (four upper and four lower ones), it was possible to create $n = 2$ MPs. Here, the upper and lower coils having the same or opposite polarity is referred to as even or odd parity (with the option of 0° or 90° toroidal orientation for the latter). For a given magnetic equilibrium, i.e. $q_{95}$-value, one of the two parities will be resonant with the magnetic field lines (the

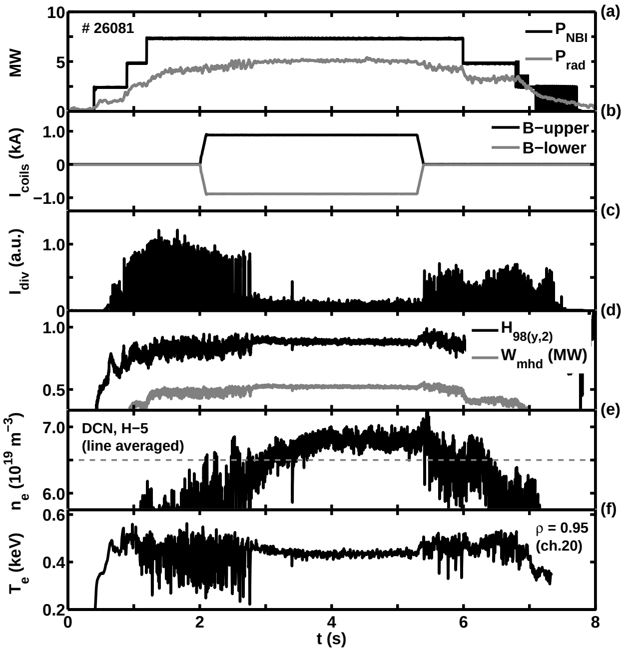


**Figure 8.1** *Mitigation of type-I ELMs in an AUG H-mode discharge (# 26081): in (a), the NBI input and radiated power is shown and, in (b), the currents in the upper and lower magnetic perturbation (B-) coils. From the time trace of the divertor thermo-current, (c), it can be seen that the large spikes due to type-I ELMs disappear from $t = 2.80$ s onward (and return again at the switch off of the coils). This is the phase of ELM mitigation. In this phase, as is shown in (d), the $H_{98(y,2)}$-factor and the plasma stored energy remain at the same level as before in the type-I ELM phase. The time traces of edge (electron) density and temperature are shown in (e) and (f). The minimum line-averaged edge density required for ELM mitigation ($n_e = 6.5\times10^{19}$ m$^{-3}$) is indicated by the dashed line in (e).*

other will be non-resonant). As is shown in [Suttrop11a] and [Suttrop11b], mitigation of type-I ELMs in high density plasmas is indeed also achieved in AUG. A remarkable observation is that, at high collisionality, the resonance condition does not seem to be so strict (also seen on DIII-D, [Osborne05]), and mitigation is achieved during MP application in both odd and even parity. Furthermore, access to the regime of mitigated type-I ELMs does not seem to depend on the plasma rotation. Instead, it was empirically found that there is a density threshold above which type-I ELMs are completely suppressed and only small events can still be seen (with reduced plasma energy loss and divertor power loads).

In Figure 8.1, an overview is shown of a discharge (# 26081) in which mitigation of type-I ELMs was achieved. The discharge has a magnetic field of $B_t = -2.5$ T, a plasma current of $I_p = 0.8$ MA, and an edge $q$-value of $q_{95} = 5.7$. For this equilibrium, the n = 2 odd parity coil configuration (at 0° toroidal orientation) is resonant. The used coil current is $I_{B\text{-coil}} = 900$ A, switched on at $t = 2.1$-$5.4$ s (see Figure 8.1(b)). The input powers are $P_{NBI} = 7.4$ MW from neutral beam heating and $P_{ECRH} = 1.8$ MW central deposition. The deuterium gas puff rate was at a constant level of $9\times10^{21}$ s$^{-1}$. From the divertor thermo-currents, Figure 8.1(c), it can be seen that the type-I ELMs disappear from $t = 2.8$ s untill the switch off of the coils at $t = 5.4$ s. This is the phase of ELM mitigation. In this phase, the $H_{98(y,2)}$-factor and the plasma stored energy remain at the same level as before in the type-I ELM phase (Figure 8.1(d)). The time traces of edge (electron) density and temperature, Figure 8.1(e) and (f), show strongly reduced levels of $T_e$ and $n_e$ fluctuations during the phase of ELM mitigation. The minimum line-averaged edge density required for ELM mitigation, $\bar{n}_e = 6.5\times10^{19}$ m$^{-3}$ (for this $I_p$), is indicated by the dashed line in Figure 8.1(e). From analysis of the $n_e$ and $T_e$ profiles in discharge # 26081, it was found that differences between the MP and non-MP phase are small and can mainly be attributed to non-axisymmetric, three-dimensional deformation of the magnetic equilibrium [Fischer11], [Fischer12].

## 8.2. Mitigation of type-I ELMs

### *8.2.1. Observations from ECEI during the absence of type-I ELMs*

The ECEI measurements during the discharge shown in Figure 8.1 were obtained in 'edge' setting: for the magnetic field of $B_t = -2.5$ T, $f_{BWO}$ was chosen 105 GHz so that the radial range of the observation window covered both the plasma edge and a part of the SOL (i.e. a normalized flux surface range of $\rho = 0.90$-$1.10$, cf. Figure 5.2 and/or Figure 6.2). The sampling rate was set to 200 kHz, covering the entire length of the discharge at this rate. For the representation of the ECEI measurements, radial averaging as also used in Chapter 5 and Chapter 6 (e.g. Figure 5.6, or Figure 6.7) has been applied.

In Figure 8.2, the ECEI observations during the phase of mitigated type-I ELMs are shown, combined with the measurements from the divertor thermo-current $I_{div}$. Here, the ($T_e$) fluctuations seen in the absence of type-I ELMs are dubbed 'small ELMs'. For comparison, in Figure 8.2(a), $I_{div}$ is shown in the time window just after the switch on of the MPs, where both large type-I ELMs and the small ELMs are present (the crosses denote the time instants where ELMs are observed). As can be seen here, the $I_{div}$ peak height of the small ELMs is at most half of that observed for the type-I ELMs. In Figure 8.2(b), the radially averaged $T_e$ fluctuations (from ECEI) during a few small ELMs are shown, with $I_{div}$ on top for direct comparison. A zoom into a typical example of such a small ELM is shown in Figure 8.2(c). Note that this small ELM was not detected as a spike in the divertor current (Figure 8.2(b)). This is commonly observed and can e.g. already be seen in Figure 8.2(a) between $t = 2.55$-$2.56$ s. In Figure 8.2(d), a second example of a small ELM is shown. In this example, after a few passes of the mode in upward direction, two filaments can be seen which rotate in the downward direction.

For the small ELMs, the velocity with which the $T_e$ fluctuations pass through the ECEI observation window is of the order of 5-8 km s$^{-1}$. Per small ELM, there are normally not more than 5-15 passes of $T_e$ fluctuations and the duration of the ELM is about half a millisecond. For the example shown in Figure 8.2(c), it is estimated that the mode is located around $\rho = 0.96$. From the same figure, it is also estimated that about two modes fit in the observation window of ECEI (i.e. a poloidal wavelength of about 20 cm). Using the same approach as described in paragraphs 5.3.3 and 6.3.3, it is possible to approximate the poloidal mode number from these two estimates. The calculation of the straight field line angle yields a ration of $d\theta/d\theta^* = 4.34$ for the flux surface at $\rho = 0.96$ and the observation angle covered by the ECEI window. This rough estimate results in a poloidal mode number $m$ of the order of 90. With a $q$-value of 5.5 for this flux surface, the corresponding toroidal mode number is of the order of $n \sim 17$.

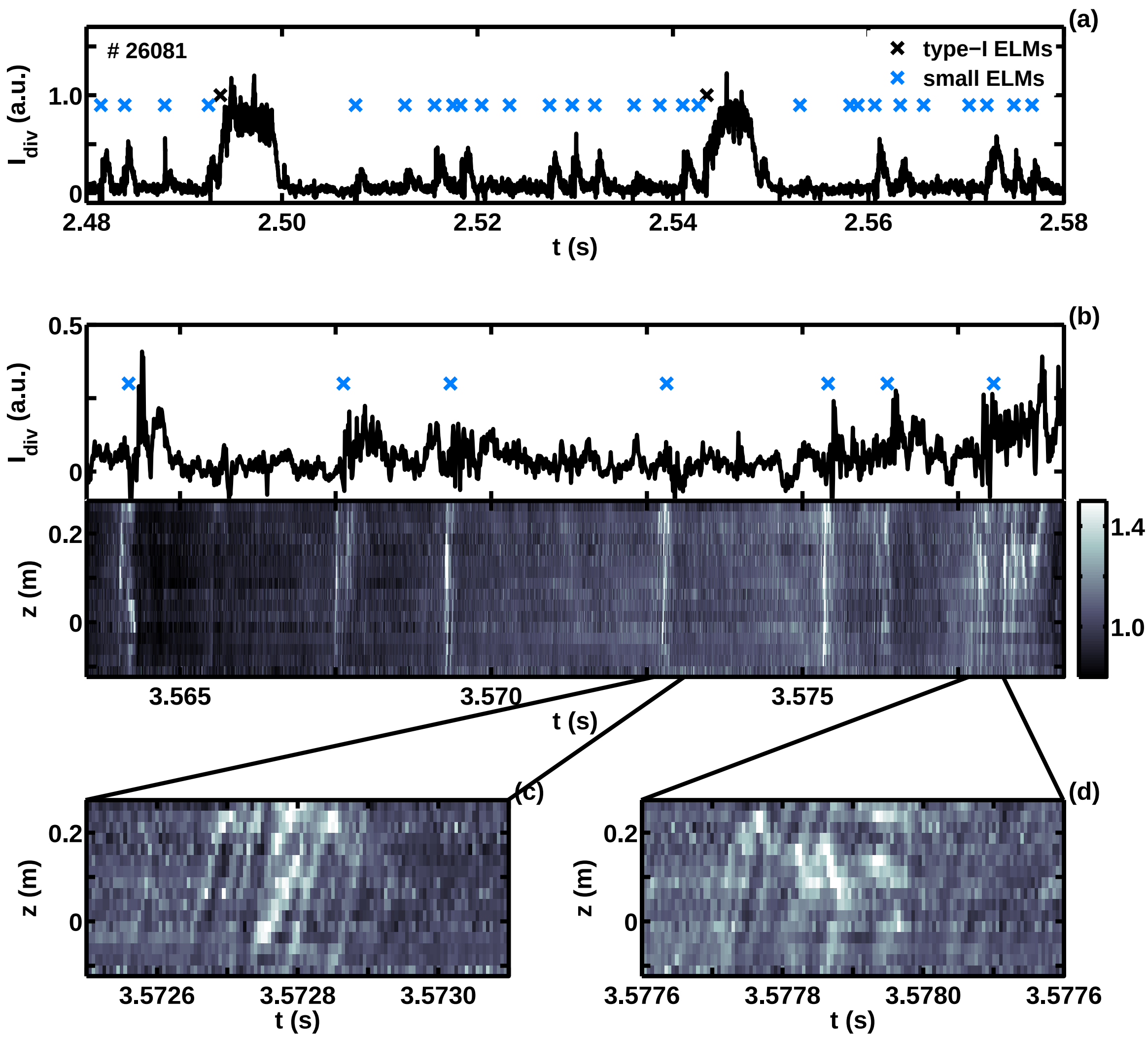


**Figure 8.2** *Overview of ECEI observations combined with the divertor thermo-current measurements during application of MPs. The time trace in (a) shows the different impacts on the divertor thermo-current for large type-I ELMs (black crosses) and the intermittent small ELMs (blue crosses). In (b), fluctuations of the mean $T_e$ (radially averaged over all eight channels) in the absence of type-I ELMs are shown. A zoom into a typical example of such a small ELM is shown in (c). Note from the comparison in (b), that these ELMs are not always detected as spikes in the divertor current. In (d), a second example of a small ELM is shown, where filaments can be seen to rotate in the downward direction.*

### *8.2.2. Frequency behaviour during transition*

With the characterization of the small ELMs as given in the previous paragraph, it is now possible to identify their occurrence from the combined study of the ECEI and $I_{div}$ measurements. In Figure 8.3, the frequency behaviour of both the small ELMs and type-I ELMs is shown from about one second before the application of the MPs until about half a second after switch off. In Figure 8.3(a), the frequency is displayed as the number of ELMs per 100 ms. As can remarkably be seen here, small ELMs are already detected before the MPs are switched on, albeit only in low numbers. The moment the coils are switched on, the frequency of the small ELMs rises to a level just below 500 Hz, reached shortly after $t = 3.0$ s. From this time on, the frequency of the small

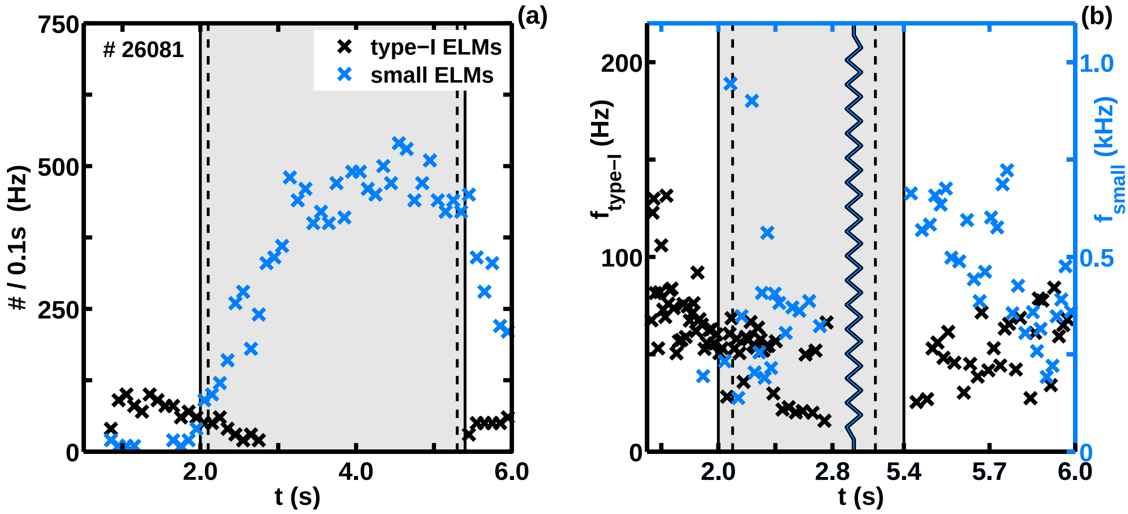


**Figure 8.3** *ELM frequency behaviour during application of MPs: in (a), the number of ELMs (large type-I or small) per 100 ms is shown as a function of time. Note that some small ELMs are already observed before the application of the coils. The shaded area indicates the activation of the coils from 2.0 -5.4 s (flat top of 900 A between the dashed lines at 2.1 s and 5.3 s). During the two transition phases at the switch on and off of the MPs, the frequency development of the type-I ELMs and small ELMs is shown in more detail in (b). Here, the frequency is determined as the reciprocal time with respect to the previous ELM of the same type.*

ELMs stays constant until the coils are switched off at $t = 5.4$ s. For the type-I ELMs, the frequency shows a continuous decrease from about 100 Hz at $t = 1.0$ s to below 25 Hz at $t = 2.8$ s, which does not seem to be affected by the application of the MPs. From a comparison of Figure 8.3(a) and Figure 8.1(e), it can indeed be seen that at $t = 2.8$ s the density threshold is reached after which the type-I ELMs no longer occur. Furthermore it can be seen from this comparison that the frequency development of the small ELMs actually follows closely the trend of the edge (line-averaged) density. Indeed, the edge density continues to rise until $t = 3.0$ s and then stays constant, decreasing again as the MPs are switched off.

The frequency development of the type-I ELMs and small ELMs during the two transition phases (where both occur simultaneously) is shown in more detail in Figure 8.3(b). Here, the frequencies for each ELM, $f_{\text{type-I}}$ and $f_{\text{small}}$, are determined as the reciprocal time with respect to the previous ELM of the same type. This representation is chosen to separate the frequency behaviour of the two kinds: due to the long duration of the type-I ELM, a reduction of the number of type-I ELMs alone would already result in an increase in the number of small ELMs (per unit time) even if their frequency $f_{\text{small}}$ would stay the same. However, from comparing this representation to Figure 8.3(a), it can be learned that the increase in the number of small ELMs per 100 ms (in the transition phase at the switch on of the coils) is caused by an increase in $f_{\text{small}}$ itself and not by a decrease of the type-I ELM frequency alone. In the transition phase after the switch off of the MPs, the same feature occurs in the opposite manner: the decrease in the number of small ELMs per 100 ms is caused by the decrease of $f_{\text{small}}$ itself and not by the increase in the type-I ELM frequency.

### *8.2.3. Comparison to previous observations of type-I and -II ELMs*

Using the description of the small ELMs given in the previous paragraph, the following remarks can be made comparing the appearance of these ELMs to observations obtained in the studies of type-I (Chapter 5) and type-II ELMs (Chapter 6).

The small ELMs can clearly be distinguished from type-I ELMs. First of all because they obviously do not display such large crashes: the $T_{e,ped}$ drop over a typical small ELM is less than 10 % (the effect on the profiles is also small [Fischer12]) and the peak heights measured by $I_{div}$ are more than a factor of two lower. Second, type-I ELMs and small ELMs show opposite behaviour with respect to variation of the edge (line-averaged) density: the frequency of the small ELMs increases with increasing density, whereas the type-I ELM frequency decreases. Furthermore, no $T_e$ fluctuations with strong off-mid-plane features (cf. paragraph 5.3.3) were observed for the small ELMs. The only observation common to both type-I ELMs and the small ELMs, is the occurrence of filaments rotating in the downward direction as can be seen in both Figure 5.6(d) and Figure 8.2(d).

The small ELMs observed here are also different from the small ELMs as observed during type-II ELMs. The main difference is that the type-II ELMs display continuous $T_e$ fluctuations, whereas the small ELMs are only seen for very short times. Furthermore, the type-II ELMs have a clear off-mid-plane character, which is not seen in the small ELMs. Finally, the apparent s-shaped passage of single $T_e$ fluctuations in the type-II ELMs (thought to be caused by the beating of multiple modes, cf. paragraph 6.3.3) is not observed for small ELMs. From Figure 8.2(c), it can however be seen that the small ELMs do have a broadband character.

## 8.3. Type-III ELMs

In the previous section, it is shown that the small ELMs remaining after mitigation of type-I ELMs are neither little versions of type-I ELMs nor type-II ELMs. Therefore, in this section, a description will be given of another type of commonly observed small ELMs, i.e. type-III ELMs. Type-III ELMs are defined by two characteristic features: first, their frequency decreases with increasing energy flux across the separatrix into the SOL (as already mentioned in Chapter 2). The type-III ELM frequency generally tends to be higher than that of type-I ELMs as well. Second, type-III ELMs exhibit a characteristic precursor with a frequency of about 60 kHz which is observed in the magnetic pickup coils closest to the plasma [Kass98].

In Figure 8.4, an overview is shown of the features of type-III ELMs occurring just after the L-H transition in discharge # 26081 (cf. Figure 8.1). The ELM frequency (i.e. reciprocal time; determined from the combined measurements of ECEI and $I_{div}$ as shown in Figure 8.5) is shown in Figure 8.4(a). Figure 8.4(b) displays a time trace and a spectrogram of one of the ballooning coils on the outer mid-plane (see paragraph 3.3.1), where the 60-80 kHz precursor oscillation is clearly seen as the type-III ELM frequency becomes constant. During the time window shown in Figure 8.4, the NBI input power remains at a constant level (of 2.5 MW). Alternatively, the electron temperature at the pedestal is used as a measure for the energy flux across the separatrix. In Figure 8.4(c) and (d) the increase in edge electron temperature and density is shown. As can be seen in Figure 8.4(c), the temperature rises about 100 eV from $t = 0.610$-$0.655$ s and then flattens after the occurrence of the first type-I ELM.

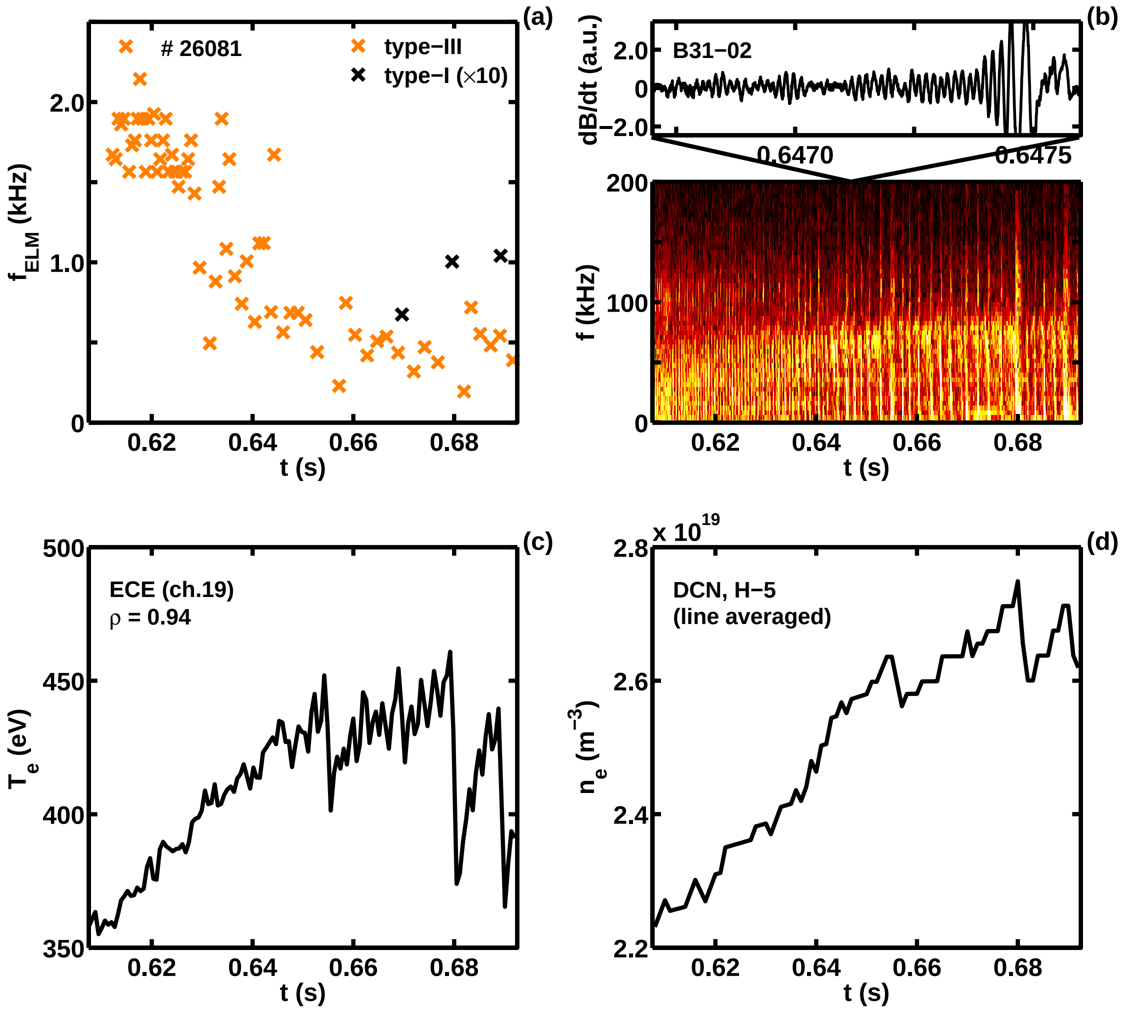


**Figure 8.4** *Overview of the type-III ELMs observed just after the L-H transition of # 26081 (cf. Figure 8.1). In (a), the decrease of the type-III ELM frequency, as reciprocal time, is shown. The precursor oscillation typically observed in the magnetic pickup coils is shown in the time trace and spectrogram of (b). In (c) and (d) the increase in edge electron temperature and density is shown. Due to the first type-I ELMs occurring (after t = 0.655 s), the temperature increase flattens and the type-III ELM frequency stays at a constant level of 500 Hz.*

During the same time, the type-III ELM frequency can be seen to rapidly decrease first from 2 kHz down to 500 Hz and then (from $t = 0.655$ s on) it stays constant at this level.

The appearance of type-III ELMs in ECEI is shown in Figure 8.5. In Figure 8.5(a), the time trace of $I_{div}$ shows how the type-III ELMs start off with a high frequency and small size (i.e. peak height in $I_{div}$). As their size increases, and frequency goes down, the first type-III ELM also becomes visible in the ECEI measurements (about 10 ms later). In the later phases, it is also noted that occasionally type-III ELMs are observed in the ECEI measurement but do not show up in $I_{div}$. It can furthermore be seen that a few type-I ELMs are already occurring before the ELM free phase around $t = 0.83$ s. These cause large edge temperature collapses (as can also be seen in Figure 8.4(c)), which the type-III ELMs do not display. This difference can also be seen comparing Figure 8.5(b) and Figure 8.5(c). Note that the onset of the type-I ELM in Figure 8.5(c)

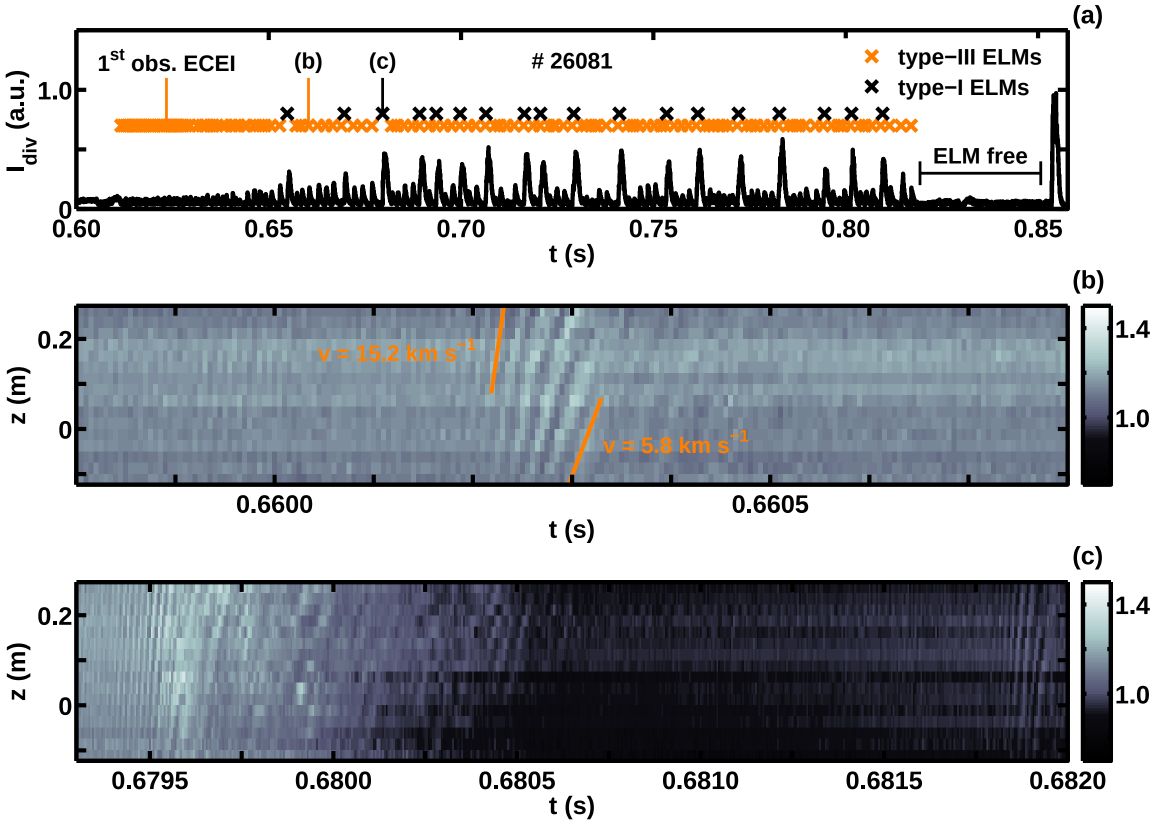


**Figure 8.5** *Overview of ECEI measurements during the type-III ELM phase just after the L-H transition in discharge # 26081: in (a), the divertor thermo-currents are shown as indicators for the occurrence of ELMs. Type-III ELMs are first seen around t = 0.60 s in $I_{div}$ alone. As their frequency decreases (cf. Figure 8.4(a)) and their size (i.e. peak height in $I_{div}$) increases they also become visible in the ECEI measurements. Furthermore, it can be seen that before the ELM free phase around t = 0.83 s, type-I and -III ELMs occur simultaneously. Here, the main difference between the type-III and type-I ELMs seen in this phase is that the type-I ELMs cause an edge temperature collapse (cf. Figure 8.4(c)), whereas the type-III ELMs do not display such a $T_e$ crash. This can also be seen from the difference in (b) and (c). A typical feature in the ECEI measurement of type-III ELMs is that the poloidal velocity of the mode slows down about a factor of two over the duration of its life time, as shown in (b). However, the number of modes visible in the ECEI observation window stays constant; i.e. the poloidal wavelength of the mode stays around 19 cm.*

very much resembles a type-III ELM followed by a few filaments (and then the temperature crash). The typical duration of a single type-III ELM is less than 0.5 ms; in the example shown in Figure 8.5(b) it is even just 0.1 ms. A remarkable feature in the ECEI measurements of type-III ELMs is that the poloidal velocity of the mode slows down about a factor of two (from 15 km s$^{-1}$ to 6 km s$^{-1}$) over the duration of its short life time. Using the same approach as was done for the small ELMs in paragraph 8.2.1, the mode number of the example shown in Figure 8.5(b) can be estimated: first, the type-III ELM is located on the $\rho = 0.97$ flux surface. The straight field line angle calculation yields a ratio of $d\theta/d\theta^* = 3.65$ for this flux surface and the observation angle covered by the ECEI window. The $q$-value belonging to the $\rho = 0.97$ flux surface is 5.5. From Figure 8.5(b) is it estimated that two modes fit in the ECEI observation window; i.e. the poloidal wavelength is around 19 cm. This results in estimated poloidal and toroidal mode numbers of $m \sim 75$ and $n \sim 14$, which is in agreement with [Kass98].

## 8.4. Conclusions

The small ELMs, observed with ECEI in a discharge where type-I ELMs were mitigated, are characterized by:

- causing only small $T_e$ drops (< 10 % of $T_{e,ped}$),
- their short duration: lasting < 0.5 ms and displaying 5-15 passes of $T_e$ fluctuations,
- being occasionally accompanied by filaments (also downward moving),
- being not always simultaneously observed in both ECEI and $I_{div}$ (which suggests toroidal localization),
- a poloidal wavelength of about 20 cm,
- being located around the $q = 5.5$ flux surface with mode numbers $m \sim 90$ and $n \sim 17$,
- their ELM frequency following the trend of the edge density (reaching about 500 Hz in the shown example).

Although one or two of these features are individually shared with type-I and/or type-II ELMs, the small ELMs are clearly distinguishable from either type (as described in paragraph 8.2.3).

Analysis of the development of the small ELM frequency shows that the hypothesis, that the activation of the MPs suppresses type-I ELMs and so making room for small, does not hold. Already before the activation of the coils, the first small ELMs can be observed as well as a decrease of the type-I ELM frequency. As the edge density increases, the small ELM frequency follows and this is not just because of a reduction of the number of type-I ELMs. However, the MPs do seem to influence the behaviour of the type-I ELMs: as the coils are switched off, they immediately return. As the density decreases then, the small ELM frequency follows and the type-I frequency increases again.

Comparing the small ELMs to the type-III ELMs described in section 8.3, the following remarks can be made. Both types do not cause (large) edge temperature crashes. For both types, the duration of the event is comparably short (< 0.5 ms). The modes observed in both types seem located on the same $q = 5.5$ flux surface with a poloidal wavelength of about 20 cm, albeit with slightly different poloidal and toroidal mode numbers ($m/n \sim 90/17$ for the small ELMs, vs. $m/n \sim 75/14$ for the type-III ELMs). The most prominent feature in the ECEI measurement of type-III ELMs, i.e. the slowing down of the apparent poloidal rotation whilst keeping the same mode number, is not observed for the small ELMs. Also, the magnetic precursor found for the type-III ELMs (and commonly used in defining ELMs as being of this type) is not found for the small ELMs. However, if the small ELMs are indeed most closely related to type-III ELMs, this might help explain for the fact that in some discharges (most noticeable # 26854 and # 26855) type-I ELM suppression is already achieved before activation of coils.

# Chapter 9

# Conclusions and outlook

With the installation of ECE-imaging on the ASDEX Upgrade tokamak, it has become possible for the first time to study in 2D the electron temperature dynamics of instabilities in H-mode plasmas. Whereas most diagnostics observe plasma quantities along a single line of sight, ECE-imaging can follow temperature fluctuations in both the radial and vertical direction. This enabled the detailed study of the phenomenon that is almost unavoidably associated with the H-mode, i.e. edge localized modes (ELMs). ELMs are of complex nature and there still is a lack of complete understanding of the governing physics. The latter is required for developing a consistent model that can be extrapolated to larger tokamaks (e.g. ITER), where the expelled energy and particle loads could prove difficult to handle.

In this thesis it is shown that ECE-imaging is indeed a suitable diagnostic for obtaining information on electron temperature dynamics at the edge of H-mode plasmas. For most experiments it was found useful to set up the diagnostic in such a way that the inner half of the observation window covered the edge of the confined plasma and the outer half covered part of the scrape-off-layer. It is shown that inside the confined region, the optical thickness of the plasma is generally high enough to treat the detected radiation as a measure for the plasma electron temperature. In the outer half of the ECE-imaging observation window, the optical thickness becomes low and the detected radiation contains a mixed contribution from electron temperature and density. However, it is still possible to follow the motion of localized structures in this region.

The capabilities of ECE-imaging as a 2D diagnostic have proven useful in the characterization of the various ELM regimes that are achieved in ASDEX Upgrade. From the acquired measurements it is possible to identify the different types of ELMs and determine properties such as ELM frequency, precursor frequency, and poloidal rotation velocities of both precursor modes and filaments. Furthermore, despite the fact that the ECE-imaging observation window covers only a relatively small part of the plasma's poloidal circumference, it is shown how poloidal mode numbers can be estimated from these measurements (and the toroidal mode numbers derived from that).

Although the different types of ELMs described in this thesis display features that clearly distinguish them from each other, there are also similarities between the various modes and temperature fluctuations that closely link the diffent types together. For example, the mode (with a poloidal wavelength of 10 cm and mode number $m \sim 110$) that is only seen in the 'slow' type-I ELM cycle has a distinct poloidal asymmetry: its amplitude has a minimum on the plasma mid-plane and maxima above and below. A similar poloidal asymmetry is also found in the time averaged 2D amplitude distribution of the broadband $T_e$ fluctuation that characterizes type-II ELMs (with a poloidal wavelength of 10 cm and $m \sim 100$). Moreover, whereas this mode with the asymmetric poloidal amplitude distribution seems to delay the occurrence of the next $T_e$ crash in type-I ELMs, it seems that this mode causes the complete absence of $T_e$ crashes in the type-II case. It should also be noted here that both these modes with short poloidal wavelengths do not result in crashes, whereas the modes with longer poloidal wavelengths do (> 15 cm, i.e. observed at the ELM onset, for type-III ELMs, and during mitigation of type-I ELMs). This is in agreement with the theoretical prediction that higher-*m* ballooning modes are more localized radially and therefore have a smaller impact on the confinement.

A further similarity between the different types of ELMs is e.g. found in the transitions from type-I ELMs to regimes of smaller ELMs. In both the transition from type-I to type-II ELMs and from type-I to the small ELMs observed with the application of magnetic perturbation coils, it is seen that the substituting type is already present before the type-I ELMs have stopped occurring. Another resemblance is found in the poloidal mode numbers observed at the onset of the type-I ELM and for the type-III ELMs, both have a value of $m \sim 75$. However, whereas the poloidal velocity of the type-I onset mode is observed to spin up and is followed by a $T_e$ crash, the poloidal velocity of the type-III ELMs slows down and a $T_e$ crash does not occur.

Finally, an observation common to all described ELMs is that all the modes rotate in the electron diamagnetic drift direction and that their frequencies (not the repetition frequency of the ELM events) are usually in the 20-60 kHz range.

## 9.1. Characterization of ELMs with ECE-imaging

In this section, the answers to the research question posed in the introductory chapter of this thesis (section 1.4) are presented.

**Type-I ELMs**

In Chapter 5, the first 2D electron temperature measurements of the ELM crash are presented. For type-I ELMs, it is seen that a difference between the ‘slow’ and ‘fast’ ELM cycles is the occurrence of a mode with a strong asymmetry in its poloidal amplitude distribution: this has a minimum on the plasma mid-plane and maxima above and below. The modes poloidal and toroidal mode numbers are estimated as $m \sim 110$ and $n \sim 28$, respectively. Although the presence of this mode does not cover the full delay of the slow cycle compared to the fast one, this fluctuation does suggest that its presence regulates the plasma edge condition in such a way that a stable situation is prolonged at least 2 ms longer until the $T_e$ crash comes.

While the actual appearance of an individual type-I ELM can vary significantly, the ELM crash typically develops as follows. Apart from the presence of the above described mode, the ELM onset is announced by the short (a few tens of $\mu$s) appearance of a mode with mode numbers $m \sim 75$ and $m \sim 18$ that can sometimes be seen to increase its mode number and poloidal velocity (in the electron diamagnetic drift direction) towards the $T_e$ crash. During the early phase of the temperature collapse, incoherent and chaotic $T_e$ fluctuations are seen. The duration of the crash phase varies for each ELM, but it is only during this phase that filaments are seen in the region just outside the separatrix. Usually they are observed to rotate in the upward direction (i.e. the same as the onset mode), but occasionally some of the first filaments are seen to move downward. This makes it somewhat difficult to directly relate the motion of those filaments to that of the onset mode. However, nonlinear simulations with JOREK (a 3D reduced resistive MHD code) indicate the possibility of filament motion in both up- and downward direction [Pamela10].

Observations like those of the filaments show the benefit of the 2D capability of ECE-imaging; as such features could not have independently been derived from 1D measurements. Furthermore, even though the ECE-imaging observation window does not cover a large part of the poloidal plasma circumference, it does allow for direct estimates of the poloidal mode number of a passing $T_e$ fluctuation. In the calculations for the mode number, the straight field line approach should of course be taken into account.

**Type-II ELMs**

The measurements described in Chapter 6 focus on the transition from type-I to type-II ELMs which shows the development of a broadband $T_e$ fluctuation characteristic for the type-II ELM regime. Over this transition, it can be seen that the amplitude of $T_e$ fluctuations forms a peak in the 20-60 kHz range. The 2D distribution of the fluctuation's amplitude displays a distinguished minimum around the mid-plane when averaged over a longer time window. This, however, could not directly be confirmed by the measurements from the nearby magnetic pickup coils (which did show a small broadband peak; but with a maximum at a lower frequency, equally distributed over the poloidal array of coils). From the analysis of single $T_e$ dips and peaks, the poloidal and toroidal mode numbers are estimated as $m \sim 100$ and $n \sim 21$.

Fully developed, the relative amplitude of this broadband peak reaches a value of almost 20 % just inwards of the top of the $T_e$ pedestal. Simultaneously, the temperature profile flattens in this region whilst leaving the pedestal gradient unaffected. In the fully developed type-II phase, the large $T_e$ crashes are absent. This indicates that the flattening of the temperature profile at the pedestal top has a regulating function and that the stability criteria for the type-I ELMs are also sensitive to this area of the edge pedestal.

When the broadband $T_e$ fluctuations are observed on the timescale of several milliseconds (covering a few hundred single passages of $T_e$ dips and peaks), a beat wave with a low beat frequency is seen. This suggests that the broadband mode actually consists of multiple modes with slightly different mode numbers or frequencies. The beat wave behaviour also gives a plausible explanation for the observation that the poloidal propagation velocity of single $T_e$ flucuations does not always appear to be constant. As a single $T_e$ fluctuations moves from bottom to top through the ECE-imaging observation window, it alternately passes through regions of destructive and constructive interference. This causes an apparent s-shaped curve: lower velocities at the top and bottom of the observation window and higher velocities over the mid-plane. The beat wave might also play a role in causing the observed amplitude minimum around the mid-plane. However, it cannot be the sole explanation since the beat wave passes multiple times during the longer time window from which the 2D amplitude distribution becomes apparent.

**The influence of electron density fluctuations**

As the measurements described in Chapter 5 and Chapter 6 show, there are modes in both type-I and type-II ELMs that display an amplitude distribution that is poloidally asymmetric: i.e. an amplitude minimum around the mid-plane. In Chapter 7, the hypothesis is investigated that (due to the closeness to cut-off of the pedestal density) small increases in the plasma edge density could lead to large deflections of the ECE-imaging lines of sight, especially for the top and bottom lines of sight. For these off-mid-plane channels, the mechanism would work in two ways: first, the outward deflection of those lines of sight would be largest. Second, the steep $T_e$ gradient along the (vertical) cold resonance chord would cause the measured temperatures to be considerably lower compared to what is measured at the mid-plane.

With the use of a 2D ray tracing code it is shown that a local density blob on top of the edge pedestal can indeed cause the upper ray of an ECE-imaging channel to be deflected. However, the maximum deflection (that would result in an apparent temperature drop of more than 20 %, which is what is measured) is only found in the small window of a 5-6 % increase of the pedestal top density (i.e. 99-100 % of the cut-off density). Larger increases result in a direct cut-off on the modelled density blob and increases below 3 % do not result in a large enough beam deflection. The modelling of a rotating edge density blob furthermore showed, that the apparent temperature fluctuation due to the passing of an edge density blob does decrease much faster (radially inward) than is e.g. seen for the broadband $T_e$ fluctuations of type-II ELMs. Finally, the modelling of a poloidally rotating flux surface deformation (in the style of a ballooning mode) revealed that in this case the beams on the mid-plane would also be deflected. Due to the varying angle between the local gradient of the refractive index and the incoming (horizontal) beam, the deflection would be both up- and downwards and result in apparent $T_e$ variations just as large on the mid-plane as above and below.

In a rough estimate, the height of the pedestal density (for a given magnetic field) scales with the plasma current. ECE-imaging measurements during the H-mode phase of a discharge with a 40 % lower pedestal density reveal that an off-mid-plane fluctuation is still observed for slow ELMs. So, even though the 2D modelling has shown that local density perturbations at the pedestal top could lead (under specific circumstances) to an apparent off-mid-plane $T_e$ drop, this measurement shows that that alone cannot be the sole explanation.

**Mitigation of type-I ELMs**

Since the installation of a set of magnetic perturbation coils, it has become possible at ASDEX Upgrade to achieve plasma conditions under which the large type-I ELMs are mitigated. To date, the exact mechanism that causes the mitigation is not fully understood: especially the role of the edge electron density threshold seems critical. In Chapter 8, it is shown that the remaining small ELMs can be distinguished from type-I and type-II ELMs (but also have some features in common with either type). In comparison to type-I ELMs, obviously, these small ELMs do not cause such large $T_e$ crashes. Whereas the type-I ELM frequency decreases with increasing edge density, the frequency of the small ELMs increases and closely follows its variation. Filaments rotating in the downward direction are observed for both type-I and the small ELMs. In comparison to type-II ELMs, small ELMs do not display a continous fluctuation. An asymmetry in the poloidal amplitude distribution is also not observed. However, both types do seem to have a broadband character.

Already before the activation of the coils, the first small ELMs can be observed. As the perturbation coils are switched on, the small ELM frequency starts to increase following the increase of the edge density. The increase in the frequency of the small ELMs is not caused solely by the decrease in the type-I ELM frequency. It seems, on the contrary, that the decrease in the type-I ELM frequency is a result of the increasing small ELM frequency.

In the same discharge where the type-I ELMs were mitigated and replaced by small ELMs, type-III ELMs were observed just after the L-H transition. A direct relation between the two is not easily established. As was the case for the type-I and -II ELMs, the small ELMs can clearly be distinguished from type-III ELMs, but they also display a few common features. Both modes have a short duration and localisation on the same $q$-surface in common. However, the most prominent observation for the type-III ELMs, i.e. the slowing down of the apparent poloidal rotation (whilst keeping the same mode number), is not observed in the small ELMs. If the small ELMs are indeed most closely related to type-III ELMs, regardless of this difference, that might help explain the fact that in some discharges suppression of type-I ELMs is already achieved before activation of the perturbation coils.

## 9.2. Outlook

Summarizing, the work described in this thesis shows that ECE-imaging is a valuable diagnostic and that its measurements at the plasma edge can contribute new insights to the research field of ELM physics. With the use of this diagnostic, many of the research questions posed at the beginning of thesis have been answered. Some of the answers lead to new research themes. In order to further increase the understanding of the ELM phenomenon, the following topics are suggested for future investigations.

Without changing the existing ECE-imaging set up, a deeper investigation of the poloidal rotation velocity observed for the various modes can be performed. It is expected that they rotate with the $\boldsymbol{E}\times\boldsymbol{B}$-drift. In fact, for different depths of the $E_r$-well at the plasma edge (obtained by changing edge pressure gradients) there are varying contributions of the $\boldsymbol{E}\times\boldsymbol{B}$-force in the electron diamagnetic drift direction. This should then show in ECE-imaging measurements as different poloidal velocities of the modes, and it might be a confirmation that the complicated rotation behaviour of theses mode is consistent with that of the (time varying) $E_r$-well.

Two (foreseen) improvements of the ECE-imaging diagnostic can be used to gain insight in the behaviour of the filaments observed during the $T_e$ crash phase. The filaments are shown to occur in the plasma region where the optical thickness is low. In this region, the optical thickness condition for O-mode radiation is different from that for X-mode radiation at the same frequency. Therefore, by including a polarizer in the optical path of a few lines of sight of ECEI, it might become possible to separate the contributions from $n_e$ and $T_e$ to filaments. For the installation of a second ECE-imaging system, an observation window located at a different toroidal position is foreseen. This could not only be used to reveal how deep the $T_e$ crash penetrates towards the plasma core (by using the two systems simultaneously covering different radial ranges), it will also help increase the toroidal localisation of ELMs and filaments. As the two observation windows will not be far apart, this can be done by comparing the instants a perturbation enters in one of the two fields of view.

Several measurements described in this thesis have already pointed towards the fact that ELMs and filaments can have toroidally and poloidally localized structures. In the research field of ELM modelling there are also first indications in this direction; meanwhile even modes have been found that occur above and below the mid-plane [Hölzl12]. Unfortunately, consistent ELM models that can predict in detail all the features shown in this thesis do not yet exist. With a model like that, it would be worth though, to investigate how close the onset mode of type-I ELMs is related to the type-III ELM (and whether indeed the slowing down of poloidal rotation of the latter prevents the $T_e$ crash).

# Acknowledgements

Although there is just one name on the cover, writing a thesis is by no means a solo endeavour. If it were not for the many contributions from lots of people, I would have never arrived at writing this last part of the thesis. I feel fortunate to have been surrounded by all those who offered support and/or distraction whenever I needed it.

First of all, I would like to thank my daily supervisor, Ivo Classen, for his guidance throughout the whole project. Ivo, I have enjoyed thoroughly working together with you and have very much appreciated your ability to put complicated matter (not only concerning plasmas) in simple terms. I am grateful for the continuous support you gave me in searching for the right physics questions to ask, and for your patience with and confidence in my approach to the project.

I am especially indebted to my promotor, professor Tony Donné, who offered me the opportunity to work as a Ph.D. student in the ECE-imaging team (even before he took on the role of being promotor). He has been a constant source of encouragement and his eagerness to read ‘something new’ has kept up the pace in the final stages of this project. Here, I would also like to thank professor Niek Lopes Cardozo for being promotor during the first two years and for raising my enthusiasm for the field of fusion science, already during my time at university.

Further, I would like to express a deep gratitude to my co-promotor, Peter de Vries, for his remote guidance. Although being located at JET (Culham, UK) himself, he was actually at arm’s-length since we had weekly phone calls at times. Despite the distance, he was still able to clearly communicate his profound knowledge, his great excitement, and all his new ideas on whatever topic I brought forward. Also, I would like to extend my gratitude to Roger Jaspers, who was my co-promotor during the first two years and introduced me to the field of plasma diagnostics.

From the first day I officially started this project, I was seconded to the Max-Planck-Institut für Plasmaphysik in Garching bei München (Germany) and ever since, I have felt part of the ‘home team’ there. I thank the entire ASDEX Upgrade team for the inspiring environment it has created and for all the substantial and subtle contributions to this work. Many thanks go to professor Hartmut Zohm, Elisabeth Wolfrum, Wolfgang Suttrop, Marc Maraschek, Garrard Conway, and Josef Neuhauser. Their wealth of knowledge, patient explaining, and careful reading were indispensable.

For their efforts in keeping the diagnostic up and running, I am grateful to all the members of the ECE-imaging team around the world; particularly to Ivo Classen, who adapted it to be used on ASDEX Upgrade, and to Ben Tobias, whose dedication to the diagnostic (and the physics being explored with it) is unparalleled.

The Plasma Diagnostic Group is the best group to be part of at FOM Rijnhuizen/ DIFFER, especially since no one of the group is actually stationed there. During all the video conferences we had, there were many interesting discussions on diagnostics and how to increase the understanding of plasma physics with them. For all the conversations that also went beyond these topics, I would like to extend my appreciation to Manfred von Hellermann, Peter de Vries, Ivo Classen, Thijs Versloot, Anton Bogomolov, Athina Kappatou, Mikhail Kantor, and Maximos Tsalas.

I would also like to acknowledge my former room-mates and all of the other aspiring young scientists, who made my time at ASDEX Upgrade most enjoyable, most gratifying, and most memorable: Ben Geiger (for organizing beautiful walks in the mountains), Philip Schneider (for throwing great parties), Bernd Wieland, Steffen Potzel, Pascal de Marne, Sina Fietz, Mike Dunne, Diarmuid Curran, Ronald Wenninger, Matthias Hölzl, Christian Vorpahl, Andreas Burckhart, Jonathan Citrin, Tim Happel, Eleonora Viezzer, Sylvia Rathgeber, Fabian Sommer, Matthias Willensdorfer, Rachael McDermott, Matthias Bernert, and all those who joined for coffee, lunch, or afternoon ice cream.

There is also a number of people whose main contribution to this thesis actually was to keep my mind off of all things physics related. The Tango Argentino is a dance that is almost completely improvised; for their help in getting a wooden Dutchman a bit more creative, I thank Mireille Granet, Dieter Raab, Gundula Herdeg, Isabella Medri, Romy Bonitz, and all of the Munich milongueros. Good foil fencing requires accuracy, a fast reaction time, and thought-through tactics; I thank Philipp Stein, Dorothea Goschenhofer, Isabell Preuß, Felix Schneider, and the others from ZHS-Fencing for all the times they literally pointed out on me that I still need to improve those skills.

The distance between Eindhoven, where I grew up, and Munich is more than 700 kilometer. Although the saying goes ‘out of sight, out of mind’, there are several people who kept in contact through the years. For their visits to Munich, and the typical Dutch gifts they brought, I would like to thank the ‘Chaoten’ Rob Tummers, Jan Küchel, Juri Snijders, and Pier Dolmans. For their inquiries to my well-being, I am thankful to my piano teacher Guy de Werd and former dance partner Franny Dekkers.

To conclude these acknowledgements, I would like to express the highest appreciation to my family. I am very grateful to my parents, Rob and Rina Boom, for having been raised in their unconditional love and support. Special thanks go to my brother, Alan, for designing the cover, and to my sister, Winnie, (and her fiancée, Joran) for always keeping in touch. I would also like to thank my soon-to-be parents-in-law, Eberhard and Heidrun Herdeg, and the whole Herdeg-family (including Aunt Gotelind Göttle) for their unwavering help and their keen interest in the progress of the thesis.

Dear Gundi, there are no words that describe my deepest gratitude for your motivation, support, and patience; especially during the most stressful periods towards the end of this project. But most of all, I will eternally be thankful to you for having given me a son, who cheers me up every day, Casimir.

# Curriculum vitae

On the 27th of September 1980, I was born in the city of Eindhoven, The Netherlands. I started my secondary education in 1992 at the ‘Eindhovens Protestants Lyceum’, later renamed ‘Christiaan Huygens College’. In 1998, I obtained the Gymnasium-Beta diploma (a pre-university degree that includes the study of both Latin and Greek, as well as the natural and formal sciences) at this high school.

After that, I began studying Applied Physics at the Eindhoven University of Technology (TU/e). As a part of this study, I performed a three month internship on the physical and chemical processes in the mesosphere and lower thermosphere at ‘The Auroral Observatory’, University of Tromsø, Norway. In addition to these studies, I attended the preparatory class of the Tilburg Conservatory (piano) for two years. This led to participation in a public master class at the Frits Philips Concert Hall (Eindhoven) and contributions to various CD-recordings. My enthusiasm for the research field of nuclear fusion was triggered by a visit to the TEXTOR tokamak, located at the Forschungszentrum Jülich in Germany. I did a final internship there (seconded by the FOM Institute for Plasma Physics Rijnhuizen) on helium transport and exhaust measurements using charge exchange recombination spectroscopy and obtained my master’s degree in 2007.

In January 2008, I started working as a Ph.D. student in the high temperature plasma diagnostics group of the FOM Institute for Plasma Physics Rijnhuizen. For the full duration of the project, I was seconded to the Max-Planck-Institut für Plasmaphysik in Garching bei München to work at the ASDEX Upgrade tokamak. The experimental work on the characterization of edge localized modes with ECE-imaging, which was carried out on this device, is presented in this thesis.

# Bibliography


[Aiba07] Aiba N. *et al.* 2007 *Nucl. Fusion* **47** 297

[Aston20] Aston F.W. 1920 *Phil. Mag.* **xxxix** 611

[Audi03] Audi G., Wapstra A.H. and Thibault C. 2003 *Nucl. Phys. A* **729** 337

[Bartlett78] Bartlett A.A. 1978 *Am. J. Phys.* **46** 876

[Bekefi66] Bekefi G. 1966 'Radiation processes in plasmas' *John Wiley & Sons, Inc.*

[Biglari90] Biglari H., Diamond P.H. and Terry P.W. 1990 *Phys. Fluids B* **2** 1

[Blaney75] Blaney T.G. 1975 *Space Sci. Rev.* **17** 691

[Bobkov10] Bobkov Vl.V. *et al.* 2010 *Nucl. Fusion* **50** 035004

[Bolzonella04] Bolzonella T. *et al.* 2004 *Plasma Phys. Control. Fusion* **46** A143

[Boom11] Boom J.E. *et al.* 2011 *Nucl. Fusion* **51** 103039

[Bornatici82] Bornatici M. 1982 *Plasma Phys.* **24** 629

[Bornatici83] Bornatici M. *et al.* 1983 *Nucl. Fusion* **23** 1153

[Burckhart10] Burckhart A. *et al.* 2010 *Plasma Phys. Control. Fusion* **52** 105010

[Burrell05] Burrell K.H. *et al.* 2005 *Plasma Phys. Control. Fusion* **47** B37

[Cima97] Cima G. *et al.* 1997 *Fusion Eng. Des.* **34-35** 515

[Classen07] Classen I.G.J. 2007 'Imaging and control of magnetic islands in tokamaks' *Ph.D. thesis, Technische Universiteit Eindhoven*

[Classen10] Classen I.G.J. *et al.* 2010 *Rev. Sci. Instrum.* **81** 10D929

[Connor98a] Connor J.W. *et al.* 1998 *Phys. Plasmas* **5** 2687

[Connor98b] Connor J.W. 1998 *Plasma Phys. Control. Fusion* **40** 191

[Connor00] Connor J.W. and Wilson H.R. 2000 *Plasma Phys. Control. Fusion* **42** R1

[Connor04] Connor J.W. *et al.* 2004 *Nucl. Fusion* **44** R1

[Conway07] Conway G.D. *et al.* 2007 'Doppler reflectometry on ASDEX Upgrade: Foundations and latest results' *Proc. 8th International Reflectometry Workshop (St. Petersburg, Russia, 2007)*

[Conway12] Conway G.D. 2012 (private communication)

[Costley09] Costley A.E. 2009 *Fusion Sci. Technol.* **55** 1

[D'haeseleer91] D'haeseleer W.D. *et al.* 1991 'Flux Coordinates and Magnetic Field Structure' *Springer-Verlag Berlin Heidelberg* ISBN 3-540-52419-3

[Deng99] Deng B.H. *et al.* 1999 *Rev. Sci. Instrum.* **70** 998

[DIII-D Team91] DIII-D Team 1991 *Plasma Physics and Controlled Nuclear Fusion Research 1990 (Proc. 13th Int. Conf. Washington DC, 1990) Vienna: IAEA* **1** 69

[Dunne11] Dunne M.G. *et al.* 2011 'Inter-ELM pedestal current density evolution in ASDEX Upgrade' *Proc. 38th EPS Conf. on Plasma Physics (Strasbourg, France, 2011)* vol 35G (ECA) P-1.070 (CD-ROM)

[Dux11] Dux R. *et al.* 2011 'Impurity density determination using charge exchange and beam emission spectroscopy at ASDEX Upgrade' *Proc. 38th EPS Conf. on Plasma Physics (Strasbourg, France, 2011)* vol 35G (ECA) P-1.056 (CD-ROM)

[Eddington20] Eddington A.S. 1920 *The Observatory* **XLIII** 341

[Eich03] Eich T. *et al.* 2003 *Phys. Rev. Lett.* **91** 195003

[Eich05] Eich T. *et al.* 2005 *Plasma Phys. Control. Fusion* **47** 815

[Einstein05] Einstein A. 1905 *Ann. d. Phys.* **18** 639

[Engelmann73] Engelmann F. and Curatolo M. 1973 *Nucl. Fusion* **13** 497

[Evans04] Evans T.E. *et al.* 2004 *Phys. Rev. Lett.* **92** 235003

[Federici03] Federici G., Loarte A. and Strohmayer G. 2003 *Plasma Phys. Control. Fusion* **45** 1523

[Ferron94] Ferron J.R. *et al.* 1994 'The effect of the edge current density on confinement and kink mode stability in H-mode and VH-mode discharges' *Proc. 21st EPS Conf. on Controlled Fusion and Plasma Physics (Montpellier, France, 1994)* vol 18B (ECA) I-86

[Fischer08a] Fischer R. *et al.* 2008 *Plasma Phys. Control. Fusion* **50** 085009

[Fischer08b] Fischer R. *et al.* 2008 *Fusion Sci. Technol.* **58** 675

[Fischer11] Fischer R. *et al.* 2011 'Effect of non-axisymmetric magnetic perturbations on profiles at ASDEX Upgrade' *Proc. 38th EPS Conf. on Plasma Physics (Strasbourg, France, 2011)* vol 35G (ECA) P-1.072 (CD-ROM)

[Fischer12] Fischer R. *et al.* 2011 'Response of kinetic profiles to non-axisymmetric magnetic perturbations at ASDEX Upgrade' *subm. to Plasma Phys. Control. Fusion*

[Freidberg87] Freidberg J.P. 1987 'Ideal magnetohydrodynamics' *Plenum Press, New York* ISBN 0-306-42512-2

[Fundamenski12] Fundamenski W. *et al.* 2012 *Nucl. Fusion* **52** 062003

[García Muñoz09] García Muñoz M. *et al.* 2009 *Rev. Sci. Instrum.* **80** 053503

[Geiger11] Geiger B. *et al.* 2011 *Plasma Phys. Control. Fusion* **53** 065010

[Gernhardt92] Gernhardt J. 1992 'Magnetic diagnostic on ASDEX Upgrade with internal and external pick-up coils' *IPP-Report* 1/262

[Giannone09] Giannone L. *et al.* 2009 *Fusion Eng. Des.* **84** 825

[Gohil88] Gohil P. *et al.* 1988 *Phys. Rev. Lett.* **61** 1603

[Goldston84] Goldston R.J. 1984 *Plasma Phys. Control. Fusion* **26** 87

[Greene62] Greene J.M. and Johnson J.L. 1962 *Phys. Fluids* **5** 510

[Greenwald99] Greenwald M. *et al.* 1999 *Phys. Plasmas* **6** 1943

[Gruber09a] Gruber O. 2009 *Fusion Eng. Des.* **84** 170

[Gruber09b] Gruber O. *et al.* 2009 *Nucl. Fusion* **49** 115014

[Hartfuss97] Hartfuss H.J., Geist T. and Hirsch M. 1997 *Plasma Phys. Control. Fusion* **39** 1693

[Hegna96] Hegna C.C. *et al.* 1996 *Phys. Plasmas* **3** 584

[Hender92] Hender T.C. *et al.* 1992 *Nucl. Fusion* **32** 2091

[Herrmann03] Herrmann A. and Gruber O. 2003 *Fusion Sci. Technol.* **44** 569

[Hicks10] Hicks N.K. *et al.* 2010 *Fusion Sci. Technol.* **57** 1

[Hobirk00] Hobirk J. *et al.* 2000 'First Measurements of the Radial Electric Field with the Motional Stark Effect Diagnostic on ASDEX Upgrade' *Proc. 27$^{th}$ EPS Conf. on Contr. Fusion and Plasma Physics (Budapest, Hungary, 2000)* vol 24B (ECA) 984 (CD-ROM)

[Hölzl12] Hölzl M. *et al.* 2012 *Phys. Plasmas* **19** 082505

[Hutchinson99] Hutchinson I.H. *et al.* 1999 *Plasma Phys. Control. Fusion* **41** A609

[Hutchinson05] Hutchinson I.H. 2005 'Principles of Plasma Diagnostics' (2$^{nd}$ edition) *Cambridge University Press* ISBN 0-521-80389-6

[Huysmans95] Huysmans G.T.A. *et al.* 1995 *Proc. 22$^{nd}$ EPS Conf. on Controlled Fusion and Plasma Physics (Bournemouth, UK, 1995)* vol 19C (ECA) I-201

[Huysmans98] Huysmans G.T.A, Hender T.C. and Alper B. 1998 *Nucl. Fusion* **38** 179

[Huysmans05] Huysmans G.T.A. 2005 *Plasma Phys. Control. Fusion* **47** B165

[Huysmans07] Huysmans G.T.A. and Czarny O. 2007 *Nucl. Fusion* **47** 659

[Huysmans09] Huysmans G.T.A. *et al.* 2009 *Plasma Phys. Control. Fusion* **51** 124012

[IEA11] International Energy Agency 2011 'Key World Energy Statistics'

[Igochine10] Igochine V. *et al.* 2010 'Hotlink based Soft X-ray diagnostic on ASDEX Upgrade' *IPP-Report* 1/338

[Ikeda10] Ikeda K. 2010 *Nucl. Fusion* **50** 014002

[ITER_PB99] ITER Physics Basis 1999 *Nucl. Fusion* **39** 2137

[Jakubowski09] Jakubowski M. W. *et al.* 2009 *J. Nucl. Mater.* **390-391** 781

[Kallenbach02] Kallenbach A. *et al.* 2002 *Nucl. Fusion* **42** 1184

[Kamada00] Kamada Y. *et al.* 2000 *Plasma Phys. Control. Fusion* **42** A247

[Kass98] Kass T. *et al.* 1998 *Nucl. Fusion* **38** 111

[Keilhacker84] Keilhacker M. *et al.* 1984 *Plasma Phys. Control. Fusion* **26** 49

[Kirk04] Kirk A. *et al.* 2004 *Phys. Rev. Lett.* **92** 245002

[Kirk12] Kirk A. *et al.* 2012 *Phys. Rev. Lett.* **108** 255003

[Kočan12] Kočan M. *et al.* 2012 *Nucl. Fusion* **52** 023016

[Koch07] Koch B. *et al.* 2007 *J. Nucl. Mater.* **363-365** 1056

[Kojima09] Kojima A. *et al.* 2009 *Nucl. Fusion* **49** 115008

[Kurzan07] Kurzan B. *et al.* 2007 *Plasma Phys. Control. Fusion* **49** 825

[Kurzan11] Kurzan B. and Murmann H.D. 2011 *Rev. Sci. Instrum.* **82** 103501

[Lackner08] Lackner K. 2008 *Fusion Sci. Technol.* **54** 989

[Lang12] Lang P.T. *et al.* 2012 *Nucl. Fusion* **52** 023017

[Laval74] Laval G., Pellat R. and Soule J.S. 1974 *Phys. Fluids* **17** 835

[Lawson57] Lawson J.D. 1957 *Proc. Phys. Soc. B* **70** 6

[Leonard99] Leonard A.W. *et al.* 1999 *J. Nucl. Mater.* **266-269** 109

[Leuterer09] Leuterer F. *et al.* 2009 *Fusion Sci. Technol.* **55** 31

[Liang10] Liang Y. *et al.* 2010 *Nucl. Fusion* **50** 025013

[Loarte07] Loarte A. *et al.* 2003 *J. Nucl. Mater.* **313-316** 962

[Lönnroth04] Lönnroth J.-S. *et al.* 2004 *Plasma Phys. Control. Fusion* **46** 767

[Maggi10] Maggi C.F. 2010 *Nucl. Fusion* **50** 066001

[Maingi05] Maingi R. *et al.* 2005 *Nucl. Fusion* **45** 1066

[Manickam92] Manickam J. 1992 *Phys. Fluids B* **4** 1901

[McCarthy99] McCarthy P.J., Martin P. and Schneider W. 1999 'The CLISTE Interpretive Equilibrium Code' *IPP-Report* 5/85

[Meo08] Meo F. *et al.* 2008 *Rev. Sci. Instrum.* **79** 10E501

[Mikhailovskii97] Mikhailovskii A.B. *et al.* 1997 *Plasma Phys. Rep.* **23** 844

[Mlynek10] Mlynek A. *et al.* 2010 *Rev. Sci. Instrum.* **81** 033507

[Müller05] Müller H.W. *et al.* 2005 'Plasma flow in the scrape-off layer of ASDEX Upgrade' *Proc. 32nd EPS Conf. on Plasma Physics (Tarragona, Spain, 2005)* vol 29C (ECA) P-1.009 (CD-ROM)

[Murmann92] Murmann H. *et al.* 1992 *Rev. Sci. Instrum.* **63** 4941

[Neuhauser08] Neuhauser J. *et al.* 2008 *Nucl. Fusion* **48** 045005

[Nunes04] Nunes I. *et al.* 2004 *Nucl. Fusion* **44** 883

[Nunes07] Nunes I. *et al.* 2007 'Small ELMs in quasi-double null plasmas at JET' *Proc. 34th EPS Conf. on Plasma Physics (Warsaw, Poland, 2007)* vol 31F (ECA) P-5.137 (CD-ROM)

[Osborne97] Osborne T.H. *et al.* 1997 'Scaling of ELM and H-Mode Pedestal Characteristics in ITER Shape Discharges in the DIII-D Tokamak' *Proc. 24th EPS Conf. on Contr. Fusion and Plasma Physics (Berchtesgaden, Germany, 1997)* vol 21A, Part III, P.1101

[Osborne05] Osborne T.H. *et al.* 2005 'Edge Stability Analysis and Pedestal and ELM Characteristics in I-Coil ELM Suppressed Discharges on DIII-D' *Proc. 32nd EPS Conf. on Plasma Physics (Tarragona, Spain, 2005) vol 29C (ECA) P-4.012 (CD-ROM)*

[Oyama04] Oyama N. *et al.* 2004 *Nucl. Fusion* **44** 582

[Oyama06] Oyama N. *et al.* 2006 *Plasma Phys. Control. Fusion* **48** A171

[Oyama11] Oyama N. *et al.* 2011 *Nucl. Fusion* **51** 033009

[Ozeki90] Ozeki T. *et al.* 1990 *Nucl. Fusion* **30** 1425

[Pacher11] Pacher G.W. *et al.* 2011 *Nucl. Fusion* **51** 083004

[Pamela10] Pamela S. *et al.* 2010 *Plasma Phys. Control. Fusion* **52** 075006

[Parail02] Parail V.V. 2002 *Plasma Phys. Control. Fusion* **44** A63

[Park04] Park H.K. *et al.* 2004 *Rev. Sci. Instrum.* **75** 3787

[Perez04] Perez C.P. *et al.* 2004 *Plasma Phys. Control. Fusion* **46** 61

[Pillsticker84] Pillsticker M. and Werner F. 1984 *J. Phys. Colloques* **45** C1-171

[Poli01] Poli E. *et al.* 2001 *Comput. Phys. Commun.* **136** 90

[Preis91] Preis R. 1991 'Neutronen- und $\gamma$-Ratenmessungen am Tokamak-Experiment ASDEX' *IPP-Report* III/182

[ProgIPB07] Progress in the ITER Physics Basis 2007 *Nucl. Fusion* **47** S1

[Pütterich09] Pütterich T. *et al.* 2009 *Phys. Rev. Lett.* **102** 025001

[Rathgeber10] Rathgeber S.K. *et al.* 2010 *Plasma Phys. Control. Fusion* **52** 095008

[Reich07] Reich M. *et al.* 2007 'Calibration Method for the MSE diagnostic at ASDEX Upgrade' *Proc. 34$^{th}$ EPS Conf. on Plasma Physics (Warsaw, Poland, 2007)* vol 31F (ECA) P-2.127 (CD-ROM)

[Reimerdes00] Reimerdes H. *et al.* 2000 *Plasma Phys. Control. Fusion* **42** 629

[Reiter09] Reiter B. *et al.* 2009 'Application of AXUV Diodes For Broad-Band Plasma Radiation Studies in ASDEX Upgrade' *Proc. 36$^{th}$ EPS Conf. on Plasma Physics (Sofia, Bulgaria, 2009)* vol 33E (ECA) P-1.161 (CD-ROM)

[Reiter90] Reiter D., Wolf G.H. and Kever H. 1990 *Nucl. Fusion* **30** 2141

[Saarelma03] Saarelma S. *et al.* 2003 *Nucl. Fusion* **43** 262

[Saarelma09] Saarelma S. *et al.* 2009 *Plasma Phys. Control. Fusion* **51** 035001

[Saibene02] Saibene G. *et al.* 2002 *Plasma Phys. Control. Fusion* **44** 1769

[Saibene05] Saibene G. *et al.* 2005 *Nucl. Fusion* **45** 297

[Salmon94] Salmon N.A. 1994 *Int. J. Infrared Millim. Waves* **15** 53

[Sattler93] Sattler S. 1993 'Fluktuationen der Elektronentemperatur gemessen durch Intensitätsinterferometrie am Stellarator W7-AS' *IPP-Report* III/193

[Schirmer05] Schirmer J. 2005 'Plasma turbulence studies using correlation Doppler reflectometry on the ASDEX Upgrade tokamak' *Ph.D. thesis, Ludwig-Maximilians-Universität München*

[Schittenhelm97] Schittenhelm M. and Zohm H. 1997 *Nucl. Fusion* **37** 1255

[Schmitz12] Schmitz L. *et al.* 2012 *Phys. Rev. Lett.* **108** 155002

[Schneider12] Schneider P.A. 2012 'Characterization and scaling of the tokamak edge transport barrier' *Ph.D. thesis, Ludwig-Maximilians-Universität München*

[Smeulders99] Smeulders P. *et al.* 1999 *Plasma Phys. Control. Fusion* **41** 1303

[Snipes98] Snipes J.A. *et al.* 1998 *Plasma Phys. Control. Fusion* **40** 765

[Snyder02] Snyder P.B. *et al.* 2002 *Phys. Plasmas* **9** 2037

[Snyder04] Snyder P.B. *et al.* 2004 *Nucl. Fusion* **44** 320

[Sontag11] Sontag A.C. *et al.* 2011 *Nucl. Fusion* **51** 103022

[Stangeby90] Stangeby P.C. and McCracken M.G. 1990 *Nucl. Fusion* **30** 1225

[Stober01] Stober J. *et al.* 2001 *Nucl. Fusion* **41** 1123

[Stober05] Stober J. *et al.* 2005 *Nucl. Fusion* **45** 1213

[Stott05] Stott P.E. 2005 *Nucl. Fusion* **47** 1305

[Strait93] Strait E.J. *et al.* 1993 'Beta-limiting instabilities in DIII-D discharges with large bootstrap current' *Proc. 20th EPS Conf. on Controlled Fusion and Plasma Physics (Lisbon, Portugal, 1993)* vol 17C (ECA) I-211

[Streibl03] Streibl B. *et al.* 2003 *Fusion Sci. Technol.* **44** 578

[Suttrop97] Suttrop W. and Peeters A.G. 1997 'Practical Limitations to Plasma Edge Electron Temperature Measurements by Radiometry of Electron Cyclotron Emission' *IPP-Report* 1/306

[Suttrop00] Suttrop W. 2000 *Plasma Phys. Control. Fusion* **42** A1

[Suttrop07] Suttrop W. *et al.* 2007 'Active in-vessel coils and a conductive wall for MHD control in ASDEX Upgrade' *Proc. 34th EPS Conf. on Plasma Physics (Warsaw, Poland, 2007)* vol 31F (ECA) P-5.119 (CD-ROM)

[Suttrop09] Suttrop W. *et al.* 2009 *Fusion Eng. Des.* **84** 290

[Suttrop11a] Suttrop W. *et al.* 2011 *Phys. Rev. Lett.* **106** 225004

[Suttrop11b] Suttrop W. *et al.* 2011 *Plasma Phys. Control. Fusion* **53** 123014

[Szepesi09] Szepesi T. *et al.* 2009 *Plasma Phys. Control. Fusion* **51** 125002

[Terry07] Terry J.L. *et al.* 2007 *J. Nucl. Mater.* **363-365** 994

[Thomsen02] Thomsen K. *et al.* 2002 *Plasma Phys. Control. Fusion* **44** A429

[Tobias09] Tobias B. *et al.* 2009 *Rev. Sci. Instrum.* **80** 093502

[Ullrich97] Ullrich W. *et al.* 1997 *Rev. Sci. Instrum.* **68** 4434

[UNFPA11] United Nations Population Fund 2011 'State of World Population 2011'

[Verbeek86] Verbeek H. 1986 *J. Phys. E: Sci. Instrum.* **19** 964

[Viezzer11] Viezzer E. *et al.* 2011 *Plasma Phys. Control. Fusion* **53** 035002

[Viezzer12] Viezzer E. *et al.* 2012 *Rev. Sci. Instrum.* **83** 103501

[VonThun08] Perez von Thun C.P. *et al.* 2008 *Plasma Phys. Control. Fusion* **50** 065018

[Wagner82] Wagner F. *et al.* 1982 *Phys. Rev. Lett.* **49** 1408

[Wagner08] Wagner D. *et al.* 2008 *Nucl. Fusion* **48** 054006

[Watts04] Watts C., Hartfuss H.J. and Häse M. 2004 *Rev. Sci. Instrum.* **75** 3177

[Wesson04] Wesson J. 2004 'Tokamaks' (3rd edition) *Oxford University Press* ISBN 978 0 19 850922 6

[Wesson99] Wesson J. 1999 'The science of JET' JET-R(99)13

[Willensdorfer12] Willensdorfer M. *et al.* 2012 *Rev. Sci. Instrum.* **83** 023501

[Wilson99] Wilson H.R. and Miller R.L. 1999 *Phys. Plasmas* **6** 873

[Wilson06] Wilson H.R. *et al.* 2006 *Plasma Phys. Control. Fusion* **48** A71

[Wilson12] Wilson H.R. 2012 *Fusion Sci. Technol.* **61** 122

[Wolfrum93] Wolfrum E. *et al.* 1993 *Rev. Sci. Instrum.* **64** 2285

[Wolfrum11] Wolfrum E. *et al.* 2011 *Plasma Phys. Control. Fusion* **53** 085026

[Xing08] Xing Z. Li, Qing M. Wei and Bin Liu 2008 *Nucl. Fusion* **48** 125003

[Zohm96] Zohm H. 1996 *Plasma Phys. Control. Fusion* **38** 105

In the early twentieth century, scientists understood that nuclear fusion is the process that keeps the Sun burning and that controlling this process could also be a huge potential energy source on Earth.

The most successful scenario for fusion reactors, as currently foreseen, is tokamak operation of a plasma in high-confinement mode (H-mode). In H-mode, however, the plasma confinement suffers from an instability known as the edge localized mode (ELM). During a periodic collapse of the plasma edge, the ELM ejects hot parts of plasma. For larger tokamaks, this might lead to intolerable power loads on the plasma facing components. It is therefore crucial to understand the dynamics of the ELM cycle and its underlying physics.

For the work described in this thesis, a high resolution microwave camera was installed on the ASDEX Upgrade tokamak. With this diagnostic, it became possible for the first time to observe (in 2D) a variety of electron temperature fluctuations associated with the ELM. Describing the characteristics and dynamics of these various modes and their roles in the ELM cycle forms the major part of this work.

ISBN 978-90-386-3258-2